An upscaled study of a membrane filtration process in presence of biofilms

Sepideh Habibi

THÈSE

POUR L'OBTENTION DU GRADE DE

DOCTEUR DE L'ÉCOLE CENTRALE DES ARTS ET MANUFACTURES

SPÉCIALITÉ : GÉNIE DES PROCÉDÉS

Caractérisation multi-échelles d'un système de filtration en présense d'un biofilm

---

PRÉSENTÉE PAR : SEPIDEH HABIBI

DIRECTEURS DE THÈSE : BENOÎT GOYEAU,MOHAMMED RAKIB

ENCADRANTS : FABIEN BELLET, ESTELLE COUALLIER, FILIPA LOPES

SOUTENUE LE 08/07/2014

JURY

PATRICE	BACCHIN	PROFESSEUR-LGC-TOULOUSE	(RAPPORTEUR)
GÉRALD	DEBENEST	PROFESSEUR-MIFT-TOULOUSE	(RAPPORTEUR)
BENOÎT	GOYEAU	PROFESSEUR-ECP	(DIRECTEUR)
MOHAMMED	RAKIB	PROFESSEUR-ECP	(DIRECTEUR)
PATRICK	DI MARTINO	PROFESSEUR-ERRMECE	(EXAMINATEUR)
MURIELLE	RABILLER-BAUDRY	PROFESSEUR-UNIV-RENNES-1	(EXAMINATRICE)
FABIEN	BELLET	MAÎTRE DE CONFÉRENCES-ECP	(CO-ENCADRANT)
ESTELLE	COUALLIER	CHARGÉE DE RECHERCHE	(CO-ENCADRANTE)
FILIPA	LOPES	ENSEIGNANT-CHERCHEUR-ECP	(CO-ENCADRANTE)

DÉLIVRÉ PAR : ÉCOLE CENTRALE PARIS - ÉCOLE DOCTORALE 287 - SCIENCES POUR L'INGÉNIEUR

UNITÉ DE RECHERCHE : LABORATOIRE DE GÉNIE DES PROCÉDÉS ET MATÉRIAUX - EA 4038

ACKNOWLEDGMENTS

Research activity requires a high level of planning, executing and discussing. One needs innovative opinions, active contributions, continuous support and encouragement to elaborate the maximum of results . I think that a thesis project is not a personal achievement but the result of an enriching experience involving a group of researchers. During these last three years, I have been supported by many people to whom I am very grateful.

I would like to express my deep gratitude to my supervisor Professor Benoît Goyeau. He gave me great intellectual freedom to pursue my interests and provided encouragement and guidance throughout this work's lifetime. But, most I would like to thank him for his moral support during the ups and downs of my thesis years.

I would also like to thank my research supervisors, Professor Mohammed Rakib, for providing me such a good opportunity to work with him and letting me enter and enjoy the research world.

I would like to express my sincere gratitude to my supervisor Dr. Fabien Bellet, who gave me a lot of his time, pushed my limits constantly with his encouragement and supported me with positive energy. During the past three years, he not only helped me with my research project, but also cared for difficult moments I have been through both in personal and professional levels.

Special thank to my supervisor Dr. Filipa Lopes, for her guidance, valuable scientific participation and useful critics of this research work.

I would also like to thank deeply my supervisor Dr. Estelle Couallier, for her contribution in this research project and for her continuous encouragement and helpful discussions during these years. I would also like to extend my thanks to the jury members; reviewers and invited professors. First I would like to send my gratitude to Pr. Patrice Bacchin, Pr. Géerard Debenest for accepting to review my thesis. Then, I would especially like to thank Pr. Murielle Rabiller-Baudry for both for accepting to review this work and also for teaching me the FTIR-ATR technique. I truly appreciated her moral support during our collaboration in Rennes. I would also like to thank Pr. Patrick Di Martino for accepting to participate as an invited member and for his eventual remarks. Last and not least, I would like to thank Pr. Francisco Valdes-Parada for his assistance in developing the biofilm model, but most for being humble and so friendly.

My special thanks are extended to the Laboratory staff Nathalie, Barbara, Hélène, Vincent, Cyril and Thierry for their help in offering me the resources in running my experiments and in treating the results.
And of course, I would like to thank my office colleagues that changed every now and then, but even so we managed to create a special bound that I wish last with time. So, special thanks to Barbara, Quentin, Carmen and Zhaohuan who already left the laboratory while ago. Best wishes for Pascal on his research projects, and a special thank to Nadine for her continuous encouragement and support.
A special thank to my family. Words cannot express how grateful I am to my mother and father for all the sacrifices that they made so that I can achieve my dreams. The distance separated us for so long but you were always with me, making me stronger. Special thanks to my sister for her special support and patience. And last but not least, special thanks to my boyfriend for his love and support. Without them, I can not overcome any difficulties.

RÉSUMÉ

Dans un procédé de filtration, un fluide traverse une membrane (barrière sélective). Une force motrice s'applique entre les deux cotés de la membrane qui peut être un gradient de pression, température ou un potentiel électrique/chimique. Dans les procédés de filtration par un gradient de pression, certains composés du milieu fluide, traversent la membrane alors que d'autres sont retenues sur la surface membranaire. Ces procédés sont très utiles dans différents domaines de l'industrie, notamment en ce qui concerne le traitement des eaux et des effluents, biotechnologie, agroalimentaire et pharmacie. En plus les procédés de filtration offrent des installations plus compactes avec une optimisation des coûts opérationnels comparant avec des procédés traditionnels de séparation notamment distillation et cristallisation. Par ailleurs, ces procédés se réalisent en absence des additifs chimique et changement de la phase. Dans cette étude, on se focalise sur les procédés de microfiltration.

L'inconvénient principal de ces procédés est l'accumulation continue de particules/molécules sur la surface de la membrane. Ceci affecte la sélectivité de la membrane, modifie la qualité et la quantité de liquide passant à travers la membrane et conduit à une augmentation des coûts et de l'énergie. Le Colmatage (encrassement) membranaire se produit dans tous les types de procédés membranaires et par conséquent est connu le principal obstacle à l'utilisation répandue de ces procédés.

Différentes techniques sont utile pour surmonter les effets de l'encrassement de la performance de la membrane: le traitement physico-chimique des membranes utilisées, la modification des conditions opératoires (flux tangentiel de la solution d'alimentation sur la surface de la membrane est souvent appliqué pour réduire au minimum l'accumulation de particules), l'utilisation de membranes moins sensibles au colmatage, etc.

Tout dépendant de la nature des solutions traitées, les particules déposées sont très variables. Les micro-organismes, des matières organiques naturelles notamment les protéines, les polysaccharides, les substances humides, les oxydes inorganiques et les sels contribuent au colmatage des membranes.

Dans les dernières années, un grand nombre d'études expérimentales ont été investis pour comprendre les mécanismes de colmatage. Il a été souligné que les propriétés physico-chimiques de la membrane, la chimie des solutions et les conditions opératoires sont les trois principaux facteurs influant sur les mécanismes de colmatage. En par-

allèle, les modèles théoriques ont été proposés pour confirmer / décrire les observations expérimentales.
La modélisation du colmatage membranaire est un outil essentiel pour évaluer les mécanismes qui le causent. Il permet également prédire la performance du système de filtration et par conséquent trouver des stratégies adaptées pour empêcher la modification de la performance membranaire pendant le procédé de filtration.

En général, les modèles de classifient en deux grandes catégories: les modèles de transport de masse qui se concentrent sur la transport de solutés dans le procédé de filtration, et les modèles de colmatage basés sur le blocage des particules/molécules sur la surface ou à lntérieur de la membrane. Dans la plupart des cas, les modèles dépendent fortement des paramètres empiriques ou semi-empiriques et restent phénoménologique.
Deux objectifs principaux ont été fixés pour le travail présent:

1. Avoir une meilleure compréhension des mécanismes du colmatage membranaire lors de la filtration d'un milieu liquide contenant les micro-organismes en suspension. Il est important de souligner que des eaux industrielles et des eaux usées dans plusieurs domaines appartiennent à ce type d'effluents.

2. Proposer un modèle macroscopique décrivant les mécanismes de colmatage observés.

Au cours de la filtration de ce type de solution, d'une part, les bactéries se déposent à la surface de la membrane et développent progressivement un film biologique (biofilm) et d'autre part les matières organiques naturelles secrétées par le biofilm sccumulent sur la surface de la membrane et adsorbent partiellement ou bloquent les pores intérieurs. Il est intéressant de noter que le colmatage membranaire issue des matières organiques naturelles (telles que les protéines, les polysaccharides, les substances humides), est elle-même un phénomène complexe impliquant la formation d'un gradient de concentration à proximité de la surface de la membrane (la polarisation de concentration) et d'une série de mécanismes (formation d'un gteau, adsorption, blocage des pore).
durant le procédé de filtration, la résistance initiale de la membrane augmente non seulement par la résistance supplémentaire du biofilm; mais aussi par la pénétration et l'adsorption / dépôt de composés sécrétés (de biofilm) sur les pores de la membrane interne. En conclusion, les deux mécanismes simultanés (formation de biofilm à la surface de la membrane et le colmatage membranaire en volume) méritent d'être étudiées séparément afin d'obtenir une description plus précise des phénomènes mis en jeu dans chacun d'eux.
Les structures des biofilm et membrane sont très complexes et hétérogènes dans l'espace et le temps. Ils peuvent être considérés comme des milieux poreux multi-échelle. En fait, plusieurs longueurs caractéristiques sont présentes à l'échelle du pore: des composés chimiques comme des protéines (quelques nanomètres), les bactéries (1-2 μm) et les pores de la membrane (cent nanomètres). En outre, l'épaisseur du biofilm et la membrane varie entre quelques μm jusqu'à des centaines de μm. Il ne faut pas oublier que le temps

caractéristique des phénomènes de transport (convection, diffusion, adsorption, réaction céllulaire) est très variable également. Il convient de souligner que l'hétérogénéité du biofilm et la membrane rend l'approche de la modélisation difficile.
En raison de la complexité du problème du colmatage membranaire, deux systèmes (membrane et biofilm) sont étudiées et modélisées séparément dans ce travail.
Tout d'abord l'adsorption des protéines à la surface de la membrane est étudiée expérimentalement et théoriquement. On rappelle que les protéines ne sont pas les seules espèces produites par le biofilm, cependant, dans ce travail, ils représentent le produit extracellulaire du biofilm pour simplifier les complexités. En suite, l'évolution de la performance du système membranaire au cours de la filtration est déterminée expérimentalement. Les paramètres physiques locaux (constantes d'adsorption) et les propriétés structurelles de la membrane (porosité et perméabilité ainsi que les tailles caractéristiques) sont également caractérisés. Il est à noter que les expériences sont spécifiquement définis pour deux raisons: fournir des données initiales pour le modèle à l'échelle du pore et la validation éventuelle du modèle macroscopique par comparaison entre les résultats du modèle et les données de la filtration expérimentale à l'échelle de la membrane. En outre, un modèle macroscopique est développé pour décrire l'adsorption des protéines à l'intérieur des pores membranaires.

Le système de biofilm est étudié théoriquement. Un modèle macroscopique présentant des équations de transport de la masse et de la quantité de mouvement dans un volume représentatif est obtenu.
Pour les deux modèles, la stratégie suivante de la modélisation est appliquée: dans un volume élémentaire représentatif (VER), les équations locales de la masse et de la quantité de mouvement sont décrites et données, les conditions aux limites appropriées sont fixées également. En appliquant une méthode de homogénéisation, la méthode de la prise moyenne volumique, les équations macroscopiques non fermées sont obtenues avec des termes supplémentaires dus aux conditions limites.
La résolution des problèmes de fermeture locale est nécessaire dne part pour obtenir la forme fermée des équations moyennes et d'autre part, pour déterminer les propriétés effectives des milieux poreux (biofilm et membrane). Les paramètres physiques à l'échelle locale ainsi que des variations de la microstructure sont impliqués dans l'expression de ces propriétés effectives.
Le manuscrit est organisé en quatre chapitres: Dans le premier chapitre (état de l'art), des définitions fondamentales des procédés membranaires avec une attention particulière aux procédés de microfiltration sont donnés. Le concept du colmatage biologique (formation de biofilm) et dutres mécanismes associés au colmatage sont décrits. Par la suite, une vue dnsemble des procédés de filtration des solutions des protéines, formation des biofilms et des modèles associés est donnée. Dans la dernière partie de ce chapitre, les objectifs spécifiques de ce travail sont présentés.
Le deuxième chapitre est consacré à l'étude expérimentale de l'adsorption des deux biomolécules modèles (bovine sérum-albumine et L-glutathion) sur les membranes de microfiltration. a mérite de souligner que ces deux biomolécules ont été choisi

spécifiquement afin dvaluer les effets de la taille des molécules sur le phénomène ddsorption. Les expériences de filtration sont effectuées dans un module de microfiltration (Rayflow 100). L'évolution de la performance du système membranaire grce aux dépôts des protéines / adsorption est évaluée pour des solutions de protéines aux différentes concentrations. Les lois d'adsorption sont également déterminées pour chaque une des biomolécules. La technique FTIR-ATR est utilisée pour la quantification de la quantité des biomolécules adsorbé sur la surface de la membrane. Les caractéristiques structurelles des deux membranes dont la porosité moyenne, la distribution de la taille des pores, la taille moyenne des pores sont également mesurée par une analyse couplée sur les images de la microscopie électronique à balayage (MEB), la porométrie capillaire et la porosimétrie au mercure.
Dans le troisième chapitre, un modèle macroscopique est élaboré afin de prédire lvolution de la microstructure de la membrane due à ldsorption. A cet effet, des phénomènes locaux de transport de masse (diffusion et de convection) avec l'adsorption des protéines à l'interface de la membrane sont pris en compte. Le modèle macroscopique est ensuite développé en utilisant la méthode de la prise de moyenne volumique et les théorème associés avec cette méthode. Les équations moyennes de la masse et la quantité de mouvement avec l'expression des propriétés effective de la membrane (diffusivité et perméabilité) sont déterminées. Les équations moyennes de la mass et quantité de mouvement comprennent des termes supplémentaires liés à l'évolution de la microstructure de la membrane qui est elle même due à l'adsorption des protéines à l'interface. à la fin de ce chapitre, des simulations numériques sont réalisées pour la validation qualitative de la performance du système. A cet effet, la couche active de la membrane est remplacé par une surface de séparation et les équations de transport de masse et de quantité de mouvement sont résolues dans le fluide et de la membrane support poreuse avec une condition de saut de massique et mécanique couplée à l'interface.
Dans le quatrième chapitre, les équations macroscopiques de la masse et la quantité de mouvement dans le biofilm sont déterminées. Dans cette partie, la Convection et la diffusion des espèces décrivent les phénomènes locaux du transport de la masse alors que la réaction se fait seulement à l'interface cellulaire. Trois régions sont identifiées dans le volume de biofilm: des cellules bactériennes, la matrice des exopolymères (EPS) et des canaux daux. Les équations macroscopiques sont obtenues en appliquant la méthode de la prise de moyenne volumique basée sur lchelle des pores. Les propriétés effectives du biofilm (perméabilité et de la diffusivité) et les profils de concentration des espèces et des vitesses sont prédits en fonction du temps. En plus, l'évolution de la porosité de chaque région est dérivée dne manière explicite à l'échelle du biofilm et est représenté à dépendre de la réaction cellulaire. Enfin, des problèmes de fermeture locale de la quantité de mouvement sont résolues numériquement et le tenseur total de la perméabilité du biofilm est déterminée dans une région cellulaire représentative avec des conditions périodiques aux interfaces.

GENERAL CONTEXT

During a membrane filtration process, a liquid medium is filtered through a membrane (selective barrier). The applied driving force between two sides of the membrane can be a gradient of pressure, temperature or a chemical/electrical potential.
In pressure driven filtration processes (application of a pressure gradient as driving force between two sides of the membrane), certain components of the liquid medium pass through the membrane, while others are retained at the membrane surface. These processes are widely used as separation techniques in different industrial fields like waste water treatment, biotechnology, food and pharmacy. Compared to conventional techniques of separation (distillation, crystallization, ...), membrane processes offer more compact installations with more optimized operational costs. Moreover, membrane processes are mainly performed in absence of chemical additives and phase change. In this work we focus on the pressure-driven microfiltration membrane processes.
The main disadvantage of these processes is the continuous accumulation of particles on the membrane surface. This affects the membrane selectivity, modifies the quality and the quantity of the liquid passing through the membrane and leads to an increase of energy costs. Membrane fouling occurs in all types of membrane processes and therefore is known as the major obstacle for widespread use of these processes.
Different techniques are used to overcome the effects of fouling on the membrane performance: physical-chemical treatment of used membranes, modification of the operational conditions (tangential flow of the feed solution to the membrane is often applied for minimizing the particle accumulation to the membrane surface), use of membranes less susceptible to fouling, etc.
Depending on the nature of the treated solutions, the deposited particles are highly variable. Microorganisms, natural organic matter such as proteins, polysaccharides, humid substances, inorganic oxides and salts contribute notably to membrane fouling.
It should be noted that membrane fouling problem is a multi-physics (hydrodynamics, mass transport, physics, chemistry), multi-scale (different length scales are involved: molecules, pores and membrane surface) and time dependent (evolution of the membrane microstructure and the molecule-surface interactions) phenomena.
In the last decades, a huge number of experimental studies have been invested to understand fouling mechanisms. It has been pointed out that membrane physicochemical

properties, solution chemistry and operational conditions are the three major factors affecting the fouling mechanisms. In parallel, theoretical models have been proposed to confirm/describe the experimental observations.
Modeling of membrane fouling is an essential tool for assessing the fouling mechanisms. It helps predicting the membrane performance and consequently finding adapted strategies to prevent their modification during the filtration process.
In general, the models can be classified into two main categories: mass transport models which focus on solute permeation during the filtration process, and fouling models based on particle or solute blocking within the membrane porous structure. In most of the cases, models depend strongly on the empirical or semi-empirical parameters and thus remain phenomenological.

Two main objectives have been set for the present work:

1. Get a better understanding of the membrane fouling mechanisms during filtration of a liquid medium containing suspended microorganisms. It should be pointed out that several Industrial streams and wastewaters belong to this kind of effluents.

2. Propose a macroscopic model describing the observed fouling mechanisms.

During the filtration of this kind of solution, on one hand, the bacteria attach to the membrane surface and gradually develop a biofilm and on the other hand natural organic matter issued from the biofilm deposit on the membrane surface and partially adsorb or block its inner pores. It is worth to note that the membrane fouling caused by natural organic matter (such as proteins, polysaccharides, humid substances), is itself a complicated phenomenon involving the formation of a concentration gradient near the membrane surface (concentration polarization) and a series of mechanisms (cake formation, adsorption, pore blocking).
During filtration, the initial membrane resistance to flow increases not only due to the additional biofilm resistance; but also due to the penetration and consequent adsorption/deposition of secreted compounds (from biofilm) on the membrane internal pores. To conclude, the two simultaneous mechanisms (biofilm formation on the membrane surface and membrane fouling in volume) deserve to be studied separately in order to get a more clear description of the involved phenomena in each of them.
Biofilm and membrane structures are highly complex and heterogeneous both in space and time. They can be both considered as multi-scale porous media. In fact, several characteristic lengths are present at pore scale: compounds such as proteins (several nanometers), the bacteria (1-2μm) and the membrane pore (hundred nanometers). Moreover, the thickness of the biofilm and membrane varies between a few μm up to hundreds of μm. It should be stressed that heterogeneity of biofilm and membrane makes the modeling approach challenging.
Due to the complexity of the membrane fouling problem, two systems (membrane and biofilm) are studied and modeled separately in this work.

First the protein adsorption to the membrane surface is studied both experimentally and theoretically. We remind that proteins are not the only species produced by the biofilm, however, in this work, they represent the biofilm extracellular product, to simplify the complexities. The evolution of the membrane system performance during filtration is determined experimentally. Local physical parameters (adsorption constants) and membrane structural properties are also characterized. It should be noted that experiments are specifically set for two reasons: provide initial data to the model at pore scale and further model validation by comparison between the model results and data from membrane filtration experiments at membrane scale. Furthermore, an upscaled model is developed to describe the protein adsorption to the membrane internal pores.

The biofilm system is only studied theoretically. An upscaled model presenting equations of mass and momentum transport in its volume are derived.

For both models, the following modeling strategy is applied: in a representative elementary volume (REV), the local mass and momentum transport equations are given and the appropriate boundary conditions are set. By applying an upscaling method, the volume averaging method, the averaged but non-closed form of these equations with additional terms due to boundary conditions at the local scale are derived. The local closure problems are defined and solved in order to obtain the closed averaged form of the equations, in one hand, and to determine the effective properties (biofilm and membrane) on the other hand. Both physical parameters at local scale along with microstructural variations are involved in the expression of the effective properties.

The manuscript is outlined as follows: In the first chapter, a research based review of the fundamental definitions of pressure-driven membrane processes with special attention to the microfiltration processes are given. The concept of biofouling (biofilm formation) and the associated fouling mechanisms are described. Thereafter, an overview of filtration processes of protein solutions, biofilms formation and associated models are described. In the last part of this chapter, the specific objectives of this work are presented.

The second chapter is devoted to the experimental study of the adsorption of two model biomolecules (bovine serum albumin and L-glutathione) on microfiltration membranes. The filtration experiments are carried out in a microfiltration module (Rayflow 100). The evolution of the membrane system performance due to protein deposition/adsorption is evaluated for protein solutions at different concentrations. The protein adsorption laws are also determined. The FTIR-ATR technique is used for the quantification of the amount of adsorbed biomolecule on the membrane surface. The structural characteristics of two microfiltration membranes including mean porosity, pore size distribution, mean pore size are also measured by coupling Scanning Electron Microscopy (SEM) images with extended bubble point (porometry) and mercury porosimetry.

In the third chapter, an upscaled model predicting the membrane structure is elaborated. For this purpose, the local mass transport phenomena (convection and diffusion) with protein adsorption at membrane interface are taken into account. The upscaled model is then developed by using the volume averaging method. The averaged equations of mass, momentum with expression of the membrane effective properties (diffusivity and perme-

ability) are derived. Both averaged mass and momentum equations include an additional term for evolution of the membrane microstructure which is due to protein adsorption to the interface. At the end of this chapter numerical simulations with the aim of qualitative validation of the system performance are run. For this purpose the membrane active layer is replaced by a dividing surface and coupled equations of mass and momentum transport are solved in the bulk fluid and membrane porous medium with a mechanical and a mass jump condition at the interface.
In the fourth chapter, the governing upscaled equations of mass and momentum in the biofilm are determined. Convection and diffusion of species describe the local mass transport phenomena while reaction only takes place at the cellular interface. Three regions are identified in the biofilm volume: bacterial cells, EPS (exopolymers) matrix and water channels. The upscaled equations are obtained by applying the volume averaging method to the pore-scale equations. The effective properties of the biofilm (permeability and diffusivity) and the profiles of species concentration and velocities are predicted with time. The porosity evolution of each region is explicitly derived at the biofilm scale and is shown to depend on the cellular reaction. Finally, the local closure problems of the momentum transport are numerically solved and the biofilm total permeability tensor is determined in a representative cellular region with periodic flow conditions at the interface.

CONTENTS

A LITERATURE REVIEW

1 A LITERATURE REVIEW

The objective of this work is to get a better understanding of microfiltration membrane processes of mixed mixtures (containing bacteria and organic matter). This chapter provides a research review of background information on the membrane processes, solutions to be treated and their compositions and the presented obstacles for further improvement of the membrane technology.
This chapter is divided into eight parts:

- The first part presents the principles of the membrane processes, their applications and the analytical methods to investigate the physical-chemical characteristics of the membranes
- The second part presents the membrane fouling mechanisms, description of models and mechanisms taken into account in each model
- The third part provides a general vision of membrane biofouling (on surface by biofilm formation and in volume by adsorption or pore blocking)
- The fourth part focused on the characterization on quantification of membrane fouling by proteins and also a brief presentation of biofilms (definition and significant parameters on their development and growth)
- The fifth part consists of literature based review of the membrane fouling models and biofilm models
- The last part represents the specific objectives of this work with adapted strategies

1.1 PRESSURE-DRIVEN MEMBRANE PROCESSES

1.1.1 DEFINITION

Membrane separation technologies are widely used in the past decades in almost all kind of chemical, pharmaceutical, food and dairy industry. A membrane process is capable of performing a certain separation by use of a membrane. Memebrane is a selective barrier that permits certain mass transport of solutes and solvents across the barrier. The driving force for the transport is generally a gradient of a potential such as pressure, temperature, concentration or electric potential[17],[172].
The two main advantages of the membrane separation process are listed:

- It consists of physical separation in which there is neither addition of chemicals nor phase change during the filtration process.
- The installation designs are mainly simple, adaptable and economical (in order of several kWhm^{-2}).

In the following sections, operational principles, different membrane compositions, configurations, and characteristics are given.

1.1.2 OPERATIONAL PRINCIPLES

During a filtration process, the bulk solution arrives to the membrane surface and divides to two parts:

- A part which passes the membrane (permeate or filtrate)
- A part which does not pass the membrane (retentate or concentrate) in which the concentration of retained molecules or particles will increase.

Depending on the industrial application, the permeate or retentate streams can be both objectives of the membrane processes: for example the In waste water treatment, several filtration processes are performed in order to collect a permeate stream with improved water quality which can be either reused or recycled, whereas retentate stream in the extraction of protein solutions or concentration of fruit juice is the aim of membrane process.
Transmembrane pressure TMP is the averaged pressure applied between two sides of the membrane (permeate and retentive streams) and represents the driving force of the filtration process. It determines the productivity (permeate flow) of the membrane process.

$$\Delta P = ((P_{re} + P_{re'})/2) - P_p \tag{1}$$

Where P_{re}, $P_{re'}$ are the applied pressure of the entrance and exist of the membrane module at the retentate side stream. P_p is the absolute pressure at the permeate side stream and is generally equal to the atmospheric pressure. Technically, the membrane processes can be performed either in fixed pressure mode or in fixed permeate flow mode.

1.1.3 CROSS FLOW AND DEAD-END FILTRATION

In conventional filtration processes, the liquid flow is brought perpendicularly to the membrane surface which is presented as dead-end filtration. In this process, there is no retentate flow (no circulation of the retentate) and the continuous particle accumulation on the membrane surface results in reduction of permeate flow with time.
In crossflow filtration, the bulk fluid flow is tangential to the membrane surface and divides into two streams. The retentate is recirculated and mixed with the feed solution, where the permeate flow is collected on the other side of the membrane. In crossflow filtration, the decrease in permeate flow is also caused by the continuous accumulation of particles on the membrane surface.
The dead-end mode is relatively less costly and easy to implement. The main disadvantage of a dead-end filtration is the extensive membrane fouling, which requires periodic interruption of the process to clean or substitute the filter [63]. The tangential flow devices are less susceptible to fouling due to the sweeping effects and high shear rates of the passing flow.These two configurations of membrane filtration processes are presented in Fig.1

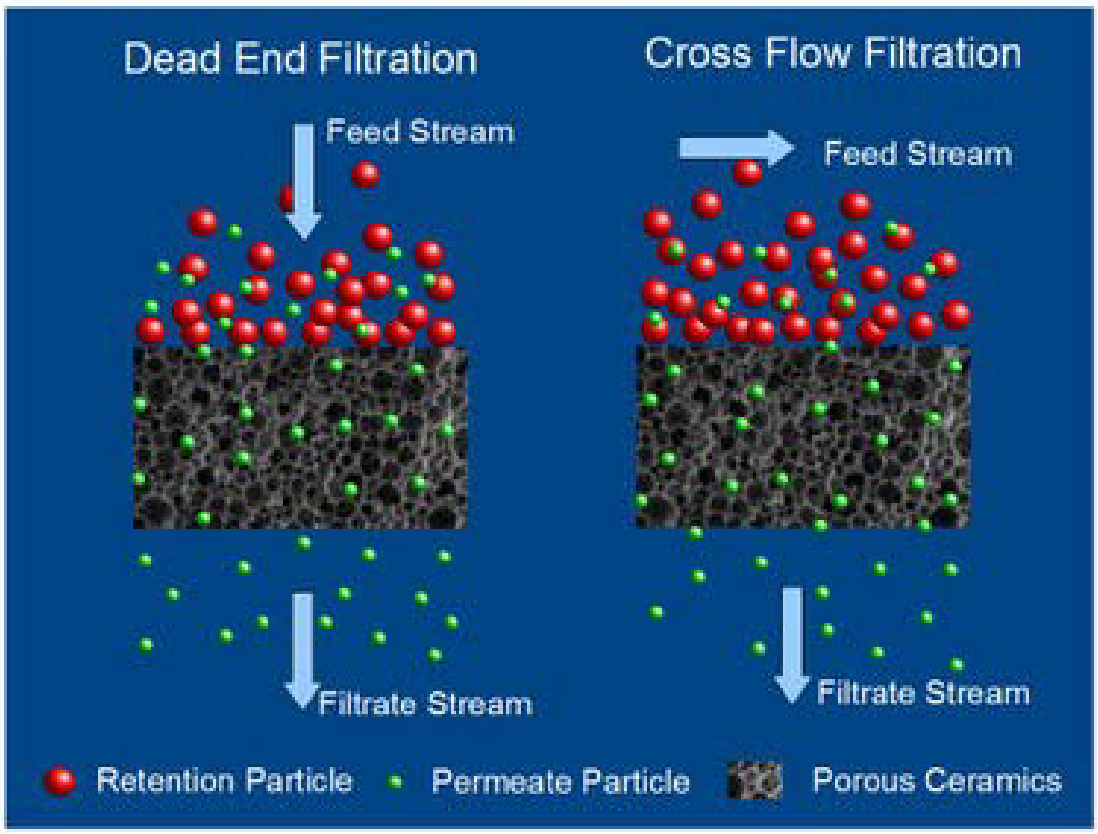

Figure 1: Membrane flow configurations. Left: Dead-end filtration. Right: Cross flow filtration. Source: www.induceramic.com/porous-ceramics-application/filtration-separation-application

1.1.4 MEMBRANE PERFORMANCE AND ASSOCIATED LIMITATIONS OF MASS TRANSFER

The major limitation in the membrane performance is related to the inevitable accumulation of solutes and/or particles to the membrane surface. This phenomenon is called fouling and affects significantly the performance of the membranes in terms of productivity (permeate flow) and selectivity (membrane capability to retain certain particles). Different parameters have been shown to play important roles in fouling phenomenon (e.g. hydrodynamic conditions, membrane-solutes interactions, membrane properties).

1.1.5 TYPES OF MEMBRANES: MICROFILTRATION, ULTRAFILTRATION, NANOFILTRATION, REVERSE OSMOSIS

In the field separation of liquid solutions by membrane processes, four main categories have been identified microfiltration (MF), ultrafiltration (UF), nano filtration (NF) and reverse osmosis (RO) which are distinguished by the membrane's selectivity and subsequent retained particles in each process. (Fig.2) The retentate/permeate flow and nature of interactions between membranes and particles are also function of chosen membranes in each process.
The membrane's molecular weight cut off (MWCO) corresponds to the molar mass of the solute that is (or would be) retained 90% by the membrane.It is usually expressed in Da (1 Da= 1 g/mol^{-1}). However, this definition remains inaccurate since neither the nature of the retained solutes nor the electrostatic interactions between the membrane and solutes are not taken into account in the definition. Therefore, considerable differences between absolute membrane cut-off and those quoted by the manufacturers have been reported.
In Table.1, different types of membranes with corresponding applied pressures and retained particles are presented.

Table 1: Size of material retained, driving force, and type of membrane[172]

Process	**Minimum particle size removed**	**Applied pressure**	**Type of membrane**
Microfiltration	0.025-10 μm, microparticles	(0.1-2 bar)	Porous
Ultrafiltration	5-100 nm, macromolecules	(1-10 bar)	Porous
Nanofiltration	0.5-5 nm, molecules	(4-20 bar)	Porous
Reverse osmosis	$<$1 nm, salts	(20-80 bar)	Nonporous

Microfiltration (MF)
Microfiltration membranes (mean pore size between 0.1 to a few μm) are applied to retain macromolecules and colloidal particles from a bulk fluid. Fluids containing bacteria or large viruses, oil emulsions, proteins or yeast, colloidal particles or pigments are subject of microfiltration processes. The microfiltration membrane structure is porous and the

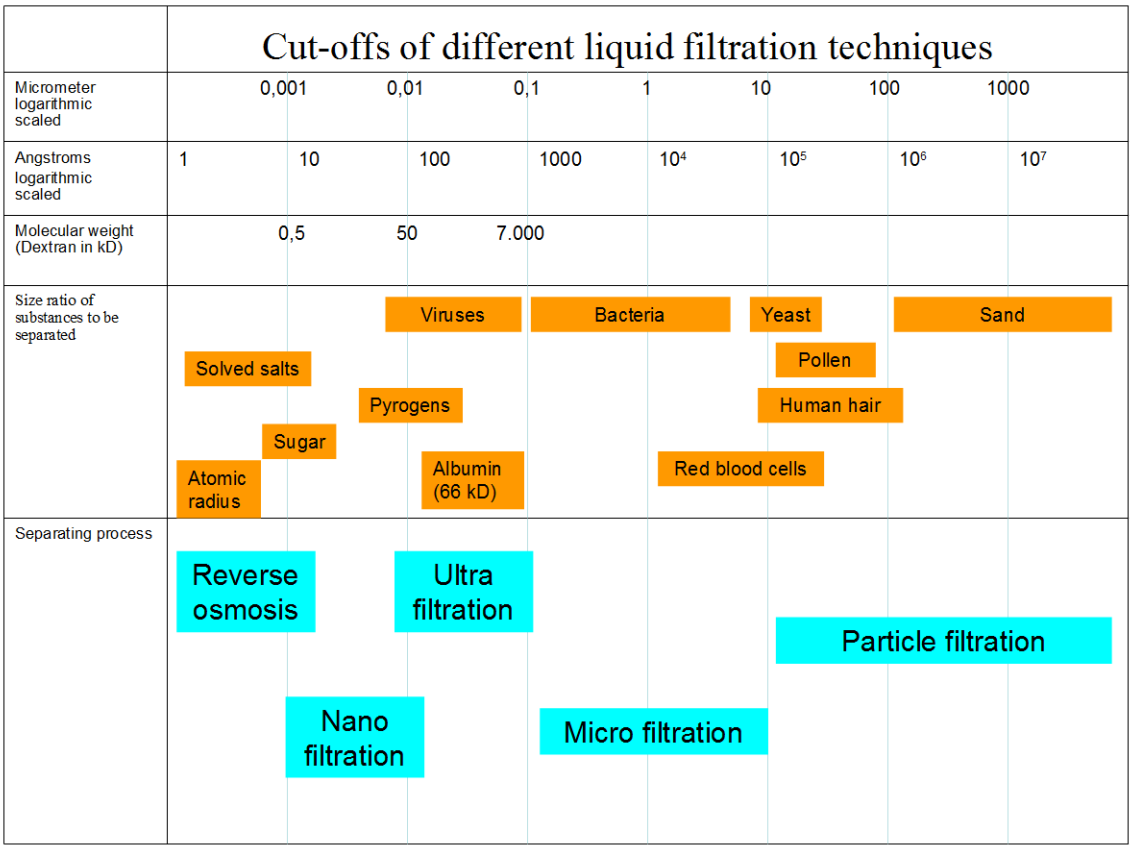

Figure 2: Cut-offs of different liquid filtration techniques, from[151].

applied pressure gradient is lower than 2 bar. MF processes have been widely used in food, dairy and biotechnology installations [156], [209].

Ultrafiltration (UF)

In ultrafiltration processes, suspended solids and solutes with molecular weight higher than 300 kDa are retained.Therefore UF processes can be useful for retaining proteins, antibiotics and certain ions [104], [115]. The membrane pore size varies between 2 and 100 nm and the applied pressure gradient is larger than 1 bar.In theory, there is a clear difference between microfiltration and ultrafiltration pore sizes, however these techniques can be combined technically in different domains in order to minimize the particle accumulation to the membrane surface and consequent energy loss.

Nanofiltration (NF)

The NF processes are known for retaining small particles and dissolved molecules, specially multivalent ions in complex solutions. The processes are applied mostly for treating the surface water and fresh groundwater in order to softening (removal of multivalent ions) the water or retaining natural and synthetic organic matter. [215],[225]. NF membranes properties are between reverse osmosis (RO) membrane and UF membranes. The membrane pores are less than 1 nom and the applied pressure gradient is in the range of 4 and 20 bar[63].

Reverse osmosis (RO)

Reverse osmosis membranes are dense membranes without distinct pores. In these processes monovalent ions ($< 10A°$)[63] can be retained. The applied pressure gradient range is between 40 and 100 bar. In RO processes, the solvent is forced by pressure gradient to pass through the dense membrane from a region of high solute concentration (retentate) to a region of low solute concentration (permeate). The most important application of RO is for desalination of sea water and brackish waters and to production of pure water. Recently, RO processes are also used in food sector for concentrating the food liquids (fruit juice for example) because of their low operational costs compared to convectional heat treatment/vacuum evaporation methods [113], [152], [206].

1.1.6 MICROFILTRATION PROCESS DESCRIPTION

Microfiltration membrane processes are extensively used for in different industrial fields. One major use of MF processes contains the treatment of potable water supplies. The MF process is the key step in the primary disinfection in the membrane filtration series for production of pure water. The initial stream might contain resistant pathogens to the traditional disinfectants (chlorine for example). MF processes offer a physical separation of these particles with use of the membrane as barriers [15]. Another useful application for MF processes includes the cold sterilization both in food sector and pharmacy[49]. This is one main advantage compared to traditional heating methods in which there is major loss of effectiveness for pharmaceuticals and flavor and freshness modification of food products. In past decades, MF processes have also got interest in petroleum refining, dairy industry, biochemical and bioprocessing applications [15].

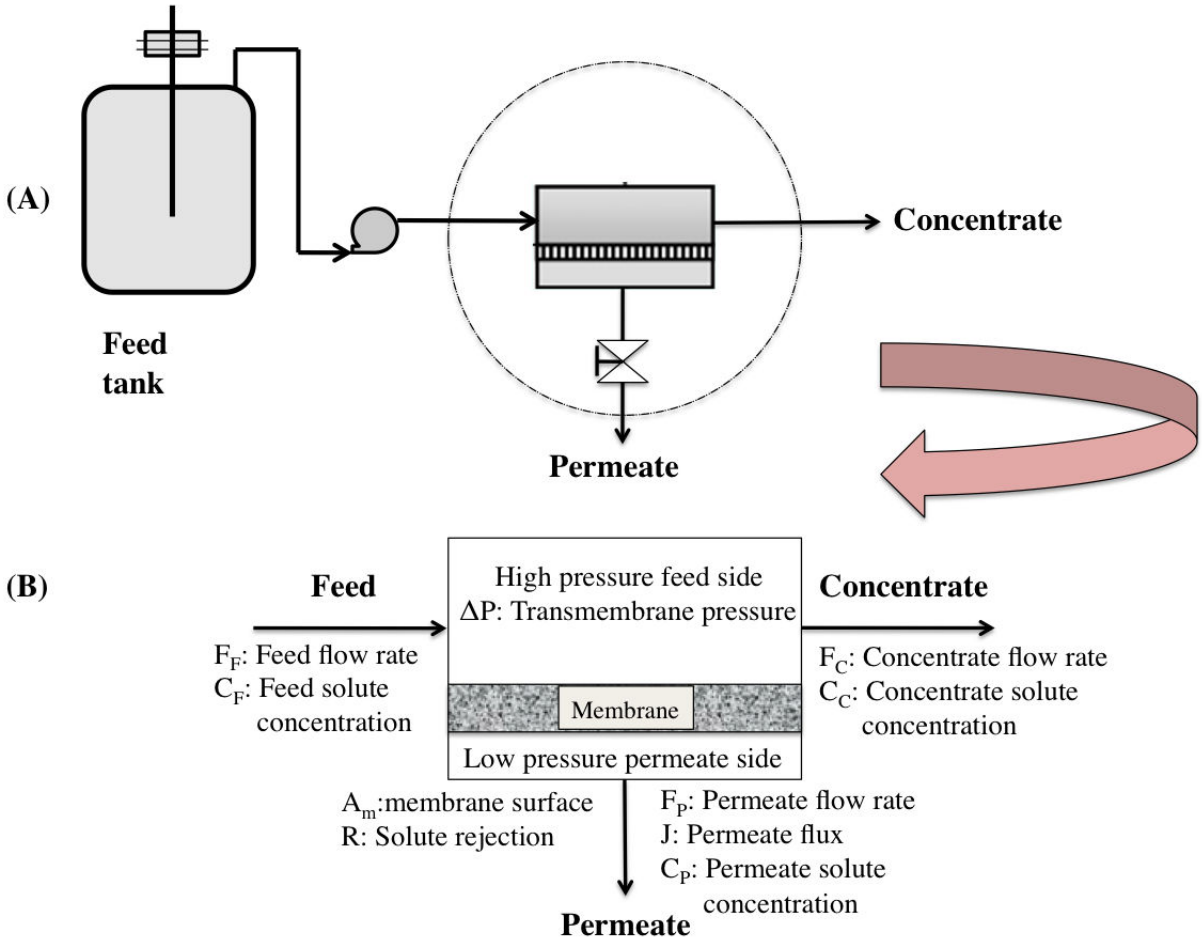

Figure 3: Scheme of (A) Microfiltration process and (B) Microfiltration streams.

A diagram of a microfiltration process is shown in Fig.3-(A). The microfiltration process consists of a feed solution, a pressure pump and the microfiltration module. Three streams including feed, permeate and concentrate (retentate) are shown in Fig.3-(B). The solvent transfer through the membrane determines the efficiency of the process in terms of productivity. In literature, the permeate flow is presented by Darcy law, where it is proportional to the applied pressure and the membrane membrane permeability. This resistance is inversely proportional to the membrane permeability.

$$J = \frac{K\Delta P}{\mu\delta_m} = \frac{\Delta P}{\mu R_m} = L_p \times \Delta P \tag{2a}$$

$$R_m = \frac{\delta_m}{K} \tag{2b}$$

The permeate flux, is also proportional to the permeate flow rate and the membrane surface

$$J = \frac{F_P}{A_m} \tag{2c}$$

In Eq. (2a), J is the permeate flow per unit surface of the membrane (m/s), ΔP is the transmembrane pressure (Pa), μ is the fluid viscosity (Pa.s), K is the membrane intrinsic permeability (m^2), δ_m is the membrane thickness (m), R_m is the membrane hydraulic resistance (m^{-1}) and L_p is the membrane hydraulic permeability ($m.s^{-1}.Pa^{-1}$ or $Lh^{-1}.m^{-2}.bar^{-1}$) . Solute separation is measured in terms of rejection, R, defined as

$$R = 1 - \frac{C_P}{C_F} \tag{2d}$$

The permeate flux is sometimes normalized relative to the initial or pure water flux (J_W) as J/J_W, Thus the flux decline is defined as

$$\text{Flux decline} = 1 - \frac{J}{J_W} \tag{2e}$$

1.1.7 MEMBRANE MATERIALS AND STRUCTURE

The membranes are porous or dense materials composed of organic (polymers) or inorganic (ceramic, glass, minerals) materials [194]. In general, the organic membranes are composed of different layers (active layer, intermediate layer and mechanical support). The thin top layer of the membrane (active layer) is mainly responsible for the particle retention and determines the membrane selectivity. The thickness of this layer varies between 0.3-3 μm [24]. The membrane overall thickness is in range of 100 μm. the membrane's active layer can be composed of different polymers such as polysulfone (PSU), Polyethersulfone (PES), Polyvinylidene fluoride (PVDF), polycarbonate (PC), cellulose acetate (CA), nylon (N), etc. The interactions between the membrane and solutes are function of chosen polymers for membrane fabrications. A sectional SEM image of a PES microfiltration membrane is shown (three layers) in Fig. 4.
Polyethersulofon (PES) membranes are widely used in microfiltration processes, however polyvinylidene fluoride (PVDF) [31] offer a better performance in terms of permeate flow in filtration processes. Polycarbonate track-etched membranes are mostly used for research experiments. The pores of track-etched membranes are more uniform than industrial membranes and can be used to better understanding of fouling mechanisms.
Mineral membranes are composed of an alumina (Al_2O_3) or carbon matrix, on top of which a variable number of inorganic oxide layers (ziecone, alumni, TiO_2) are deposited. They offer excellent chemical and thermal resistances compared to organic membranes, however their price remain high [24].
Depending on the application, There are also different membrane configurations (flat membranes, spiral modules, tubular membranes and hollow fibers). The operational costs depend on the membrane systems configuration. Industrial fields are more interested

in compact installations with a high ratio of membrane surface/module volumes (spiral modules).

Different membrane materials, mean pore size and module configurations are presented in Table.2.

Table 2: Microfiltration membrane materials and module configurations for filtering the protein solutions

Membrane material	Module configuration	Characteristic pore size	References
Ceramic	Plane	$0.1\mu m$	[62], [95], [156]
Polyethersulfone (PES)	Plane/Spiral/Hollow fiber	0.1, 0.16, 0.2, 0.4 μm	[66], [169], [186], [193], [222], [223]
Polycarbonate	Plane	0.1,0.2,0.4,1 μm	[33],[99], [189], [129]
Cellulose	Plane	0.1,0.22 μm	[109], [110], [111], [132]
Nylon	Plane	0.2,0.45 μm	[112], [193]
Polyvinylidene fluoride (PVDF)	Plane	0.1,0.2 μm	[31], [85]

1.1.8 MEMBRANE CHARACERIZATION

membrane morphology and its surface chemistry affect the particle deposition and the resulting membrane fouling. Membrane structure (mean pore size, pore size distribution and porosity) are determining parameters for retained particles on the membrane. Nevertheless the membrane chemical composition and surface charge can also modify the electrostatic interactions between particles and membrane surface. For instance the hydrophilicity of the membrane plays an important role on the quantity of particle deposition on the membrane surface.

The membrane efficiency is usually evaluated in terms of permeate flow through the membrane or permeability in the filtration process as well as solute rejection or selectivity. However, these separation properties depend in the characteristics of the membrane surface (especially the active layer), thus, there is an inevitable need for obtaining the membrane characteristics to provide better information of explanation of the observed membrane performance.

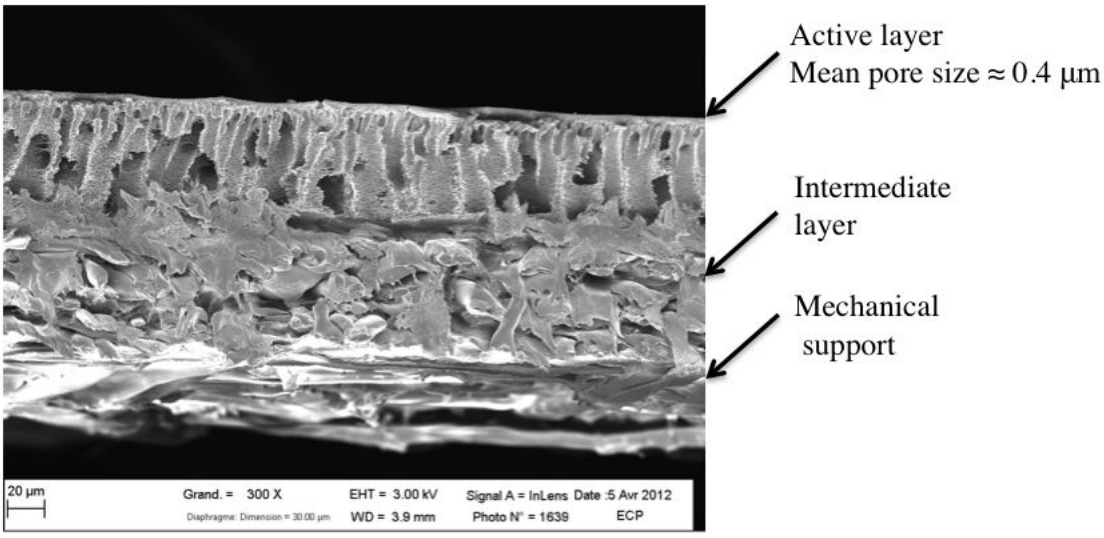

Figure 4: SEM image of three layers of a PES microfiltration membrane. (purchased from ORELIS)

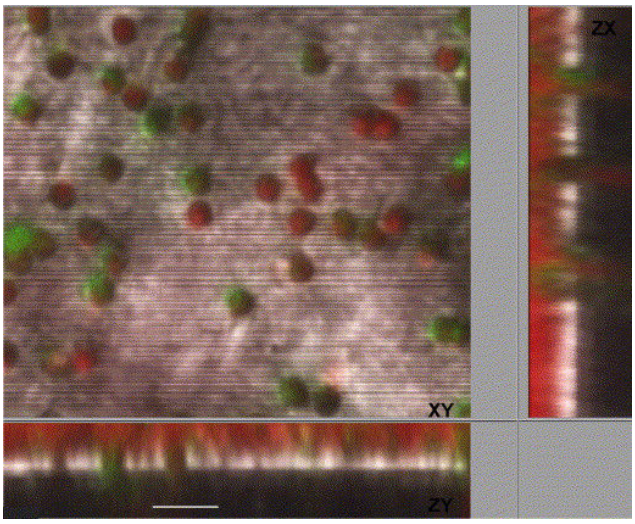

Figure 5: A 3D reconstruction of a 0.8 μm polycarbonate membrane fouled by a protein binary solution of BSA-fluorescein conjugate and OVA-Texas red conjugate. Green and red signal corresponds to adsorption/deposition of BSA-fluorescein conjugate and OVA-Texas red conjugate respectively. Black and gray colors show pores and membrane surface. Scale bar = 2 μm [81].

1.1.9 CHARACTERIZATION OF MEMBRANE MORPHOLOGY

The information of porous structure of membrane (active layer and sublayers) are provided by direct microscopic techniques. The most commonly applied methods are scanning electron microscopy (SEM) and atomic force microscopy (AFM). Confocal scanning laser microscopy (CSLM), Transmission electron microscopy (TEM) and SEM can be applied to characterize the membrane structural properties, however, the resolution of CSLM is only sufficient for characterization of MF membranes [46], [47], [111],[119], [152], [268] (maximum resolution of 180 nm in the focal plane (x,y) and only 500-800 nm along the optic axis (z)). In the work of [81], the microfiltration membrane fouling by a binary solution of proteins has been studied and membrane reconstruction from CSLM images has been shown in Fig. 5.

Scanning electron microscopy (SEM) allows the direct observation of membrane morphology and the fouling layer from surface images or cross section images of the membrane [95], ,[111],[215], [222],[223]. In SEM measurements, a fine beam of electrons scans the membrane surface, causing several kinds of interactions which generate signals like secondary electrons (SE) and backscattered electrons (BSE). The number of secondary electrons (SE) is a function of the angle between the surface and the beam The images of SE can be used to visualize membrane morphology, such as pore geometry, pore size, pore size distribution and surface porosity. Low-voltage SEM is typically conducted in an FEG-SEM because the field emission guns (FEG) is capable of

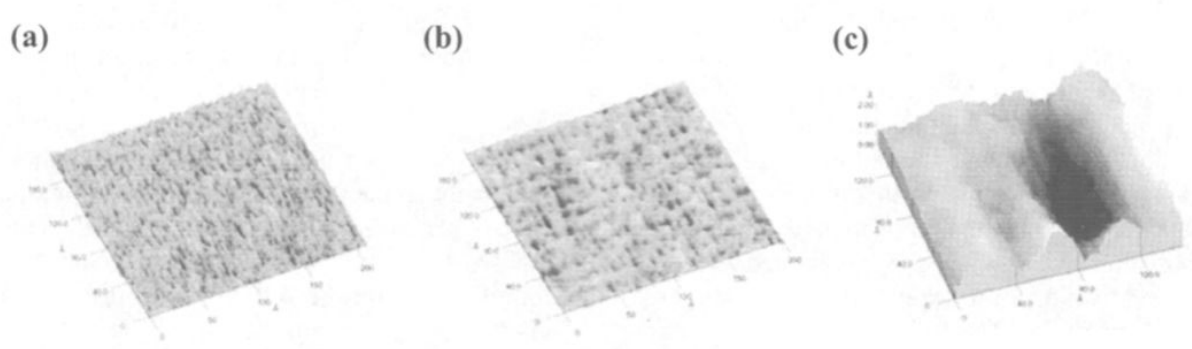

Figure 6: Visualization of membrane surface by AFM. (a) image of a ES 404 membrane (MWCO = 4 kDa) (b) AFM image of a modified XP 117 membrane (MWCO = 4 kDa) (c) image of a single pore of 4 nm in NF membranes. From [101]

producing high primary electron brightness and small spot size even at low accelerating potentials. FEG-SEM provides the highest resolution of images (no larger than 5 nm). Therefore,macrostructure information of MF and UF membranes are possible to obtain. One main disadvantage of SEM technology is that it includes always an underestimation of pore size determination. This is caused by the metallic layer deposited to the membrane surface which partly covers the membrane pores. Environmental scanning electron microscopy (ESEM) may also be useful for determination the macrostructure of the membrane(resolution limits only for MF membranes). One main advantage of ESEM is that there is no need of sample preparation and wet membranes can be analyzed.

Transmission electron microscopy (TEM) is based on the same principles as scanning electron microscopy. The nature of analyzed enelctrons are different in these techniques. In TEM technology,passing electrons through the sample are analyzed: diffracted electrons which interact with the sample and deflected from their coarse and transmitted electron with interact (or not) with the sample and are not deflected. The samples must be dry and have a thickness of the order of (100 nm- 10 μm). TEM technology has been used both for surface analysis of UF and NF membranes. It has also been applied to visualize the deposited layers of BSA to the membrane surface [152], [173].

Atomic force microscopy (AFM) can be applied both in the determination of the membrane morphology (mean pore size and pore size distribution)[215] and also determination the force of adhesion of particles to the interacting membrane surface [30],[101]. In AFM, the probe is mounted on a free end of a tiny cantilever sprig. It moves by a mechanical scanner over the membrane surface sample. Each variation in the surface height

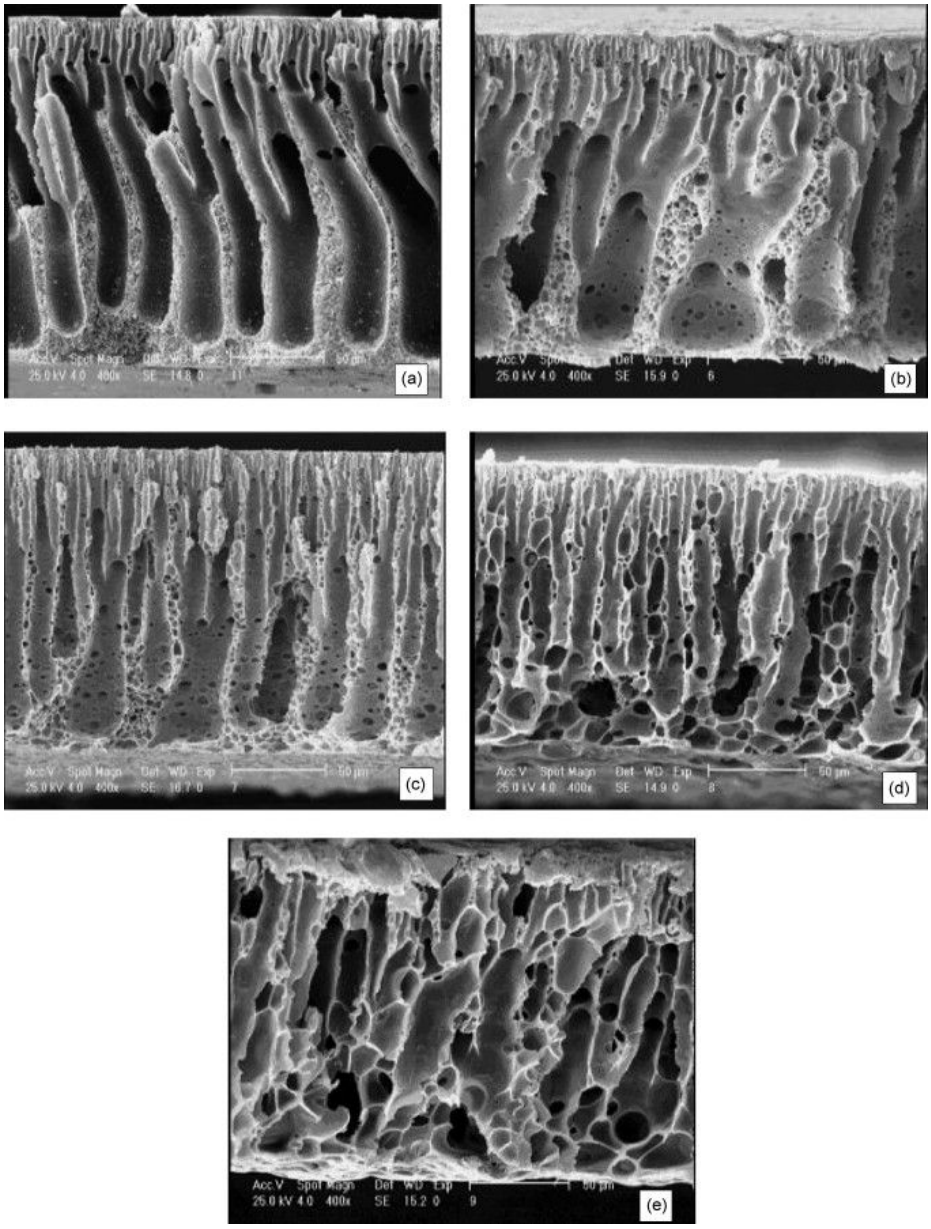

Figure 7: SEM cross sectional images of PES/CAP mixed membranes with 2 wt% of PVP: (a) 100/0, (b) 90/10 (c) 80/20, (d) 70/30, (e) 60/40. From the work of [215].

modifies the interactions (Van der Waals in order of some nanonewtins) between the tip of the probe and the sample and consequently varies the bending of the tip [152]. Images of the membrane morphology are then reconstructed by specific softwares associated with AFM. Four different modes including contact, non-cotact, tapping and double electric layer modes [30] are used for characterization of different membrane morphologies from MF to RO membranes, for the determination of pore size, surface porosity, pore density, pore size distribution and surface roughness [95],[215],[243], [265]. The membrane surface visualization by AFM are shown in Fig. 6. AFM technique has also been applied directly for measuring the physicochemical interactions (adhesion force, affinity) of particles with the membrane surface. Bowen et al. determined the interaction forces between PES membranes with Bovine serum albumin (BSA) and yeast particles and showed that the adhesion potential is more important for BSA molecules than yeast particles [32].

Mean pore size and pore size distribution of porous materials (membranes, paper, textile, hollow fibers, etc.) can be determined by capillary flow porometry method. Pore sizes in the range of 15 nm to 500 μm can be detected by this technique. This technique is based on the displacement of a wetting liquid inside a porous network by means of an inert gas flow. The wetting liquid enters spontaneously the pores in a material as a result of the capillary force until the height of liquid equilibrates with gravity. It is known that the Young-Laplace equation establishes between the pressure across an interface between two fluids (in the case of wetting liquid and air) and the radius of a capillary. The equation that relates these two variable is:

$$\text{Pressure} = 4 \times \gamma \times cos\theta \times (\text{shape factor})/\text{diameter} \tag{3}$$

Where γ is the surface tension of the wetting liquid, θ the contact angle of the liquid on the solid surface. The shape factor is a parameter depending on the shape and the depth of the pore inside the material. The surface tension is a measurable physical property and is available for many liquids. the contact angle θ however, depends on the interaction between the material and the wetting liquid. Typical wetting liquid used in porometry are perfluoethers. They have a low surface tension (16 dynes/cm) and a contact angle of $0°$ and chemically inert almost with all materials.
A typical measurement s shown in Fig. 8 which consists of : first bubble point or largest pore, mean flow pore, smallest pore, cumulative flow, differential flow and correlated differential flow. The smallest pore represents the smallest openings inside the porous material. there are opened right before the material has become completely dry. The smallest pores are therefore calculated at the point where the wet curve and dry curve start to coincide. The average pore size or mean flow pore size is calculated at the pressure where the wet curve and the half-dry curve cross. The half-dry curve itself is obtained by the mathematical division by 2 of the data originating from the dry curve.

Mercury intrusion porosimetry (MIP) is another useful technique to characterize the porosity and the distribution of pore sizes in porous media (pores between 2μm-10mm).

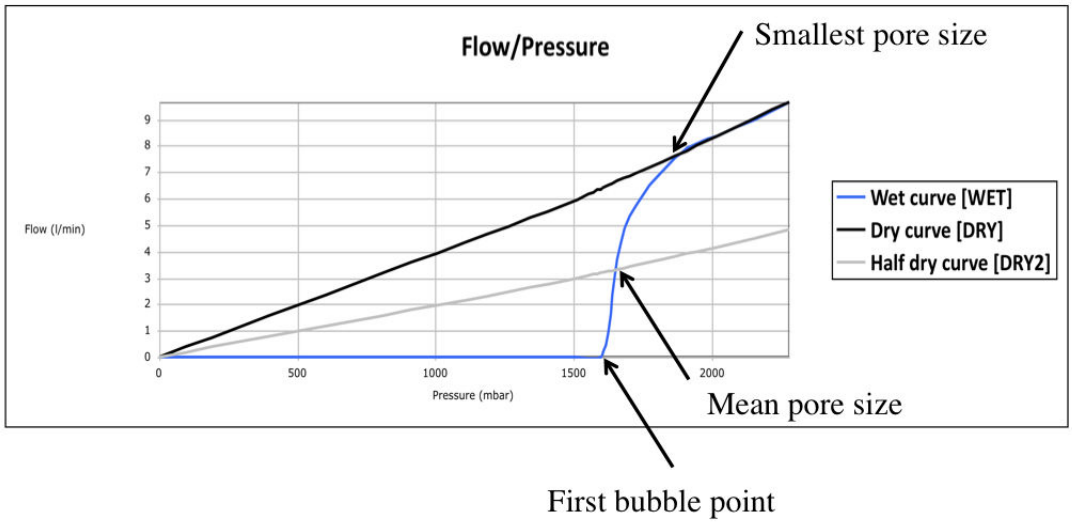

Figure 8: Typical measurements of capillary flow porometer (microfiltration PES membrane, supplied by KOCH: Mean pore size=0.4μm), blue: wet curve, grey: half dry curve, black: dry curve.

Mercury (non-wetting liquid, with a contact angle greater than $90°$) .must be forced using pressure into the pores of a porous material. The pore size distribution is then determined from the volume intruded at each pressure increment. Total porosity is determined from the total volume intruded[3]. The relationship between the pressure and capillary diameter is described by Washburn (1920) (Eq). (1.3).

$$\text{Pressure} = \frac{-4\gamma Cos\theta}{d} \tag{4}$$

Where P is pressure, γ is the surface tension, θ is the contact angle and d is the pore diameter. In this model it is assumed that pores are regular, interconnected and not affected by penetration of mercury inside the pores. Therefore, Irregular pore geometries can not thoroughly be characterized by this technique.
The choice of characterization method is generally made based on the problem to which an answer is required and on the time, cost and resources available. However, the best knowledge is always obtained by combining results from different characterization methods.

The X-ray tomography can also be used in order to determine the distribution of the membrane pore size, 3-D structure of the membrane and also the distribution of the particles/molecules trapped within the membrane pores and results in membrane permeability drop [68],[242]. It should be pointed out that this technique can be used for the microfiltration membranes and the image resolution does not permit to determine the pores smaller than 30-40 nm.

1.1.10 CHARACTERIZATION OF MEMBRANE CHARGE

When a solid charged surface is in contact with an electrolyte, an electric double layer forms at the solid-liquid interface. This electric double layer plays an important role in colloidal/membrane systems. The charged sites of a membrane surface affect the spatial distribution ions adjacent to the membrane surface. Subsequently there is attractive interactions between the opposed charged particles and a repulsive one between the same charged particles with the membrane surface.
Streaming potential (SP) measurements between two membrane surfaces provide information about the overall membrane surface charge. Moreover, the membrane isoelelectric point (IEP, pH in which membrane is neutral)[62], [221]and the evolution of the membrane charge (caused by deposited particles) during the filtration can be determined [108], [270], [152].

1.1.11 CONTACT ANGLE MEASUREMENTS FOR MEMBRANES

During a membrane filtration process, the membrane hydrophilicity is modified progressively due to particle deposition on the membrane surface [95]. Thus the membrane

performance depends on the evolving surface characteristics which depends itself on the nature of deposited particles and their interactions with the membrane.

Contact angle measurement is the most common technique for obtaining the global characteristics of the hydrophilicity (wettability) of solid surfaces. The interfacial tensions of a solid surface play role on the measured contact angles, therefore, the technique can also be used to characterize theses interactions.

Membrane hydrophilicity is a crucial factor affecting membrane performance when organic molecules are separated from aqueous solutions [95], [152]. The hydrophilicity can be described by the degree of wettability of the solid surface. It is important to determine the membrane hydrophilicity to investigate the relationship between membrane performance and its surface characteristic. Moreover, membrane fouling can modify the membrane hydrophilicity. For example in the work of Kaplan et al.[123], it has been shown that the initial hydrophilicity of a PES membranes (NF) has been reduced during the filtration of proteins (lysozyme), In other fords, the deposited/adsorbed layer makes the membrane surface more hydrophobic.

1.2 MEMBRANE FOULING

During the filtration process through a membrane, solutes/particles accumulate/deposit continuously on the membrane surface. Thus the membrane properties (selectivity and permeate flux) are significantly modified with time. This phenomenon is called fouling and is known as the major obstacle for the widespread use of filtration processes. Fouling is a multi-scale (occurring both on the membrane surface and in the membrane pores) and multi-physical phenomena which is influenced by three important factors: structural characteristics of the membrane (composition, porosity, permeability, hydrophilicity and roughness), hydrodynamic operational conditions (velocity, transmembrane pressure and temperature) and solvent characteristics (ionic strength, pH, solute concentration, etc.). Two categories of membrane fouling have been identified : reversible and irreversible fouling. Both mechanisms increase the membrane hydraulic resistance and decrease the solute mass transport through the membrane. The reversible fouling occurs mostly at the membrane surface and can be removed by physical treatments . The irreversible fouling on the other hand is caused mainly by irreversible attachment/deposition of particles (due to electrostatic or hydrophobic interactions) with the membrane surface and can be removed partly by chemical cleaning of the membranes. Membrane fouling causes severe decline of the permeate flux, quality modification of the permeate stream, increase of the transmembrane pressure drop and energy loss.

Depending on the filtration applications, the nature of deposited particles (fouling agents) are different: organic particles (polysaccharides, proteins, humid substances), inorganic particles (metallic ions/oxides, ions, salts), colloidal particles (suspended solids, flocs) and biological particles (bacteria, virus, algae) can all be present in the feed solutions to be treated.

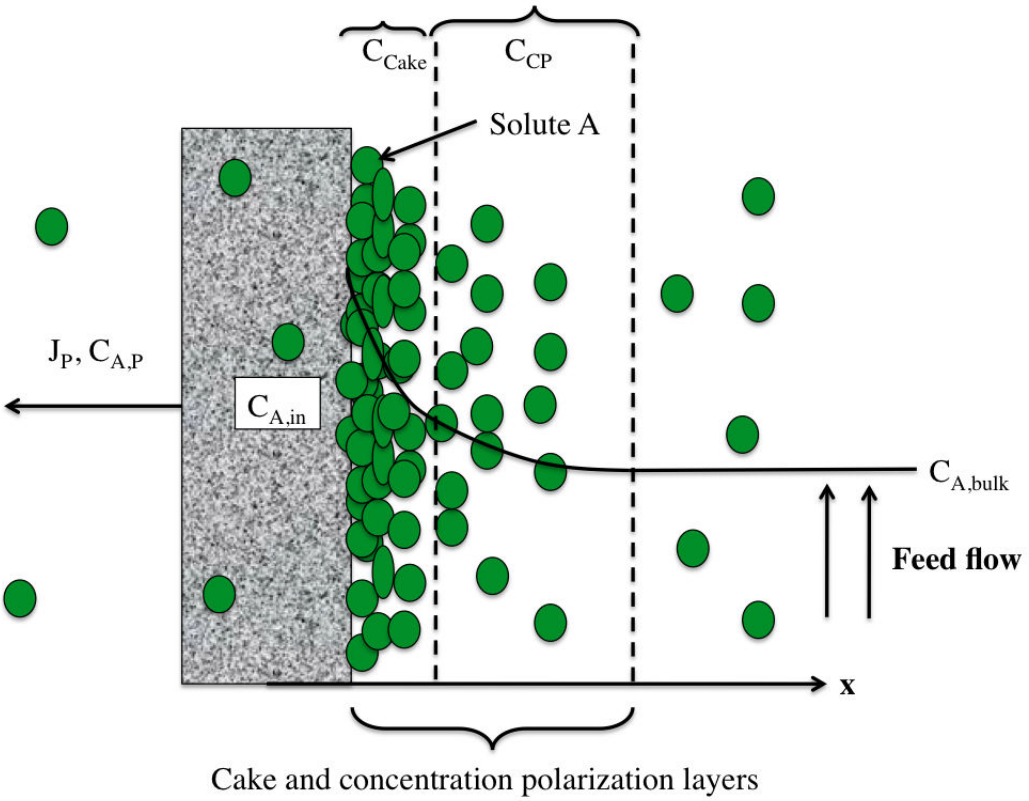

Figure 9: Concentration polarization, cake formation, and internal adsorption phenomenon in a crossflow filtration process.

During the pressure-driven filtration processes through a membrane, particles/solutes are transferred by convective force to the membrane surface. Subsequently they are partly retained on the surface or passed through the membrane. The accumulated solutes will gradually form a thin layer adjacent to the membrane surface generating a concentration gradient. In other words, the concentration of solutes at the membrane surface is higher than the bulk fluid. This phenomenon is called concentration polarization (C_{CP}) and increases the hydraulic resistance to the permeate flow. Concentration polarization is a reversible phenomenon and can be eliminated by simple water rinsing from the membrane surface.
When the solute concentration attain a critical value on the membrane surface a gel-like cake forms on the membrane surface. This gel layer arises when the concentration at the membrane surface due to concentration polarization (CP) reaches the solubility limit of the solutes.This phenomenon is called cake formation (C_{Cake}) and increases the membrane resistance to the permeate flow. Cake formation can partly be removed from the membrane surface by physical-chemical membrane cleaning.
Solutes with smaller size than membrane pores will pass partially through the membrane. They either block completely the pores or adsorb to the internal membrane pores resulting in a reduction of the membrane internal pore size. This phenomenon is called internal blocking (C_{in}) and is counting for the irreversible fouling which can not be treated by membrane cleaning procedures [5],[53], [31], [178], [218]. In internal blocking, adsorption refers to a surface phenomenon occurring at the membrane interface.
Despite the fact that membrane fouling is the inevitable phenomenon occurring in all filtration processes, some strategies can be adapted in order to minimize the loss of the membrane performance.The membrane-solutes interaction/affinity is one of the important factors on the membrane fouling. Thus, the first useful strategy consist of the characterization of the feed solutions (nature, charge, pH) and then choosing a membrane which is less likely to be fouled. The operational conditions also play an important role on the particle deposition on the membrane surfaces. For instance, in cross flow filtration processes, the tangential bulk flow to the membrane surface destabilizes the particle accumulation and partly remove them from the membrane surface. High feed flow velocity and/or use of spacers in spiral membrane modules can also increase the shear stress and turbulence near the membrane surface and reduce the fouling pattern. Conventional physical/chemical cleaning procedures are also useful to remove the reversible and irreversible fouled layers during the filtration processes.

1.3 MEMBRANE BIOFOULING

Several membrane processes with industrial applications (wastewater treatment, food sector) include filtration of mixed solutions (microorganisms, suspended particles, natural organic matter, solutes, ions, surfactants, etc.)[10]. During the filtration of solutions containing microbial cells, not only the classical fouling mechanisms exist (concentration polarization, adsorption, pore blocking), but also the irreversible attachment of microbial

cells to the membrane surface leads to biofilm formation. Biofilm is a complex hydrated matrix of microbial cells entrapped in an extracellular polymeric substances (EPS). EPS is composed of polysaccharides, proteins, humid acids, nucleic substances, etc. (see section 1.5.8). Biofouling is inherently more complicated than other membrane fouling phenomena because in one hand it consists of a dynamic process in which microorganisms can grow, multiply, and relocate and in the other hand secreted substances from the matrix can adsorb on/block the membrane pores. in other words, biofilm counts for a progressive hydraulic resistance both in the membrane pores and on the membrane surface. Therefore, biofouling during the membrane filtration has been studied in the past decades and models have been proposed to predict the evolution of permeate flux, membrane permeability, solute transport and biofilm growth [41], [55],[67],[92] [120]. The models mainly provide a vision of the overall membrane performance and do not include pore scale information of mass and momentum transport inside the membranes and the biofilms. However, it is important to understand properly all interactions involved with biofouling in oder to develop a model in which local mechanisms of mass transport would be taken int account. For this reason, in next sections, membrane filtration of protein solutions in literature will be briefly reviewed and important parameters of protein-membrane interactions will be determined. Then, biofilms will be introduced and important parameters on their development will be given respectively.

1.4 MEMBRANE FOULING BY PROTEINS

Natural organic matter (proteins, polysaccharides, humid substances) are mainly responsible for membrane fouling and consequent permeate flux decline in filtration processes[125], [135],[157],[186]. Consequently the membrane rejection properties are irreversibly modified. Therefore, membrane filtration processes of proteins and macromolecules have been vastly studied in the past decades in order to give a better vision of the membrane performance of the membrane and fouling mechanisms in function of time.

It is often supposed that fouling of macromolecular solutions is only caused by the gel formation (cake) and concentration polarization on the membrane surface. The cake formation or concentration polarization theories are often used to describe the temporal evolution of transmembrane pressure, permeate flux and solute transfer through the membrane. It is obvious that models must take into account all important properties of macromolecules and their interaction with the membrane surface. However, one important factor that is not included in most models is the ability of macro solutes to adsorb at almost any solid interface.The adsorption on the membrane surface is probably the first step in the fouling process and could have great effect on the membrane characteristics. In the work of [148], [149]. Therefore, another aspect of fouling modeling that has recently received attention is macromolecular adsorption to the membrane. The adsorption affects both the hydraulic permeability and the rejection properties of the membrane. In

Table. 3, a summary of filtration experiments of BSA solutions with different membranes at different operational conditions has been given.

In the work of Matiasson [160], it was shown that the BSA adsorption would reduce 5% of permeate flux for the cellulose acetate membranes and up to 35% of performance for the polysulfone and polyamide membranes. From this results, it is clear that adsorption has an important role in the flux reduction of filtration processes. Moreover the adsorption kinetics of BSA have been studied. The agreement between the adsorbed BSA amount and the increase in hydraulic resistance in function of time is quite good. It was also shown that after 10 minutes, the adsorption of BSA on cellulose membranes would attain the saturated value, while this took around 1 hour for the polysulfone membranes. The results also indicate that there are at least two distinct steps in the adsorption process of BSA on different membrane components notably a rapid adsorption step followed by more slow step which both increase the hydraulic resistance of the membrane.

In the following, a brief description of parameters affecting the protein adsorption on membrane surface including the chemical properties of the solution, membrane properties and properties of the proteins is given. In Table 3, different studies on the filtration of proteins with specific objectives are presented.

1.4.1 CHEMICAL PROPERTIES OF THE PROTEIN SOLUTIONS

Chemical properties of the protein solutions (pH, ionic strength) influence significantly the membrane fouling by proteins. The solution charge, affects the protein conformation, stability, membrane-protein interactions and tendency of the proteins to deposit to the membrane surface. Moreover, pH of the solution plays important role on the effective protein's size and can also modify the protein-membrane interactions resulting into more or less adsorption/desorption rates. In literature, a number of studies studies the protein filtration at different values of pH[5], [34], [79], [99], [115], [169], [186],[193]. It has been shown that proteins adsorption is maximal at its isoelectric point (IEP). When the pH equals the isoelectric point (pI)of a protein the number of negative and positive charges are in balance resulting in a net neutral molecule. The electrostatic protein-protein repulsions are minimum at isoelectric point allowing higher adsorption densities on the surface [35]. Burn and Zydney [42],[62] investigated the effect of solution pH on the transport of globular proteins on PES membranes; the results show a maximum protein-sieving coefficient near the isoelectric point (IEP) of proteins. The non-linear dependance of the sieving coefficient on pH was seemed to be a reason as the non-linear dependance of BSA charge on the solution pH. Moreover, attractive electrostatic interactions occurred when the protein and membrane had large opposite charges.

The ionic strength of the protein solutions is another controlling parameter in the adsorption phenomena. The ionic strength basically determines the Debye length correlating with the damping distance of the electric potential of a fixed charge in an electrolyte. That means the higher the ionic strength the shorter are the electrostatic interactions between the charged particles. As a consequence the adsorption of charged proteins to op-

Table 3: A review of invested approaches on membrane filtration by protein solutions.

Protein	Range of concentration (g/L)	Membrane type	Membrane composition	Objectives	Ref.
BSA , Lysozyme, Glutamicum, Humic acid	0-40	MF/UF/ NF/RO	PES, Amicon, PSU, polyamide, Polycarbonate (TE), ceramic	Solution chemistry (pH and ionic strenght) effects on membrane fouling	[62], [79], [169], [187], [116], [168], [142], [193], [8]
BSA , Dextran	0.5-2	MF/RO	Mixed cellulose, polyamide	Operational contains (TMP and flow velocity) effects on membrane fouling	[111], [110], [266]
Lysozyme, Cytochrome, Myoglobin, Hemoglobin, BSA, Pepsin β-lactoglobulin α-lactalbumin	0-2	MF/UF	Cellulose, PES, Polycarbonate (TE)	Influence of single or binary protein mixtures on membrane fouling	[132], [190],[180]
BSA	1-10	MF	Polycarbonate (TE)	Observation of successive fouling steps during filtration process	[99],[33]
C-labelled BSA, BSA Ovalbumine	0-10	UF/MF	PVP, Nylon, PES, PVDF,PSU	Influence of membrane nature on membrane fouling	[218], [112], [95], [184], [174]
C-labelled BSA, BSA	1-10	MF/UF	Cellulose acetate, PSU, PES	Determination of the hydraulic permeability of fouled layers	[186], [162]
BSA	0.5-2.5	UF	PES	Determination of the effective diffusivity of proteins through the membrane	[222], [223]

positely charged substrates is restrained whereas the adsorption to like-charged surfaces is increased. Moreover, high ionic strength conditions increase the tendency of proteins to form aggregates [241].

Temperature has a double effect both on the equilibrium state and on the kinetics of protein adsorption. Increased adsorption rates can be expected due to acceleration of protein diffusivity towards the sorbent surface. The major driving force of protein adsorption is an entropy gain arising from the release of surface adsorbed water molecules and salt ions and from structural rearrangements inside the protein [97],[153],[181]. As a result the amount of surface adsorbed proteins increases in general at high temperatures.

1.4.2 INFLUENCE OF PROTEIN PROPERTIES ON PROTEIN ADSORPTION

Proteins are complex biopolymers composed in average of 20 amino acids as monomeric units plus some possible chain sides like phosphides, oligosaccharides or lipids introduced after translation. A classification of proteins with respect to their interfacial behavior can be archived by considering properties like size, structural stability and composition. The group of proteins called hard proteins (Lysozyme, β-Lactoglubin) suggesting a generally little tendency to structural modifications after adsorption upon solid surfaces [183], [182]. Intermediate size proteins such as Albumin, Transferrin, Immunogolubins are usually able to undergo some conformational reorientations once contacting a solid surface. The couplex structure of these proteins can be decomposed into individual domains exhibiting specific properties like hydrophilic/hydrophobic, polar/non-polar, or charged/uncharged parts [7]. The class of high molecular weight proteins include polymer-like lipoproteins and glycoproteins are structurally labile and therefore show a strong affinity to hydrophobic surfaces including significant conformational reorientations.

1.4.3 INFLUENCE OF SURFACE PROPERTIES ON PROTEIN ADSORPTION

Protein-surface interactions are influenced by the protein's properties on one side and by the surface properties on the other side. The important parameters to be considered are surface polarity, charge, and morphology. The adhesion energy between proteins and solid surfaces can be directly measured using atomic force microscopy (AFM) [77], [96], [130],[131],[219]. It has been observed that proteins tend to adhere more strongly to non-polar than to polar, to high surface tension than to low surface tension and to charged than to uncharged surfaces [34]. In general, experimental results showed that proteins adsorb more strongly to hydrophobic surfaces than hydrophilic ones. This can be explained by the fact that there are less hydrogen bondings between water molecules and hydrophobic solid surfaces which facilitate consequently the protein accumulation to solid surfaces.

1.4.4 PROTEIN ADSORPTION MODELS AT SOLID INTERFACE

When proteins approach a solid interface they typically behave like symmetric rigid particles that can either adsorb on or desorb from a surface. These two process were the only ones taken into account in the Langmuir law where the theory of adsorption of gas molecules on a solid surface has been developed [136]. This theory is still served to develop the substantial description for the protein adsorption phenomena, however it is too simplistic to match the complex behavior of the proteins. Protein secondary and tertiary structures, protein orientation to the solid surfaces [124], structural rearrangements after adsorption [165],[183], [252] and protein aggregation are parameters which should take into account to develop comprehensive models for protein adsorption. However, it is extremely complicated to develop a model taking into account all the mechanisms in adsorption phenomena.
The simplest model existing is the linear model which relates the adsorbed quantity to the equilibrium protein concentration near the solid surface.

$$\theta = kc^* \tag{5}$$

In this model, θ is the adsorbed protein quantity, k is the adsorption constant which includes the physicochemical properties of the substrate and the protein. The main problem of this model is that it accounts only for the adsorption process and hence it can not be useful for prediction of desorption and/or final equilibrium state of adsorption phenomena. The reference model in this field is the Langmuir adsorption model.

$$\frac{\mathrm{d}\theta}{\mathrm{d}t} = k^{ads} \cdot c_s \left(1 - \frac{\theta}{\theta_{max}}\right) - k^{des} \cdot \theta \tag{6}$$

In Eq. 6, θ refers to the protein coverage θ_{max} is the maximum surface coverage, k^{ads} and k^{des} are respectively the adsorption and desorption constants and c_s is the protein concentration in the vicinity of the solid interface. the adsorption of proteins from the bulk solution causes a depletion of the surface concentration c_s which in turn leads to a protein transport from bulk solution to the region above the surface. As a consequence, the surface concentration varies during the adsorption process.
Other models for description of protein adsorption are the Freundlich and Freundlich-Langmuir (combination between Langmuir and Freundlich models). The empirical Freundlich isotherm is employed to describe multilayer adsorption with interactions between molecules on a heterogeneous substrate.

$$\theta = k \cdot c^n \tag{7}$$

Where θ is the adsorbed quantity at equilibrium, c is the concentration of proteins in the solution, k is the relative sorption capacity, and n is an indicator of sorption intensity or surface heterogeneity. The value of n indicates the degree of non-linearity between solution concentration and adsorbed proteins as follows: if n is equal to one, the adsorption

is linear; if n is inferior to one, this implies that the adsorption process is chemical and the surface is relatively homogeneous; if the value of n is more than one, adsorption is a physical process and the sorbent is relatively heterogeneous.
Although these models are mostly used in almost every study invested in protein adsorption on solid interfaces, more complicated models have been also developed to describe more detailed phenomena such as lateral interactions involved between proteins and solid surface [34],[75], overshooting effects, irreversible and reversible adsorption [164], and structural rearrangements during the adsorption [150].

1.4.5 PROTEIN QUANTIFICATION

In several filtration studies, proteins are quantified both in solution and on the membrane surface in order to obtain the adsorption kinetic models, hydraulic resistance due to protein deposition and membrane rejection properties. Different technique are applied for this purpose.
AFM is often applied to image the distribution of protein layer (aggregates) on a solid surface. This technique can also be used to measure the structural rearrangement of individual proteins. he limiting factor of many AFM studies is that imaging is after performed after drying the surface which potsntially affects the folding state of the individual proteins or the structure of the protein layer [2],[77].
The Fourier transform infrared spectroscopy (FTIR) with attenuated total reflectance (ATR) mode is a sampling technique which enables samples to be examined directly in the solid or liquid state without further preparation. ATR uses a property of total internal reflection resulting in an evanescent wave. A beam of infra red light is passed through the ATR crystal in such a way that it reflects at least once off the internal surface in contact with the sample. The penetration depth into the sample is typically between 0.5 and 2 μm [65].The number of reflections depend on the angle of incidence. The beam is then collected by a detector as it exits the crystal.
Recently, FTIR-ATR is applied to characterize the composition of organic membranes, and the evolution of their composition or degradation and also the nature of fouling components with time. The interest of using this technique, in studying the fouled membranes with proteins, is the possibility of quantification of the clogging agents on the surface and in the volume of the membranes. This is feasible by tracing a calibration curve for each specific clogging agent. For this purpose, the known mass of the desired compound (in solution) is deposed on the membrane surface and the corresponding infrared spectra are obtained. The calibration curve consists of the amount of the specific component on the membrane surface in function of the infrared spectra. later the quantity of the unknown clogging agents on the fouled membranes can be determined[66],[222],[223].
In several studies, protein concentration in protein solutions is directly measured by ultraviolet-visible spectrophotometer absorption. In the work of [222],[223], BSA concentration in solution has been measured at $\lambda = 277$nm. Combination of calorimetric methods with spectrophotometer absorption has also been used for determining the total

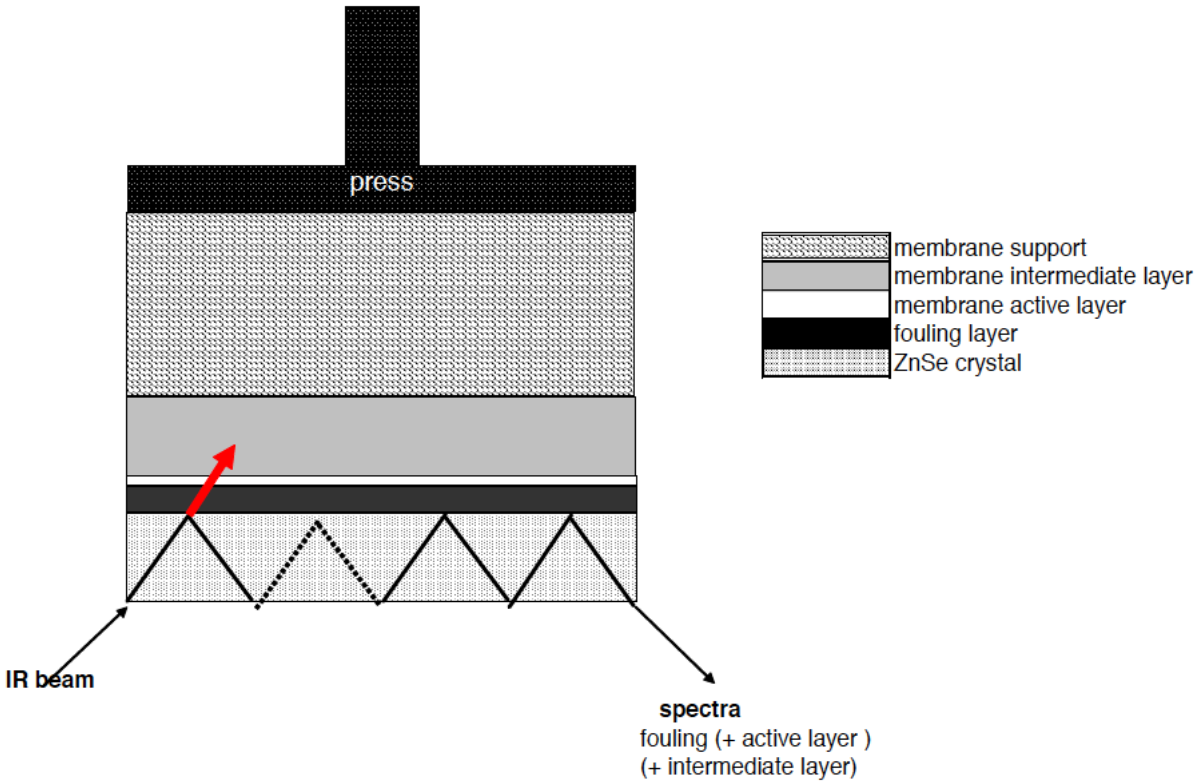

Figure 10: Penetration of IR beam in a sample:successively fouling layer (thickness $\sim 1-10\mu$m)/active layer of membrane (thickness $\sim$ 200 nm) and support layer of membrane,from the work of [66].

protein concentrations in a mixture [44]. These methods are based on the reaction of chromophore agents with the peptide bonds or with certain amino acids of the proteins. The reaction yields coloration (in the visible region) in which intensity (absorbance) is directly proportional to the protein concentration [1]. The most used methods in this field for protein quantification are Biuret, Lowry and Bradford. In the work of Kimberly et al. [116], UF membranes were immersed in surfactant (SDS) solutions. The adsorbed proteins were deorbed in surfactant solution. A micro-lowry method is then applied to measure the protein concentration.

1.5 BIOFILMS

A biofilm is an assemblage of microbial cells that is irreversibly associated with a surface (not removed by gentle rinsing)and enclosed in a matrix of extracellular polymeric material (EPS). This matrix is mainly composed of polysaccharides, proteins, polyuronic and nucleic acids and lipids [64],[224]. The general composition of biofilms has been determined by [234] and is summarized in Table 4.

Non-cellular materials such as mineral crystals, corrosion particles, clay or blood components, depending on the environment in which the biofilm has developed, may also be found in the biofilm matrix. It should be also pointed out that biofilm-associated organisms also differ from the planktonic (freely suspended) counterparts with respect to the genes that are transcribed.

Biofilms may form on a wide variety of surfaces including living tissues, indwelling medical devices, industrial or potable water system piping or natural aquatic systems.

They are responsible for most microbial conversions in natural environments. Natural biofilms can approximately develop on all kind of solid surfaces like rocks and plants in seawater and fresh water and sediment grains. Consequently, biofilms have been associated with a wide range of problems both in industry and medicine and have been used for various bioprocesses. Biofouling of heat exchangers, of industrial and drinking water pipelines and medical devices have been reported. Additionally, biofilms also offer a huge potential for biological wastewater treatment (domestic and industrial), bioremediation of hazardous waste sites and leaching of metals.

Table 4: General composition of biofilm [234]

Component	% (mass) of matrix
Water	up to 97%
Microbial cells	2-5%
Polysaccharides	1-2%
Proteins	$\leq$1-2%
DNA and RNA	$\leq$1-2%
Ions and inorganic	not known

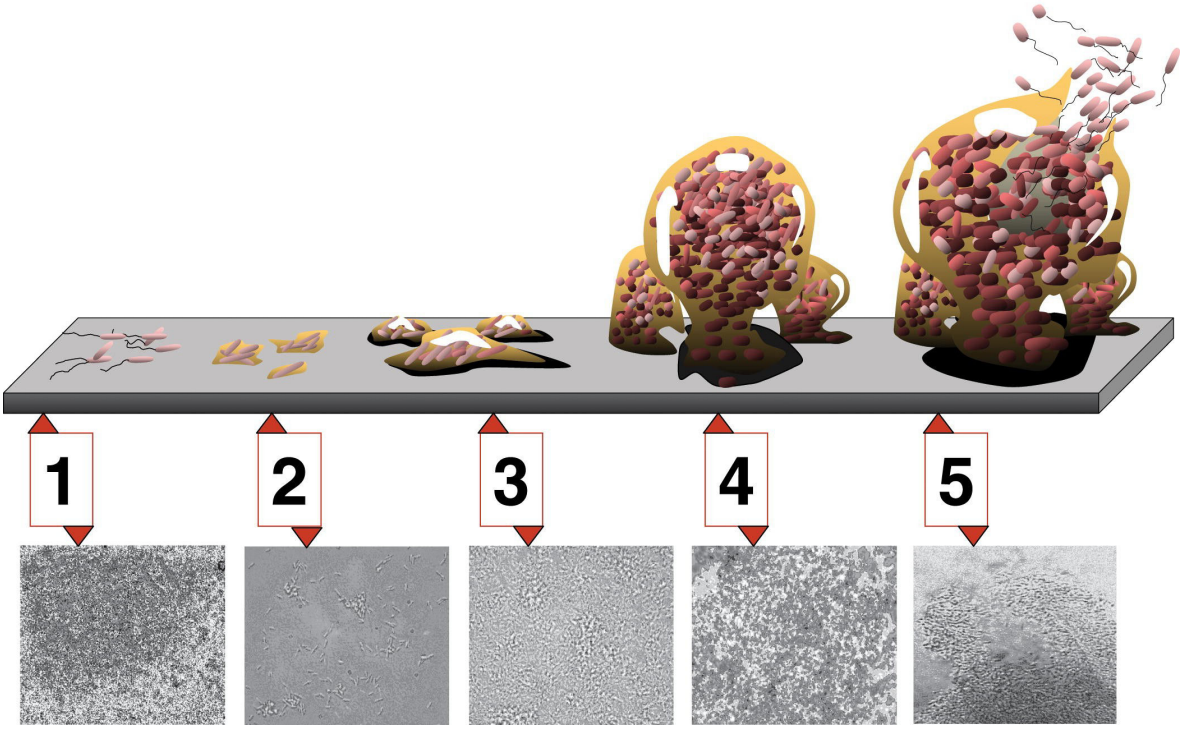

Figure 11: Different stages of biofilm development:(1) Initial attachment, (2) Irreversible attachment, (3,4) Maturation, (5) Dispersion. Adapted from the work of [57]

Three main process have been identified in biofilm development[**?**] and are shown in Fig.11: initial attachment of the cells to the surface (colonization), growth of the attached cells into a mature biofilm and production of extracellular polymeric substances and detachment of single cells (erosion) or large pieces (sloughing off).

The initial attachment of microorganisms to the solid surface is a complicated process depending on both surface and liquid physicochemical properties such as charge and ionic strength of the liquid, surface hydrophobicity, roughness and charge, hydrodynamic conditions of the surrounding liquid and the interfacial properties of the microorganisms. See section 1.5.1.

In the following section, a brief description of the important physical and chemical parameters affecting biofilm development is detailed. A description of biofilm composition and structure and mass transfer in biofilms is also given.

1.5.1 IMPORTANT PHYSICOCHEMICAL PARAMETERS ON BIOFILM FORMATION

1.5.2 SUBSTRATUM EFFECTS

The solid surface may have several characteristics which can affect the attachment and biofilm development. It has been noted [45] that the surface roughness appears to increase the microbial colonization. The physiochemical properties of the surface may also have a strong influence on the rate and the extent of attachment. It has been reported that microorganisms attach more rapidly to the hydrophobic, nonpolar surfaces such as Teflon and other plastics [25],[84],[204] than to hydrophilic materials such as glass. This can be a result of some hydrophobic interactions between the cells and the surface which would enable the cells to overcome the repulsive forces active within a certain distance from the surface and irreversibly attach.

1.5.3 CONDITIONNING FILMS

A solid surface exposed in an aqueous medium will immediately and inevitably become conditioned or coated by polymers from that medium, and the resulting chemical modifications will affect the rate and the extent of microbial attachment. Loeb and Neilhof [144] have reported that these films were naturally organic and formed within minutes of exposure, and continued to grow for several hours.

1.5.4 CHARACTERISTICS OF THE AQUEOUS MEDIUM

The characteristics of the aqueous medium, such as pH, nutrient availability, ionic strength, and temperature may play a role in the rate of microbial attachment to a substratum[72],[80]. It has been found that an increase in the concentration of several cations (sodium, calcium, ferric ion) affected the attachment of Pseudomonas fluorescens to glass by reducing the repulsive forces between the negatively charged bacteria and the glass surface. [82],[83]. It has been also noted that an increase in nutrient concentration can be correlated with an increase in the number of attached bacterial cells [55].

1.5.5 PROPERTIES OF THE CELL

Cell surface hydrophobicity, presence of fimbriae and flagella, and production of EPS influence the rate of attachment of microbial cells. The hydrophobicity of the cell surface is important in cell attachment because hydrophobic interactions tend to increase with an increasing nonpolar nature of one or both surfaces involved. Most bacteria are charged negatively but still contain hydrophobic surface components [220]. Fimbriae, non-flagellar appendages, contribute to cell surface hydrophobicity. Fimbriae play a role in cell surface hydrophobicity and attachment, probably by overcoming the initial electrostatic repulsion barrier that exists between the cell and substratum. Other cell surface properties may also facilitate the attachment process. Several studies have shown that the treatment of adsorbed cells with proteolytic enzymes caused a marked release of attached

bacteria, providing evidence for the role of proteins in attachment[18],[58]. In 1971, Marshall [158] provided evidence, based on SEM, that the attached bacteria were associated with the surface via fine extracellular polymeric fibrils. Korber [133] used motile and non-motile strains of *P. fluorescens* to show that motile cells attach in greater numbers and attach against the flow more rapidly than the non-motile strains. Therefore, flagella present on the surface of motile cells seem to play an important role in attachment. In light of these findings, cell surface structure such as fimbriae, other proteins, LPS, EPS, and flagella all clearly play an important role in the attachment process.
As a conclusion, attachment will occur more rapidly on surfaces that are rougher, more hydrophobic, and coated by surface conditioning films. An increase in flow velocity, water temperature, or nutrient concentration may also lead to increased attachment, if these factors do not exceed critical values.

1.5.6 QUORUM SENSING

Cell-to-cell signaling has recently demonstrated to play a role in cell attachment, biofilm development and detachment[264],[147]. By sensing cell-produced compounds, (e.g., N-acyl-homoserine lactones), cells recognize the local cell density (therefore called "quorum-sensing") and react by switching on or off certain sets of functional genes. It has been proved that quorum-sensing determines biofilm structure. In the work of [59] cell-to-cell signals are involved to produce a biofilm. At sufficient bacterial population densities, these signals reach concentrations required for activation/mutation of genes involved in biofilm formation, but unlike the wild type, their biofilms were much thinner, cells were more densely packed, and the typical biofilm architecture was lacking.

1.5.7 BIOFILM STRUCTURE

1.5.8 EXTRACELLULAR POLYMERIC SUBSTANCES (EPS)

The proportion of EPS in biofilms can range from 50% to 80% of the total organic matter. This is the main structural component of biofilms. The physical properties of the biofilm are largely determined by the EPS while the physiological properties are determined by bacterial cells.
As EPS were considered mainly composed by polysaccharides, many detection techniques focus on this group of compounds [20],[52],[179]. However recent studies revealed that proteins are the most abundant component in the EPS matrix (50% or even more). Consequently, more research on the EPS composition is needed, since EPS has been linked with many processes and properties integral to biofilm behavior: attachment, detachment, mechanical strength, antibiotic resistance and exo-enzymatic degradation activity.
Research also demonstrated that the composition and structure of EPS determine the structure of biofilms and that the EPS in biofilms may vary spatially and temporally.

It has been shown that the EPS matrix also affects solute's diffusion in biofilms. According to [40], the diffusion of small molecules is not strongly inhibited by the biofilm matrix, whereas the diffusion of large molecules are impeded.

Other studies focusing on EPS properties reported that the forces keeping the polymers together in the matrix are not strong covalent bonds, but weak hydrophobic and electrostatic interactions and hydrogen bonds. It is clear that further research is needed on both physical and chemical properties of EPS which appears to play a critical role in the structure and activity of biofilms.

1.5.9 HETEROGENEITY

Biofilm structure is the spatial arrangement of microorganisms, cells clusters and EPS and eventually solid particles. Since the structure affects solute's transport, it is a significant determinant in the activity of the biofilm.

Despite the initial reports of biofilms as planar and homogenous structures, recent microscopic observations indicated that biofilms are not flat and the distribution of microorganisms is not uniform. Instead, multispecies biofilms were observed with complex structures, heterogeneous both in space and time, containing voids, water channels, cavities and with cells arranged in clusters or layers[230]. Biofilms have been considered to be highly porous polymer gels and diffusion studies of [52] demonstrated their gel-like characteristics.

Depending on growth conditions and age, the biofilm thickness can vary from a few micrometers up to a centimeter [23].

Density, volume fraction of water phase (porosity) and tortuosity of biofilms change with biofilm depth, showing biofilm heterogeneity (see section 1.5.10). The non-uniform distribution of these parameters also affects the mass transfer mechanisms inside biofilms.

Owning to the microscopic dimensions of biofilms, their structural analysis strongly depends on the microscopic methods used. Most microscopic techniques for structural characterization of biofilms involve preparation of samples, such as dehydration and embedding, which causes damage to the soft biofilm structure biofilm-microscopic-methods.

After the introduction of confocal scanning laser microscopy (CSLM), biofilm structure perception changed drastically. CSLM images revealed that biofilms can consist of biomass clusters separated by interstitial voids [21]. It was also concluded from the images that voids were water channels in connection with the bulk water phase. The presence of voids has considerable consequences for mass transfer inside the biofilms (convection) and exchange of nutriments and products with the water phase.

Table 5: List of microscopic techniques for studying biofilms

Microscopy technique	Spatial resolution	Application	Sample treatment	References
LM	1μm	EPS and cells	Dehydration, freezing, sectioning, staining	[48]
FM	1μm	EPS and cells	Dehydration, freezing, sectioning, staining	[20], [205], [92]
TEM	1 nm	Cells and EPS	Dehydration, sectioning, staining	[16], [19]
SEM	1 nm	Cell and EPS surfaces	Dehydration, sputter coating	[19]
ESEM	10 nm	Celle and EPs surfaces	None	[192]
CSLM	1μm	EPS, cells, voids	staining	[22], [139]
AFM	0.1μm	Cell and EPS surfaces	None	[37], [93]

Abbreviations: LM: light microscopy; FM: fluorescence microscopy; SEM: scanning electron microscopy; ESEM: environmental scanning electron microscopy; CSLM: confocal scanning electron microscopy; AFM: atomic force microscopy.

1.5.10 Density, porosity and hydraulic permeability of biofilms

In the work of Zhang [269], the spatial distributions of biofilm density, porosity and mean pore radius were determined with biofilm depth using experimental data and modeling approaches.

The volume fraction of water or the porosity of biofilm is defined as the portion of a biofilm occupied by water outside of the cells[246]. In this work, biofilm porosities change from 84-93% in the top layers to 58-67% in the bottom layers.

Additionally, an average dry density of the biofilm of 1.17 mg-TS/cm^3 (TS means Total Solids) dry biomass was measured. On the other hand, the wet densities of biofilms increased from 1.001-1.003 g-TS/cm^3 in the top layers to 1.01-1.02 g-TS/cm3 in the bottom layers. The density in the bottom layers were 5-10 higher than those in the top layers. This corresponds to the increase of the TS with depth (observed in this study) indicating that cells are more densely packed in the bottom layers. This is also in agreement with the decrease of the porosity with depth.

In contrast, the biofilm mean pore size decreased from 1.6-2.4 μm in the top layers to 0.3-0.4 μm in the bottom layers[269].

Hydraulic permeability is another major parameter characterizing a porous biofilm medium. It has been shown to depend on the relative content of cells and gel-like polymeric matrix ([163]. Moreover, Fowler and Robertson [86] suggested that the ability of cells to move with respect to one another in immobilized bacterial cell aggregates affected the hydraulic resistance of this bacterial medium. In the work of 83, values of biofilm hydraulic permeability and porosity of 10E-16 m2 and 0.8, respectively were reported.

1.5.11 DISPERSAL

Biofilm cells may be dispersed either by shedding of daughter cells from actively growing cells, detachment as a result of nutrient limitation or quorum sensing, or shearing of biofilm aggregates (continuous removal of small portions of biofilm) because of flow effects [71].
The mechanisms underlying the process of shedding by actively growing cells in a biofilm are not well understood. It has been shown that the surface hydrophobicity of newly divided daughter cells spontaneously dispersed from biofilm differ substantially from mature cells in biofilm. These differences might explain the detachment of newly divided daughter cells. Hydrophobicity was reported lowest for the newly dispersed cells.
Detachment caused by physical forces has been studied more in detail. The importance of physical forces in detachment has been proved. The three main processes for detachment are erosion or shearing (continuous removal of small portions of the biofilm), sloughing off (rapid and massive removal), and abrasion (detachment due to collision of particles from the bulk with the biofilm). It has been noted that the rate of erosion from biofilm increases with the biofilm thickness and fluid shear at the biofilm-bulk liquid interface. Sloughing is a more random process and is thought to be a result of nutrient or oxygen depletion within the biofilm structure. Sloughing off is more commonly observed with thicker biofilms that have developed in nutrient-rich media.
The mode of dispersal may evidently affect the phenotypic characteristics of the organisms. Eroded or sloughed aggregates from the biofilm are likely to retain certain biofilm characteristics, such as antimicrobial resistance properties, whereas cells that have been shed as a result of growth may revert quickly to the planktonic phenotype.

1.5.12 MASS TRANSFER AND MICROBIAL ACTIVITY

Substances for biofilm growth are usually supplied by the water phase, and metabolic products are eventually released into the water phase. The rates of exchange between the biofilm and the water phase are determined by the mass transfer processes of diffusion and convection. It should be pointed out that microbial conversions in biofilms, related mostly to cell growth and division, are dependent and often limited by mass transfer.
A common property of microbial biofilms is resistance for mass transfer of different solutes. This is due to the limited water flow inside the matrix and the presence of a hy-

drodynamic boundary layer between the matrix and the surrounding water phase [117], [118],[203].
Transport of solutes is thought to be primarily by diffusion inside the biofilm matrix and in the boundary layer near the solid surface. Consequently, when the internal chemical composition (substrates and products) differs from the bulk medium, steep gradients develop. This has strong effects on the type and the rates of microbial conversions within the biofilm.
The simplest biofilm concept is a planar geometry with microbial activity distributed homogeneously and constant transport parameters regardless of biofilm depth. The biofilm surface is separated from the mixed bulk liquid by a mass boundary layer (MBL) in which the transport of species gradually changes from diffusion (biofilm) to convection (bulk liquid). This is illustrated in Figure 2 presenting the O_2 micro-profile in and above an active biofilm. This concept is simple and facilitates mathematical modeling of transport.
The mass transfer resistances can be separated into external, in the MBL, and internal, in the biofilm matrix. The resistance in the MBL is proportional to its thickness δ as shown in Fig. 12, which mainly depends itself on the velocity of the fluid phase surroundingg the biofilm matrix. The mass transfer coefficient k_s and the thickness of the MBL can be calculated by the liquid flow velocity [226].

$$k_s = 0.0889 u_\infty Sc^{-0.704} \tag{8a}$$

$$Sc = \frac{\eta\rho}{\mathbf{D_{eff}}} \tag{8b}$$

With Sc as the Schmidt number, η as the dynamic viscosity, ρ as the density of the water phase and $\delta = \mathbf{D_{eff}}/\mathbf{k_s}$.
Both diffusion and convection of solutes are important when considering transfer phenomena in biofilms. They are both hindered by the biofilm matrix; obviously the matrix is an effective barrier not only for water movement (convection) but also for the random movement of solutes (diffusion).
Internal mass transfer is usually considered to be diffusional and frequently described using a single effective diffusion coefficient (D_{eff}). Diffusion is the only transport mechanism when there is no flow inside the biofilm matrix, however convection becomes the dominant mechanism when the matrix is sufficiently permeable to allow the liquid flow.
Solute transport due to convection equals the velocity of the liquid inside the biofilm, and even if it is in the order of 1 μm.s^{-1}, convection is as important as diffusion for biofilms, which typically range from a few hundred μm to several mm thick.
As previously reported, microscopic observations indicate that biofilms can be highly porous, thus the common assumption that diffusion is the only transport mechanism must be treated carefully.
Numerous studies reporting measurements of the Deff of several compounds in biofilms have been reviewed. Literature values show a wide range of variation D_{eff} being 1-900 % of the diffusion coefficient in water D_w. This reflects the variety of biofilm studies

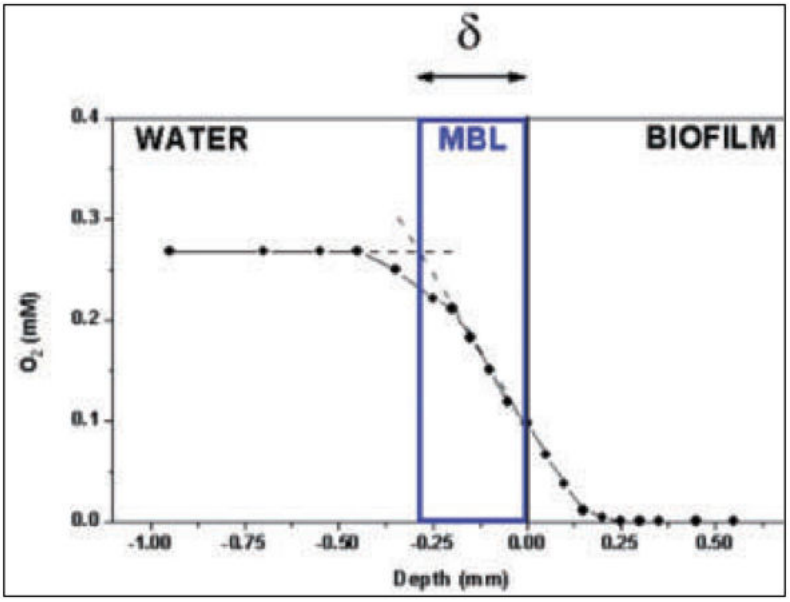

Figure 12: Oxygen profile measured in an active biofilm demonstrating that a significant part of the mass transfer resistance occurred out side the biofilm adopted from the work of De Beer [23]

as well as the different measurement methods. The D_{eff}/D_w ratios for small molecular weights such as oxygen, glucose and nitrate in growing biofilms are assumed to be around 0.9 [52]. Diffusion of macromolecules such as DNA, dextrans and proteins may be more strongly influenced by biofilm matrices. This is due to the gel-matrix polymers obstructing diffusion of macromolecules.
To describe transport inside biofilms, transport in the voids (diffusion and convection) and in cell clusters (diffusion only) must then be distinguished and considered when studying biofilms. For this purpose, measuring techniques with high spatial resolution are needed and described in the literature[23].

1.5.13 EXPERIMENTAL CHARACTERIZATION OF BIOFILMS: MICROSCOPIC AND STAINING METHODS

As previously reported, most microscopic methods (Fig.5) involve some preparation of the sample, including staining, fixation, freezing, dehydration, embedding and sectioning. As biofilms are soft structures mostly consisting of water, the preparation procedure may significantly change, destroy or deform the matrix. As a result, in most cases, there is an underestimation of the spatial heterogeneity. EPS appears as strands connecting the cells. EPS morphology changes by dehydration: diffuse polymeric matter is condensed to strands, leading to overestimation of the pore-size. According to a study of

citebeeftink1986), from SEM images the pore-size appears to be in the order of 1μm whereas TEM preparations show a pore size of 100 nm.

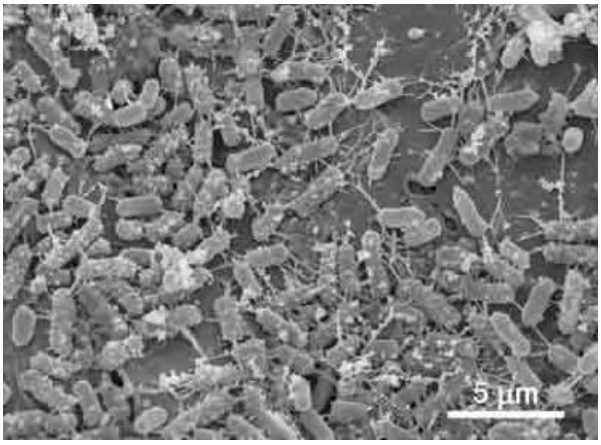

Figure 13: SEM image of biofilm formation by Escherichia coli from [9]

Images acquired by environmental scanning electron microscopy (ESEM) [143] and atomic force microscopy (AFM) [36] (no dehydration) do not reveal the biofilm heterogeneity, but rather a smooth smear. A possible disturbing artifact from ESEM is the filling of voids by water and drowning the roughness elements of the surface.

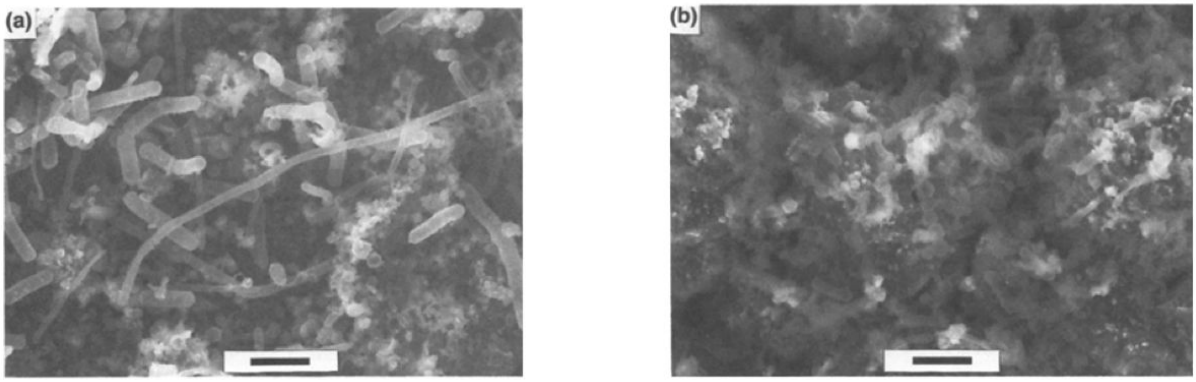

Figure 14: ESEM image of biofilm formation on (a) aluminum foil, (b) copper foil, (marker 5mum) [143]

Confocal laser scanning microscopy (CSLM) is one of the tools most widely used at present to study biofilm because it enables the direct *in situ* and non-destructive investigation of native multicellular structures using specific fluorescent stains.

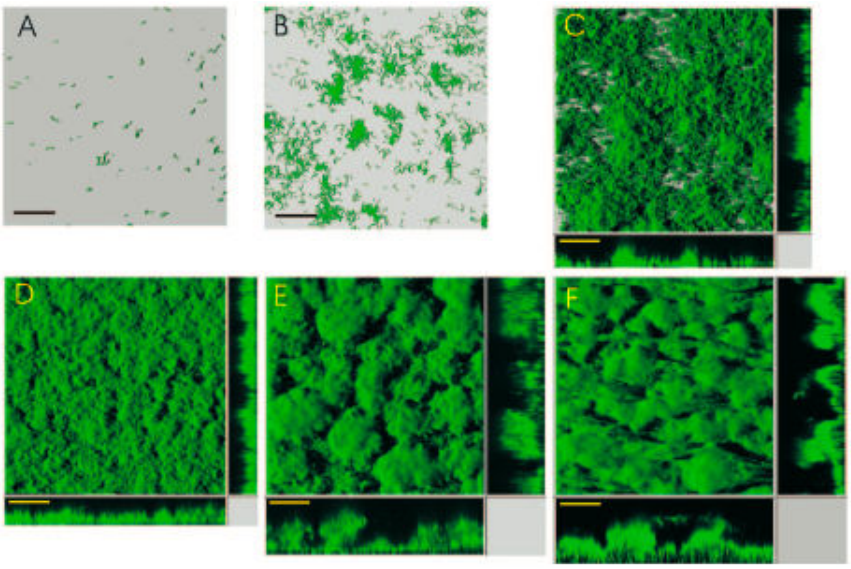

Figure 15: Visualization of *Shewanella* cells labeled with green fluorescence protein (GFP) using confocal laser-scanning microscopy (CSLM) in different times, (A): After 1h, (B) 8h, (C) 16h, (D) 24h, (E) 48h, (F) 120h. The first 3D construction of biofilm was done after 12h. from the work of [236].

Specific staining is an important tool to determine the spatial distribution of different biofilm components, most importantly in cells, EPS and voids. For viewing cells, non-specific stains for DNA, such as acridine orange, diamidino-phenylindole (DAPI), ethidium bromide and hexidium iodide are most useful. These dyes can also be combined with confocal microscopy for giving of cell distribution in undisturbed biofilms. Staining of EPS for fluorescent microscopy or CSLM is also possible for proteins (fluorescein isothiocyanate) and polysaccharides (lectin conjugates).
The recent development of image analysis software's also provides an opportunity to obtain detailed quantitative structural parameters on biofilms directly from confocal image stacks. Structural parameters such as porosity, thickness, biovolume, substratum coverage by cells and EPS have been determined in several studies [38], [126].

1.6 MEMBRANE-BIOFILM FOULING MODELS

1.6.1 MEMBRANE FOULING MODELS

Modeling of the membrane fouling has been investigated in several sturdies during the past years[98], [114], [135],[233]. The classical models are used to describe the flux decline during the filtration processes. These models are mainly based on the work of Hermia [98] and consist of four main blocking mechanisms: complete pore blockage, intermediate pore blockage, pore constriction (standard blocking) and cake filtration. These

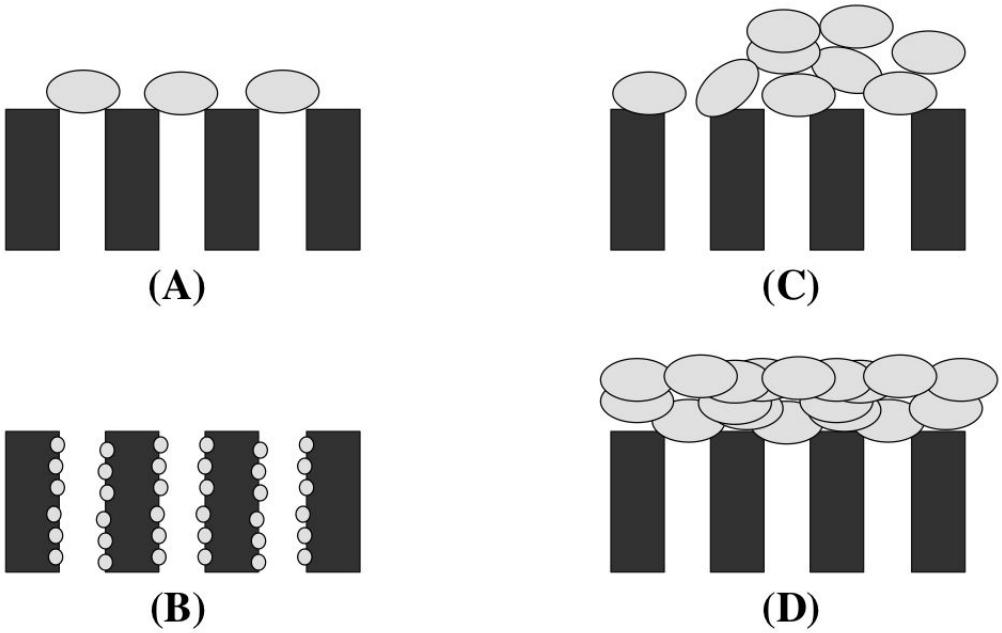

Figure 16: Fouling mechanisms described by Hermia: (A) Complete blocking, (B) Pore constriction, (C) Intermediate blocking, (D) Cake filtration.

mechanisms are presented in Fig.16. The mathematical expressions of these mechanisms are also listed in Table. 1.6.1.

Table 6: Mathematical expressions for classical fouling models

Model	**Governing equations**	**Normalized flow rate**
Complete pore blockage	$\frac{dA_u}{dt} = -\alpha Q_u C_b$	$\frac{Q}{Q_0} = exp\left(-\alpha \frac{\Delta p}{\mu R_m} C_b t\right)$
Intermediate pore blockage	$\frac{dA_u}{dt} = -\alpha^{'} Q_u C_b \frac{A_u}{A_0}$	$\frac{Q}{Q_0} = \left(1 + \alpha^{'} \frac{\Delta p}{\mu R_m} C_b t\right)^{-1}$
Cake filtration	$\frac{dR_{cake}}{dt} = f' R' J_b C_b$	$\frac{Q}{Q_0} = \left(1 + f' R' \frac{2\Delta p}{\mu R_m^2} C_b t\right)^{-1/2}$
Pore constriction/Standard blocking	$\frac{d(N_0 \pi r_p^2 \delta_m)}{dt} = -\alpha_{in} Q_u C_b$	$\frac{Q}{Q_0} = \left(1 + \alpha_{in} \frac{Q_0}{\pi r_0^2 \delta_m} C_b t\right)^{-2}$

Abreviations: A_u: Area of unblocked membrane (m^2), Q_u: Flow rate through unblocked membrane area (m^3/s), C_b: Bulk concentration (g/L), α: Pore blockage parameter, representing blocked membrane area per unit mass of solutes convected to the membrane surface (m^2/kg), R_P: Resistance of the deposits (m^{-1}), $f^{'}$: Fractional amount of foul ants contributing to solute deposition, $R^{'}$: Specific resistance of solutes (m^{-1}), J_b Permeate flux within the blocked area (m/s) , R_m Resistance of the clean membrane (m^{-1}), r_p Radius of membrane pores (m), δ_m: Membrane thickness (m). Adapted from [74].

In the complete pore blocking model, the permeate flow is drastically declined by particle aggregation on the membrane surface and liquid flow can only pass through the unblocked pore area. In this model, it is assumed that each particle reaching the membrane surface, dispose on a free site of the membrane surface.Therefore, the rate of pore blockage is function of permeate flow rate (Q_u) and bulk concentration (C_b). The pore blockage parameter α represents the blocked surface per unit mass of aggregates deposited to the membrane surface. The permeate flow decreases exponentially with time [98]. The intermediate pore blocking model is similar to complete pore blocking model with additional possibility of particle disposition on top of other particles already attached. In this model, the particles does not necessarily block a pore but the probability of for a particle to block a pore is evaluated. In this case, the rate of pore blockage is assumed to be proportional to the ratio of unblocked surface to the total surface.

The cake filtration model assumes that a uniform cake layer is formed over the membrane surface, and this fouling layer is permeable to fluid flow with resistance R_{cake}. In this case particles locate on the other ones previously accumulated on the membrane surface and new ones can not directly block the membrane surface. The cake layer resistance modifies with time and is proportional to the convective transport of formed aggregates to the membrane surface ($Jf'C_b$), where f' is the fraction of aggregates in the feed solution, and R' is the specific cake layer resistance. The hydraulic resistance of cake layer

on the membrane surface by protein filtration (BSA) has been estimated in the work of Mochizuki et al. [169] and Opong et al. [186].

The pore constriction model (standard blocking) takes into account the fouling which occurs in the internal structure of the membrane. In this fouling mechanism, the column occupied by membrane pores decreases due to particle deposit in the pore walls. The rate of change of pore volume is proportional to the flow rate (Q) and bulk concentration (C_b). Parameter α_{in} denotes the volume of particles in the internal pores per unit mass of protein filtered through the membrane.
Although, all these models provide a mechanistic description for each fouling progress, significant differences between the flux decline data and model descriptions have often been observed[81],[140],[238]. Consequently, a considerable number of studies developed combined fouling models accounting for coupled fouling mechanisms to describe the flux decline. Ho and Zydney [102] developed a fouling model taking into account for both pore blockage and cake filtration which was in good agreement with experimental data obtained during bovine serum albumin (BSA) filtration using polycarbonate track-etched membranes. De la casa et al. [62] developed a model by pore constriction and cake formation model taking into account the electrostatic effects of the BSA solution to the permeate flux. Fouladitajer et al. [85] studied the filtration of oil-water mixtures through polyvinylidene fluoride microfiltration membranes. They obtained five combined fouling models including different mechanisms. Moreover, Duclos-Orsello et al. [74] developed a combined fouling model of complete blocking, pore constriction and cake filtration to describe the flux decline through the microfiltration membrane.

Another approach of modeling the membrane fouling is a series of resistances superimposing progressively to the membrane initial resistance for the solvent passage throughout he membrane [14],[51], [110], [156], [239]. Depending on the filtration process, one should take some or all the fouling mechanisms in the resistance series models As presented in Eq. (9a) The permeate flux is proportional to the transmembrane pressure and membrane initial resistance. However in a series of resistances to membrane resistance would be the sum of resistances due to different fouling mechanisms (concentration polarization (R_{CP}), cake formation (R_{Cake}) and internal blockage (R_{in}), see Eq. (9b). Furthermore, each resistance is determined by empirical or semi empirical equations depending on both solvent properties and operational conditions.

$$J = \frac{\Delta P}{\mu R_m} \tag{9a}$$

$$J = \frac{\Delta P}{\mu(R_m + R_{CP} + R_{Cake} + R_{in})} \tag{9b}$$

In general, these resistances depend on the bulk concentration of particles, flow velocity, particle concentration at membrane surface and shear stress. They can be estimated by classical models (pore blocking, cake formation, etc.) or by empirical relations between

parameters [239]. One possible way to estimate the polarization thickness layer (resistance) is a film theory defined by Eq.(10). The polarization layer thickness can be used both for determination of CP resistance individually [107] and in combination with other fouling resistances [156].

$$\delta_{pol} = \frac{D}{v_P} \ln(\frac{C_P}{C_b}) \tag{10}$$

In this definition, D is the diffusion coefficient of solutes passing the membrane, $\mathbf{v_P}$ is the permeate velocity, C_P and C_b are the concentration of solutes at bulk and membrane surface respectively.

In parallel, numerical simulations of membrane models have been performed to compare theoretical data with experimental data of the filtration processes. Rahimi et al. [214] developed a 3-D CFD (computational fluid dynamics) model for predicting the water flux through a microfiltration membrane. The experimental set up consisted of microfiltration of blue indigo (insoluble in water) suspensions in a crossflow module. The pattern of particle deposition on the membranes has been studied at different hydrodynamic velocities. The flow distribution in the porous membrane has been modeled based on Navier-Stokes conservation equation for momentum and results from simulations have been used to explain the experimental observations. It has been concluded that in higher crossflow velocities, particles have less time to dispose to the membrane surface and thus the fouling is less important. Ahmed et al. [6] obtained a 2-D theoretical CFD model to predict concentration polarization, mass transfer coefficient and wall shear stress in a narrow membrane channel. in the work of Bacchin et al. [13] a 2-D CFD model of mass and momentum transfer was developed to describe the accumulation of colloids on membrane surface. Numerical simulations integrated detailed modeling of physicochemical properties of the colloidal dispersions (due to repulsive and attractive interactions at colloidal interface. These interactions are fitted then to the CFD code. The model has been compared to the experimental data which included filtration of latex particles through microfiltration crossflow modules. Delaunay et al. [66] used the protein quantification of proteins by FTIR-ATR on the membrane surface as an indirect proof of velocity and shear stress profiles in a complex geometry (porous membrane) and validated the experimental data with CFD modeling approach. In the work of Marcos et al. [156], a 2-D model based on a finite element method has been developed to simulate numerically the flow (mass and momentum equations) and concentration of whey proteins in a hollow fiber. ultrafiltration module.

1.6.2 BIOFILM MODELING

Among the problems associated with biofilms, energy losses, equipment damage, product contamination and medical infections are generally reported. Understanding the interactions between physical, chemical and biological phenomena on biofilm's dynamics is challenging and will help preventing damages caused by unwanted biofilms. In the

particular case of membrane systems, biofilm development induces a decline of process performance. Consequently cleaning procedures and replacement of the membranes are required.

Mathematical modeling of biofilms is therefore crucial to attain a broader and deeper insight into those interactions and to assess the complex structure of the biofilm at different steps of its development. Consequently, a huge number of studies have been invested in this field for the last decades.

One critical point that should be taken into account when developing a biofilm model is its structural heterogeneity both in space and time (see section1.5.9) Additionally, in biofilm structure, very different length scales are presented. They vary from a few nanometers (size of extracellular polymeric fibers), to several millimeters or centimeters (biofilm thickness), with the size of bacterial cells (1- 2 μm) as an intermediate length scale.

Although it seems crucial to take into account a multi-scale description of a biofilm, this strategy for biofilm modeling remains challenging for three main reasons:

- Experimental techniques can not characterize properly the biofilm structure at all scales
- Computational resources are limited
- Not all the information provided at microscopic scale can be used at the macroscopic biofilm scale, thus the model can not be validated at microscale.

1.6.3 1-DIMENSIONAL CONTINUUM MODELS

The first attempts in biofilm modeling consisted in the development of continuum models primarily in one space dimension [127],[216],[217],[249], [250]. These studies concentrated mostly on the steady-state biofilm growth dynamics including the biofilm thickness and spatial distribution of microbial species and substrate concentrations. For instance the model developed by Wanner and Gujer [246], based on a continuum description of biofilms and the conservation of species, predicts the evolution of biofilm's thickness, dynamics and spatial distribution of microbial species and nutrients in the biofilm. It also includes a biomass detachment mechanism due to shear stress and sloughing.

Single and multi-species biofilm were studied and modeled with this approach. Additionally, these continuum models also explain how the microbial composition and activity depend on the kinetics, nutrient concentration and other mechanisms such as initial attachment and detachment.

However, the one-dimensional models significantly simplify the interactions between the nutrients and biofilm and also the spatial dynamics of the biofilm. They also lack the ability to characterize the multidimensional structure of the biofilm [245].

1.6.4 DIFFUSION-LIMITED AGGREGATION (DLA) MODEL FOR BIOFILM GROWTH AND PATTERN FORMATION

In general, the growth mechanism of the bacterial colonies is highly complex, in which the substrate concentration plays an important role. One way to model this growth pattern is the class of models called diffusion-limited aggregation (DLA) models.
The first biological DLA model described in the literature was a DLA model describing the colony growth of *Bacillus subtilis* given by [87]. Later on, more experimental and modeling studies were done [88],[161] .
The rule of DLA model is as follows: one chooses a seed particle as the origin of a square lattice on a plane. Another particle is released far from the origin and is allowed to move at random. When it arrives at the nearest neighboring site to the origin, it sticks to the site. Then another particle is launched and it moves until it reaches the nearest neighboring of a cluster made of the two particles. Through the repetition of these procedures, a cluster grows with an outwardly open and randomly structure (Wang and Zhang, 2010).

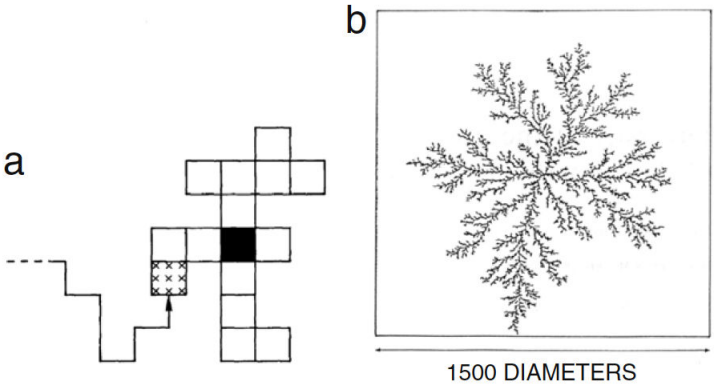

Figure 17: DLA on compute simulation: (a) the rule of the 2D DLA growth. The solid cell is the origin. The hatched cell is a new cell that has aggregated to the cluster. (b) a typical example of a 2D DLA cluster which consists of 100000 particles, adapted from the work of [237].

1.6.5 DISCRETE-CONTINUUM/CELLULAR AUTOMATON (CA) MODEL

The Cellular Automaton (CA) model consists of a regular grid of cells, each in one of a finite number of states. The grid can be in any finite number of dimensions. The state of a cell at time t is a function of discrete states of a finite number of cells at time t-1. Every cell has the same rule for updating, based on the values of in her neighborhood. Each time a set of rules are applied to the whole grid and a new generation is created. One advantage of the CA model is its simplicity and the ability to produce a complex behavior. It is then particularly attractive when simulating biological systems with heterogeneous spatial structures [69],[257].

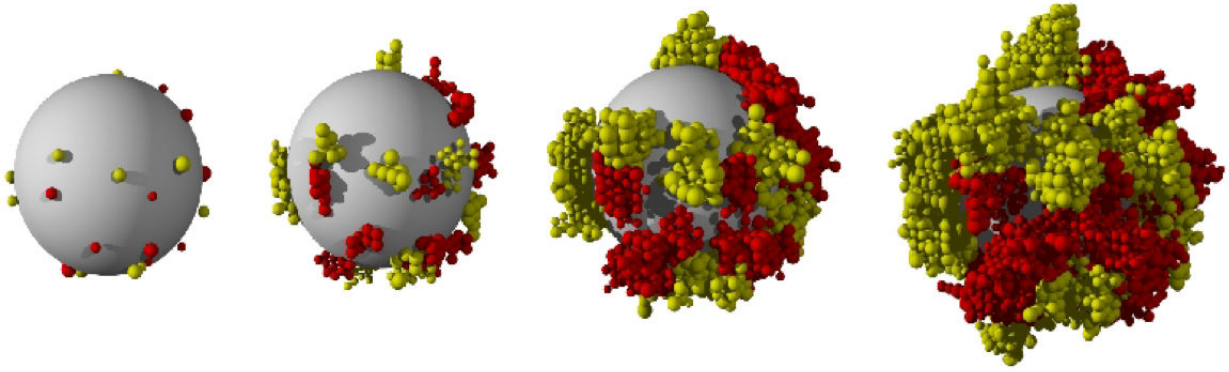

Figure 18: Modeling of the formation of a two species biofilm on a sphere in a mass transfer limited regime using cellular automata adapted from[195].

CA models for biofilms incorporating the following phenomena : bacterial growth and movement, cell to cell communication and the diffusion of nutrients [245]. These models can validate various biofilms growth profiles observed in experiments demonstrating that the biofilm's structure is significantly determined by the surrounding substrate concentration. Picionearu et al.[195] developed a combined differential-discrete CA biofilm model, in which the nutrient concentration was assumed to be continuous and governed by convectional diffusion-reaction equation. In this model the biomass density was computed by a direct integration of the biomass balance equation, taking into account that the growth is only the result of nutrient consumption. The biofilm spreading is modeled by CA model and the newly formed biomass finds a place by pushing its neighbors and takes the unoccupied space. Numerical simulations were carried out in 2D and 3D. Calculated values of the global oxygen uptake rate, the concentration profiles for the oxygen, and the biomass and the colonies size were both qualitatively and quantitatively in good agreement with experimental data [61],[256]. It should be pointed out that in these models, the effect of the surrounding bulk on biofilm growth, distribution or movement is not taken into account.

1.6.6 BIOFILM MODELS WITH BIOMASS AND FLOW COUPLING

In most of the models presented previously, transport in the biofilm is only modeled by diffusion and the effect of the surrounding bulk fluid is not explicitly coupled to biofilm development. However, experiments confirmed that the hydrodynamics of the bulk fluid plays an important role in shaping the structure of biofilms through both the convection of nutrients and the detachment of biomass by shear stress [231],[232].

Based on the previously established models and a better understanding of the biofilm's properties through experiments, several biofilm models coupled with bulk fluid were developed.
Picioreanu et al. [196], [197],[198] developed 2D and 3D hybrid discrete-continuum models in which the flow over the irregular biofilm's surface, convective and diffusive mass transfer of nutrients, biofilm growth and biomass spreading were all taken into account. In this model, the biomass growth is modeled by the discrete CA (cellular automaton) model, the mass balance of the substrate is modeled by the continuity equation and the convection- diffusion-reaction equation, respectively. The flow field is governed by the momentum balance (Navier-Stokes) equation.
The fluid flow affects the biofilm's growth by both regulating the substrate concentration at the biofilm-fluid interface and by shearing the biofilm's surface. On the other hand, the interaction is reciprocal since a new biofilm's shape leads to a different boundary condition and thus different flow and substrate concentration.
The set of governing equations for biofilm model development in work of [196] are given below :

- The continuity equation for the fluid phase (incompressible)

$$\nabla \cdot \mathbf{u} = 0 \tag{11a}$$

- Momentum conservation for the fluid phase surrounding the biofilm (Navier-Stokes)

$$\frac{\partial \mathbf{u}}{\partial t} + \mathbf{u} \cdot \nabla \mathbf{u} = -\frac{1}{\rho}\nabla p + \mu \nabla^2 \mathbf{u} \tag{11b}$$

- Mass conservation for the limited nutrient

$$\frac{\partial C_S}{\partial t} + \mathbf{u} \cdot \nabla C_S = -R_S(C_S, C_X) + D\nabla^2 C_S \tag{11c}$$

- A kinetic equation for biomass growth

$$\frac{dC_X}{dt} = R_X(C_S, C_X) \tag{11d}$$

In the work of [198] a two-dimensional model was developed where biofilm detachment was considered. It was based on the internal stress created by a moving fluid in the biofilm. Two detachment mechanisms, erosion (small-particle size) and sloughing (large-biomass-particle removal) were modeled in this study.
Modeling studies reporting the effect of biofilm development on process performance are also described in the literature. 2D and 3D models for assessing the effects of biofilm development on the performance of spiral reverse osmosis membrane were also elaborated by [210], [211], radu2010, [244]. These micro-scale models combine hydrodynamics

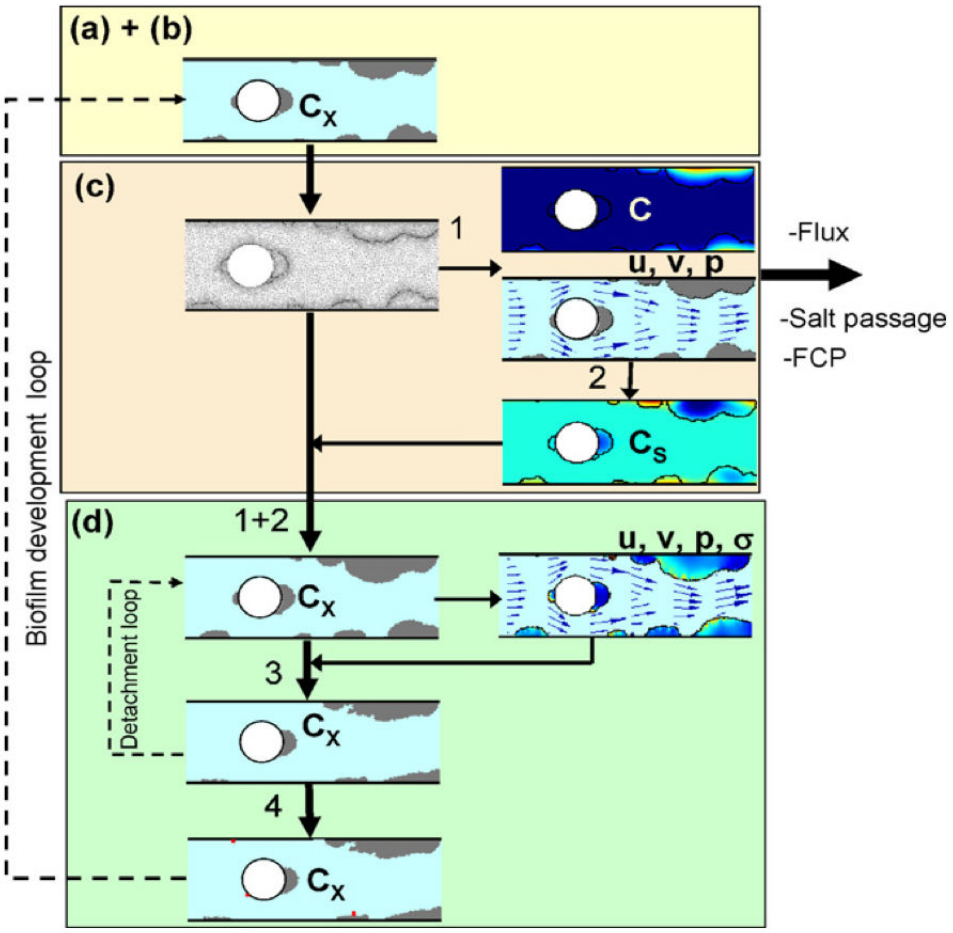

Figure 19: For a given biofilm geometry, (a) first the sub-domains, equations and boundary conditions are defined, (b) the finite element mess is created. Next (c1) the hydrodynamics and mass transport of salt are simultaneously solved followed by (c2) the solution of substrate transport and section. Based on the resulted substrate distribution (d1+d2) the biomass grows and spreads according to the cellular automaton mechanism. (d3) Mechanical stress in the biofilm is calculated and detachment steps are repeatedly performed (remeshing after each step), followed by (d4) biomass attachment (newly attached biomass). Finally, time is updated and with the newly obtained biofilm geometry the whole cycle is repeated. [212]

and mass transfer of solutes (salt and nutrients) with biomass attachment, biofilm growth and detachment due to mechanical stress of liquid flow. Models were validated by experiments. One example of model development (biofilm growth coupled with hydrodynamics flow) algorithm is given in Fig.19.

Simulation results showing biofilm development on the spiral reverse osmosis membranes are presented in Fig.fig.biofilm-development

1.6.7 UPSCALED MODELS FROM CELL-SCALE TO BIOFILM-SCALE

More recently, an increasing interest of the research community in considering the multi-scale characteristics of a biofilm from the nanometer (EPS, protein in the matrix) to the μmeter/centimeter (biofilm thickness)) in model development is reported[28], [121],[122],[261].

The idea that biofilm models should be upscaled directly from microscopic scale has been first proposed by Wanner and Gujer [247], [250]. The main advantages of the upscaled techniques, in general, and the volume averaging, in particular, are the following: 1) the resulting model relates the microscopic parameters to the observable macroscopic ones. For instance, the effective diffusivity at macroscopic scale accounts for local diffusivities, the microstructure and dispersion caused by the local velocity field; 2) upscaled equations can be used in averaged continuos volumes. Volume averaging method is one of the rigorous techniques for modeling of the porous media with different scales. Applying averaging theorems associated with this technique, continuum equations for multiphase are derived [255],[94]. This means that equations that are valid in a particular region can be homogenized in order to derive equations that are valid everywhere, This way, a discontinuous porous structure will be transformed to equivalent continuous media with effective properties containing both local and structural properties of the porous medium (See Fig.fig.voleme-av-method) .

In several studies upscaled models based on volume averaging method have been obtained to describe the cellular reactive media including cellular growth, diffusion and reaction in biofilms [60],[90],[188], [259] ,[260], [262]. More recently, the upscaled equations of mass and momentum transport in the biofilm matrix have been derived [122].

In general, most of the works with the volume averaging method focused on local mass equilibrium conditions in a representative elementary volume. Under these circumstances, all intrinsic quantities (e.g. concentration, velocity field) can be assumed to be equal in a representative elementary volume and one mass balance equation is sufficient to describe mass and momentum transport. However, it should be noted that non-equilibrium conditions with moving interfaces are closer to reality. However, one should keep in mind that in the presence of an averaged behavior (e.g. biofilm formation), the volume averaged can be applied and associated technical difficulties can be overcome.

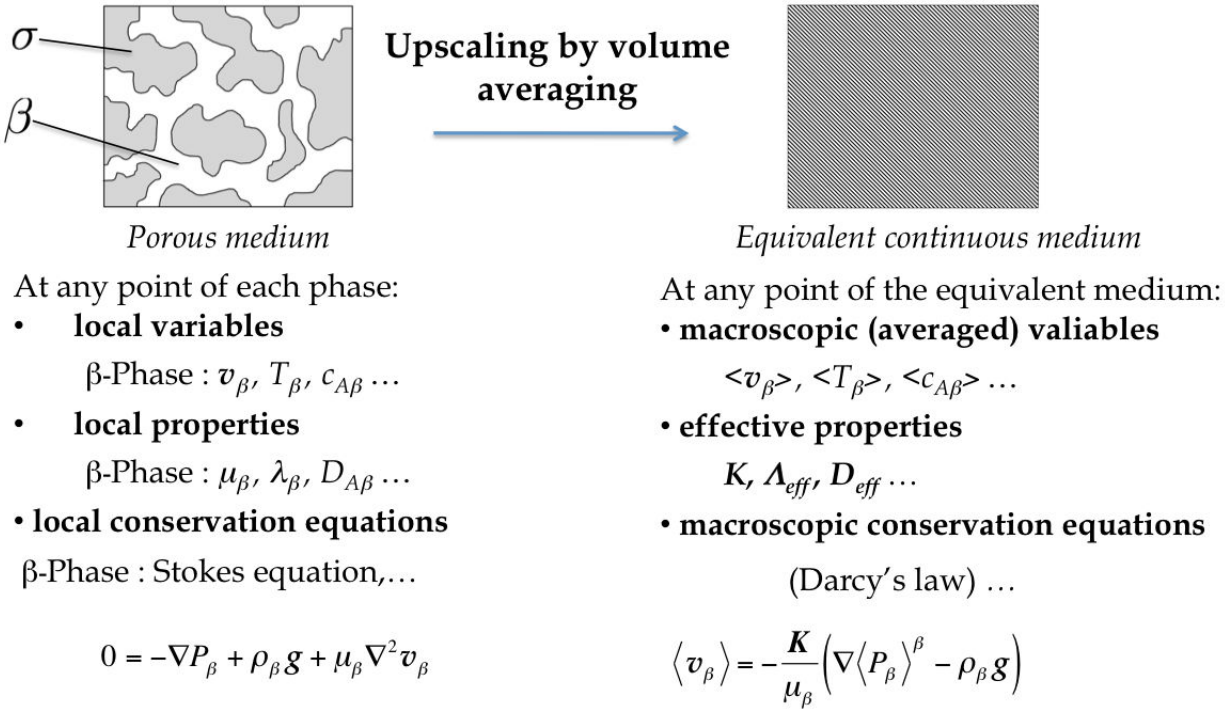

Figure 20: General principles of the volume averaging method. Left: local porous medium. Right: equivalent averaged medium with effective properties.

1.6.8 MEMBRANE FILTRATION OF MIXED SOLUTIONS

As previously discussed, the main limitations of wild spread application of membrane systems and optimization on their performance is membrane fouling leading to flux decline and modification of properties (selectivity and retention). During the filtration of different mixtures, various interactions (hydrogen bonding, Van der Waals, ionic exchange, etc.) are generated between the membrane and the particles/solutes. Recent studies are mainly invested to understand the successive steps of the membrane fouling. [4], [12], [62], [66], [74],[76], [156], [222], [235]. Electrostatic interactions between solutes and membranes have been determined [62], [125],[166], [169],[186]. The complex morphology of the membrane has been described in numerous studies [81], [215], [223]. All these experimental observations are useful to provide data for advanced models which are based on individual or combined mechanisms during a filtration process (biofilm formation cake formation, concentration polarization, pore blockage, pore constriction and series of membrane resistances). Up to now, the developed models for membrane fouling are mostly macroscopic (at membrane scale) [56], [98], [156], [212], even though a limited number models are developed at molecular scale [253]. In molecular scale models, a very high number of finite elements are needed in order to explain the local transport mechanisms. This is not optimized in terms of time and cost. Moreover the molecular scale models can only be validated macroscopically due to limitations of analytical methods. Therefore, an upscaled model based on the local description of the physical transport mechanisms is useful to give a better vision of the overall behavior of the system including both local and macrostructural information of the studied problem.

1.7 OBJECTIVES, ADAPTED STRATEGIES

The present work aims at studying the performance of a microfiltration membrane system during filtration of solutions containing bacteria and to describe the consequent fouling mechanisms.
During filtration, a biofilm develops on the membrane surface while the penetration/accumulation of secreted substances from the biofilm to the membrane internal pores occurs simultaneously. As a result, an additional dynamic resistance (both on membrane surface and in its volume) to the flow is formed which affects significantly the membrane selective properties and permeate flux.
The diagram of the problem we intend to study in this work, in all its complexity, is presented in Fig. 21. It also describes the proposed modelling and experimental approaches. As it is shown in Fig. 21, different length scales are presented in the global fouling problem: from the mean pore size of the membrane (nm to μ m), proteins (several nm), bacteria (1-2 μm) to membrane ($\sim$ 200 μ m) and biofilm thickness (from a few up to hundreds μm).
In the biofilm, three regions are considered at the local scale: cells, EPS and water channels. The transport mechanisms are convection and diffusion of species while reaction occurs at the cell-EPS interface. In the membrane compartment, proteins are transported

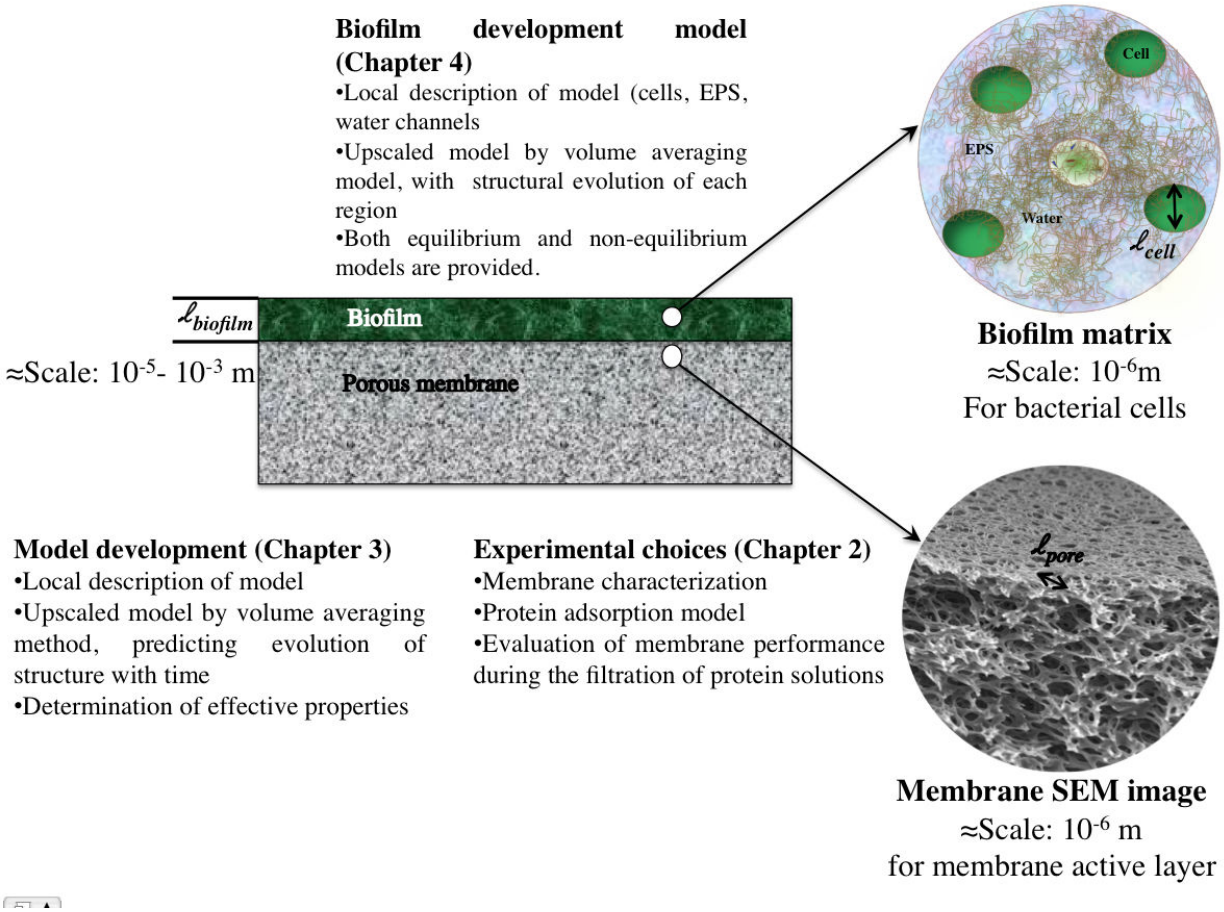

Figure 21: Thesis objectives.

by convection and diffusion to the membrane interface where protein adsorption takes place. It should be pointed out that proteins are not the only species penetrating into the membrane pores. Polysaccharides, humid substances, nucleic acids, DNA, etc. are also present in the biofilm matrix, however, in order to maintain a simple system, we only study protein adsorption to the membrane interface.

The objective of this work is to study the membrane system performance experimentally and to propose two macroscopic (upscaled) models to describe the fouling of microfiltration membranes. In the first model, fouling due to protein adsorption to the membrane pores is developed. The model is based on the transport phenomena at local scale. Governing equations of mass and momentum transport are given at this scale and boundary conditions including adsorption at interface are set. The upscaled model is then obtained using the volume averaging method. It provides averaged equations of mass and momentum transport and the effective properties of the membrane (permeability and diffusivity). The effective properties contain information of physical parameters at the pore scale along with structural parameters at the membrane scale. Some numerical simulations are run to evaluate the system performance qualitatively (more specifically the drastic changes in the concentration fields in the fluid phase and in the membrane porous structure). In parallel, experiments are specifically carried out to (1) get a better comprehension of the fouling mechanisms by proteins and (2) provide parameters for both model development at local scale and eventual validation that will be done in further work.

Membrane structural properties are obtained by a combination of analytical methods. Scanning electron microscopy (SEM) images are coupled with two porosimetry techniques (perfluoethers and mercury) in order to characterize the membrane. Three different layers are detected. Thickness, porosity and the mean pore size are measured. The initial membrane permeability is measured by filtration of milliQ water through the membrane. Two proteins are chosen in this work: BSA (Bovine Serum Albumin) and L-Glutathione. The physical-chemical properties of these molecules are significantly different. BSA is a well-known protein which can correspond to the secreted macro molecules from the biofilm. L-GLutathione is a small biomolecule (polypeptide) which can pass all through the membrane. Experiments are carried out in order to determine the adsorption isotherms laws for the two proteins. The membrane filtration of proteins is performed in a microfiltration module. The evolution of the permeate flux in function of time is evaluated for solutions of each protein. The amount of adsorbed proteins on the membrane surface is quantified by FTIR-ATR technique.

Finally, a preliminary upscaled model is developed to describe the mass and momentum transport within the biofilm. A more realistic presentation of biofilms is taken into account consisting of three regions (bacterial cells, EPS and water channels). Initial attachment of bacteria, detachment caused by shear stress and biofilm growth are not described in the model. At local scale, mass and momentum equations are described with the appropriate boundary conditions. The cellular reaction takes place at cell-EPS region. The species (glucose, polysaccharides, oxygen, etc.) associated to cell metabolism are supposed to be transported by convection and diffusion in the EPS matrix and wa-

ter channels. The solute transport to the cells is only described by diffusion. The volume averaging method is also used to derive the upscaled equations. In general, upscaled models are mostly developed under the local equilibrium conditions. The effective properties (permeability, diffusivity) of each biofilm region are expressed and can be calculated by numerical solutions of the local closure problems. The effective properties contain some additional information from both local (cell) scale and biofilm structure. The effective permeability of the biofilm is then calculated from the results of the numerical simulations in representative cellular regions with periodic flow conditions at the boundaries. Experiments are necessary both at pore-scale (e.g. local diffusivity, porosity of each region) and biofilm-scale to provide local information to the model and subsequent model validation. However, these experiments are not subject of the present work.

MICROFILTRATION MEMBRANE FOULING BY PROTEINS : CHARACTERIZATION OF MEMBRANE AND ADSORPTION

List of symbols

BSA	Bovine serum albumine
C	Bulk concentration (gL^{-1})
Cell	Regenerated cellulose
J	Permeate flux ($Lh^{-1}m^{-2}bar^{-1}$)
J_w	Permeate water flux ($Lh^{-1}m^{-2}bar^{-1}$)
K_{BSA}	The equilibrium constant for BSA sorption (Lg^{-1})
MWCO	Molecular weight cut off
PAN	Polyacrylonitrile
PC	Polycarbonate
PES	Polyethersulfone
PVP	Poly(vinylpyrolidone)
q	Mass of protein quantified per per unit of apparent membrane surface (μgcm^{-2})
q^*	Mass of protein adorned per unit of accessible membrane surface (μgcm^{-2})
K_{BSA}^{max}	Maximum sorption capacity for BSA (μgcm^{-2})
TMP	Transmembrane pressure
T	Temperature
$\alpha_{Glu}(10^6 Lcm^{-2})$	Linear adsorption constant for L-Glutathione
$\beta_{Glu}(\mu gcm^{-2})$	Linear adsorption constant for L-Glutathione

In this chapter, accumulation of organic matter on the membrane surface or into the membrane pores and its influence on permeation during filtration on polyethersulfone (PES) microfiltration membrane was studied. Two different organic compounds were selected: Bovine Serum Albumin (BSA, 66 Kg mol^{-1}, 583 peptides) and polypeptide L-Glutathione (0.307 Kg mol^{-1}, composed of three amino acids). The structure of two polyethersulfone microfiltration membranes was characterized by scanning electron microscopy and porosimetry (perfluoroethers and mercury). Despite the same chemical composition of the membrane, they presented different properties (pore diameter of active layer and structure of the intermediate layer). One of these microfiltration membranes was used to study the fouling behavior during the filtration process and to understand the different fouling mechanisms due to adsorption, reversible and irreversible pore blockage . Adsorption Isotherm experiments were carried out in static conditions. A linear adsorption isotherm was obtained for L-Glutathione (solution concentration:0-18 gL^{-1}) and a Langmuir isotherm for BSA (solution concentration: 0-24 gL^{-1}). Isotherms developed in dynamic conditions in the absence of the permeate flow and filtration experiments confirmed the linear adsorption of Glutathione whereas BSA presented lower adsorption rate compared to the static tests. Local adsorption laws could be obtained from membrane structure characterization and adsorption isotherms. For BSA solution of the relative permeate flux was linearly declined probably due to the accumulated mass of BSA on the membrane during filtration. Additionally, reversibility of the fouling was studied for Glutathione and BSA. Whereas Glutathione was totally desorbed from the membrane, results from cleaning experiments performed in membranes fouled with BSA showed the presence of polarization concentration, reversible fouling, cleanable fouling and irreversible fouling.

1 INTRODUCTION

1.1 CONTEXT

Membrane fouling is a complex mechanism associating accumulation of colloids, mineral and natural organic matter (biomolecules like proteins and polysaccharides) and biofilm development etc.

Although the nature of the fouling agents depend highly on the type of the solutions to be treated, the natural organic matter (NOM) is well known to highly participate on the membrane fouling in different filtration processes. Organic fouling may come from natural matter (humic acids), organic material coming from the filtered product or excreted by microorganisms (proteins, polysaccharides) and specific pollutants. Porous membrane fouling by organic matter occurs for example during water treatment (tap water production, wastewater or industrial effluent treatment, grey water recycling), filtration of complex media from food industry (milk, fruit juice, fermentation broth etc.). This paper focuses on the fouling of microfiltration membranes by proteins and polypeptides. Classic modeling of membrane fouling usually take into account the following phenomena:

adsorption (accumulation of solutes on the external and internal surface, changing membrane hydrophobicity and its pore diameter), pore blocking (accumulation of compounds at the pore entrance, diminishing pore diameter), concentration polarization (rise of solute concentration in the layer near the membrane surface) and cake formation (accumulation of particles on the membrane forming a second porous media). It should also be noted that depending on the particle membrane interactions (electrostatic interactions, hydrogen bonding, van der waals) the particle attachment to or accumulation on the membrane surface can be reversible (removable by physicochemical treatments) or irreversible. Up to now, several number of research works are based on Hermia description of fouling [98]. Adsorption here is a generic word describing local interactions between membrane material and solute from the bulk. In the context of protein/peptide filtration, the effect of some parameters have been deepened [208]: nature and concentration of the protein (or peptide) [5], [8], [89], [116], [129], [132], [175], [177], [184] membrane molecular weight cut off and properties, filtration mode (cross-flow or dead-end filtration)[175], and also the physicochemical properties of the solution through its pH and ionic strength [8], [62], [78], [99], [116], [141],[159], [167], [175], [176], [177], [184], [187], [189], [191], [193], [218], [266]. The physicochemical properties of the membrane can promote or prevent protein adsorption. Among these properties, roughness, tortuosity, surface charge, hydrophobicity and polarity are the main characteristics. It has been stated that the nonpolar surfaces destabilize some proteins and thereby facilitate conformational reorientations leading to strong inter protein and protein-surface interactions. This explains also the general experimental results showing that proteins adsorb more strongly on hydrophobic organic surfaces than onhydrophilic ones. Several studies investigated the effect of pH on the amount of adsorbed protein on membrane surfaces and consequent membrane fouling. It should be pointed that the pH determines the electrostatic state of proteins. When the pH equals the isoelectric point (IEP) of a protein, the number of negative and positive charges is balanced. The protein is then in neutral state. Since electrostatic protein-protein repulsions are minimized at the isoelectric point, adsorbed protein densities were found to be higher on the membrane surface at this pH. Additionally, the effective radius of proteins also depends on pH and can significantly vary in function of it and with the hydratation sphere, from 3.5 nm to 440.9 nm for Bovine Serum Albumin [62]. In several studies, membrane performances (permeability, retention) have been investigated at different electrostatic conditions (salt concentration). The ionic strength of the protein solution is a controlling parameter on the protein adsorption. The ionic strength basically determines the Debye length correlating with the damping distance of the electric potential of a fixed charge in an electrolyte. That means the higher the ionic strength, the shorter the electrostatic interactions between the charged particles. As a consequence, the adsorption of charged proteins to oppositely charged substrates is restrained whereas the adsorption to like-charged surfaces is increased. Moreover, high ionic strength conditions increase the tendency of proteins to form aggregates whilst they remain partly soluble in the solution. Hydrodynamics can also affect the quantity and the quality of protein adsorption on membranes. Convective forces increase the species accumulation

near the membrane surface [3, 38-40]. In this chapter, accumulation of proteins/peptides on or into a microfiltration membrane of polyethersulfone (PES) was studied. The effect of proteins accumulation on membrane permeation during filtration of proteins in one component solutions was also evaluated. Two different compounds were selected: a large one, which is well known, Bovine Serum Albumin (BSA, 66 Kg mol^{-1}). Thus, results from this work can be easily compared with those of the literature. A small one is also chosen, in order to get rid of eventual pore blocking or cake phenomena, and to focus on adsorption: L-Glutathione (0.307 Kg mol^{-1}). To facilitate the discussion, both compounds will be called biomolecules in the rest of this chapter. It is worth to mention that BSA exists in monomer and dimer forms, moreover the BSA molecules can form aggregates in the solution which can cause immediate pore blocking on the membrane surface. However all these effects have been neglected in this work and can be subject of future studies. Experimental values of BSA accumulation on membrane during isotherms in static conditions or filtrations from the literature are listed in Table.1.1 . To clarify, the presentation includes only experiments with low ionic strength and near pH 7 (in which BSA is negatively charged). A large dispersion of adsorption values is obtained, depending on the membrane (nature, pore size), the protein concentration, hydrodynamics, but maybe also due to the analytical method. Several authors proposed to quantify BSA in solution with UV analysis after desorption from the membrane by surfactant solutions. This step introduces uncertainty on desorption and quantification of the protein. In this work, proteins were directly quantified on membranes by FTIR methodology developed by Rabiller-Baudry [66]. In the first part, two PES membranes were characterized. The goal is to show the high variability of membrane structures. For one of the membranes, a complete description of the whole porous media (active layer, intermediate layer and mechanical support) and of the whole active surface available for adsorption was obtained. In a second part, the accumulation of BSA and L-Glutathione on this membrane was studied during isotherm in static and dynamic conditions, and during filtration experiments. The impact of protein/peptide accumulation on the flux decline was analyzed for both proteins.

2 MATERIAL AND METHODS

2.1 PROTEIN AND PEPTIDE

Bovine serum albumin (BSA) and L-Glutathione were supplied from Sigma-Aldrich. The physicochemical properties of the proteins are listed in Table 1.2. The protein solutions were prepared with milliQ water and stored in 4°C. pH of the protein solutions was 7±0.4.

Table 1.1: Experimental values of BSA adsorption during static isotherms or filtration tests in literature.

	Solution			Membrane			Adsorption process					Ref.
	C_b	other compounds	pH	Type	Nature	Pore size	Mode	TMP	T	q	J/J_W	
Static adsorption	1	Buffer phasphate	7	UF	PES	45	Quartz crystal microbalance, flow chamber	0	26	0.34	-	[95]
	1.5	-	-	MF	Glass	0.1 μm	Static adsorption	-	25	0.25	-	[177]
	20	-	5.2	-	PVP	-	Adsorption on active layer	-	-	1	-	[129]
	25	NaCl 0.001M	4.7	UF	Cell	30-100	AMicon	0	20	0.64	-	[116]
Filtration	0.05	Buffer phasphate	7	UF	PES	45	Crossflow, Hollow sibers	0.5	-	-	0.65	[95]
	1	-	5.5	UF	-	30	Amicon (filtration with stirring)	1	30	50	-	[79]
	1	NaCl 0.2 M	5.5	UF	-	30	Amicon (filtration with stirring)	1	30	100	-	[79]
	1	-	6.8	MF	PC	0.1 μm	Dead end filtration	0.7	25	130	0.45	[99]
	5	-	5.2	-	PVP	-	Filtration	-	-	7	-	[129]
	10	-	6.8	MF	PC	0.1 μm	Dead end filtration	0.7	25	165	-	[99]
	10	-	7.2	UF	PAN	20	Filtration	2	18	80	-	[5]
	24	-	7.2	UF	PAN	20	Filtration	2	18	80	-	[5]
	25	NaCl 0.001 M	4.7	UF	Cell	30-100	Amicon(Filtration with stirring)	1.38	20	1	0.18	[116]

Abreviations : PES: Polyethersulfone, PC: Polycarbonate, Cell: Regenerated cellulose, PVP: Poly(vinykpryyolidone), PAN: Polyacrykonitrile, C_b: Bulk concentration, MWCO: Molecular weight cut off, TMP: Transmembrane pressure, T: Temperature, q: Mass of BSA per unit of apparent surface, J/J_W: Permeate flux/ permeate water flux ratio.

Table 1.2: Properties of BSA and L-Glutathione

Protein	**Number of amino acids**	**Molecular weight** (kg/mol^{-1})	**Isoelectric point**	**Stokes radius** (nm)
L-Glutathione	3	0.307	-	0.38
BSA (monomer)	583	66	4.7-4.9	3.22

2.2 MEMBRANES

The microfiltration membranes used in this study were supplied by KOCH society (MFK-618) and ORELIS (FORM005FRAY), referred as membrane A and membrane B in the following paragraphs, respectively. The mean pore diameter provided by the suppliers is $\sim 0.1\mu$m. The membranes are made of three different layers: a thin active layer, an intermediate layer and a mechanical support. According to the information provided by KOCH society, the two first layers were composed of polyethersulfone (PES) and the mechanical support was composed of polyester. The original membranes were conserved in glycerol and stored at 4 °C. Before use, they were placed in the filtration system (see Fig. 1.1) and cleaned following the protocol described in Table 1.3.

Table 1.3: Protocol for membrane cleaning

Step	Solution	Time (min)	Recirculation to the feed tank
1	Demineralized water	10	no
2	NaOH 0.4%	20-30	yes
3	water	Up to neutral pH	no
4	Nitric acid 0.63%	20-30	yes
5	water	Up to neutral pH	no
6	Bleech 0.3%	20	yes
7	Demineralized water	10	no

2.3 FILTRATION SET UP AND EXPERIMENTS

A flat type microfiltration module, PLEIADE Rayflow 100 (Novasep, 7.6 $\times$17.2 cm2) and a peristaltic pomp (Watson Marlow 624U) were used for the filtration experiments. The Experimental set-up is presented in Fig. 1.1. Filtrations experiments were carried out in total recycling mode (retentate and permeate streams are recycled to the feed tank corresponding to a volume reduction ration (VRR) equal to 1). In order to determine

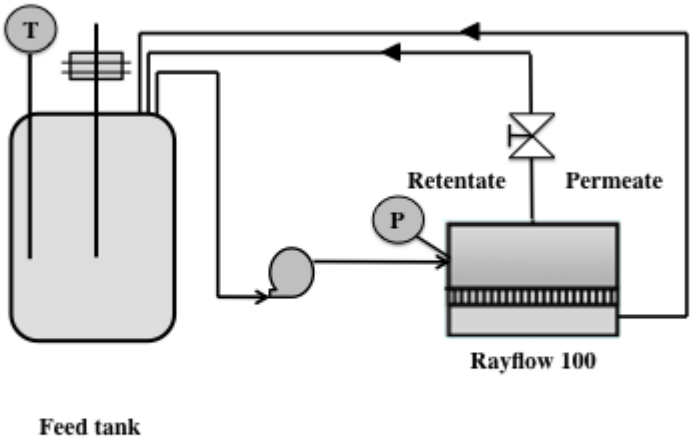

Figure 1.1: Crossflow microfiltration experimental set-upt

the evolution of membrane permeability with time, before each experiment, the initial permeability of clean membranes was measured by filtering milliQ water over a range of transmembrane pressure of 0.5-1.5 bar. Then organic solutions (protein and polypeptided) (6-12 gL^{-1} for BSA and 6 gL^{-1} for L-Glutathione) were microfiltered with an approximate cross flow velocity of 0.3 $m.s^{-1}$, transmembrane pressure of 1.00 ± 0.05 bar and at ambient temperature of 22 ± 2 °C. All given permeate fluxes are corrected at 20°C to facilitate comparisons between experiments. Permeate and retentate flows were measured manually. Filtration experiments lasted 6h for BSA and 4h for L-Glutathione solutions. It was verified that permeate flux were stable after this filtration times (data not shown). Four replicates with Glutathione 6 g and BSA 7.5 gL^{-1} were carried out to verify flux repeatability and standard deviations were calculated. To evaluate the cleanibility of the membrane fouling, water permeability of the membranes fouled with Glutathione (6 g L^{-1}) and with BSA (7.5 gL^{-1}) were measured as following: 1- directly at the end of filtration of the biomolecule solutions, 2-after 30 min water rinsing, 3-after 30 min cleaning with NaOH (0.4%wt). Experiments were repeated twice.

2.4 ADSORPTION ISOTHERMS

Adsorption isotherms experiments of the studied proteins were carried out in static conditions. Membranes were placed in Erlenmeyer sealed flasks (250 ml) in a stirred table (180 rpm, 25 °C) for 24h. Cleaned wet membrane pieces (7.5 × 2,5 cm) were brought in contact with 100 mL of protein solutions. The tested protein concentration ranged from 0 to 18 g L^{-1} for L-Glutathione and from 0 to 24 g L^{-1} for BSA. In order to evaluate the hydrodynamic effect on protein adsorption and to prevent the direct access of the proteins to the mechanical support of the membrane (like in static conditions), isotherm adsorption experiments were performed in the microfiltration system (Fig. 1.1). The tested protein concentrations were in the range of 0.5-7.5 g L^{-1} and 0.5-6 g L^{-1} for L-Glutathione and BSA respectively. Protein solutions were pumped to the filtration module without transmembrane pressure for 24h at ambient temperature. After filtration and adsorption in static and hydrodynamic conditions, membrane pieces were gently rinsed with milliQ water to remove unbounded proteins and then dried under vacuum at room temperature for 24h. The adsorbed protein's mass was measured by FTIR-ATR. In order to quantify the mass of protein adsorbed on the membrane surface in the filtration set-up, membranes were divided into 9 equivalent according to the methodology described by Delaunay et al [66]. The total adsorbed mass is then calculated as the average value of the 9 measurements and bars represent the standard deviation.

2.5 FTIR-ATR MEASUREMENT

The mass of adsorbed biomolecules on the membrane surface was measured directly by FTIR-ATR. The protocol was adapted from the work of [66] measuring the protein quantity on the ultrafiltration PES membranes.For this purpose, The FTIR-ATR spectra were registered with a spectrometer PerkinElmer (Paragon 1000, spectrum for windows software) equipped with a ZnSe crystal with an incidence angle of 45° and 12 reflections [38]. The background spectra were recorded in air. The conditions of acquisition were as follows: 20 scans, 2 cm^{-1} resolution. The samples of the original and fouled membranes were dried under vacuum before measurements. Proteins, inside and/or along the membrane surface, can be detected from the amide II bond due to CN + NH vibrations and located in the range of 1520-1550 cm^{-1}. PES exhibits a band located near 1240 cm^{-1} corresponding to a C-O vibration of the C-O-C ether group. In this work BSA and L-Glutathione present an amide bond 1528 cm^{-1}. This region is without any superimposition with any bond due to PES. The amide I bond due to C=O vibration located close to 1650 cm-1 is partly overlapped by a bond of the original membranes and an harmonic of water that can exist if the drying is not well controlled. Consequently, this band is less suitable for further quantifications. In order to take into account the difference in penetration depth of the light beam in the PES (active and intermediate layers), due to variable

thickness of the fouling layer, the quantification is based on the height ratio defined as:

$$\text{Height ratio} = \frac{H^{amide,\text{II}}}{H^{1240}} \tag{1.1}$$

Where H^{1528} is the peak height of the bond located close to the wavelength of the protein amide II vibration and H1240 is the peak height of the band located at 1240 cm^{-1} due to C-O vibration of the C-O-C group of PES. The baseline was taken in the the wavenumber range of 2129-2262 cm^{-1} for which there is no specific absorbance on the spectra. Finally, quantification was possible according to the following expression:

$$\text{q} = a \times \frac{H^{1528} - H^{baseline}}{H^{1240} - H^{baseline}} + b \tag{1.2}$$

Where $H_{baseline}$ is the average height of the baseline in the chosen range of wavenumber, corresponding to non-specific absorbance of the membrane as commonly observed, q is the quantity of protein adsorbed on the membrane (expressed in μg of protein per membrane apparent surface μg/cm^{-2}) and a and b are constants specific to each couple (membrane-biomolecule) studied. Calibration curves determined for BSA et Gluthatione are described in Fig. 1.2 and Table. 1.4.

Table 1.4: Calibration parameters for FTIR quantification of L-Glutathione and BSA on PES membrane A (KOCH), 8 samples were used and experiments were repeated twice for each biomolecule

	a	b	R^2	Uncertainty
L-Glutathione	1202.9	-35.3	0.99	$\pm$ 25 μg cm^{-2} for H^{1528}/H^{1240}¡0.35
BSA	1443.2	-40.8	0.96	$\pm$ 20 μg cm^{-2} for H^{1528}/H^{1240}¡0.04 $\pm$ 50 μg cm^{-2} for H^{1528}/H^{1240}¿0.04

2.6 DETERMINATION OF PROTEIN CONCENTRATION IN SOLUTIONS

The protein concentration in solutions were determined with a spectrophotometer at λ=277 nm [222].

2.7 MEMBRANE CHARACTERIZATION

2.7.1 SCANNING ELECTRON MICROSCOPY (SEM)

Membrane's structure (surface and section) was examined by a FEG-SEM (Leo 1530). Dried membrane samples (cleaned and fouled) were frozen in liquid nitrogen (77 K) and fractured [215]. After coating with tungsten, they were viewed with the microscope at 3

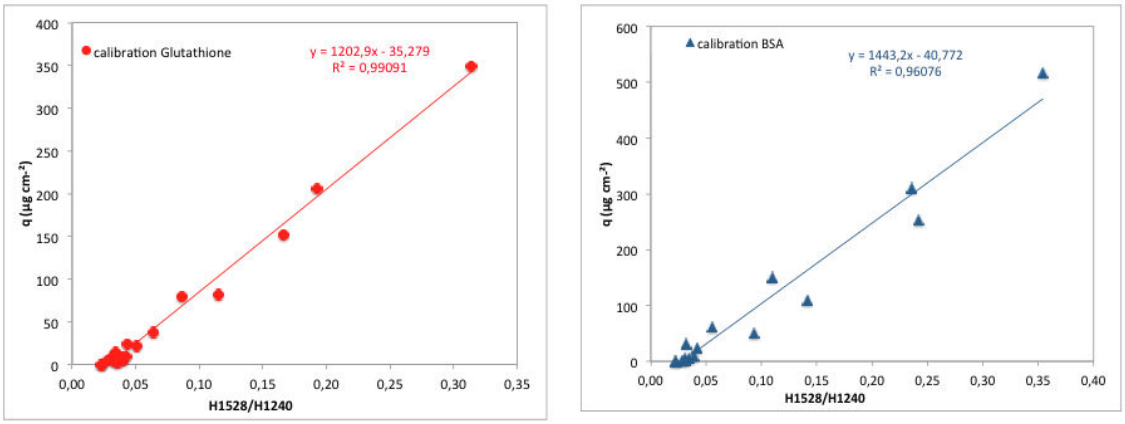

Figure 1.2: Calibration curves of adsorbed mass of proteins/ membrane surface in function of H^{1528}/H^{1240}

kV. Working distance (WD) varies between 3 -10 mm. The sample chamber is held under estimated vacuum of 10^{-5} Torr. After image acquisition by SEM, membrane's layers analysis were done using the ImageJ software. The surface porosity of the membrane active layer was determined after calibration of the contrast and the brightness of the SEM images in order to obtain binary (black and white images). The sum of black pixels over the examined surface represents the surface porosity. The analysis was duplicated for each image.

2.7.2 MEAN PORE SIZE AND PORE SIZE DISTRIBUTION

The pore size of the active layer of clean and dry membrane samples was measured by porosimetry (Porolux 1000) [26]. This device allows accurate measurements of pore size distributions from 13 nm to 500 μm. It uses a bubble-point extended method based on the measurement of the pressure necessary to blow air through the liquid-filled porous membrane. The samples were previously wetted with a liquid (perfluoethers of low surface tension 16×10^{-3} N m^{-1}), that can be assumed to have a zero contact angle with most materials, included biological ones. The wetted sample was subjected to increasing pressure, with a compressed clean and dry air. As the pressure increased, it reached a point where it overcame the surface tension of the liquid in the largest pores and pushed the liquid out. Increasing the pressure still further allowed the air to flow through smaller pores. By monitoring the applied pressure and the gas flow through the sample, a wet run was obtained, followed by a dry run performed with the dry sample (with no liquid

in the pores). The measurement of the flux for wet and dry runs, combined with a model for gas transport through the pores, over the membrane allows one to obtain the pore size distribution.

2.8 MERCURY INTRUSION POROSIMETRY

Porosity and mean pore diameter of the intermediate layer and the mechanical support of the membrane were determined using a mercury porosimeter (Autopore 9500, Micromeritics). This measures the non-wetting mercury volume penetrating the pores for an increasing pressure applied on the mercury. By use of Washburn (1921) relation between pressure and pore size and considering the volume filled by mercury as the pore volume, the cumulative porosity versus pore distribution is obtained [26]. Penetrometer reference is [13-0135], 3 bulb, 0.39 Stem, Solid], mercury filling pressure is set to 0.42 psi and equilibration time is about 30 s.

3 RESULTS AND DISCUSSION

First, the structure characterization of the microfiltration membranes A (KOCH) and B (ORELIS) is presented. The methods used were SEM, bubble point measurement on Porolux 1000 and mercury porosimetry. Later, the fouling of membrane A by the tripeptide L-Glutathione or BSA is deepened. Adsorption isotherms in static and dynamic conditions are compared. Finally, the impact of the protein adsorption on the permeate flux during filtration is discussed.

3.1 MEMBRANES CHARACTERIZATION

Two microfiltration membranes in PES with mean pore diameter of 0.1 μm (value supplied by membrane societies) were compared. In Fig. 1.3 and 1.4, SEM images of membrane A and B are presented, respectively. Despite the same type of membrane, it is evident that the structures are different. Active layer of membrane A is a loose net with many interconnections with the layer below and a large dispersion of pores diameters (20-600 nm) whereas for membrane B, the active layer looks denser, with less interconnections and a more narrow dispersion of pore diameters (10-60 nm) (See table. 1.5).Active layer pore diameters determined by bubble point extended method (Porolux) fit with maximum pore diameter determined by SEM. The intermediate layers intermediate layer, just below, are also quite different. The intermediate layer for membrane A has the same structure of the active layer but it is homogeneously distributed in the 3 dimensions and with larger pores. The intermediate layer of membrane B presents presents large cylindrical pores (up to 10 μm diameter) across the whole layer, from the active layer to mechanical support. A similar net pattern as membrane A with pores of 1 μm or less represent the walls of theses macropores. Mechanical supports are clothes of fibers (diameter: 15-20 μm, measured with SEM images). The porosity and the mean pore diameter of the intermediate layer

and mechanical support of membrane A were analyzed with mercury intrusion porosimetry. The whole porosity of the membrane (neglecting the void volume in the active layer) is equal to 0.683 and is due to two pores distributions: the first one between 12 and 430 μm with a mean pore diameter around 88 μm, the second one between 0.06 and 11 μm, with a mean pore diameter around 2.9 μm (Fig. 1.5). Unfortunately the first calculations (not detailed here) showed that these two pore distributions can not be directly associated with the mechanical support and the intermediate layer, respectively. This is probably due to the superimposition of the pore profiles of both materials. Tortuosity was evaluated at 1.46. The estimated active area of the intermediate layer and mechanical support layers all together is 7.6 m^2g^{-1} and the average pore diameter is 895 nm. The structural parameter S detailed in Eq. (1.3) was calculated with mercury porosimetry results.

$$S = e \cdot \tau\varepsilon \tag{1.3}$$

with e: thickness of the membrane, τ the tortuosity and ε the porosity. S=459 μm The results of pore distribution, porosity of the global material and structural parameter are similar to those found in the literature using the same measurement method [155], [154]. The structural characteristics of membranes A and B are summed up in Table. 1.5.

Table 1.5: Membrane characteristics (A:KOCH-MFK and B:ORELIS-FROM005FRAY)

	A:KOCH-MFK-618				B: ORELIS-FROM005FRAY			
	Mb	**AL**	**IL**	**MS**	**Mb**	**AL**	**IL**	**MS**
Thickness (μm) SEM	215±2	0.1-0.5	95-105	115-125	186±2	60-80	100-120	-
Mean pore diameter μm	-	0.39-0.6 (porolux)	2.9 (Hg)	88 (Hg)	-	0.057 (porolux)	-	-
Pore distribution μm	-	0.02-0.6 (Porolux)	0.06-11 (Hg) 0.06-450 (Hg)		-	0.01-0.06 (Porolux)	-	-
Porosity %	68.3 (Hg)	28-30 (SEM)	-	-	-	20-25 (SEM)	-	-
Fiber diameter μm	-	-	-	15	-	-	-	20

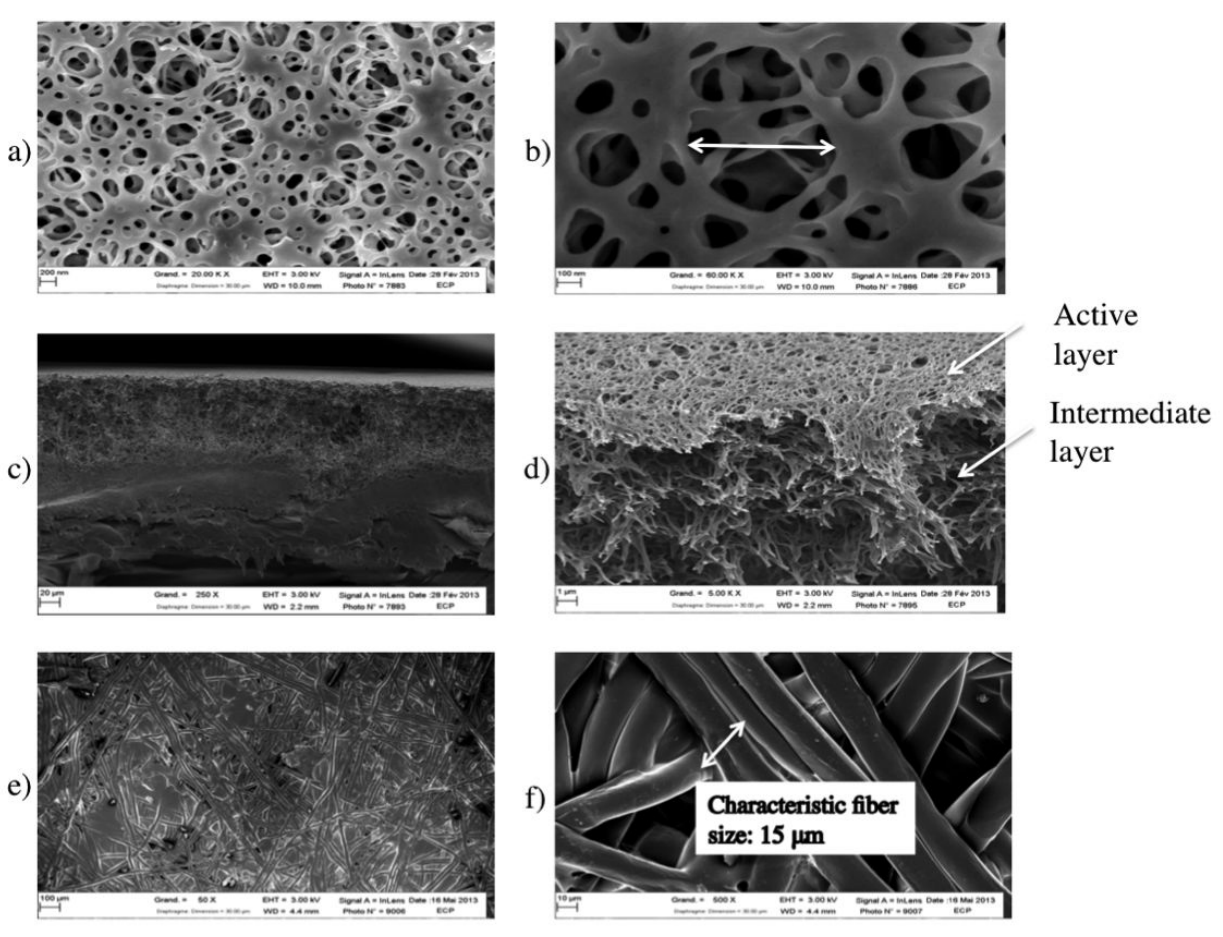

Figure 1.3: Active layer and cross-sectional SEM images of KOCH membranes a,b) active layer with mean pore size of 0.4 μm c,d) membrane cross section with different layers, e,f) mechanical support

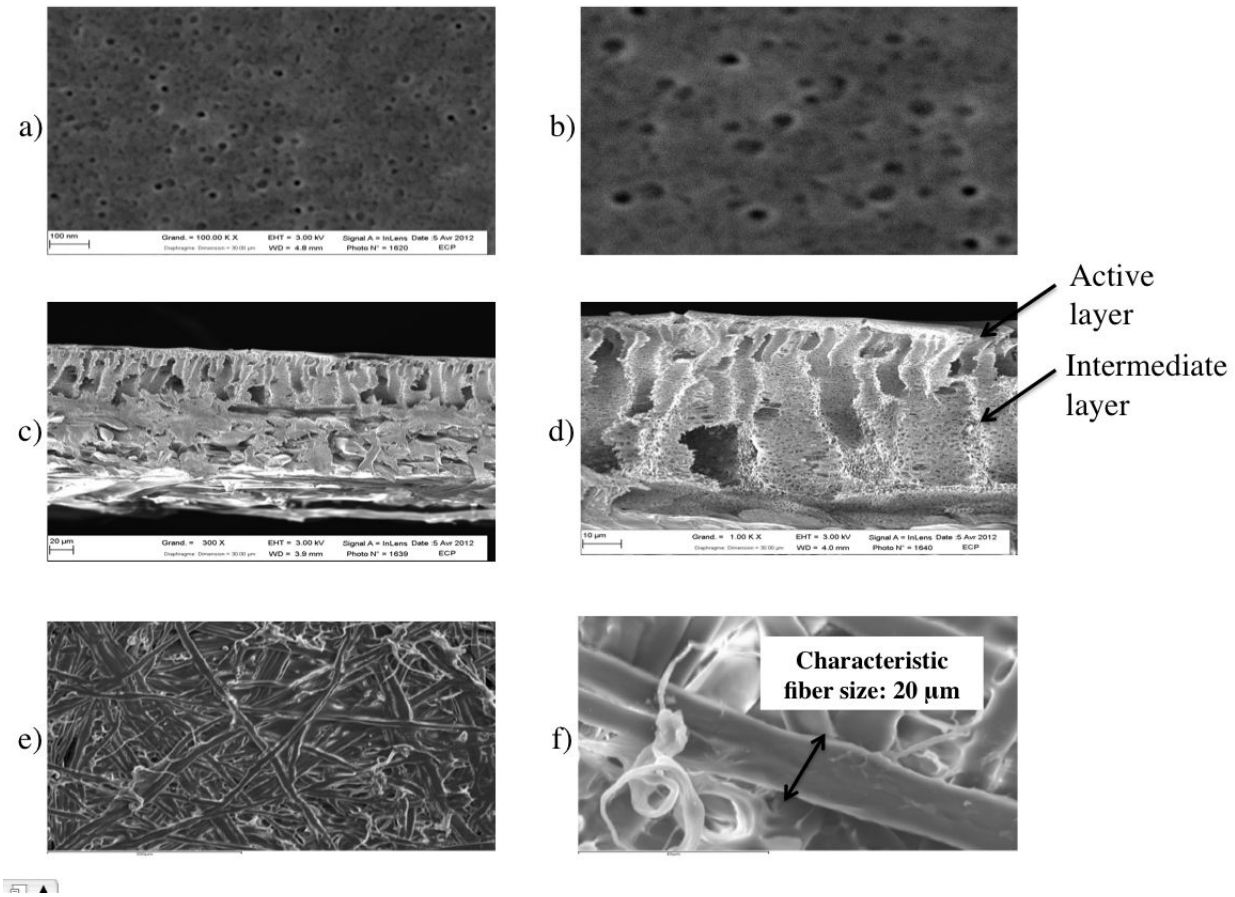

Figure 1.4: SEM images of Orelis membranes : a,b)active and c,d)intermediate layers, e,f) mechanical support

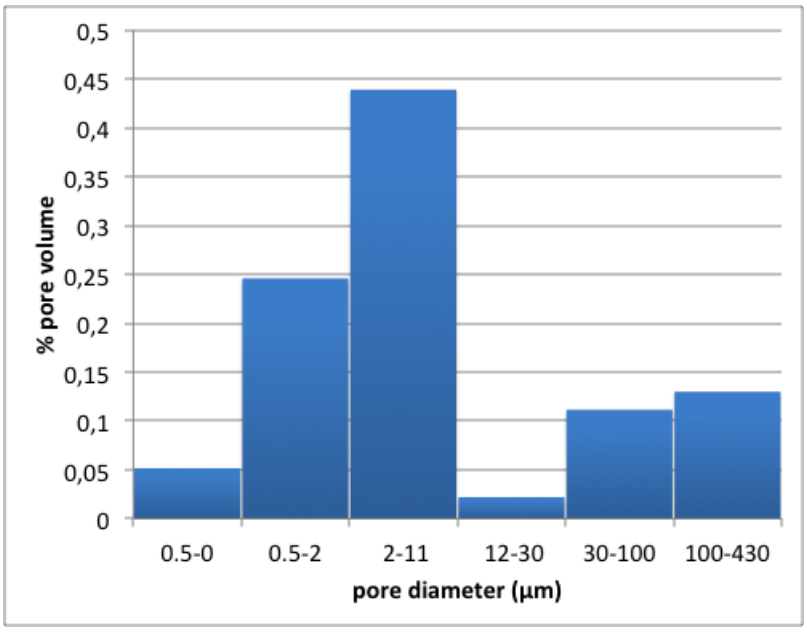

Figure 1.5: Pore diameter histogram for the intermediate layer and the mechanical support determined with mercury intrusion porosimetry

3.2 FOULING OF MEMBRANE A BY PROTEINS

In the following paragraphs, results from the experiments assessing the fouling of membrane A by Glutathione and BSA will be described. According to SEM and Porolux measurements, the active layer has pore diameters between 20-600 nm with a mean pore diameter of 400-600 nm (Table. 1.5). Taking into account the estimated stokes radius of both proteins (0.38 nm for Glutathione and 3.5 nm for BSA), nor cake formation nor pore blocking are expected to occur during filtration. Adsorption on the external or internal surface of the membrane should be then the main mechanism. But it is well known that protein effective radius depends on the pH and the ionic forces of the medium. According to De La Casa [62], effective BSA radius is 3.5 nm at its isoelectric point pH 4.9, 41.5 nm at pH 6, 440.9 nm at pH 7, and 304.9 nm at pH 8. In the pH conditions of this study (pH 7$\pm$ 0.4), BSA is expected to be partly retained on the active layer. For glutathione, no data showing the effect of pH on the Stokes radius was found. In the following paragraphs, for comparison purposes, it was chosen to use weight concentrations instead of molar concentrations for both proteins. Weight concentrations are representative of the number of peptide units adsorbed on the membrane (0.10-0.12 kg mol^{-1} per peptide), whatever the protein.

Adsorption in Erlenmeyer flasks: Glutathione or BSA were adsorbed on membrane A following the protocol described in paragraph 2.4. In these experiments the entire membrane material is accessible for the proteins, which can adsorb on the active and

intermediate layers as well as in the mechanical support. Variations of protein concentrations in the bulk solutions, thus the amount of adsorbed proteins on the membrane, were not measurable by spectrometry. Instead, the biomolecules were directtly measured on the membrane surface by application of FTIR-ATR. Two areas can be used to report the amount of protein adsorbed and to calculate the sorption capacity q. The area of the apparent membrane surface and the area of the active surface measured with mercury porosimetry. First, the isotherm constants were calculated using the apparent membrane surface. The results are presented in Fig. 1.6 (red disc) and Fig.1.7 (blue triangle). From the results, L-Glutathione adsorption isotherm is linear Eq. (1.4a) whereas BSA isotherm has a Langmuir form Eq. (1.4b).

$$q = \alpha_{glu} C_b + \beta_{glu} \quad \text{For L-Glutathione} \tag{1.4a}$$

$$q = \frac{q_{BSA,max} K_{BSA} C_b}{1 + K_{BSA} C_b} \quad \text{For BSA} \tag{1.4b}$$

With q the mass of protein adsorbed per membrane apparent surface unit (μg cm^{-2}), C the bulk concentration (g L^{-1}), α_{glu} (10^6Lcm^{-2}), β_{glu} (μg cm^{-2}) the linear equation constants for L-Glutathione, q_{BSA}^{max}(μg cm^{-2}) and K_{BSA} (L g^{-1}) the maximum apparent sorption capacity and the equilibrium constant for BSA sorption, respectively. Equations parameters are gathered in Table. 1.6.

In the range of the bulk concentrations studied, the mass of BSA adsorbed is larger than the one of L-Glutathione at the same bulk concentration. However the maximum sorption capacity for BSA is lower than the one L-Glutathione could reach at higher bulk concentrations, this tripeptide being still in a linear part of isotherm at the studied bulk concentrations. Considering the global active surface (taking into account the active, intermediate layers and the mechanical support) obtained with the intrusion mercury porosimetry method, a local adsorption law is calculated. The ratio between the active surface (cm^2) of each layer (AL and IL+MS) and the apparent surface (cm^2) are respectively 0.3cm^2 AL cm^{-2} apparent and 1003.7 cm^2 IL+MS cm^{-2} apparent. Global active surface ratio is 1004. The local adsorption of L-Glutathione and BSA are then described in Table.1.7. The methodology is the same as the one used for adsorption on active carbon for example [171]. These values are interesting because they could be used to evaluate the mass of protein involved in local fouling and simulate the progressive fouling of this porous media (not presented here).

Table 1.6: Apparent adsorption laws on membrane A (mass of protein per unit of membrane active layer surface)

Protien	Adsorption law	experimental parameters	
L-Glutathione	$q = \alpha_{Glu} C + \beta_{Glu}$	$\alpha_{Glu} = 0.199 \times 10^{-3}$ m	$\beta_{Glu} = 1.27 \times 10^{-3}$ gm^{-2}
BSA	$q = \frac{q_{BSA}^{max} K_{BSA} C}{1+K_{BSA} C}$	$q_{BSA}^{max} = 7.5 gm^{-2}$	$K_{BSA} = 0.09 \times 10^{-3} m^3 g^{-1}$

Table 1.7: Local adsorption laws on membrane A (mass of protein per unit of accessible membrane active layer)

Protien	Adsorption law	experimental parameters	
L-Glutathione	$q^* = \alpha_{Glu}^* C + \beta_{Glu}^*$	$\alpha_{Glu}^* = 0.199 \times 10^{-6}$ m	$\beta_{Glu}^* = 1.27 \times 10^{-6}$ gm^{-2}
BSA	$q^* = \frac{q_{BSA}^{max*} K_{BSA}^* C}{1+K_{BSA*} C}$	$q_{BSA}^{max*} = 7.5 gm^{-2}$	$K_{BSA}^* = 0.09 \times 10^{-3} m^3 g^{-1}$

Adsorption process in filtration module with TMP $\approx$ 0 bar: Adsorption isotherms in the Rayflow filtration module with TMP approximately equal to zero were carried out during 24h; It should be pointed out that under these conditions, the intermediate layer and the mechanical support were not directly in contact with the protein solution. The crossflow velocity was set lower than filtration tests in order to facilitate the protein deposition to the membrane surface. Tangential average speed was 0.1 m s^{-1}. The influence of hydrodynamics was noticed: the protein accumulation on the membrane is not homogenous. The highest amount of mass of adsorbed protein is measured in the center of the membrane, as described by Delaunay et al.[66].

Results of the adsorption isotherms in the filtration module are presented in Fig.1.6 (white disc) and Fig. 1.7 (white triangle). In the case of L-Glutathione, the data fit very well with the linear isotherm performed in static conditions. L-Glutathione is small enough to penetrate all the layers and adsorb on the membrane in the same manner as during tests in Erlenmeyers. In the case of BSA, the mass adsorbed is only 56% of the total mass adsorbed in the Erlenmeyer tests at the same bulk concentration. This can be explained by the fact that BSA has not access to the whole material as during the tests in Erlenmeyer. The BSA effective radius is equivalent to the pore diameter of the membrane at pH 7. The 56% represent only the fraction of protein adsorbed on the active layer and a small part that may have penetrated.

Adsorption during filtration at TMP $\approx$ 1 bar: Filtrations in full recycling mode were carried out with membrane A, during 4h with Glutathione concentrations at 6 g L^{-1} or 6h with BSA solutions at 3, 6, 7.5, 10 and 12 g L^{-1}. Adsorption results are presented in Fig. 1.6 (black disc) and Fig. 1.7 (black triangle). L-Glutathione adsorption during filtration of 6 g L^{-1} solution fits completely with data from isotherms developed in the filtration system without TMP. Therefore, no effect of TMP is noticed. In the case of BSA, the large protein present an adsorbed mass in the same order of magnitude in the experiments at TMP $\approx$ 0 bar and TMP $\approx$ 1 bar. Nevertheless, measured values were lower than in static conditions (isotherm in Erlenmeyer). Additionally, in the range between 6 and 12 g L^{-1}, the maximum adsorbed amount of BSA is attained. As discussed in former paragraph, because of steric effect, a fraction of BSA is retained at the membrane surface, limiting the accumulation into the intermediate layer and the mechanical support. This can be due to pore blocking mechanisms. The convection can also limit the accumulation of BSA on the active layer, balancing the rise of TMP. Results can be compared to the literature (Table 1.1, Fig.1.7). It can be noticed that our results show the same order of magnitude of those obtained Herrero et al [99] on 0.1 μm microfiltration membranes. UF experiments show less adsorption, demonstrating the role of active layer pore diameter in the accumulation of protein (Table. 1.1). It should also be pointed out that the difference in time scales between the adsorption isotherms (24h) and filtration experiments (6h) can effect the total adsorbed mass on the membrane surfaces. This latter is observed clearly in the case of BSA protein along with the steric hinderance of this protein.

In order to evaluate the impact of protein accumulation on the permeate flux reduction, experiments were carried out. Fig. 1.8 shows the evolution of the relative permeate flux (J/Jw) with time for one concentration of L-Glutathione and BSA in replicated assays. The repeatability of the assays have been verified Fig. 1.8. Values of the permeate flux are presented in Table. 1.8 and Table.1.9.

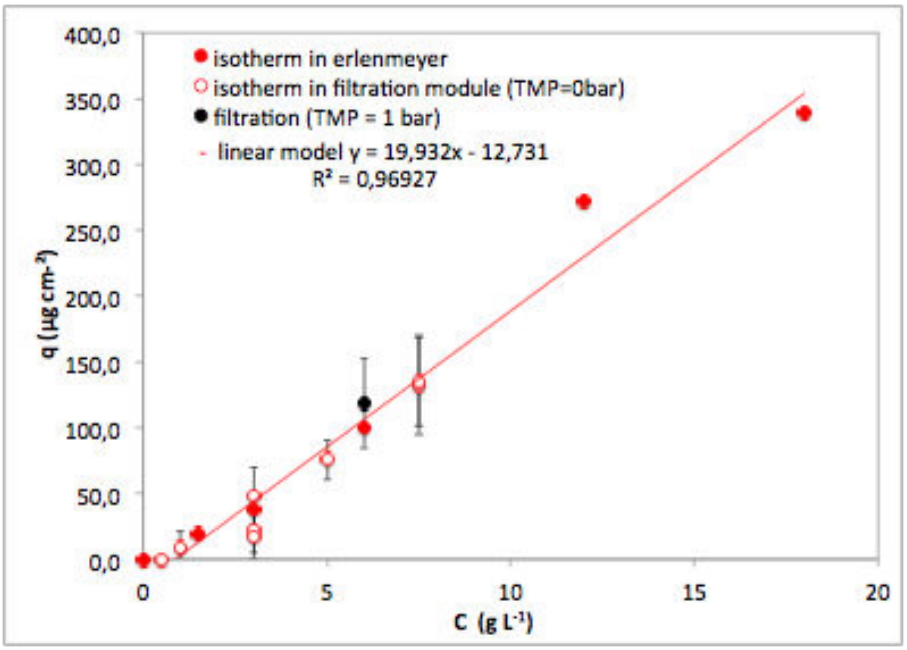

Figure 1.6: Isotherm adsorption of L-Glutathione (25°C) on membrane A in Erlenmeyers (red disc) and in filtration module (white disc) and L-Glutathione retained on membrane A during filtration (black disc)

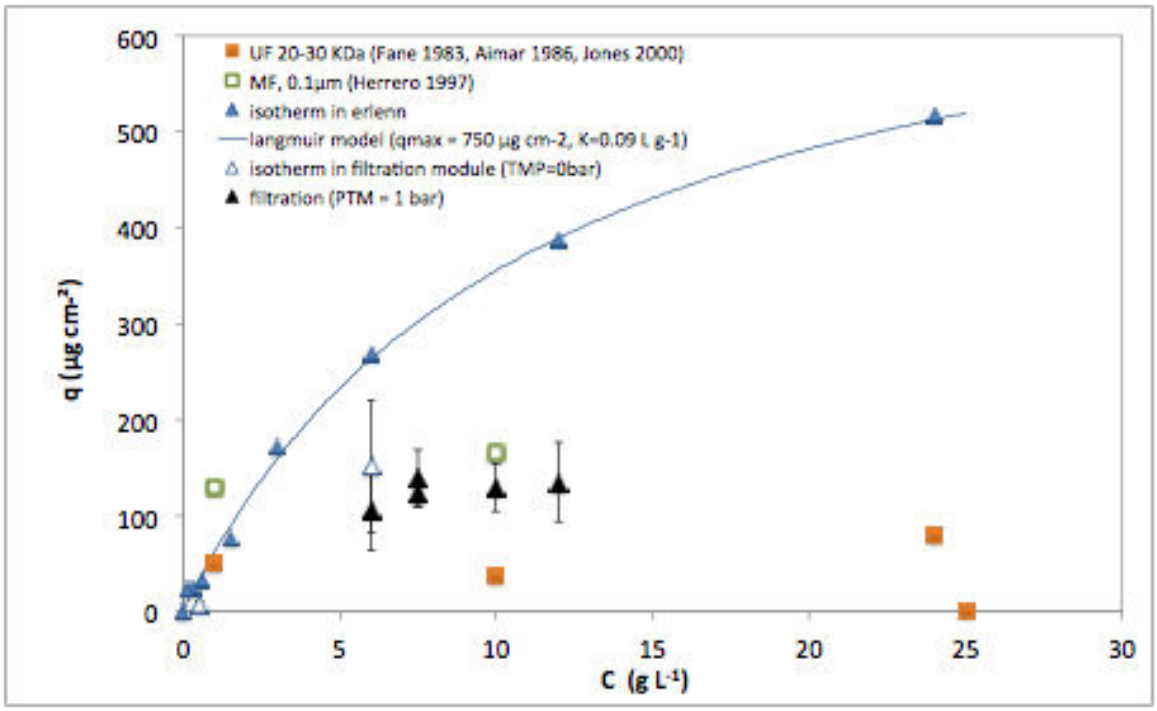

Figure 1.7: Isotherm adsorption of BSA (25°C) on membrane A in Erlenmeyers (blue triangle) and in filtration module (white triangle) and BSA retained on membrane A during filtration (black triangle), compared to literature values obtained during filtration of BSA.

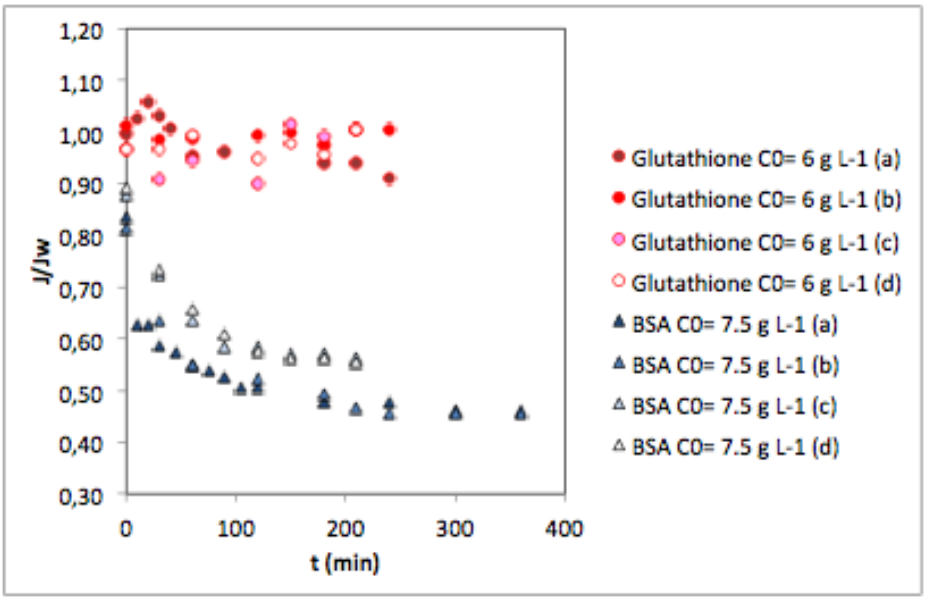

Figure 1.8: Repeatability tests for membrane A (KOCH) fouling with synthetic solutions of L-Glutathione (6 gL^{-1}) or BSA (7.5 gL^{-1}) (filtration at 1bar, 0,3m s^{-1}): relative flux at 20°C versus time of filtration (min)

At the lowest feed concentration tested (4 g L^{-1}), L-Glutathione can improve the permeate flux (Fig. 1.9), suggesting that the membrane is more hydrophilic in the presence of this protein. On the contrary, BSA already generates 27% of flux decline. At the highest concentration (12 g L^{-1}) tested, the flux decline is 18% for L-Glutathione and 51 % for BSA. Mass adsorption of L-Glutathione is 271 μg cm^{-2} and 135 μg cm^{-2} for BSA (Fig. 1.6 and 1.7), but permeability is not impacted by L-Glutathione adsorption, on the contrary with BSA. L-Glutathione has probably access to a larger surface of adsorption due to its small size and its penetration into the material, even if it does not generate pore blocking. The strong link between relative flux J/Jw (measured after 180 min of filtration) and the mass of protein accumulated on membrane in the case of BSA is demonstrated in Fig. 1.10. This linear relation could not be generalized: The flux decline was not the same at all for L-Glutathione even with the same mass of protein accumulated on the membrane. The relative flux presented here are comparable with those described for BSA by Hashino et al. (0.65 for BSA at 0.05 g L^{-1}, [95]) and Herrero et al. (0.45 for BSA at 1 gL^{-1} and 130μg cm^{-2} ,[99]).

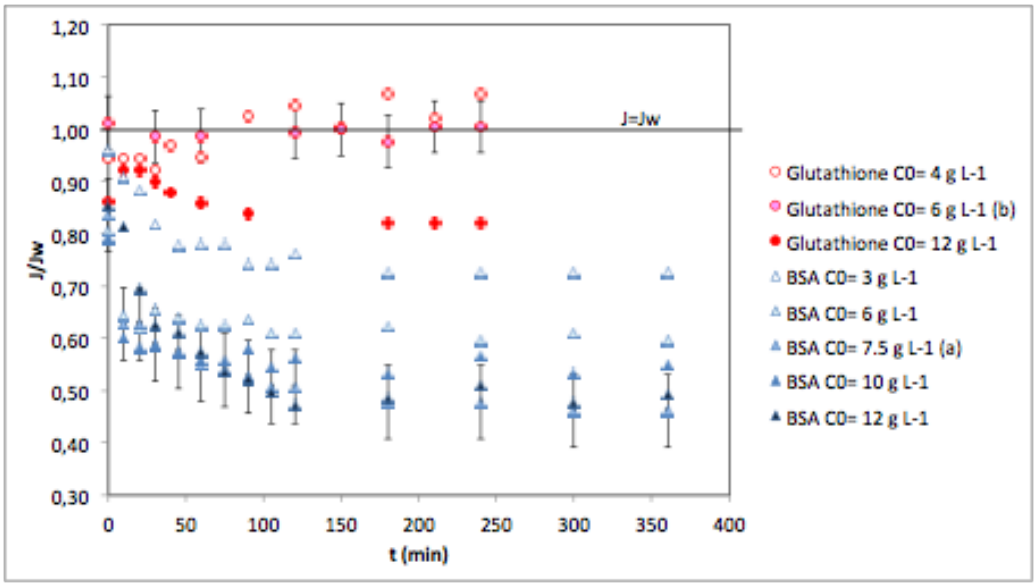

Figure 1.9: membrane A (KOCH) fouling with synthetic solutions of L-Glutathione or BSA at different concentrations (filtration at 1bar, 0,3m s^{-1}): relative permeate flux corrected at 20°C versus time of filtration (min)

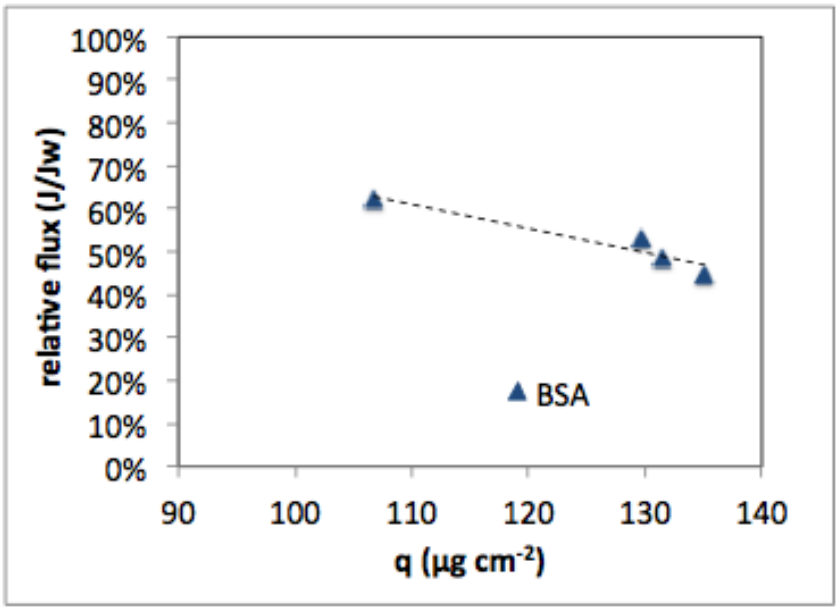

Figure 1.10: membrane A (KOCH) fouling with synthetic solutions of BSA at different concentrations (filtration at 1bar, 0,3m s^{-1}): relative permeate flux corrected at 20°C versus mass of protein adsorbed on membrane.

Table 1.8: Membrane A (KOCH) filtered with syntethic solutions of L-Glutathione at different concentrations (filtration 1 bar, 0.3 ms^{-1}): new clean membrane water flux (J_w), permeate flux during filtration of protein solution (J), water flux with fouled membrane J_{w-f}, after 30 min of water rinsing J_{w-r} and after 30 min of NaOH cleaning J_{w-c}

	J ($Lh^{-1}m^{-2}$) during the filtration of L-Glutathione, 20°C					
	4 gL^{-1}	6 gL^{-1} (a)	6 gL^{-1} (b)	6 gL^{-1} (c)	6 gL^{-1} (d)	12 gL^{-1}
J_w $Lh^{-1}m^{-2}$, 20°C	104.4	158.2	143.5	190.1	142.49	213.7
J (t=0 min) $Lh^{-1}m^{-2}$	98.5	157.6	145.2	183.9	137.9	183.9
J (t=180 min) $Lh^{-1}m^{-2}$	111.4	148.6	140.1	188.6	136.2	175.1
J_{w-f} with fouled membrane $Lh^{-1}m^{-2}$	-	-	-	183.9	137.9	-
J_{w-r} after rinsing 30 min $Lh^{-1}m^{-2}$	-	-	-	183.9	137.9	-
J_{w-c} after cleaning 30 min $Lh^{-1}m^{-2}$	-	-	-	183.9	137.9	-

Table 1.9: Membrane A (KOCH) filtered with syntethic solutions of BSA at different concentrations (filtration 1 bar, 0.3 ms^{-1}): new clean membrane water flux (J_w), permeate flux during filtration of protein solution (J), water flux with fouled membrane J_{w-f}, after 30 min of water rinsing J_{w-r} and after 30 min of NaOH cleaning J_{w-c}

	J ($Lh^{-1}m^{-2}$) during the filtration of BSA, 20°C							
	3 gL^{-1}	6 gL^{-1}	7.5 gL^{-1} (a)	7.5 gL^{-1} (b)	7.5 gL^{-1} (c)	7.5 gL^{-1} (d)	10 gL^{-1}	12 gL^{-1}
J_w $Lh^{-1}m^{-2}$, 20°C	169	171.3	183.2	282.7	143.1	114.5	139.4	166.5
J (t=0 min) $Lh^{-1}m^{-2}$	162.3	137.9	153.2	229.9	125.4	102.2	110.3	141.4
J (t=180 min) $Lh^{-1}m^{-2}$	122.6	106.6	87.5	139.3	81.7	64.5	74.3	74.3
J_{w-f} with fouled membrane $Lh^{-1}m^{-2}$	-	-	-	-	98.5	76.6	-	-
J_{w-r} after rinsing 30 min $Lh^{-1}m^{-2}$	-	-	-	-	110.3	81.1	-	-
J_{w-c} after cleaning 30 min $Lh^{-1}m^{-2}$	-	-	-	-	119.9	95.1	-	-

Table 1.10: Membrane A (KOCH) filtered with synthetic Solutions L-Glutathione (6 gL^{-1}) and BSA (7.5 gL^{-1}). Filtration at 1bar, 0.3 ms^{-1}. Mass of adsorbed protein on membrane after fouling (membrane b) and after cleaning (membrane c,d

	C (L-Glutathione)	q	±Δq	C(BSA)	q	±Δq
Membrane	(gL^{-1})	μgcm^{-2}	μgcm^{-2}	(gL^{-1})	μgcm^{-2}	μgcm^{-2}
b	6	118.2	34.2	7.5	123.6	14.2
c	6 (cleaned)	0	2.4	7.5 (cleaned)	54.7	8.4
d	6 (cleaned)	0	1.3	7.5 (cleaned)	13.1	3.4

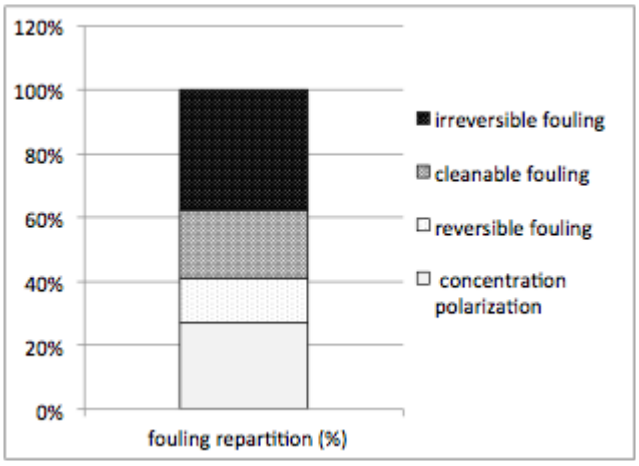

Figure 1.11: Membrane A (KOCH) fouling with synthetic solution of BSA 7.5 g L^{-1}. Attribution of flux decline to concentration polarization, reversible, cleanable and irreversible fouling.

In order to evaluate the fouling reversibility, a cleaning procedure was carried out. (See section 2.3). Flux decline with L-Glutathione is very low at 6 g L^{-1} even if adsorption is measured (118.2 μgcm^{-2}). Rinsing with water and cleaning with NaOH have no major effect on this parameter even if that quantification of protein before and after cleaning shows that all accumulated L-Glutathione is removed (Table. 1.8 and 1.10). On the contrary, with BSA at 7.5 g L^{-1}, after 180 min of filtration, flux decline has reached 43-44$\%$, with the same order of magnitude of protein adsorbed as L-Glutathione (123.6 μ g cm^{-2}) (Table. 1.9 and 1.10). When filtrating water instead of BSA solution with the fouled membrane, 31-33$\%$ of flux decline was observed. The difference of flux decline corresponds to the impact of polarization of concentration. After water rinsing, reversible fouling elimination leads to a flux decline of 23-29$\%$ .After cleaning with NaOH, 83-84$\%$ of the initial water flux is recovered after the elimination of 72$\%$ of the adsorbed protein. Attribution of the flux decline to concentration polarization, reversible fouling, cleanable fouling (which needs cleaning operations) and irreversible fouling is described in Fig. 1.11.

4 Conclusion

In this chapter the structure of two polyethersulfone microfiltration membranes was characterized by scanning electron microscopy, extended bubble point and mercury porosimetry. For both membranes three layers were identified (active layer, intermediate layer and mechanical support). The relative thickness of each layer has been identified by a combination of SEM images and ImageJ software. It can be concluded that despite the same

nature of the membrane's composition, they presented different properties (pore diameter of active layer and structure of the intermediate layer). Pore diameters and porosity of active layer, porosity, pore distribution and active surface of global support were characterized. One of these membranes (PES from KOCH) was used to study the fouling of a microfiltration module by two organic prodcts: L-Glutathione and Bovine Serum Albumine. Static isotherm experiments showed a linear type adsorption for L-Glutathione and Langmuir type for BSA. Dynamic isotherm and filtration experiments confirmed the linear adsorption of L-Glutathione whereas BSA presented lower adsorption than in static tests, which can be result of steric exclusion of this large protein. Relative flux (J/Jw) was linearly related to the mass of BSA accumulated on membrane during filtration. Local adsorption laws could be deduced from membrane structure characterization (membrane active surface) and adsorption isotherms. Despite comparable values of protein accumulation on the membrane, BSA generate high fouling whereas L-Glutathione no impact of adsorption on permeability. Reversibility of the fouling was studied for L-Glutathione and BSA. L-Glutathione could be totally desorbed whereas, cleaning experiments with BSA showed the presence of polarization concentration, reversible fouling, cleanable fouling and irreversible fouling.

UPSCALED MODELING OF MICROLTRATION MEMBRANE FOULING BY PROTEIN SOLUTIONS : THEORETICAL STUDY

List of symbols

$-_\eta$	related to the bulk fluid
$-_\gamma$	related to the fluid phase
$-_\kappa$	related to the solid phase
$-_\omega$	related to the membrane active layer
$-_p$	related to the membrane porous structure
$-_s$	related to the fluid-solid phase
$a_{\gamma\kappa}$	specific surface area between γ, κ phases, m^{-1}
$A_{\gamma\kappa}$	interfacial area between $\gamma - \kappa$, m^2
b_γ	closure variable used to represent the adsorptive source
$\mathbf{b}_\gamma$	vector used to represent $\tilde{p}_\gamma$, m^{-1}
$\mathbf{B}_\gamma$	second order tensor used to represent $\tilde{\mathbf{v}}_\gamma$
$c_{A\gamma}$	specific concentration of species A in γ phase, kgm^{-3}
$c_{A\kappa}$	specific concentration of species A in κ phase, kgm^{-3}
$\langle c_{A\gamma} \rangle$	superficial average concentration of species A in γ phase, kgm^{-3}
$\langle c_{A\gamma} \rangle^\gamma$	intrinsic average concentration of species A in γ phase, kgm^{-3}
$\tilde{c}_{A\gamma}$	spatial deviation concentration of species A in γ phase, kgm^{-3}
d_p	characteristic pore size of the membrane, m
$\mathscr{D}_\gamma$	diffusivity of species A in the γ phase (water), $\mathrm{m}^2\mathrm{s}$
$\mathbf{D}^*$	effective dispersion tensor ($\mathbf{D_{eff}} + \mathbf{D_{dis}}$),$\mathrm{m}^2\mathrm{s}$
K_{lan}	Langmuir adsorption constant for species A, m
K'_{lan}	Langmuir adsorption constant for species A, $\mathrm{m}^3\mathrm{kg}$
K_{lin}	linear adsorption constant for species A, m
$\mathbf{K}_\gamma$	permeability tensor, m^2
ℓ_γ	characteristic length scale for γ phase, m
ℓ_κ	characteristic length scale for κ phase, m
ℓ_{mb}	characteristic length scale of the membrane, m
ℓ_η	macroscopic length scale for η phase (fluid), m
ℓ_ω	macroscopic length scale for ω region (active layer), m
ℓ_p	macroscopic length scale for p region (porous structure), m
L_{ε_γ}	characteristic length scale associated with ε_γ, m
M_A	intrinsic molar mass of species A, kgmol^{-1}
$\mathbf{n}_{\gamma\kappa}$	-$\mathbf{n}_{\kappa\gamma}$, unit normal vector from γ phase to κ phase
$\mathbf{n}_{\gamma\kappa} \cdot \mathbf{w}_{\gamma\kappa}$	displacement velocity at $\gamma - \kappa$ interface

p_γ	local pressure in the γ phase, Pa
$\langle p_\gamma \rangle$	superficial average pressure in the γ phase, Pa
$\langle p_\gamma \rangle^\gamma$	intrinsic average pressure in the γ phase, Pa
$\tilde{p}_\gamma$	spatial deviation of pressure in the γ phase, Pa
$\mathbf{s}_\gamma$	vector field used to represent $\tilde{c}_{A\gamma}$
$\mathbf{u}$	dimensionless vector used to represent the non-local diffusion
$\mathbf{v}_{A\gamma}$	velocity of species A in the γ phase, ms^{-1}
r_0	radius of the averaging volume, m
$\mathbf{v}_\gamma$	velocity of the γ phase, ms^{-1}
$\langle \mathbf{v}_\gamma \rangle$	superficial velocity of the γ phase, ms^{-1}
$\langle \mathbf{v}_\gamma \rangle^\gamma$	intrinsic velocity of γ phase, ms^{-1}
$\tilde{\mathbf{v}}_\gamma$	spatial deviation velocity of the γ phase, ms^{-1}

Greek letters

δ	$1 - \frac{\rho_A}{\rho_\gamma}$, shrinkage parameter
ε_γ	volume fraction of the γ phase
ε_κ	volume fraction of the κ phase
μ_γ	dynamic viscosity of the fluid (γ) phase, Pa.s
ρ_γ	mass density of the γ phase, kgm^{-3}
$\langle \rho_\gamma \rangle$	superficial mass density of the γ phase, kgm^{-3}
$\langle \rho_\gamma \rangle^\gamma$	intrinsic mass density of the γ phase, kgm^{-3}
$\tilde{\rho}_\gamma$	spacial deviation of mass density in the γ phase, kgm^{-3}
τ_A^{diff}	characteristic time of diffusion transport, s
τ_A^{conv}	characteristic time of convection transport, s
τ_A^{ads}	characteristic time of adsorption, s

1 INTRODUCTION

Membrane technology has received considerable interest in separation, purification and concentration of macromolecules such as proteins in different industrial fields. The principle is to separate components of a solution by application a membrane filtration system with pressure gradient between two sides of the membrane as driving force. The membrane is a porous separator which lets small compounds like water to pass through in the permeate stream, whereas it retains larger molecules like proteins in the retentate. The tangential flow devices are less susceptible to fouling than dead-end filtration systems due to the sweeping effects and high shear rates of the passing flow. However membrane fouling still exists and leads to a decrease in performance with a loss in solvent permeability and modification in selectivity. Fouling is a common phenomenon observed in all industrial domains with chemical, environmental, pharmaceutical and biomedical applications. It is due to chemical (organic or mineral) and biological (biofilm formation) fouling and scale formation. Organic fouling is caused by the accumulation and consequent deposition of organic materials from the feed water such as humic substances, proteins, polysaccharides, surfactants etc. onto or within the membrane structure. The problem is multidisciplinary involving multiphysics (hydrodynamics, mass transport, physical chemistry), multiscale (molecules, membrane pores and membrane scales) and time dependent (microstructure, molecules-surface interactions). In this paper, fouling of microfiltration membranes by proteins is deepened and an upscaled model associated with protein adsorption to the membrane is proposed.

The main parameters that influence the behaviour of proteins during the filtration are pH, isoelectric point and ionic strength: the apparent net charge of the protein thus its hydration volume and apparent size, depend on the isoelectric point (IEP) of the molecule and the pH [62], [272]. It can be concluded from several studies that the protein adsorption is maximum at the IEP where protein is neutral in the aqueous solution[191]. The electrostatic interaction with membrane material depends on the pH (charge density of the protein and the membrane) and the ionic force of the solution. [62],[156], [207],[222],[223].The surface charge density and hydrophobicity of the membrane depend also on membrane fouling and evolve with time.

In literature, the reduction of permeability versus time of filtration has been discussed as a function of different parameters: the intrinsic resistance of the membrane, the composition of the feed solution, the fouling mechanisms. Membrane pores are mostly represented as a package of cylindrical, non-intersecting, homogeneously distributed capillaries with uniform radius assuming (although in most of the cases this assumption is far from reality) and the solution o be treated is considered a Newtonian fluid with constant properties (density, viscosity) [49],[239]. For instance, concentration polarization in the diffusion layer caused by steric or electrostatic retention of some solutes adjacent to the membrane interface can be modeled by the film theory. In this model, there is an equilibrium between the convective transport from bulk to membrane surface, diffusive transport from menbrane surface to bulk and diffusive transport from membrane side to

the permeate side [156],[271]. In these models the permeate flux is dependent of solute concentration in bulk, membrane surface and permeate side and also the thickness of the boundary layer adjacent to the membrane Eq. (10). In this definition, D is the diffusion coefficient of solutes passing the membrane, v_P is the permeate velocity, C_P and C_b are the concentration of solutes at bulk and membrane surface respectively.

Another approach to predict the permeate flux is the series of resistances models based on the flow of solvent through several transport layers [156],[74],[14]. The series of resistances consist of progressive additional of membrane resistance due to fouling in which multiple mechanisms can be involved. The initial membrane resistance R_m depends on the mechanical and chemical properties like membrane thickness, composition, etc. When the membrane is applied to proteins separation, the accumulation and increase of proteins near the membrane surface gives an additional resistance due to concentration polarization R_{cp}. Above the critical value of the concentration polarization, a gel-like cake forms on the top layer of the membrane and gives an extra resistance R_c to the solvent flows the membrane. Moreover the adsorption and/or blockage of solutes at the membrane interface gives another internal resistance referred as R_{in} Eq.(2.1). Depending on the filtration process operational conditions and solvent properties, these models can include some or all of these additional resistances. In most cases, determination of these resistance, depends highly on the experimental parameters and remains phenomenological.

$$\text{Permeate flux} = \frac{\Delta P}{\mu(R_{\text{membrane}} + \underbrace{R_{\text{in}} + R_{\text{CP}} + R_{\text{cake}}}_{\text{Resistance due to fouling}})} \tag{2.1}$$

The models based on the blocking mechanisms predicting the permeate flow are also used to expiation the evolution of the flow with time[39],[62],[98],[103]. According to the assumptions taken in these models, membranes are blocked with four different mechanisms: complete blocking where it is assumed each particle blocks some pores without superposition of other particles; standard blocking in which each particle arriving to the membrane surface deposits into the internal pore walls and decreases the pore volume; intermediate blocking where particles can either deposit on other particles, or block directly some regions of the membrane surface; and finally cake filtration where particles locate directly on other particles already arrived to the membrane pores. In several studies, a combination of fouling models is used to evaluate the filtrate flow with time.

These mechanisms have been modeled using empirical or semi-empirical laws, based on macroscopic measurements. They often use global parameters difficult to link with physical laws.

The objective of this study is to build a new macroscopic model of membrane fouling based on local description of the physical problem. This first study will focus on the modeling of pore constriction generated by protein adsorption.

This is the first study where mass and momentum transport equations flowing through the membrane are modeled by upscaling methods. The models includes protein adsorption

to the membrane surface and consequent pore constriction is caused by disposed protein layer to initial membrane structure. However, it should be indicated that we do not invest in specific protein-membrane electrostatic interactions neither the effects of membrane surface modification due to adsorption. The model predicts in particular the evolution of internal structure of the membrane by protein adsorption.

In the following sections, first we provide structural information of the membrane porous structure (layers with different length scales, mean pore size, permeability and porosity). For this purpose, the membranes have been characterized experimentally. The local (pore) scale problem accounting for mass and momentum transport equations for fluid phase with adsorption at solid interface are then given. The upscaled model is elaborated using the volume averaging method in which the development is based on classical continuum physics. The upscaled model provides the effective permeability and diffusivity which involve both local and structural information of the system. Finally macroscopic numerical simulation are run to evaluate the system performance qualitatively. furthermore, The major challenge in this domain is caused by the minuscule size of the membrane active layer compared to the thickness of the bulk fluid and membrane porous structure. To overcome this pure numerical difficulty we replace the membrane active layer by a dividing surface and then derive jump conditions for mass and momentum transport equations which contain information of this layer at this new interface. Experimental data of membrane initial structure (porosity) and local protein adsorption laws are needed to run macroscopic numerical simulations. Eventually, filtration experiments can be performed to calibrate and/or validate the model.

2 LOCAL DESCRIPTION OF THE MODEL

In this section, the governing mass and momentum equations with corresponding boundary conditions at the pore scale were determined. To have a better vision the membrane schema with different layers is shown in Fig. 2.1.

In the model we consider two phases: κ refers as solid phase (membrane), and γ referred as fluid phase (protein solution). When the fluid phase passes through the membrane, proteins are partly adsorbed on the membrane solid interface leading to complete pore blocking or reduction of membrane's pore radius. Although the interactions between the proteins molecules and solid interface are extremely complex to be characterized thoroughly, the classic rules are used to model the adsorption which relate in general the equilibrium protein concentration of the liquid phase to the protein mass adsorbed to the solid surface. Among these rules, the linear, Langmuir and Freundlich laws are the most responding. In this work linear and Langmuir adsorption laws are used to model the adsorption of following model proteins including glutathione and (BSA).

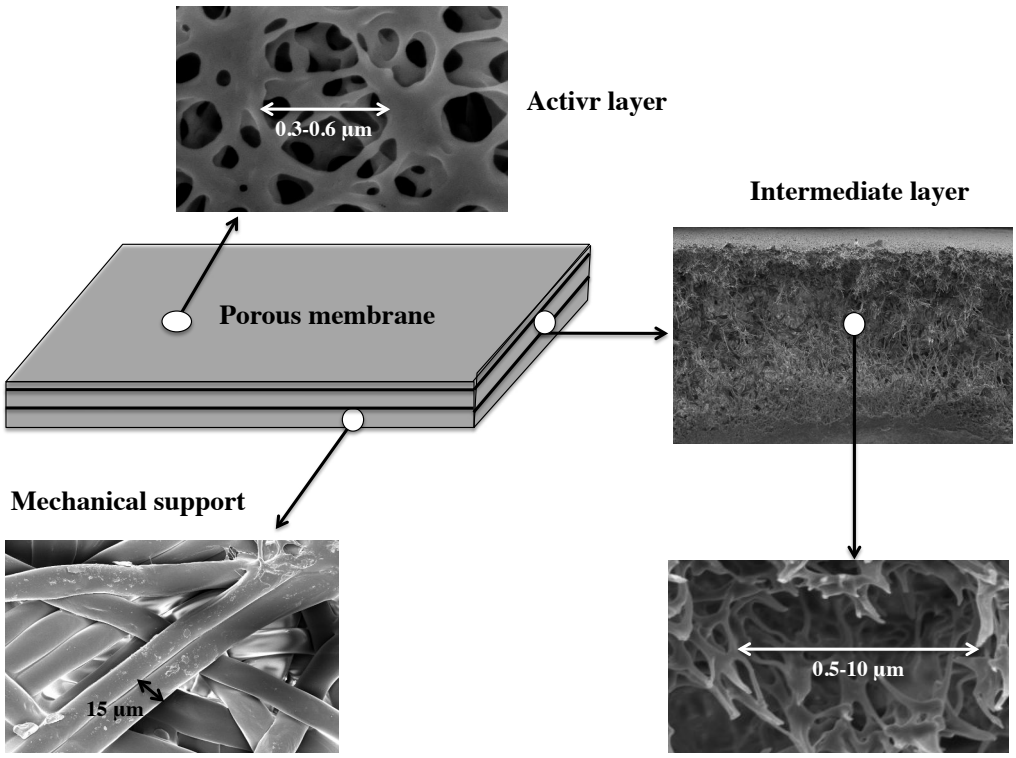

Figure 2.1: Microfiltration membrane (supplied by KOCH society) SEM images. 3 layers have been identified: active layer, intermediate layer and mechanical support.

2.1 HYPOTHESES ASSOCIATED WITH MODEL DEVELOPMENT

As it has been shown in Fig. 2.1, The microfiltration membrane (purchased from KOCH society) is composed of three different layers: Two first layers are made of polyethersulfone (PES) and the mechanical support is composed of polyester (PS). The characteristic properties of each layer have been obtained. Experiments (capillary flow porometry with perfluoroethers and mercury) were combined with classical equations of the porous media (Kozeny-Carman). Let us just recall that Kozeny-Carman is used to describe the porous structures composed of regular cylinder or sphere solids Eq. (2.2). It is obvious that the real membrane structure is more complex than regular pores, however it is used to provide a first approximation in order to make estimations for the simplification of the

theoretical analysis developed in this chapter.

$$K = \frac{(d_p^2 \times \varepsilon^3)}{180 \times (1-\varepsilon)^2} \tag{2.2}$$

Where K, ε, d_p are respectively permeability (m^2), porosity and mean pore size (m) of the porous media.
The membrane overall permeability has been measured for different membrane sheets by passing milliQ water through the membrane in a range of transmembrane pressure (from 0.5-1.5 bar). The range of values is between (5×10^{-17} and $2.5 \times 10^{-16} m^2$).
The results of membrane characterization (SEM images combined with image analysis by ImageJ and porosimetry) provides structural information of the membrane layers and results are shown in Table. 2.1.

Table 2.1: Membrane (KOCH) characteristic properties of each layer

Membrane layer	Pore/fiber size (μm)	Thickness (μm)	Porosity
Membrane	-	215±2	68.3 % (Mercury porosimetry)
Active layer	0.39-0.6 (Perfluoethers porometry)	0.1-3* (SEM)	30-40% (SEM image analysis)
Intermediate layer	0.4-4 (Mercury porosimetry)	95-105 (SEM)	−**
Mechanical support	$>$ 40 (Mercury porosimetry)	110-120 (SEM)	−**

*: Determination of the membrane's active layer thickness is relatively a difficult task, and is generally estimated between hundreds of nm to a few μm.
−** The porosity intermediate and mechanical support could not have been characterized separately.

If one estimates the permeability of the membrane's active layer with Eq. (2.2), the values are between 4×10^{-17} and 3×10^{-16} m^2 with porosity of 30-40% and mean pore size of 0.39-0.6 μm. On the other side, the value of mean pore size of the intermediate layer and mechanical support together has been calculated from mercury porosimetry and reported as 0.894 μm (See chapter 1, section 3.1). If one uses these values with corresponding porosity of 68.3 % the relative permeability of these layers together can be estimated around 1.4×10^{-14} m^2. Thus, it can be concluded that the active layer represents mainly the membrane selectivity for salute passage in the filtration process. Therefore as first modeling approach, we develop a model of a very thin porous active membrane layer Fig.2.1. The adsorption phenomenon is supposed to be homogenous

with the membrane active layer. The membrane is a rigid solid phase and is not subject to dilatation. Adsorption occurs only at the solid interface and there is no diffusion of adsorb proteins inside the solid phase. Finally, it is assumed that there is no diffusion of adsorb proteins inside the solid phase. Let us consider first mass and momentum governing equations at the pore scale and consider the following assumptions for the fluid phase flowing through the membrane:

- The proteins concentration is of a few g/l (or kg/m^3). Taking into account the intrinsic density of the solvant (about 10^3 kg/m^3 for pure water) and the intrinsic molar mass of each protein (0.307 kg/mol for L-gluthatione and 66 kg/mol for BSA), the proteins are diluted in the solution. The specific density of the solution can then be assumed to be constant: $\rho_\gamma \approx cst \approx 10^3$ kg/m^3.
- The pressure difference through the membrane is taken to 1 bar $= 10^5$ Pa.
- Variations of temperature and pressure during membrane filtration are neglected.
- Viscosity of the solution is assumed to be constant [170].

In the following sections, the local conservation equations (for the fluid phase) are upscaled using the volume averaging method.

2.2 PORE SCALE CONSERVATION EQUATIONS

2.2.1 FOR κ-PHASE (SOLID)

For the solid phase, mass conservation can be written

$$\frac{\partial \rho_\kappa}{\partial t} + \nabla \cdot (\rho_\gamma \mathbf{v}_\kappa) = 0 \tag{2.3}$$

The solid phase is assumed to be rigid and still ($\mathbf{v}_\kappa = \mathbf{0}$) and then

$$\frac{\partial \rho_\kappa}{\partial t} = 0 \tag{2.4}$$

2.2.2 FOR γ-PHASE (FLUID)

The mass conservation equation for the fluid phase containing diluted species A is given by

$$\frac{\partial \rho_\gamma}{\partial t} + \nabla \cdot (\rho_\gamma \mathbf{v}_\gamma) = 0 \tag{2.5}$$

With the assumption that the density ρ_γ of the γ-phase is a constant, we get

$$\nabla \cdot \mathbf{v}_\gamma = 0 \tag{2.6}$$

The momentum equation for the fluid phase is given by the transient Stokes equation. Indeed, in the present application, the pore Reynolds number has been estimated very small compared to unity so justifying the use of the Stokes equation instead of the Navier-Stokes equation. Moreover the gravity body force has been neglected compared to the pressure gradient ($\rho_\gamma g \approx 10^4$ Pa/m $\ll \Delta P/l_{mb} \approx 5 \times 10^8$ Pa/m). This momentum equation is given by

$$\frac{\partial \left(\rho_\gamma \mathbf{v}_\gamma\right)}{\partial t} = -\nabla p_\gamma + \mu_\gamma \nabla^2 \mathbf{v}_\gamma \tag{2.7}$$

The conservation equation of species A in the fluid phase takes the form

$$\frac{\partial c_{A\gamma}}{\partial t} + \nabla \cdot \left(c_{A\gamma} \mathbf{v}_\gamma\right) = \nabla \cdot \left(\mathscr{D}_\gamma \nabla c_{A\gamma}\right) \tag{2.8}$$

where $\mathscr{D}_\gamma$ is the diffusion coefficient of species A and $c_{A\gamma}$ is the specific concentration of species A. Fick's law is valid because species A is diluted in the solution.

2.3 PORE SCALE BOUNDARY CONDITIONS

2.3.1 MASS OF SPECIES

Based on the jump condition detailed by [185, 254, 255], the boundary condition at the fluid-solid interface considering adsorption is

$$c_{A\gamma}\left(\mathbf{v}_{A\gamma} - \mathbf{w}_{\gamma\kappa}\right) \cdot \mathbf{n}_{\gamma\kappa} = \frac{\partial c_{As}}{\partial t} \quad \text{at } A_{\gamma\kappa} \tag{2.9}$$

where $c_{A\gamma}\mathbf{v}_{A\gamma} = c_{A\gamma}\left(\mathbf{v}^d_{A\gamma} + \mathbf{v}_\gamma\right) = -\mathscr{D}_\gamma \nabla c_{A\gamma} + c_{A\gamma}\mathbf{v}_\gamma$ takes into account both diffusion and convection. At the interface $A_{\gamma\kappa}$, proteins (species A) in fluid phase γ are partly adsorbed and the adsorption process can be described by different models, usually depending on the bulk protein concentration. As a consequence, Eq. (2.9) can be expressed as

$$-\mathscr{D}_\gamma \nabla c_{A\gamma} \cdot \mathbf{n}_{\gamma\kappa} + c_{A\gamma}\left(\mathbf{v}_\gamma - \mathbf{w}_{\gamma\kappa}\right) \cdot \mathbf{n}_{\gamma\kappa} = \frac{\partial}{\partial t}\left[f(c_{A\gamma})\right] \quad \text{at } A_{\gamma\kappa} \tag{2.10}$$

where $c_{As} = f(c_{A\gamma})$ and f is the adsorption function for species A, which is an adsorbed mass per unit area of the interface $A_{\gamma\kappa}$.

2.3.2 TOTAL MASS

Writing, on the fluid side, that the mass flux of solvant (water) through the $A_{\gamma\kappa}$ interface is null and summing with Eq. (2.9) leads to

$$\rho_\gamma\left(\mathbf{v}_\gamma - \mathbf{w}_{\gamma\kappa}\right) \cdot \mathbf{n}_{\gamma\kappa} = \frac{\partial}{\partial t}\left[f(c_{A\gamma})\right] \quad \text{at } A_{\gamma\kappa} \tag{2.11}$$

Moreover, the intrinsic density of the solid phase is very close to the intrinsic density of species A ($\rho_\kappa \approx \rho_{glu} \approx \rho_{BSA} \approx 1.35 \times 10^3$ kg/m^3). From the point of view of mass, it can be assumed that the solid phase is made of species A only. Therefore, the mass of species A that is lost by the fluid forms a new part of the solid phase and

$$\rho_\gamma \left(\mathbf{v}_\gamma - \mathbf{w}_{\gamma\kappa}\right) \cdot \mathbf{n}_{\gamma\kappa} \approx \rho_A \left(-\mathbf{w}_{\gamma\kappa}\right) \cdot \mathbf{n}_{\gamma\kappa} \quad \text{at } A_{\gamma\kappa} \tag{2.12}$$

where ρ_A is the intrisic density of species A.

2.3.3 Boundary conditions

Combining boundary conditions (2.10), (2.11) and (2.12), the following set of relations can be obtained

$$\mathbf{w}_{\gamma\kappa} \cdot \mathbf{n}_{\gamma\kappa} = -\frac{1}{\rho_A}\frac{\partial}{\partial t}\left[f(c_{A\gamma})\right] \quad \text{at } A_{\gamma\kappa} \tag{2.13a}$$

$$\mathbf{v}_\gamma \cdot \mathbf{n}_{\gamma\kappa} = \delta\left(\mathbf{w}_{\gamma\kappa} \cdot \mathbf{n}_{\gamma\kappa}\right) = \left(\frac{1}{\rho_\gamma} - \frac{1}{\rho_A}\right)\frac{\partial}{\partial t}\left[f(c_{A\gamma})\right] \quad \text{at } A_{\gamma\kappa} \tag{2.13b}$$

$$\left(\mathbf{v}_\gamma - \mathbf{w}_{\gamma\kappa}\right) \cdot \mathbf{n}_{\gamma\kappa} = (\delta - 1)\left(\mathbf{w}_{\gamma\kappa} \cdot \mathbf{n}_{\gamma\kappa}\right) = \frac{1}{\rho_\gamma}\frac{\partial}{\partial t}\left[f(c_{A\gamma})\right] \quad \text{at } A_{\gamma\kappa} \tag{2.13c}$$

$$-\mathscr{D}_\gamma \nabla c_{A\gamma} \cdot \mathbf{n}_{\gamma\kappa} = \rho_A \left(\frac{c_{A\gamma}}{\rho_\gamma} - 1\right)\left(\mathbf{w}_{\gamma\kappa} \cdot \mathbf{n}_{\gamma\kappa}\right) \approx \frac{\partial}{\partial t}\left[f(c_{A\gamma})\right] \quad \text{at } A_{\gamma\kappa} \tag{2.13d}$$

where $\delta = 1 - \dfrac{\rho_A}{\rho_\gamma} \approx -0.35$. For the last relation, dilution of species A in the solution was used to say that $c_{A\gamma} \ll \rho_\gamma$. Finally, and whatever the phenomena in the normal direction, the no-slip condition for velocity at $A_{\gamma\kappa}$ holds: in this case, the component of $\mathbf{v}_\gamma$ tangent to the interface is null because the solid is rigid and still.

2.4 Pore scale characteristic times

2.4.1 Literal expressions

Estimation of characteristic times of each transport phenomenon (diffusion, convection and adsorption) can give a better vision of the dominant transport mechanisms and the possibility to neglect one in comparison to the other one. The characteristic time of diffusion of species A in a pore is given by

$$\frac{D_{AB}\,\tau_A^{diff}}{{\ell_\gamma}^2} = 1 \Longrightarrow \tau_A^{diff} = \frac{{\ell_\gamma}^2}{\mathscr{D}_\gamma} \tag{2.14}$$

where l_γ is a typical pore size.

The characteristic time of convection of species A in a pore can be deduced from Eq. (2.8)

$$\left|\frac{\partial c_{A\gamma}}{\partial t}\right| = \mathbf{O}\left(|\mathbf{v}_\gamma.\nabla c_{A\gamma}|\right) \Longrightarrow \tau_A^{conv} = \frac{\ell_\gamma}{v_\gamma} \tag{2.15}$$

The characteristic time of adsorption depends on the adsorption law for each protein. It can be deduced that

$$-\mathcal{D}_{AB}\nabla c_{A\gamma}\cdot\mathbf{n}_{\gamma\kappa} = \mathbf{O}\left(\frac{\partial}{\partial t}\left[f(c_{A\gamma})\right]\right) \quad \text{at } A_{\gamma\kappa} \tag{2.16}$$

For a linear law, $f_{lin}(c_{A\gamma}) = K_{lin}c_{A\gamma}$ and thus

$$\tau_{lin}^{ads} = \frac{\ell_\gamma}{\mathscr{D}_\gamma}K_{lin} \tag{2.17}$$

For a Langmuir law, $f_{lan}(c_{A\gamma}) = \dfrac{K_{lan}c_{A\gamma}}{1+K'_{lan}c_{A\gamma}}$ and thus

$$\tau_{lan}^{ads} = \frac{\ell_\gamma}{\mathscr{D}_\gamma}\frac{K_{lan}}{1+K'_{lan}c_{A\gamma}} \tag{2.18}$$

Here we remind that in several experimental studies, the Langmuir adsorption isotherms is expressed as follows:

$$q = \frac{q_{\max}K_AC_A}{1+K_AC_A} \tag{2.19}$$

Where q is the species concentration at interface, $q_{\max}$ is the maximum sorption capacity and K_A is the half saturation constant (See Chapter 1).

2.4.2 Application to L-gluthatione and BSA

For the membrane used in this work the the mean pore size bass been measured $\ell_\gamma \sim 0.6 \approx \mu$m. The pore scale diffusion coefficients of L-glutathione and BSA are calculated from the Stokes-Einstein equatio, $\mathscr{D}_\gamma(glut) = 5.40\times10^{-10}$ m^2/s and $\mathscr{D}_\gamma(BSA) = 9.04\times10^{-11}$ m^2/s. Hence, the characteristic diffusion times for both protein can be estimated as $\tau_{glu}^{diff} \approx 7\times10^{-4}$ s and $\tau_{BSA}^{diff} \approx 3\times10^{-3}$ s.
The average velocity in the pores is estimated to 10^{-5} m/s from experiments, leading to $\tau_A^{conv} \approx 6\times10^{-2}$ s. Let us note that the characteristic times of diffusion and convection have comparable order of magnitude and therefore both diffusion and convection have to be accounted for in the analysis.
For L-glutathione,a linear adsorption isotherm was found experimentally whereas and for BSA, a langmuir isotherm has been observed. The adsorption characteristic time varies then between 10^{-4} and 10^{-3} s for protein solutions, which is of the same order of magnitude than the other phenomena.

3 UPSCALING

Let us consider a schematic membrane and an associated Representative Elementary Volume (REV) where the different scales of the system are described (Fig. 2.2).

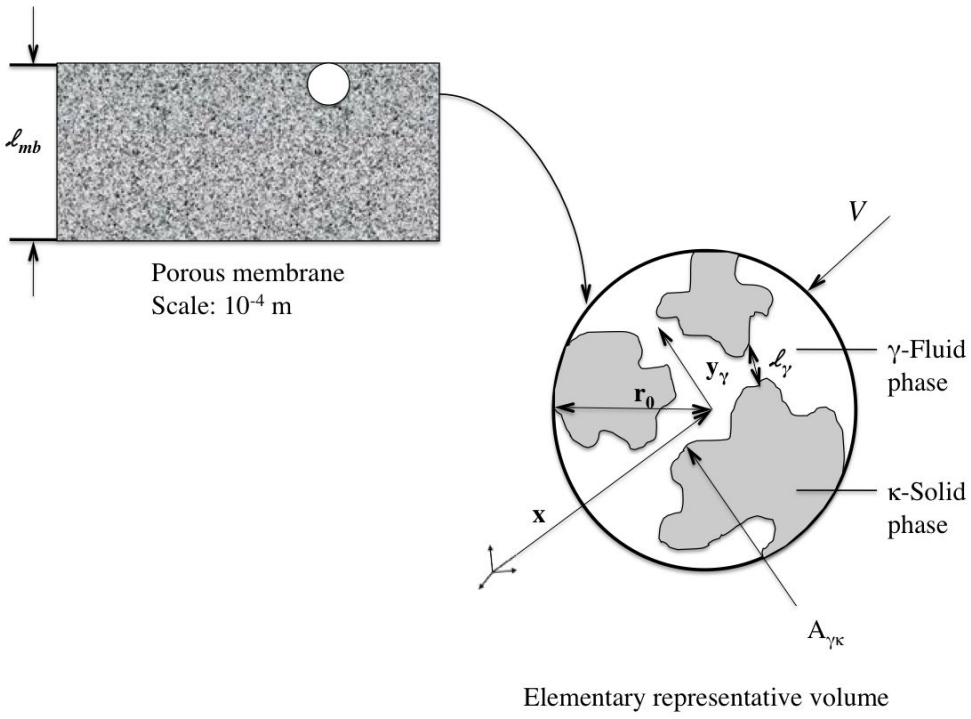

Figure 2.2: Representative Elementary Volume with fluid and solid phases and unit normal vectors

Let us recall that the superficial average of any function associated with the γ-phase is defined by [255]

$$\langle \Psi_\gamma \rangle = \frac{1}{V} \int_{V_\gamma(t)} \Psi_\gamma \mathrm{d}V \tag{2.20}$$

while the intrinsic average takes the form

$$\langle \Psi_\gamma \rangle^\gamma = \frac{1}{V_\gamma(t)} \int_{V_\gamma(t)} \Psi_\gamma \mathrm{d}V \tag{2.21}$$

These two averages being related by

$$\langle \Psi_\gamma \rangle = \varepsilon_\gamma \langle \Psi_\gamma \rangle^\gamma \tag{2.22}$$

Note that these averages make sense if the different scales of the system satisfy the scale separation given by $\ell_\gamma \ll r_0 \ll \ell_{mb}$. The upscaling procedure for the derivation of average governing transport equations requires the three following theorems (Howes and Whitaker, 1985)

$$\langle \nabla \Psi_\gamma \rangle = \nabla \langle \Psi_\gamma \rangle + \frac{1}{V} \int_{A_{\gamma\kappa}} \mathbf{n}_{\gamma\kappa} \Psi_\gamma \mathrm{d}S \tag{2.23}$$

$$\langle \nabla \cdot \mathbf{\Psi}_\gamma \rangle = \nabla \cdot \langle \mathbf{\Psi}_\gamma \rangle + \frac{1}{V} \int_{A_{\gamma\kappa}} \mathbf{n}_{\gamma\kappa} \cdot \mathbf{\Psi}_\gamma \mathrm{d}S \tag{2.24}$$

$$\left\langle \frac{\partial \Psi_\gamma}{\partial t} \right\rangle = \frac{\partial \langle \Psi_\gamma \rangle}{\partial t} - \frac{1}{V} \int_{A_{\gamma\kappa}} (\mathbf{n}_{\gamma\kappa} \cdot \mathbf{w}_{\gamma\kappa}) \Psi_\gamma \mathrm{d}S \tag{2.25}$$

where $\mathbf{w}_{\gamma\kappa}$ is the interfacial velocity of $A_{\gamma\kappa}$.

3.1 AVERAGE MASS CONSERVATION

3.1.1 FOR κ-PHASE (SOLID)

Taking the average of the mass conservation equation in the κ-phase, Eq. (2.4), gives

$$\frac{\partial \left(\varepsilon_\kappa \langle \rho_\kappa \rangle^\kappa \right)}{\partial t} - \frac{1}{V} \int_{A_{\gamma\kappa}} (\mathbf{n}_{\kappa\gamma} \cdot \mathbf{w}_{\gamma\kappa}) \rho_\kappa \mathrm{d}A = 0 \tag{2.26}$$

The solid density is a constant and then

$$\frac{\partial \varepsilon_\gamma}{\partial t} = -\frac{\partial \varepsilon_\kappa}{\partial t} = \frac{1}{V} \int_{A_{\gamma\kappa}} \mathbf{n}_{\gamma\kappa} \cdot \mathbf{w}_{\gamma\kappa} \mathrm{d}A \tag{2.27}$$

where we used the fact that $\varepsilon_\gamma + \varepsilon_\kappa = 1$.

3.1.2 FOR γ-PHASE (FLUID)

Applying the averaging operator to the mass conservation equation in the γ-phase, Eq. (2.6) leads to

$$\nabla \cdot \langle \mathbf{v}_\gamma \rangle = -\frac{1}{V} \int_{A_{\gamma\kappa}} \mathbf{n}_{\gamma\kappa} \cdot \mathbf{v}_\gamma \mathrm{d}A \tag{2.28}$$

3.2 AVERAGE MOMENTUM CONSERVATION

The average of Eq. (2.7) gives

$$\left\langle \frac{\partial \left(\rho_\gamma \mathbf{v}_\gamma \right)}{\partial t} \right\rangle = - \langle \nabla p_\gamma \rangle + \left\langle \mu_\gamma \nabla^2 \mathbf{v}_\gamma \right\rangle \tag{2.29}$$

Folllowing Bousquet-Melou et al., [29], we first develop each term of the above equation before providing the full averaged momentum equation.

3.2.1 ACCUMULATION TERM

Since the density has been assumed to be constant, the averaged accumulation term takes the form

$$\left\langle \frac{\partial \left(\rho_\gamma \mathbf{v}_\gamma\right)}{\partial t} \right\rangle = \frac{\partial \left(\rho_\gamma \varepsilon_\gamma \left\langle \mathbf{v}_\gamma \right\rangle^\gamma\right)}{\partial t} - \frac{1}{V}\int_{A_{\gamma\kappa}} (\mathbf{n}_{\gamma\kappa} \cdot \mathbf{w}_{\gamma\kappa})\rho_\gamma \mathbf{v}_\gamma \mathrm{d}A \tag{2.30}$$

or

$$\left\langle \frac{\partial \left(\rho_\gamma \mathbf{v}_\gamma\right)}{\partial t} \right\rangle = \varepsilon_\gamma \rho_\gamma \frac{\partial \left\langle \mathbf{v}_\gamma \right\rangle^\gamma}{\partial t} + \frac{\partial \varepsilon_\gamma}{\partial t}\rho_\gamma \left\langle \mathbf{v}_\gamma \right\rangle^\gamma - \frac{1}{V}\int_{A_{\gamma\kappa}} (\mathbf{n}_{\gamma\kappa} \cdot \mathbf{w}_{\gamma\kappa})\rho_\gamma \mathbf{v}_\gamma \mathrm{d}A \tag{2.31}$$

3.2.2 PRESSURE TERM

The average form of the pressure term is

$$\left\langle \nabla p_\gamma \right\rangle = \nabla \left(\varepsilon_\gamma \left\langle p_\gamma \right\rangle^\gamma\right) + \frac{1}{V}\int_{A_{\gamma\kappa}} \mathbf{n}_{\gamma\kappa} p_\gamma \mathrm{d}A \tag{2.32}$$

Using the Gray decomposition and a length scale constraint to take $\left\langle p_\gamma \right\rangle^\gamma$ out of the integral, it can be written

$$\frac{1}{V}\int_{A_{\gamma\kappa}} \mathbf{n}_{\gamma\kappa} p_\gamma \mathrm{d}A = -\left(\nabla \varepsilon_\gamma\right)\left\langle p_\gamma \right\rangle^\gamma + \frac{1}{V}\int_{A_{\gamma\kappa}} \mathbf{n}_{\gamma\kappa} \tilde{p}_\gamma \mathrm{d}A \tag{2.33}$$

and therefore the average pressure term is given by

$$-\left\langle \nabla p_\gamma \right\rangle = -\varepsilon_\gamma \nabla \left\langle p_\gamma \right\rangle^\gamma - \frac{1}{V}\int_{A_{\gamma\kappa}} \mathbf{n}_{\gamma\kappa} \tilde{p}_\gamma \mathrm{d}A \tag{2.34}$$

3.2.3 DIFFUSION TERM

The averaged viscous term, assuming constant liquid viscosity, is given by

$$\begin{aligned} \left\langle \mu_\gamma \nabla^2 \mathbf{v}_\gamma \right\rangle &= \mu_\gamma \nabla^2 (\varepsilon_\gamma \left\langle \mathbf{v}_\gamma \right\rangle^\gamma) + \frac{1}{V}\int_{A_{\gamma\kappa}} \mathbf{n}_{\gamma\kappa} \cdot (\mu_\gamma \nabla \mathbf{v}_\gamma) \mathrm{d}A \\ &+ \mu_\gamma \nabla \cdot \left(\frac{1}{V}\int_{A_{\gamma\kappa}} \mathbf{n}_{\gamma\kappa} \mathbf{v}_\gamma \mathrm{d}A\right) \end{aligned} \tag{2.35}$$

If there was no-slip and no-penetration at $A_{\gamma\kappa}$, the last area integral would disappear. However, for now, the interfacial velocity is non zero. Using the Gray decomposition of

velocity in the last term of Eq. (2.35) provides

$$\begin{aligned} & \frac{1}{V}\int_{A_{\gamma\kappa}} \mathbf{n}_{\gamma\kappa}\cdot(\mu_\gamma\nabla\mathbf{v}_\gamma)\mathrm{d}A \\ \approx\ & -\mu_\gamma\left(\nabla\varepsilon_\gamma\right)\cdot\left(\nabla\left\langle\mathbf{v}_\gamma\right\rangle^\gamma\right)+\frac{1}{V}\int_{A_{\gamma\kappa}}\mathbf{n}_{\gamma\kappa}\cdot(\mu_\gamma\nabla\tilde{\mathbf{v}}_\gamma)\mathrm{d}A \end{aligned} \tag{2.36}$$

and then

$$\begin{aligned} & \left\langle\mu_\gamma\nabla^2\mathbf{v}_\gamma\right\rangle=\mu_\gamma\nabla^2(\varepsilon_\gamma\left\langle\mathbf{v}_\gamma\right\rangle^\gamma)-\mu_\gamma\left(\nabla\varepsilon_\gamma\right)\cdot\left(\nabla\left\langle\mathbf{v}_\gamma\right\rangle^\gamma\right) \\ & +\frac{1}{V}\int_{A_{\gamma\kappa}}\mathbf{n}_{\gamma\kappa}\cdot(\mu_\gamma\nabla\tilde{\mathbf{v}}_\gamma)\mathrm{d}A+\mu_\gamma\nabla\cdot\left(\frac{1}{V}\int_{A_{\gamma\kappa}}\mathbf{n}_{\gamma\kappa}\mathbf{v}_\gamma\mathrm{d}A\right) \end{aligned} \tag{2.37}$$

Finally, writing

$$\begin{aligned} & \mu_\gamma\nabla^2(\varepsilon_\gamma\left\langle\mathbf{v}_\gamma\right\rangle^\gamma)=\varepsilon_\gamma\mu_\gamma\nabla^2\left\langle\mathbf{v}_\gamma\right\rangle^\gamma+\mu_\gamma\left(\nabla\varepsilon_\gamma\right)\cdot\left(\nabla\left\langle\mathbf{v}_\gamma\right\rangle^\gamma\right) \\ +\ & \mu_\gamma\nabla\cdot\left[\left(\nabla\varepsilon_\gamma\right)\left\langle\mathbf{v}_\gamma\right\rangle^\gamma\right] \end{aligned} \tag{2.38}$$

we get

$$\begin{aligned} \left\langle\mu_\gamma\nabla^2\mathbf{v}_\gamma\right\rangle= & \quad \varepsilon_\gamma\mu_\gamma\nabla^2\left\langle\mathbf{v}_\gamma\right\rangle^\gamma+\mu_\gamma\nabla\cdot\left[\left(\nabla\varepsilon_\gamma\right)\left\langle\mathbf{v}_\gamma\right\rangle^\gamma\right]+\frac{1}{V}\int_{A_{\gamma\kappa}}\mathbf{n}_{\gamma\kappa}\cdot(\mu_\gamma\nabla\tilde{\mathbf{v}}_\gamma)\mathrm{d}A \\ & +\mu_\gamma\nabla\cdot\left(\frac{1}{V}\int_{A_{\gamma\kappa}}\mathbf{n}_{\gamma\kappa}\mathbf{v}_\gamma\mathrm{d}A\right) \end{aligned} \tag{2.39}$$

3.2.4 NON-CLOSED EQUATION

Finally, combination of Eqs. (2.31), (2.34), (2.39) leads to the non-closed average momentum equation for the fluid flow through the porous membrane

$$\begin{aligned} & \varepsilon_\gamma\rho_\gamma\frac{\partial\left\langle\mathbf{v}_\gamma\right\rangle^\gamma}{\partial t}+\rho_\gamma\left\langle\mathbf{v}_\gamma\right\rangle^\gamma\frac{\partial\varepsilon_\gamma}{\partial t} \\ = & -\varepsilon_\gamma\nabla\left\langle p_\gamma\right\rangle^\gamma+\varepsilon_\gamma\mu_\gamma\nabla^2\left\langle\mathbf{v}_\gamma\right\rangle^\gamma+\mu_\gamma\nabla\cdot\left[\left(\nabla\varepsilon_\gamma\right)\left\langle\mathbf{v}_\gamma\right\rangle^\gamma\right] \\ + & \frac{1}{V}\int_{A_{\gamma\kappa}}\mathbf{n}_{\gamma\kappa}\cdot(-\mathbf{I}\tilde{p}_\gamma+\mu_\gamma\nabla\tilde{\mathbf{v}}_\gamma)\mathrm{d}A+\mu_\gamma\nabla\cdot\left(\frac{1}{V}\int_{A_{\gamma\kappa}}\mathbf{n}_{\gamma\kappa}\mathbf{v}_\gamma\mathrm{d}A\right) \\ + & \frac{1}{V}\int_{A_{\gamma\kappa}}(\mathbf{n}_{\gamma\kappa}\cdot\mathbf{w}_{\gamma\kappa})\rho_\gamma\mathbf{v}_\gamma\mathrm{d}A \end{aligned} \tag{2.40}$$

The originality of the non-closed averaged form of momentum transport is that it explicitly involves the time evolution of the membrane porosity due to adsorption. This additional term depends on the adsorption law of the protein.

3.3 AVERAGE SPECIES CONSERVATION

The average of Eq. (2.8) is the sum of the averaged of each terms of the pore scale species conservation equation

$$\left\langle \frac{\partial c_{A\gamma}}{\partial t} \right\rangle + \langle \nabla \cdot (c_{A\gamma} \mathbf{v}_\gamma) \rangle = \langle \nabla \cdot (\mathscr{D}_\gamma \nabla c_{A\gamma}) \rangle \tag{2.41}$$

As previously, each term of Eq. (2.41) is averaged separately.

3.3.1 ACCUMULATION TERM

Using the general transport theorem, the accumulation term of Eq. (2.41) becomes

$$\left\langle \frac{\partial c_{A\gamma}}{\partial t} \right\rangle = \varepsilon_\gamma \frac{\partial \langle c_{A\gamma} \rangle^\gamma}{\partial t} - \frac{1}{V} \int_{A_{\gamma\kappa}} (\mathbf{n}_{\gamma\kappa} \cdot \mathbf{w}_{\gamma\kappa}) \tilde{c}_{A\gamma} \mathrm{d}A \tag{2.42}$$

after using Gray decomposition on concentration and Eq. (2.27).

3.3.2 CONVECTION TERM

Using the spatial averaging theorem, the convective term of Eq. (2.41) becomes

$$\langle \nabla \cdot (c_{A\gamma} \mathbf{v}_\gamma) \rangle = \nabla \cdot \langle c_{A\gamma} \mathbf{v}_\gamma \rangle + \frac{1}{V} \int_{A_{\gamma\kappa}} (\mathbf{n}_{\gamma\kappa} \cdot \mathbf{v}_\gamma) \, c_{A\gamma} \mathrm{d}A \tag{2.43}$$

Following the same steps as for the average momentum transport equation, we obtain the final expression of the convection term

$$\begin{aligned} \langle \nabla \cdot (c_{A\gamma} \mathbf{v}_\gamma) \rangle &= \varepsilon_\gamma \langle \mathbf{v}_\gamma \rangle^\gamma \cdot \nabla \langle c_{A\gamma} \rangle^\gamma + \nabla \cdot \langle \tilde{c}_{A\gamma} \tilde{\mathbf{v}}_\gamma \rangle \\ &+ \frac{1}{V} \int_{A_{\gamma\kappa}} (\mathbf{n}_{\gamma\kappa} \cdot \mathbf{v}_\gamma) \, \tilde{c}_{A\gamma} \mathrm{d}A \end{aligned} \tag{2.44}$$

3.3.3 DIFFUSION TERM

For conciseness, all the details regarding the classical averaging of the diffusion term are not repeated here. For more details, the reader is invited to consult the reference [255]. The diffusion term can therefore be written

$$\begin{aligned} \langle \nabla \cdot (\mathscr{D}_\gamma \nabla c_{A\gamma}) \rangle &= \varepsilon_\gamma \nabla \cdot (\mathscr{D}_\gamma \nabla \langle c_{A\gamma} \rangle^\gamma) + (\nabla \varepsilon_\gamma) \cdot (\mathscr{D}_\gamma \nabla \langle c_{A\gamma} \rangle^\gamma) \\ &+ \nabla \cdot \left(\frac{\mathscr{D}_\gamma}{V} \int_{A_{\gamma\kappa}} \mathbf{n}_{\gamma\kappa} \tilde{c}_{A\gamma} \mathrm{d}A \right) - \frac{1}{V} \int_{A_{\gamma\kappa}} \mathbf{n}_{\gamma\kappa} \cdot (-\mathscr{D}_\gamma \nabla c_{A\gamma}) \, \mathrm{d}A \end{aligned} \tag{2.45}$$

3.3.4 NON-CLOSED EQUATION

Finally, the non-closed species conservation takes the form

$$\begin{aligned}
&\frac{\partial \langle c_{A\gamma}\rangle^{\gamma}}{\partial t} + \langle \mathbf{v}_{\gamma}\rangle^{\gamma} \cdot \nabla \langle c_{A\gamma}\rangle^{\gamma} = \nabla \cdot \left(\mathscr{D}_{\gamma} \nabla \langle c_{A\gamma}\rangle^{\gamma}\right) \\
&+\varepsilon_{\gamma}^{-1} \nabla \cdot \left(\frac{\mathscr{D}_{\gamma}}{V} \int_{A_{\gamma\kappa}} \mathbf{n}_{\gamma\kappa} \tilde{c}_{A\gamma} \mathrm{d}A \right) + \varepsilon_{\gamma}^{-1} \left(\nabla \varepsilon_{\gamma}\right) \cdot \left(\mathscr{D}_{\gamma} \nabla \langle c_{A\gamma}\rangle^{\gamma}\right) \\
&-\varepsilon_{\gamma}^{-1} \nabla \cdot \langle \tilde{\mathbf{v}}_{\gamma} \tilde{c}_{A\gamma}\rangle - \frac{1}{V_{\gamma}} \int_{A_{\gamma\kappa}} \mathbf{n}_{\gamma\kappa} \cdot \left[-\mathscr{D}_{\gamma} \nabla c_{A\gamma} + \left(\mathbf{v}_{\gamma} - \mathbf{w}_{\gamma\kappa}\right) \tilde{c}_{A\gamma}\right] \mathrm{d}A
\end{aligned} \tag{2.46}$$

The set of non-closed averaged conservation equations obtained involve numerous deviation terms. In the next section, additional considerations and assumptions are formulated to simplify these equations in order to derive associated closure problems whose solutions are related to the effective transport properties of the closed system.

4 SIMPLIFICATIONS

4.1 SMALL PORE SCALE GROWTH VELOCITY

According to [29], the processes involving a change of the porous microstructure due to phase change or chemical / biological reactions, can generally be modeled considering that the growth velocity of the solid phase is small compared to the average fluid velocity in the direction normal to the interface

$$\left|\mathbf{w}_{\gamma\kappa} \cdot \mathbf{n}_{\gamma\kappa}\right| \ll \left|\langle \mathbf{v}_{\gamma}\rangle^{\gamma} \cdot \mathbf{n}_{\gamma\kappa}\right| \quad \text{at } A_{\gamma\kappa} \tag{2.47}$$

The authors were interested in dendritic solidification but this observation is still relevant in the present context of adsorption.

4.2 SIMPLIFIED FORM OF PORE SCALE BOUNDARY CONDITIONS

Eq. (2.13b) becomes

$$\tilde{\mathbf{v}}_{\gamma} \cdot \mathbf{n}_{\gamma\kappa} = \delta \left(\mathbf{w}_{\gamma\kappa} \cdot \mathbf{n}_{\gamma\kappa}\right) - \langle \mathbf{v}_{\gamma}\rangle^{\gamma} \cdot \mathbf{n}_{\gamma\kappa} \quad \text{at } A_{\gamma\kappa} \tag{2.48}$$

and then, with Eq. (2.47) and $|\delta| < 1$,

$$\tilde{\mathbf{v}}_{\gamma} \cdot \mathbf{n}_{\gamma\kappa} \approx -\langle \mathbf{v}_{\gamma}\rangle^{\gamma} \cdot \mathbf{n}_{\gamma\kappa} \quad \text{at } A_{\gamma\kappa} \tag{2.49}$$

This is a non-penetration condition. Associated to the no-slip condition, it gives

$$\mathbf{v}_\gamma \approx \mathbf{0} \quad \text{at } A_{\gamma\kappa} \tag{2.50}$$

It must be kept in mind that $|\mathbf{w}_{\gamma\kappa} \cdot \mathbf{n}_{\gamma\kappa}|$ is small compared to $|\langle \mathbf{v}_\gamma \rangle^\gamma \cdot \mathbf{n}_{\gamma\kappa}|$ but not null (otherwise, there would not be any adsorption).

Taking into account these considerations, the pore scale relations (2.13a), (2.13b), (2.13c) and (2.13d) leads to

$$\mathbf{w}_{\gamma\kappa} \cdot \mathbf{n}_{\gamma\kappa} = -\frac{1}{\rho_A} \frac{\partial}{\partial t} \left[f(c_{A\gamma}) \right] \quad \text{at } A_{\gamma\kappa} \tag{2.51a}$$

$$\mathbf{v}_\gamma \approx \mathbf{0} \quad \text{at } A_{\gamma\kappa} \tag{2.51b}$$

$$(\mathbf{v}_\gamma - \mathbf{w}_{\gamma\kappa}) \cdot \mathbf{n}_{\gamma\kappa} = \frac{1}{\rho_\gamma} \frac{\partial}{\partial t} \left[f(c_{A\gamma}) \right] \quad \text{at } A_{\gamma\kappa} \tag{2.51c}$$

$$-\mathscr{D}_\gamma \nabla c_{A\gamma} \cdot \mathbf{n}_{\gamma\kappa} = \frac{\partial}{\partial t} \left[f(c_{A\gamma}) \right] \quad \text{at } A_{\gamma\kappa} \tag{2.51d}$$

In this situation, growth velocity has a negligible influence on hydrodynamics and species A transport, but is important in the evolution of the porosity ε_γ with time (and is even the only source of evolution).

4.3 SIMPLIFIED FORM OF AVERAGE MASS CONSERVATION

4.3.1 FOR κ-PHASE (SOLID)

The growth velocity is known by the relation (2.51a) and the evolution of porosity can then be expressed as a function of species A concentration. Eq. (2.27) becomes

$$\frac{\partial \varepsilon_\gamma}{\partial t} = \frac{1}{V} \int_{A_{\gamma\kappa}} \left(-\frac{1}{\rho_A} \frac{\partial}{\partial t} \left[f(c_{A\gamma}) \right] \right) \mathrm{d}A \tag{2.52}$$

and consequently, with the surface transport theorem [228],

$$\frac{\partial \varepsilon_\gamma}{\partial t} = \frac{\partial}{\partial t} \left(\frac{1}{V} \int_{A_{\gamma\kappa}} -\frac{1}{\rho_A} f(c_{A\gamma}) \mathrm{d}A \right) \tag{2.53}$$

where the displacement of the surface has been assumed to be mainly normal and where the effects of curvature of the surface have been neglected. A Taylor expansion at first

order for f shows that

$$f(c_{A\gamma}) = f(\langle c_{A\gamma}\rangle^{\gamma} + \tilde{c}_{A\gamma}) = f(\langle c_{A\gamma}\rangle^{\gamma}) + \tilde{c}_{A\gamma} f'(\langle c_{A\gamma}\rangle^{\gamma}) + \cdots \approx f(\langle c_{A\gamma}\rangle^{\gamma}) \tag{2.54}$$

where $\tilde{c}_{A\gamma}$ has been assumed to be small compared to $\langle c_{A\gamma}\rangle^{\gamma}$, as in usual diffusion problems (see [255], section 1.4.2). It is indeed sufficient to neglect the terms of order higher than one for the adsorption laws considered here (linear and Langmuir).

Using the specific surface area $a_{\gamma\kappa}(\mathbf{x},t) = A_{\gamma\kappa}(\mathbf{x},t)/V$, Eq. (2.53) becomes

$$\frac{\partial \varepsilon_\gamma}{\partial t} = -\frac{1}{\rho_A}\frac{\partial}{\partial t}\left[a_{\gamma\kappa} f(\langle c_{A\gamma}\rangle^{\gamma})\right] \tag{2.55}$$

and therefore, by integration between time t and time 0

$$\varepsilon_\gamma(\mathbf{x},t) = {\varepsilon_\gamma}^0 - \frac{1}{\rho_A} a_{\gamma\kappa}(\mathbf{x},t) f(\langle c_{A\gamma}\rangle^{\gamma})(\mathbf{x},t) \tag{2.56}$$

where ${\varepsilon_\gamma}^0$ is the porosity at initial time. Indeed, the membrane has been assumed to be unfouled at initial time ($\langle c_{A\gamma}\rangle^{\gamma}(\mathbf{x},0) = 0$), and $f(0) = 0$ for any adsorption law. The function f is positive and then, as expected, the porosity ε_γ is at any time smaller than initial porosity.

In the next sections, it would be simpler if the relative gradients of porosity $\nabla\varepsilon_\gamma$ could be neglected. To assess if this assumption is correct, an expression or an equation of evolution for $a_{\gamma\kappa}$ is needed, in order to estimate its gradient. Starting with

$$a_{\gamma\kappa} \sim \frac{1}{\ell_\gamma} \sim (V_\gamma)^{-1/3} \tag{2.57}$$

and reminding that $\varepsilon_\gamma = \dfrac{V_\gamma}{V}$, the following equation is proposed for the specific surface area

$$\frac{a_{\gamma\kappa}}{{a_{\gamma\kappa}}^0} = \left(\frac{\varepsilon_\gamma}{{\varepsilon_\gamma}^0}\right)^{-1/3} \tag{2.58}$$

Consequently

$$\frac{\nabla a_{\gamma\kappa}}{a_{\gamma\kappa}} = -\frac{1}{3}\left(\frac{\nabla\varepsilon_\gamma}{\varepsilon_\gamma}\right) \tag{2.59}$$

and then Eq. (2.56) gives

$$\frac{\nabla\varepsilon_\gamma}{\varepsilon_\gamma} = \frac{-\frac{1}{\rho_A}\left(\frac{a_{\gamma\kappa}}{\varepsilon_\gamma}\right)\nabla\left(f(\langle c_{A\gamma}\rangle^\gamma)\right)}{1-\frac{1}{3\rho_A}\left(\frac{a_{\gamma\kappa}}{\varepsilon_\gamma}\right)f(\langle c_{A\gamma}\rangle^\gamma)} \tag{2.60}$$

As presented in Eq. (2.60), the expression of the porosity gradient depends only on the adsorption rate which is function of protein concentration. Even though it is clear that the porosity gradient is not null, it can be estimated that its variations at the membrane scale is negligible. Therefore one can estimate Eq. (2.60) with the following expression

$$\frac{\nabla\varepsilon_\gamma}{\varepsilon_\gamma} \approx \frac{1}{L_{\varepsilon_\gamma}} \tag{2.61}$$

L_{ε_γ} is a macroscopic length scale associated to the porosity at the membrane-scale. Using this length-scale constraint, we can neglect the porosity gradients in the rest of the analysis.

4.3.2 FOR γ-PHASE (FLUID)

Mass conservation in the fluid, Eq. (2.28), along with the boundary condition (2.51b), changes into

$$\nabla\cdot\langle\mathbf{v}_\gamma\rangle = 0 \tag{2.62}$$

and thus, with negligible gradients of porosity

$$\nabla\cdot\langle\mathbf{v}_\gamma\rangle^\gamma = 0 \tag{2.63}$$

4.4 SIMPLIFIED FORM OF AVERAGE MOMENTUM CONSERVATION

With the relation (2.51b) and divided by ε_γ, Eq. (2.40) becomes

$$\begin{aligned}&\rho_\gamma\frac{\partial\langle\mathbf{v}_\gamma\rangle^\gamma}{\partial t} + \rho_\gamma\langle\mathbf{v}_\gamma\rangle^\gamma\varepsilon_\gamma^{-1}\frac{\partial\varepsilon_\gamma}{\partial t}\\ = \quad &-\nabla\langle p_\gamma\rangle^\gamma + \mu_\gamma\nabla^2\langle\mathbf{v}_\gamma\rangle^\gamma + \frac{1}{V_\gamma}\int_{A_{\gamma\kappa}}\mathbf{n}_{\gamma\kappa}\cdot(-\mathbf{I}\tilde{p}_\gamma + \mu_\gamma\nabla\tilde{\mathbf{v}}_\gamma)\mathrm{d}A\end{aligned} \tag{2.64}$$

where gradients of porosity have been neglected again.

4.5 SIMPLIFIED FORM OF AVERAGE SPECIES CONSERVATION

With the relation (2.51b) and neglecting porosity gradients, Eq. (2.46) gives

$$\begin{aligned} & \frac{\partial \langle c_{A\gamma}\rangle^{\gamma}}{\partial t} + \varepsilon_{\gamma}^{-1} a_{\gamma\kappa} \frac{\partial}{\partial t}\left[f(\langle c_{A\gamma}\rangle^{\gamma})\right] + f(\langle c_{A\gamma}\rangle^{\gamma})\varepsilon_{\gamma}^{-1}\frac{\partial a_{\gamma\kappa}}{\partial t} + \langle \mathbf{v}_{\gamma}\rangle^{\gamma}\cdot\nabla\langle c_{A\gamma}\rangle^{\gamma} \\ = \; & \nabla\cdot(\mathscr{D}_{\gamma}\nabla\langle c_{A\gamma}\rangle^{\gamma}) + \varepsilon_{\gamma}^{-1}\nabla\cdot\left(\frac{\mathscr{D}_{\gamma}}{V}\int_{A_{\gamma\kappa}}\mathbf{n}_{\gamma\kappa}\tilde{c}_{A\gamma}\mathrm{d}A\right) \\ - \; & \varepsilon_{\gamma}^{-1}\nabla\cdot\langle\tilde{\mathbf{v}}_{\gamma}\tilde{c}_{A\gamma}\rangle \end{aligned} \tag{2.65}$$

where (2.51c) and (2.51d) were used to obtain

$$\frac{|\mathbf{n}_{\gamma\kappa}\cdot(\mathbf{v}_{\gamma}-\mathbf{w}_{\gamma\kappa})\,\tilde{c}_{A\gamma}|}{|\mathbf{n}_{\gamma\kappa}\cdot(-\mathscr{D}_{\gamma}\nabla c_{A\gamma})|} = \mathbf{O}\left(\frac{\tilde{c}_{A\gamma}}{\rho_{\gamma}}\right) \ll 1 \tag{2.66}$$

(2.67)

$$\begin{aligned} & -\frac{1}{V_{\gamma}}\int_{A_{\gamma\kappa}}\mathbf{n}_{\gamma\kappa}\cdot(-\mathscr{D}_{\gamma}\nabla c_{A\gamma})\,\mathrm{d}A \\ = \; & -\varepsilon_{\gamma}^{-1}a_{\gamma\kappa}\frac{\partial}{\partial t}\left[f(\langle c_{A\gamma}\rangle^{\gamma})\right] - \varepsilon_{\gamma}^{-1}f(\langle c_{A\gamma}\rangle^{\gamma})\frac{\partial a_{\gamma\kappa}}{\partial t} \end{aligned} \tag{2.68}$$

in the same manner as before.

4.6 SIMPLIFIED SYSTEM OF EQUATIONS

Finally, the simplified average transport equations are Eqs. (2.56), (2.58), (2.63), (2.64) and (2.65)

$$\nabla\cdot\langle\mathbf{v}_{\gamma}\rangle^{\gamma} = 0 \tag{2.69a}$$

$$\begin{aligned} & \rho_{\gamma}\frac{\partial\langle\mathbf{v}_{\gamma}\rangle^{\gamma}}{\partial t} + \rho_{\gamma}\langle\mathbf{v}_{\gamma}\rangle^{\gamma}\varepsilon_{\gamma}^{-1}\frac{\partial\varepsilon_{\gamma}}{\partial t} \\ & = -\nabla\langle p_{\gamma}\rangle^{\gamma} + \mu_{\gamma}\nabla^{2}\langle\mathbf{v}_{\gamma}\rangle^{\gamma} + \frac{1}{V_{\gamma}}\int_{A_{\gamma\kappa}}\mathbf{n}_{\gamma\kappa}\cdot(-\mathbf{I}\tilde{p}_{\gamma} + \mu_{\gamma}\nabla\tilde{\mathbf{v}}_{\gamma})\mathrm{d}A \end{aligned} \tag{2.69b}$$

$$\begin{aligned} & \left[1+\varepsilon_{\gamma}^{-1}a_{\gamma\kappa}f'(\langle c_{A\gamma}\rangle^{\gamma})\right]\frac{\partial\langle c_{A\gamma}\rangle^{\gamma}}{\partial t} + \varepsilon_{\gamma}^{-1}f(\langle c_{A\gamma}\rangle^{\gamma})\frac{\partial a_{\gamma\kappa}}{\partial t} + \langle\mathbf{v}_{\gamma}\rangle^{\gamma}\cdot\nabla\langle c_{A\gamma}\rangle^{\gamma} \\ = \; & \nabla\cdot(\mathscr{D}_{\gamma}\nabla\langle c_{A\gamma}\rangle^{\gamma}) + \varepsilon_{\gamma}^{-1}\nabla\cdot\left(\frac{\mathscr{D}_{\gamma}}{V}\int_{A_{\gamma\kappa}}\mathbf{n}_{\gamma\kappa}\tilde{c}_{A\gamma}\mathrm{d}A\right) \\ - \; & \varepsilon_{\gamma}^{-1}\nabla\cdot\langle\tilde{\mathbf{v}}_{\gamma}\tilde{c}_{A\gamma}\rangle \end{aligned} \tag{2.69c}$$

$$\varepsilon_\gamma = {\varepsilon_\gamma}^0 - \frac{1}{\rho_A} a_{\gamma\kappa} f(\langle c_{A\gamma}\rangle^\gamma) \tag{2.69d}$$

$$a_{\gamma\kappa} = {a_{\gamma\kappa}}^0 \left(\frac{\varepsilon_\gamma}{{\varepsilon_\gamma}^0}\right)^{-1/3} \tag{2.69e}$$

To conclude this section, it is worth mentioning that, at this stage, the non closed hydrodynamics problem explicitly involves the time evolution of porosity. Rigorously, that is to say that both the closed momentum equation and the solution of the associated closure problem for the determination of the permeability depend on this evolution. For the closed momentum equation, this is not a difficulty since this additional term explicitly depends on the adsorption rate. The solution of the closure problem is more complicated if the time evolution of porosity is treated as a source term. This remains a challenge which is out of reach of the present study. In the following, this dependency will be neglected and the classical closure problem will be considered for the determination of the permeability.
Moreover, the evolution of the species A concentration is described by a convection-diffusion equation with a modified accumulation term due to adsorption. For the same reason af for the momentum equation, the contribution of the time evolution of specific surface area will be discarded in the closure problem.

5 DEVIATIONS AND CLOSURE PROBLEMS

The objective of this section is to derive the associated closure problems. Only the main steps are recalled here in order to make the coupling with species transport more understandable.

5.1 CLOSURE PROBLEM FOR MOMENTUM CONSERVATION

Since the source term related to the time evolution of the porosity has been discarded from the closure problem for momentum, it reduces to a classical form. The deviation problem for momentum is given by [255]

$$0 = -\nabla\tilde{p}_\gamma + \mu_\gamma\nabla^2\tilde{\mathbf{v}}_\gamma - \frac{1}{V_\gamma}\int_{A_{\gamma\kappa}} \mathbf{n}_{\gamma\kappa}\cdot(-\mathbf{I}\tilde{p}_\gamma + \mu_\gamma\nabla\tilde{\mathbf{v}}_\gamma)\mathrm{d}A \tag{2.70a}$$

$$\nabla\cdot\tilde{\mathbf{v}}_\gamma = 0 \tag{2.70b}$$

$$\tilde{\mathbf{v}}_\gamma = -\underbrace{\langle\mathbf{v}_\gamma\rangle^\gamma}_{source} \quad \text{at } A_{\gamma\kappa} \tag{2.70c}$$

$$\tilde{p}_\gamma(\mathbf{r}+l_i) = \tilde{p}_\gamma(\mathbf{r}), \quad \tilde{\mathbf{v}}_\gamma(\mathbf{r}+l_i) = \tilde{\mathbf{v}}_\gamma(\mathbf{r}), \quad i=1,2,3 \tag{2.70d}$$

$$\langle\tilde{\mathbf{v}}_\gamma\rangle^\gamma = 0 \tag{2.70e}$$

where the relevance of periodicity conditions for both pressure and velocity fields has been frequently discussed [255]. It is worth noticing that periodicity conditions only makes sense for constant or periodic sources. In the above deviation problem, $\langle \mathbf{v}_\gamma \rangle^\gamma$ is a constant since the length-scale constraint

$$r_0 \ll \ell_{mb} \tag{2.71}$$

is satisfied, and it is then a source term for deviations. The characteristic length of the representative unit cell will always be of the order of r_0 or smaller.

The nature of the deviation momentum problem suggests that the deviation solutions can be written under the form

$$\tilde{\mathbf{v}}_\gamma = \mathbf{B}_\gamma \cdot \langle \mathbf{v}_\gamma \rangle^\gamma \tag{2.72a}$$
$$\tilde{p}_\gamma = \mu_\gamma \mathbf{b}_\gamma \cdot \langle \mathbf{v}_\gamma \rangle^\gamma \tag{2.72b}$$

Therefore, the associated closure problem for the variables $\mathbf{B}_\gamma$ and $\mathbf{b}_\gamma$ is defined by

$$0 = -\nabla \mathbf{b}_\gamma + \nabla^2 \mathbf{B}_\gamma - \frac{1}{V_\gamma} \int_{A_{\gamma\kappa}} \mathbf{n}_{\gamma\kappa} \cdot (-\mathbf{I}\mathbf{b}_\gamma + \nabla \mathbf{B}_\gamma) \mathrm{d}A \tag{2.73a}$$
$$\nabla \mathbf{B}_\gamma = 0 \tag{2.73b}$$
$$\mathbf{B}_\gamma = -\mathbf{I} \quad \text{at } A_{\gamma\kappa} \tag{2.73c}$$
$$\mathbf{b}_\gamma(\mathbf{r} + l_i) = \mathbf{b}_\gamma(\mathbf{r}), \quad \mathbf{B}_\gamma(\mathbf{r} + l_i) = \mathbf{B}_\gamma(\mathbf{r}), \quad i = 1, 2, 3 \tag{2.73d}$$
$$\langle \mathbf{B}_\gamma \rangle^\gamma = 0 \tag{2.73e}$$

The permeability tenser $\mathbf{K}_\gamma$ is defined as

$$\frac{1}{V_\gamma} \int_{A_{\gamma\kappa}} \mathbf{n}_{\gamma\kappa} \cdot (-\mathbf{I}\mathbf{b}_\gamma + \nabla \mathbf{B}_\gamma) \mathrm{d}A = -\varepsilon_\gamma \mathbf{K}_\gamma^{-1} \tag{2.74}$$

The solution of Eq. (2.73) is the classical solution of the Stokes closure problem and is explained thoroughly in [255].

5.2 CLOSURE PROBLEM FOR SPECIES CONSERVATION

5.2.1 DEVIATION PROBLEM

The objective of this section is to determine the deviation of species A concentration, $\tilde{c}_{A\gamma}$, as a function of average quantities, in order to obtain a closed form of the average species concentration equation. To get the governing differential equation for $\tilde{c}_{A\gamma}$, the non-closed

average conservation equation Eq. (2.69c)

$$\begin{aligned} & \frac{\partial \left\langle c_{A\gamma}\right\rangle^{\gamma}}{\partial t}+\varepsilon_{\gamma}^{-1} a_{\gamma\kappa} \frac{\partial}{\partial t}\left[f\left(\left\langle c_{A\gamma}\right\rangle^{\gamma}\right)\right]+\varepsilon_{\gamma}^{-1} f\left(\left\langle c_{A\gamma}\right\rangle^{\gamma}\right) \frac{\partial a_{\gamma\kappa}}{\partial t}+\left\langle \mathbf{v}_{\gamma}\right\rangle^{\gamma} \cdot \nabla\left\langle c_{A\gamma}\right\rangle^{\gamma} \\ = \quad & \nabla \cdot\left(\mathscr{D}_{\gamma} \nabla\left\langle c_{A\gamma}\right\rangle^{\gamma}\right)+\varepsilon_{\gamma}^{-1} \nabla \cdot\left(\frac{\mathscr{D}_{\gamma}}{V} \int_{A_{\gamma\kappa}} \mathbf{n}_{\gamma\kappa} \tilde{c}_{A\gamma} \mathrm{d}A\right)-\varepsilon_{\gamma}^{-1} \nabla \cdot\left\langle \tilde{\mathbf{v}}_{\gamma} \tilde{c}_{A\gamma}\right\rangle \end{aligned} \tag{2.75}$$

is substracted from the pore scale one Eq. (2.8)

$$\frac{\partial c_{A\gamma}}{\partial t}+\nabla \cdot\left(c_{A\gamma} \mathbf{v}_{\gamma}\right)=\nabla \cdot\left(\mathscr{D}_{\gamma} \nabla c_{A\gamma}\right) \tag{2.76}$$

Thus

$$\begin{aligned} & \underbrace{\frac{\partial \tilde{c}_{A\gamma}}{\partial t}}_{\text{Accumulation}}-\underbrace{\varepsilon_{\gamma}^{-1} a_{\gamma\kappa} \frac{\partial}{\partial t}\left[f\left(\left\langle c_{A\gamma}\right\rangle^{\gamma}\right)\right]}_{\text{Adsorptive source}}+\underbrace{\mathbf{v}_{\gamma} \cdot \nabla \tilde{c}_{A\gamma}}_{\text{Convection}}+\underbrace{\tilde{\mathbf{v}}_{\gamma} \cdot \nabla\left\langle c_{A\gamma}\right\rangle^{\gamma}}_{\text{Convective source}} \\ = \quad & \underbrace{\nabla \cdot\left(\mathscr{D}_{\gamma} \nabla \tilde{c}_{A\gamma}\right)}_{\text{Diffusion}}-\underbrace{\varepsilon_{\gamma}^{-1} \nabla \cdot\left(\frac{\mathscr{D}_{\gamma}}{V} \int_{A_{\gamma\kappa}} \mathbf{n}_{\gamma\kappa} \tilde{c}_{A\gamma} \mathrm{d}A\right)}_{\text{Non-local diffusion}}+\underbrace{\varepsilon_{\gamma}^{-1} \nabla \cdot\left\langle \tilde{\mathbf{v}}_{\gamma} \tilde{c}_{A\gamma}\right\rangle}_{\text{Non-local convection}} \end{aligned} \tag{2.77}$$

where the term arising from the evolution with time of the specific surface area has been discarded, as previously discussed. The thorough procedure of the simplification of this deviation equation, detailed in **Appendix A**, gives

$$\underbrace{-\varepsilon_{\gamma}^{-1} a_{\gamma\kappa} \frac{\partial}{\partial t}\left[f\left(\left\langle c_{A\gamma}\right\rangle^{\gamma}\right)\right]}_{\text{Adsorptive source}}+\underbrace{\mathbf{v}_{\gamma} \cdot \nabla \tilde{c}_{A\gamma}}_{\text{Convection}}+\underbrace{\tilde{\mathbf{v}}_{\gamma} \cdot \nabla\left\langle c_{A\gamma}\right\rangle^{\gamma}}_{\text{Convective source}}=\underbrace{\nabla \cdot\left(\mathscr{D}_{\gamma} \nabla \tilde{c}_{A\gamma}\right)}_{\text{Diffusion}} \tag{2.78}$$

5.2.2 BOUNDARY CONDITIONS

Reminding pore scale boundary condition (2.13d)

$$-\mathscr{D}_{\gamma} \nabla c_{A\gamma} \cdot \mathbf{n}_{\gamma\kappa}=\frac{\partial}{\partial t}\left[f\left(c_{A\gamma}\right)\right] \quad \text{on } A_{\gamma e} \tag{2.79}$$

the initial and boundary conditions for the deviation problem are

$$-\mathscr{D}_\gamma \nabla \tilde{c}_{A\gamma} \cdot \mathbf{n}_{\gamma\kappa} = \underbrace{\mathscr{D}_\gamma \nabla \langle c_{A\gamma} \rangle^\gamma \cdot \mathbf{n}_{\gamma\kappa}}_{\text{Diffusion source}} + \underbrace{\frac{\partial}{\partial t}\left[f(\langle c_{A\gamma} \rangle^\gamma)\right]}_{\text{Adsorptive source}} \quad \text{at } A_{\gamma\kappa} \tag{2.80a}$$

$$\tilde{c}_{A\gamma} = \mathcal{F}(\mathbf{r}, t) \quad \text{on } A_{\gamma e} \tag{2.80b}$$

$$\tilde{c}_{A\gamma} = \mathcal{G}(\mathbf{r}) \quad \text{at } t = 0 \tag{2.80c}$$

5.2.3 CLOSURE PROBLEM

There is not interest in solving $\tilde{c}_{A\gamma}$ in the whole macroscopic region because the numerical cost would be about the same as for the pore scale problem. Instead, $\tilde{c}_{A\gamma}$ will be determined in different regions that are representative of the structure of the original one. Given that $\tilde{c}_{A\gamma}$ is dominated by the small length scale, the boundary condition imposed on entrances and exits in (A.13b) can influence the $\tilde{c}_{A\gamma}$-field only in a very thin region near the entrances and exits of the macroscopic system. Therefore, each representative region will be modeled as a periodic unit cell, where boundary conditions at $A_{\gamma e}$ have been replaced by periodic boundary conditions.
This leads to the closure problem given by

$$\underbrace{-\varepsilon_\gamma^{-1} a_{\gamma\kappa} \frac{\partial}{\partial t}\left[f(\langle c_{A\gamma} \rangle^\gamma)\right]}_{\text{Adsorptive source}} + \underbrace{\mathbf{v}_\gamma \cdot \nabla \tilde{c}_{A\gamma}}_{\text{Convection}} + \underbrace{\tilde{\mathbf{v}}_\gamma \cdot \nabla \langle c_{A\gamma} \rangle^\gamma}_{\text{Convective source}} = \underbrace{\nabla \cdot (\mathscr{D}_\gamma \nabla \tilde{c}_{A\gamma})}_{\text{Diffusion}} \tag{2.81a}$$

$$-\mathscr{D}_\gamma \nabla \tilde{c}_{A\gamma} \cdot \mathbf{n}_{\gamma\kappa} = \underbrace{\mathscr{D}_\gamma \nabla \langle c_{A\gamma} \rangle^\gamma \cdot \mathbf{n}_{\gamma\kappa}}_{\text{Diffusion source}} + \underbrace{\frac{\partial}{\partial t}\left[f(\langle c_{A\gamma} \rangle^\gamma)\right]}_{\text{Adsorptive source}} \quad \text{at } A_{\gamma\kappa} \tag{2.81b}$$

$$\tilde{c}_{A\gamma}(\mathbf{r} + l_i) = c_{A\gamma}(\mathbf{r}) \quad i = 1, 2, 3 \tag{2.81c}$$

It is important to notice that at the scale of a unit cell (ℓ_γ), the macroscopic terms can be treated as constants and equal to their value at the center $\mathbf{x}$ of the unit cell. Furthermore, the solution $\tilde{c}_{A\gamma}$ of this problem is not unique since any additive constant can be added to a solution to form another solution. Nevretheless, this constant does not pass through the integral filter of Eq. (2.69c) because the representative medium is periodic. Any solution will then lead to the same result for the closed average species conservation.

5.2.4 CLOSURE VARIABLES

According to the closure problem, the macroscopic source terms are $\nabla \langle c_{A\gamma} \rangle^\gamma$ and $\frac{\partial}{\partial t}\left[f(\langle c_{A\gamma} \rangle^\gamma)\right]$. $\tilde{c}_{A\gamma}$ is then searched under the form of a first order development with

respect to these terms

$$\tilde{c}_{A\gamma} = \mathbf{s}_\gamma \cdot \nabla \langle c_{A\gamma} \rangle^\gamma + b_\gamma \frac{\partial}{\partial t} \left[f(\langle c_{A\gamma} \rangle^\gamma) \right] \tag{2.82}$$

The constant (zeroth order of the development) has been here taken equal to zero, since it does not pass through the integral filter of Eq. (2.69c), as seen before.
Introducting this expression into Eqs. (2.81) and treating source terms as constants in the unit cell, the closure variables $\mathbf{s}_\gamma$ and b_γ verify the following uncoupled systems
Problem I

$$\mathbf{v}_\gamma \cdot \nabla \mathbf{s}_\gamma + \tilde{\mathbf{v}}_\gamma = \nabla \cdot (\mathscr{D}_\gamma \nabla \mathbf{s}_\gamma) \tag{2.83a}$$

$$\text{B.C.:} \quad -\mathbf{n}_{\gamma\kappa} \cdot \mathscr{D}_\gamma \nabla \mathbf{s}_\gamma = \mathscr{D}_\gamma \mathbf{n}_{\gamma\kappa} \quad \text{at } A_{\gamma\kappa} \tag{2.83b}$$

$$\text{Periodicity:} \quad \mathbf{s}_\gamma(\mathbf{r} + l_i) = \mathbf{s}_\gamma(\mathbf{r}) \tag{2.83c}$$

Problem II

$$-\varepsilon_\gamma^{-1} a_{\gamma\kappa} + \mathbf{v}_\gamma \cdot \nabla b_\gamma = \nabla \cdot (\mathscr{D}_\gamma \nabla b_\gamma) \tag{2.84a}$$

$$\text{B.C.:} \quad -\mathbf{n}_{\gamma\kappa} \cdot \mathscr{D}_\gamma \nabla b_\gamma = 1 \quad \text{at } A_{\gamma\kappa} \tag{2.84b}$$

$$\text{Periodicity:} \quad b_\gamma(\mathbf{r} + l_i) = b_\gamma(\mathbf{r}) \tag{2.84c}$$

6 CLOSED FORM OF THE MACROSCOPIC MODEL

6.1 CLOSED AVERAGE MASS CONSERVATION

Eq. (2.69a) was already closed

$$\nabla \cdot \langle \mathbf{v}_\gamma \rangle^\gamma = 0 \tag{2.85}$$

6.2 CLOSED AVERAGE MOMENTUM CONSERVATION

In order to obtain a closed form of the macroscopic momentum conservation with adsorption, velocity and pressure deviations given by Eqs. (2.72a) and (2.72b) are introduced into Eq. (2.69c)

$$\begin{aligned} & \rho_\gamma \frac{\partial \langle \mathbf{v}_\gamma \rangle^\gamma}{\partial t} + \rho_\gamma \langle \mathbf{v}_\gamma \rangle^\gamma \varepsilon_\gamma^{-1} \frac{\partial \varepsilon_\gamma}{\partial t} \\ = \quad & -\nabla \langle p_\gamma \rangle^\gamma + \mu_\gamma \nabla^2 \langle \mathbf{v}_\gamma \rangle^\gamma \\ + \quad & \mu_\gamma \left[\frac{1}{V_\gamma} \int_{A_{\gamma\kappa}} \mathbf{n}_{\gamma\kappa} \cdot (-\mathbf{I}\mathbf{b}_\gamma + \nabla \mathbf{B}_\gamma) \mathrm{d}A \right] \cdot \langle \mathbf{v}_\gamma \rangle^\gamma \end{aligned} \tag{2.86}$$

which can be written under the more compact form

$$\rho_\gamma \frac{\partial \langle \mathbf{v}_\gamma \rangle^\gamma}{\partial t} + \rho_\gamma \langle \mathbf{v}_\gamma \rangle^\gamma \varepsilon_\gamma^{-1} \frac{\partial \varepsilon_\gamma}{\partial t} = -\nabla \langle p_\gamma \rangle^\gamma + \mu_\gamma \nabla^2 \langle \mathbf{v}_\gamma \rangle^\gamma - \mu_\gamma \mathbf{K}_\gamma^{-1} \cdot \varepsilon_\gamma \langle \mathbf{v}_\gamma \rangle^\gamma \tag{2.87}$$

It should be noticed that Eq. (2.87) represents an improvement in the derivation of the upscaled momentum transport equation for porous media for which microstructure can be time dependent. However, it is important to clearly identify its limitations. Indeed, Eq. (2.87) has been derived first by assuming a small interface velocity and secondly by neglecting in the closure problem the source term related to the evolution with time of the structure. The authors are conscious that deeper analysis is needed in order to deal with this complexity.

6.3 CLOSED AVERAGE SPECIES CONSERVATION

In order to obtain a closed form of the macroscopic species conservation with adsorption, concentration deviations given by Eq. (2.82) are introduced into Eq. (2.69c)

$$\begin{aligned}
&\left[1 + \varepsilon_\gamma^{-1} a_{\gamma\kappa} f'(\langle c_{A\gamma} \rangle^\gamma)\right] \frac{\partial \langle c_{A\gamma} \rangle^\gamma}{\partial t} + \varepsilon_\gamma^{-1} f(\langle c_{A\gamma} \rangle^\gamma) \frac{\partial a_{\gamma\kappa}}{\partial t} + \langle \mathbf{v}_\gamma \rangle^\gamma \cdot \nabla \langle c_{A\gamma} \rangle^\gamma \\
&= \nabla \cdot (\mathscr{D}_\gamma \nabla \langle c_{A\gamma} \rangle^\gamma) \\
&+ \varepsilon_\gamma^{-1} \nabla \cdot \left(\frac{\mathscr{D}_\gamma}{V} \int_{A_{\gamma\kappa}} \mathbf{n}_{\gamma\kappa} \left(\mathbf{s}_\gamma \cdot \nabla \langle c_{A\gamma} \rangle^\gamma + b_\gamma \frac{\partial}{\partial t} \left[f(\langle c_{A\gamma} \rangle^\gamma) \right] \right) \mathrm{d}A \right) \\
&- \varepsilon_\gamma^{-1} \nabla \cdot \left\langle \tilde{\mathbf{v}}_\gamma \left(\mathbf{s}_\gamma \cdot \nabla \langle c_{A\gamma} \rangle^\gamma + b_\gamma \frac{\partial}{\partial t} \left[f(\langle c_{A\gamma} \rangle^\gamma) \right] \right) \right\rangle
\end{aligned} \tag{2.88}$$

After some simplifications, it becomes

$$\begin{aligned}
&\left[1 + \varepsilon_\gamma^{-1} a_{\gamma\kappa} f'(\langle c_{A\gamma} \rangle^\gamma)\right] \frac{\partial \langle c_{A\gamma} \rangle^\gamma}{\partial t} + \varepsilon_\gamma^{-1} f(\langle c_{A\gamma} \rangle^\gamma) \frac{\partial a_{\gamma\kappa}}{\partial t} + \langle \mathbf{v}_\gamma \rangle^\gamma \cdot \nabla \langle c_{A\gamma} \rangle^\gamma \\
= \; & \nabla \cdot \left[\left\{ \mathscr{D}_\gamma \left(\mathbf{I} + \frac{1}{V_\gamma} \int_{A_{\gamma\kappa}} \mathbf{n}_{\gamma\kappa} \mathbf{s}_\gamma \mathrm{d}A \right) - \langle \tilde{\mathbf{v}}_\gamma \mathbf{s}_\gamma \rangle^\gamma \right\} \cdot \nabla \langle c_{A\gamma} \rangle^\gamma \right] \\
& + \nabla \cdot \left(\mathbf{u} \frac{\partial}{\partial t} \left[f(\langle c_{A\gamma} \rangle^\gamma) \right] \right) - \nabla \cdot \left(\langle \tilde{\mathbf{v}}_\gamma b_\gamma \rangle^\gamma \frac{\partial}{\partial t} \left[f(\langle c_{A\gamma} \rangle^\gamma) \right] \right)
\end{aligned} \tag{2.89}$$

where a dimensionless vector $\mathbf{u}$ was defined as

$$\mathbf{u} = \mathscr{D}_\gamma \left(\frac{1}{V_\gamma} \int_{A_{\gamma\kappa}} \mathbf{n}_{\gamma\kappa} b_\gamma \mathrm{d}A \right) \tag{2.90}$$

6.3.1 SIMPLIFICATIONS

From Eqs. (2.84b), it is possible to estimate

$$b_\gamma = \mathbf{O}\left(\frac{\ell_\gamma}{\mathscr{D}_\gamma}\right) \tag{2.91}$$

Average quantities vary over the macroscopic length scale l_{mb} and this leads to the estimates

$$\nabla\cdot\left(\mathbf{u}\frac{\partial}{\partial t}\left[f(\langle c_{A\gamma}\rangle^\gamma)\right]\right) = \mathbf{O}\left(\frac{\varepsilon_\gamma^{-1}}{\ell_{mb}}\frac{\partial}{\partial t}\left[f(\langle c_{A\gamma}\rangle^\gamma)\right]\right) \tag{2.92a}$$

$$\nabla\cdot\left(\langle\tilde{\mathbf{v}}_\gamma b_\gamma\rangle^\gamma\frac{\partial}{\partial t}\left[f(\langle c_{A\gamma}\rangle^\gamma)\right]\right) = \mathbf{O}\left(\frac{\langle v_\gamma\rangle^\gamma\ell_\gamma}{\mathscr{D}_\gamma}\frac{\ell_\gamma}{\ell_{mb}}\frac{1}{\ell_\gamma}\frac{\partial}{\partial t}\left[f(\langle c_{A\gamma}\rangle^\gamma)\right]\right) \tag{2.92b}$$

$$\varepsilon_\gamma^{-1}a_{\gamma\kappa}\frac{\partial}{\partial t}\left[f(\langle c_{A\gamma}\rangle^\gamma)\right] = \mathbf{O}\left(\frac{\varepsilon_\gamma^{-1}}{\ell_\gamma}\frac{\partial}{\partial t}\left[f(\langle c_{A\gamma}\rangle^\gamma)\right]\right) \tag{2.92c}$$

where $a_{\gamma\kappa} = \mathbf{O}\left(\frac{1}{\ell_\gamma}\right)$ and $\tilde{v}_\gamma = \mathbf{O}\left(\langle\mathbf{v}_\gamma\rangle^\gamma\right)$ from (2.51b) were used. The Péclet number defined by

$$\mathrm{Pe} = \frac{\langle v_\gamma\rangle^\gamma\ell_\gamma}{\mathscr{D}_\gamma} \tag{2.93}$$

is close to 10^{-2} for gluthatione and 7×10^{-2} for BSA. Finally

$$\nabla\cdot\left(\mathbf{u}\frac{\partial}{\partial t}\left[f(\langle c_{A\gamma}\rangle^\gamma)\right]\right) \ll \varepsilon_\gamma^{-1}a_{\gamma\kappa}\frac{\partial}{\partial t}\left[f(\langle c_{A\gamma}\rangle^\gamma)\right] \tag{2.94a}$$

$$\nabla\cdot\left(\langle\tilde{\mathbf{v}}_\gamma b_\gamma\rangle^\gamma\frac{\partial}{\partial t}\left[f(\langle c_{A\gamma}\rangle^\gamma)\right]\right) \ll \varepsilon_\gamma^{-1}a_{\gamma\kappa}\frac{\partial}{\partial t}\left[f(\langle c_{A\gamma}\rangle^\gamma)\right] \tag{2.94b}$$

because $\ell_\gamma \ll \ell_{mb}$ and $\varepsilon_\gamma \sim 1$.

The final expression of Eq. (2.89) is therefore

$$\begin{aligned}&\left[1+\varepsilon_\gamma^{-1}a_{\gamma\kappa}f'(\langle c_{A\gamma}\rangle^\gamma)\right]\frac{\partial\langle c_{A\gamma}\rangle^\gamma}{\partial t}+\varepsilon_\gamma^{-1}f(\langle c_{A\gamma}\rangle^\gamma)\frac{\partial a_{\gamma\kappa}}{\partial t}+\langle\mathbf{v}_\gamma\rangle^\gamma\cdot\nabla\langle c_{A\gamma}\rangle^\gamma\\ =\;&\nabla\cdot\left(\mathbf{D}^*\cdot\nabla\langle c_{A\gamma}\rangle^\gamma\right)\end{aligned} \tag{2.95}$$

where the effective dispersion tensor $\mathbf{D}^*$ is defined by

$$\mathbf{D}^* = \underbrace{\mathscr{D}_\gamma \left(\mathbf{I} + \frac{1}{V_\gamma} \int_{A_{\gamma\kappa}} \mathbf{n}_{\gamma\kappa} \mathbf{s}_\gamma \mathrm{d}A \right)}_{\text{effective diffusivity}} - \underbrace{\langle \tilde{\mathbf{v}}_\gamma \mathbf{s}_\gamma \rangle^\gamma}_{\text{dispersion}} \tag{2.96}$$

It is a function of pore scale diffusivity and structure, and also of dispersion caused by convection.

7 NUMERICAL RESULTS

The objective of this section is to solve numerically the coupled equation of mass and momentum transfer in the membrane active layer and determine the profile of the velocity and concentration at both sides of the membrane. As previously stated, the membrane is composed of 3 layers notably active layer, intermediate layer and mechanical support. The retention of the particles however, is mainly performed at the active layer surface. Thus the model provided the averaged equations of mass and momentum for this layer with the expression of the effective permeability. One major difficulty is that the active layer's thickness (0.3-3 μm) is really small compared to other membrane layers (200 μm) and also the thickness of the bulk fluid above it (0.5 mm). Therefore it seems reasonable to replace the membrane active layer by a jump condition and solve simultaneously the equations in the fluid bulk phase and the membrane porous medium. For this purpose, first we express these equations with the corresponding jump condition due to the membrane active layer and then we solve these equations numerically to obtain the profiles of the velocity and concentration in the bulk fluid and across the membrane.

7.1 THE VOLUME AVERAGED EQUATIONS IN EACH PHASE

We begin our analysis with the mass and momentum conservation equations in the membrane active layer.

$$\nabla \cdot \varepsilon_{\gamma\omega} \langle \mathbf{v}_\gamma \rangle_\omega^\gamma = 0 \tag{2.97a}$$

$$\rho_\gamma \varepsilon_{\gamma\omega} \frac{\partial \langle \mathbf{v}_\gamma \rangle_\omega^\gamma}{\partial t} + \rho_\gamma \langle \mathbf{v}_\gamma \rangle_\omega^\gamma \frac{d\varepsilon_{\gamma\omega}}{dt} = -\varepsilon_{\gamma\omega} \nabla \langle p_\gamma \rangle_\omega^\gamma + \mu_\gamma \varepsilon_{\gamma\omega} \nabla^2 \langle \mathbf{v}_\gamma \rangle_\omega^\gamma - \mu_\gamma \varepsilon_{\gamma\omega}^2 \mathbf{K}_\omega^{-1} \cdot \langle \mathbf{v}_\gamma \rangle_\omega^\gamma \tag{2.97b}$$

Here we have used the subscript ω as a reminder that these expressions correspond to the active layer. For the transport of chemical species (species A), the corresponding

upscaled model is

$$(\varepsilon_{\gamma\omega} + a_{\gamma\kappa\omega} f'_{\omega}) \frac{\partial \langle c_{A\gamma} \rangle^{\gamma}_{\omega}}{\partial t} + f_{\omega} \frac{da_{\gamma\kappa\omega}}{dt} + \nabla \cdot (\varepsilon_{\gamma\omega} \langle \mathbf{v}_{\gamma} \rangle^{\gamma}_{\omega} \langle c_{A\gamma} \rangle^{\gamma}_{\omega}) = \nabla \cdot (\mathbf{D}^{*}_{\omega} \cdot \varepsilon_{\gamma\omega} \nabla \langle c_{A\gamma} \rangle^{\gamma}_{\omega}) \tag{2.98}$$

In the homogenous fluid phase above the membrane surface the averaged equations of mass and momentum are also expressed

$$\nabla \cdot \langle \mathbf{v}_{\gamma} \rangle^{\gamma}_{\eta} = 0 \tag{2.99a}$$

$$\rho_{\gamma} \frac{\partial \langle \mathbf{v}_{\gamma} \rangle^{\gamma}_{\eta}}{\partial t} = -\nabla \langle p_{\gamma} \rangle^{\gamma}_{\eta} + \mu_{\gamma} \nabla^{2} \langle \mathbf{v}_{\gamma} \rangle^{\gamma}_{\eta} \tag{2.99b}$$

$$\frac{\partial \langle c_{A\gamma} \rangle^{\gamma}_{\eta}}{\partial t} + \nabla \cdot \left(\langle \mathbf{v}_{\gamma} \rangle^{\gamma}_{\eta} \langle c_{A\gamma} \rangle^{\gamma}_{\eta} \right) = \nabla \cdot \left(D_{\gamma} \nabla \langle c_{A\gamma} \rangle^{\gamma}_{\eta} \right) \tag{2.99c}$$

Here we have used the subscript η as a reminder that these expressions correspond to the fluid medium.

Finally, below the active layer there is another porous medium, and the governing equations for transport are

$$\nabla \cdot \varepsilon_{\omega p} \langle \mathbf{v}_{\gamma} \rangle^{\gamma}_{p} = 0 \tag{2.100a}$$

$$\rho_{\gamma} \varepsilon_{\omega p} \frac{\partial \langle \mathbf{v}_{\gamma} \rangle^{\gamma}_{p}}{\partial t} = -\varepsilon_{\omega p} \nabla \langle p_{\gamma} \rangle^{\gamma}_{p} + \mu_{\gamma} \varepsilon_{\omega p} \nabla^{2} \langle \mathbf{v}_{\gamma} \rangle^{\gamma}_{p} - \mu_{\gamma} \varepsilon^{2}_{\omega p} \mathbf{K}^{-1}_{p} \cdot \langle \mathbf{v}_{\gamma} \rangle^{\gamma}_{p} \tag{2.100b}$$

$$\varepsilon_{\omega p} \frac{\partial \langle c_{A\gamma} \rangle^{\gamma}_{p}}{\partial t} + \nabla \cdot \left(\varepsilon_{\omega p} \langle \mathbf{v}_{\gamma} \rangle^{\gamma}_{p} \langle c_{A\gamma} \rangle^{\gamma}_{p} \right) = \nabla \cdot \left(\mathbf{D}^{*}_{p} \cdot \varepsilon_{\omega p} \nabla \langle c_{A\gamma} \rangle^{\gamma}_{p} \right) \tag{2.100c}$$

In this first approach, we assume the continuity conditions at all the boundaries for both mass and momentum equations.

$$at\ \mathscr{A}_{\omega\eta}\quad \mathbf{n}_{\omega\eta}\cdot\varepsilon_{\gamma\omega}\langle\mathbf{v}_\gamma\rangle_\omega^\gamma=\mathbf{n}_{\omega\eta}\cdot\langle\mathbf{v}_\gamma\rangle_\eta^\gamma \tag{2.101a}$$

$$at\ \mathscr{A}_{\omega\eta}\quad \varepsilon_{\gamma\omega}\mathbf{n}_{\omega\eta}\cdot\left(-\langle p_\gamma\rangle_\omega^\gamma\mathbf{I}+\nabla\langle\mathbf{v}_\gamma\rangle_\omega^\gamma\right)=\mathbf{n}_{\omega\eta}\cdot\left(-\langle p_\gamma\rangle_\eta^\gamma\mathbf{I}+\nabla\langle\mathbf{v}_\gamma\rangle_\eta^\gamma\right) \tag{2.101b}$$

$$at\ \mathscr{A}_{\omega\eta}\quad \varepsilon_{\gamma\omega}\langle c_{A\gamma}\rangle_\omega^\gamma=\langle c_{A\gamma}\rangle_\eta^\gamma \tag{2.101c}$$

$$at\ \mathscr{A}_{\omega\eta}\quad \mathbf{n}_{\omega\eta}\cdot\varepsilon_{\gamma\omega}\left(\langle\mathbf{v}_\gamma\rangle_\omega^\gamma\langle c_{A\gamma}\rangle_\omega^\gamma-\mathbf{D}_\omega^*\cdot\nabla\langle c_{A\gamma}\rangle_\omega^\gamma\right) \tag{2.101d}$$
$$=\mathbf{n}_{\omega\eta}\cdot\left(\langle\mathbf{v}_\gamma\rangle_\eta^\gamma\langle c_{A\gamma}\rangle_\eta^\gamma-\mathscr{D}_\gamma\nabla\langle c_{A\gamma}\rangle_\eta^\gamma\right)$$

$$at\ \mathscr{A}_{\omega p}\quad \mathbf{n}_{\omega p}\cdot\varepsilon_{\gamma\omega}\langle\mathbf{v}_\gamma\rangle_\omega^\gamma=\mathbf{n}_{\omega p}\cdot\varepsilon_{\omega p}\langle\mathbf{v}_\gamma\rangle_p^\gamma \tag{2.101e}$$

$$at\ \mathscr{A}_{\omega p}\quad \varepsilon_{\gamma\omega}\mathbf{n}_{\omega p}\cdot\left(-\langle p_\gamma\rangle_\omega^\gamma\mathbf{I}+\nabla\langle\mathbf{v}_\gamma\rangle_\omega^\gamma\right)=\varepsilon_{\omega p}\mathbf{n}_{\omega p}\cdot\left(-\langle p_\gamma\rangle_p^\gamma\mathbf{I}+\nabla\langle\mathbf{v}_\gamma\rangle_p^\gamma\right) \tag{2.101f}$$

$$at\ \mathscr{A}_{\omega p}\quad \varepsilon_{\gamma\omega}\langle c_{A\gamma}\rangle_\omega^\gamma=\varepsilon_{\omega p}\langle c_{A\gamma}\rangle_p^\gamma \tag{2.101g}$$

$$at\ \mathscr{A}_{\omega p}\quad \mathbf{n}_{\omega p}\cdot\varepsilon_{\gamma\omega}\left(\langle\mathbf{v}_\gamma\rangle_\omega^\gamma\langle c_{A\gamma}\rangle_\omega^\gamma-\mathbf{D}_\omega^*\cdot\nabla\langle c_{A\gamma}\rangle_\omega^\gamma\right) \tag{2.101h}$$
$$=\mathbf{n}_{\omega p}\cdot\varepsilon_{\omega p}\left(\langle\mathbf{v}_\gamma\rangle_p^\gamma\langle c_{A\gamma}\rangle_p^\gamma-\mathbf{D}_p^*\cdot\nabla\langle c_{A\gamma}\rangle_p^\gamma\right)$$

Let us denote the domain occupied by the active layer by $\mathscr{V}_\omega$, with norm V_ω.

8 DIMENSIONLESS EQUATIONS

For the fluid phase the dimensionless equation of mass and momentum are given

$$\frac{\partial\langle\mathbf{v}_\eta\rangle^{*\eta}}{\partial t^*}=-\nabla^*p_\eta^*+\frac{1}{Re}\nabla^{*2}\langle\mathbf{v}_\eta\rangle^{*\eta} \tag{2.102a}$$

$$\frac{\partial\langle c_{A\eta}\rangle^{\eta*}}{\partial t^*}+\nabla^*\left(\langle\mathbf{v}_\eta\rangle^{*\eta}\langle c_{A\eta}\rangle^{*\eta}\right)=\frac{1}{Pe}\nabla^{*2}\langle c_{A\eta}\rangle_\eta \tag{2.102b}$$

In the membrane active layer the dimensionless equations are also summarized

$$\frac{\partial\langle\mathbf{v}\rangle^*}{\partial t^*} \tag{2.103a}$$

9 MACROSCOPIC NUMERICAL SIMULATIONS

The objective of this section is to solve numerically the coupled equations of mass and momentum transfer in the membrane active layer and determine the profile of the velocity and concentration at both sides of the membrane. As previously stated, the membrane is composed of 3 layers notably active layer, intermediate layer and mechanical support. The particles however are mostly retained at the active layer surface. Thus the model provided the averaged equations of mass and momentum for this layer with the expression

of the effective permeability. One major difficulty is that the active layer's thickness (0.3-3 μm) is really small compared to other membrane layers (200 μm) and also the thickness of the bulk fluid above it (0.5 mm). Therefore the numerical simulations require a high number of meshes in the active layer and associated interfaces which can not be done due to the limitations of the numerical softwares. Thus it seems reasonable to replace the membrane active layer by a jump condition and solve simultaneously the equations in the fluid bulk phase and the membrane porous medium. For this purpose, first we express these equations with the corresponding jump condition in the membrane active layer and then we solve these equations numerically to obtain the profiles of the velocity and concentration in the bulk fluid and across the membrane.

9.1 THE MOMENTUM VOLUME AVERAGED EQUATIONS IN EACH PHASE

We begin our analysis with the mass and momentum conservation equations in the membrane active layer.

$$\nabla \cdot \varepsilon_{\gamma\omega} \langle \mathbf{v}_\gamma \rangle_\omega^\gamma = 0 \tag{2.104a}$$

$$\rho_\gamma \varepsilon_{\gamma\omega} \frac{\partial \langle \mathbf{v}_\gamma \rangle_\omega^\gamma}{\partial t} + \rho_\gamma \langle \mathbf{v}_\gamma \rangle_\omega^\gamma \frac{\mathrm{d}\varepsilon_{\gamma\omega}}{\mathrm{d}t} = -\varepsilon_{\gamma\omega} \nabla \langle p_\gamma \rangle_\omega^\gamma + \mu_\gamma \varepsilon_{\gamma\omega} \nabla^2 \langle \mathbf{v}_\gamma \rangle_\omega^\gamma - \mu_\gamma \varepsilon_{\gamma\omega}^2 \mathbf{K}_\omega^{-1} \cdot \langle \mathbf{v}_\gamma \rangle_\omega^\gamma \tag{2.104b}$$

Here we have used the subscript ω as a reminder that these expressions correspond to the active layer. In the homogenous fluid phase above the membrane surface the averaged equations of mass and momentum are also expressed

$$\nabla \cdot \langle \mathbf{v}_\gamma \rangle_\eta^\gamma = 0 \tag{2.105a}$$

$$\rho_\gamma \frac{\partial \langle \mathbf{v}_\gamma \rangle_\eta^\gamma}{\partial t} = -\nabla \langle p_\gamma \rangle_\eta^\gamma + \mu_\gamma \nabla^2 \langle \mathbf{v}_\gamma \rangle_\eta^\gamma \tag{2.105b}$$

Here we have used the subscript η as a reminder that these expressions correspond to the fluid medium.

Finally, below the active layer there is another porous medium, and the governing equations for transport are

$$\nabla \cdot \varepsilon_{\omega p} \langle \mathbf{v}_\gamma \rangle_p^\gamma = 0 \tag{2.106a}$$

$$\rho_\gamma \varepsilon_{\omega p} \frac{\partial \langle \mathbf{v}_\gamma \rangle_p^\gamma}{\partial t} = -\varepsilon_{\omega p} \nabla \langle p_\gamma \rangle_p^\gamma + \mu_\gamma \varepsilon_{\omega p} \nabla^2 \langle \mathbf{v}_\gamma \rangle_p^\gamma - \mu_\gamma \varepsilon_{\omega p}^2 \mathbf{K}_p^{-1} \cdot \langle \mathbf{v}_\gamma \rangle_p^\gamma \tag{2.106b}$$

In this first approach, we assume the continuity conditions at all the boundaries for both mass and momentum equations.

$$at \ \mathscr{A}_{\omega\eta} \quad \mathbf{n}_{\omega\eta} \cdot \varepsilon_{\gamma\omega} \langle \mathbf{v}_\gamma \rangle_\omega^\gamma = \mathbf{n}_{\omega\eta} \cdot \langle \mathbf{v}_\gamma \rangle_\eta^\gamma \tag{2.107a}$$

$$at \ \mathscr{A}_{\omega\eta} \quad \varepsilon_{\gamma\omega} \mathbf{n}_{\omega\eta} \cdot \left(-\langle p_\gamma \rangle_\omega^\gamma \mathbf{I} + \nabla \langle \mathbf{v}_\gamma \rangle_\omega^\gamma \right) = \mathbf{n}_{\omega\eta} \cdot \left(-\langle p_\gamma \rangle_\eta^\gamma \mathbf{I} + \nabla \langle \mathbf{v}_\gamma \rangle_\eta^\gamma \right) \tag{2.107b}$$

$$at \ \mathscr{A}_{\omega p} \quad \mathbf{n}_{\omega p} \cdot \varepsilon_{\gamma\omega} \langle \mathbf{v}_\gamma \rangle_\omega^\gamma = \mathbf{n}_{\omega p} \cdot \varepsilon_{\omega p} \langle \mathbf{v}_\gamma \rangle_p^\gamma \tag{2.107c}$$

$$at \ \mathscr{A}_{\omega p} \quad \varepsilon_{\gamma\omega} \mathbf{n}_{\omega p} \cdot \left(-\langle p_\gamma \rangle_\omega^\gamma \mathbf{I} + \nabla \langle \mathbf{v}_\gamma \rangle_\omega^\gamma \right) = \varepsilon_{\omega p} \mathbf{n}_{\omega p} \cdot \left(-\langle p_\gamma \rangle_p^\gamma \mathbf{I} + \nabla \langle \mathbf{v}_\gamma \rangle_p^\gamma \right) \tag{2.107d}$$

9.2 INTRINSIC AVERAGE EQUATIONS OF THE MOMENTUM TRANSPORT IN THE FLUID AND THE MEMBRANE

In the following steps we use the superficial velocity in equations because it is the quantity which is conserved in our system following the Darcy equation. Consequently, the equations for mass transport of species A are expressed in terms of superficial velocity and intrinsic concentration.

From now on we use the following notation for the simplicity

$$\langle p_\gamma \rangle_\alpha^\gamma = p_\alpha, \quad \langle \mathbf{v}_\gamma \rangle_\alpha^\gamma = \mathbf{v}_\alpha \quad \langle c_\gamma \rangle_\alpha^\gamma = c_\alpha \quad \text{with} \quad \alpha = \eta, \omega, p \tag{2.108}$$

Fluid phase (η)

$$\nabla \cdot \mathbf{v}_\eta = 0 \tag{2.109a}$$

$$\rho_\gamma \frac{\partial \mathbf{v}_\eta}{\partial t} = -\nabla p_\eta + \mu_\gamma \nabla^2 \mathbf{v}_\eta \tag{2.109b}$$

Active layer (ω)

$$\nabla \cdot \mathbf{v}_\omega = 0 \tag{2.110a}$$

$$\rho_\gamma \frac{\partial \mathbf{v}_\omega}{\partial t} = -\nabla p_\omega + \mu_\gamma \nabla^2 \mathbf{v}_\omega + \varepsilon_\omega \mu_\gamma \mathbf{K}_\omega^{-1} \cdot \mathbf{v}_\omega \tag{2.110b}$$

mechanical support (p)

$$\nabla \cdot \mathbf{v}_p = 0 \tag{2.111a}$$

$$\rho_\gamma \frac{\partial \mathbf{v}_p}{\partial t} = -\nabla p_p + \mu_\gamma \nabla^2 \mathbf{v}_p - \varepsilon_p \mu_\gamma \mathbf{K}_p^{-1} \cdot \mathbf{v}_p \tag{2.111b}$$

Boundary conditions

$$at \quad \mathscr{A}_{\omega\eta} \quad \mathbf{n}_{\omega\eta}\varepsilon_\omega \cdot \mathbf{v}_\omega = \mathbf{n}_{\omega\eta} \cdot \mathbf{v}_\eta \tag{2.112a}$$

$$at \quad \mathscr{A}_{\omega\eta} \quad \mathbf{n}_{\omega\eta} \cdot \varepsilon_\omega \left(p_\omega \mathbf{I} + \nabla \mathbf{v}_\omega\right) = \mathbf{n}_{\omega\eta} \cdot \left(p_\eta \mathbf{I} + \nabla \mathbf{v}_\eta\right) \tag{2.112b}$$

$$at \quad \mathscr{A}_{\omega p} \quad \mathbf{n}_{\omega p} \cdot \varepsilon_\omega \mathbf{v}_\omega = \mathbf{n}_{\omega p}\varepsilon_p \cdot \mathbf{v}_p \tag{2.112c}$$

$$at \quad \mathscr{A}_{\omega p} \quad \mathbf{n}_{\omega p} \cdot \varepsilon_\omega \left(p_\omega \mathbf{I} + \nabla \mathbf{v}_\omega\right) = \mathbf{n}_{\omega p} \cdot \varepsilon_p \left(p_p \mathbf{I} + \nabla \mathbf{v}_p\right) \tag{2.112d}$$

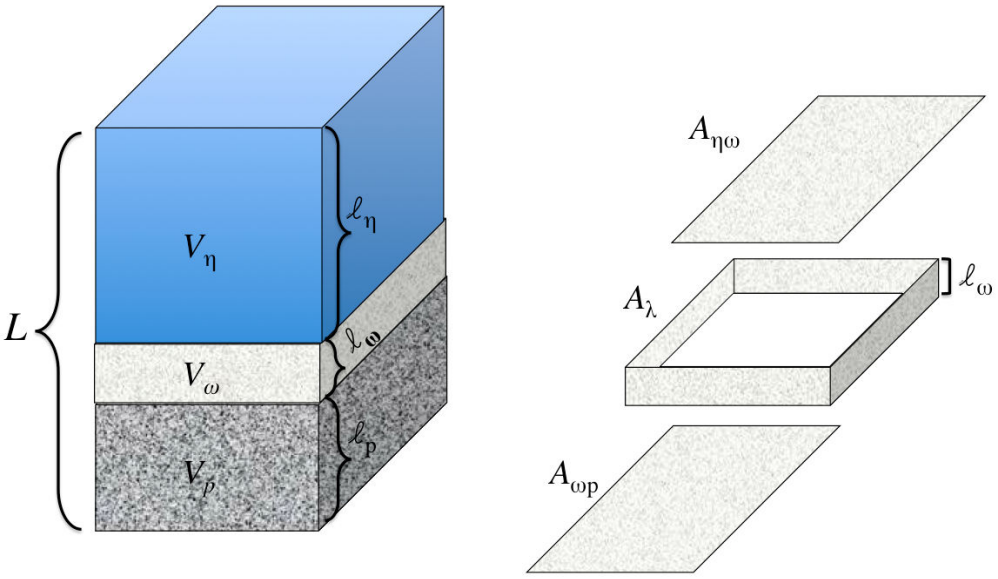

Figure 2.3: Representative three domains including fluid phase, membrane active layer and mechanical support with periodic conditions at the boundaries. The flow is in the y-direction and the velocity profile is uniform in this direction

The next step consists of replacing the membrane active layer by a jump condition which consists of replacing the equations involved for the active layer by a jump condition. Let us denote the domain occupied by the active layer by $\mathscr{V}_\omega$. We can define a global averaging operator as

$$\overline{\psi}_\omega = \frac{1}{\mathscr{V}_\omega} \int_{\mathscr{V}_\omega} \psi_\omega dV \tag{2.113}$$

Applying this operator to Eq. (2.110a), one will obtain

$$\int_{\mathscr{V}_\omega} \nabla \cdot \mathbf{v}_\omega dV = 0 \tag{2.114}$$

Using the divergence theorem, the above expressions transforms to

$$\int_{\mathscr{A}_\lambda} \mathbf{n}_\lambda \cdot \mathbf{v}_\omega \mathrm{d}A + \int_{\mathscr{A}_{\omega\eta}} \mathbf{n}_{\omega\eta} \cdot \mathbf{v}_\omega \mathrm{d}A + \int_{\mathscr{A}_{\omega p}} \mathbf{n}_{\omega p} \cdot \mathbf{v}_\omega \mathrm{d}A = 0 \tag{2.115}$$

From Fig. 2.3 we have that $\mathscr{A}_\lambda$ denotes the lateral surfaces of the domain. If we assume that, at the lateral faces, the velocity is null (in a periodic flow condition) and using the continuity of velocity fields at $\mathscr{A}_{\omega\eta}$ and $\mathscr{A}_{\omega p}$, we have

$$\int_{\mathscr{A}_{\omega\eta}} \mathbf{n}_{\omega\eta} \cdot \mathbf{v}_\eta \mathrm{d}A - \int_{\mathscr{A}_{\omega p}} \mathbf{n}_{p\omega} \cdot \varepsilon_p \mathbf{v}_p \mathrm{d}A = 0 \tag{2.116}$$

Since $\mathbf{n}_{\omega\eta} \equiv \mathbf{n}_{p\omega} \equiv \mathbf{n}_{p\eta}$ and $\mathscr{A}_{\omega\eta} \equiv \mathscr{A}_{\omega p} \equiv A_{\eta p}$, we can write on the dividing surface $A_{\eta p}$ that replaces $\mathscr{V}_\omega$

$$\int_{A_{\eta p}} \mathbf{n}_{p\eta} \cdot (\mathbf{v}_\eta - \varepsilon_p \mathbf{v}_p) \, \mathrm{d}A = 0 \tag{2.117}$$

In this way, we can deduce that

$$\mathbf{n}_{p\eta} \cdot (\mathbf{v}_\eta - \varepsilon_p \mathbf{v}_p) = 0 \quad \text{at } A_{\eta p} \tag{2.118}$$

Applying the averaging operator to the momentum equation in the active layer Eq. (2.110b)

$$\rho_\gamma \frac{\mathrm{d}\overline{\mathbf{v}}_\omega}{\mathrm{d}t} = \frac{1}{\mathscr{V}_\omega} \int_{\mathscr{A}_{\omega\eta}+\mathscr{A}_{\omega p}} \mathbf{n} \cdot (-p_\omega \mathbf{I} + \mu_\gamma \nabla \mathbf{v}_\omega) \, \mathrm{d}A - \mu_\gamma \mathbf{K}_\omega^{-1} \cdot \varepsilon_\omega \overline{\mathbf{v}}_\omega \tag{2.119}$$

Here we have neglected stress contributions at the lateral faces with respect to the stress from the upper and lower boundaries. With the continuity of velocity at both $\omega\eta$ and ωp boundaries, we can write

$$\overline{\mathbf{v}}_\omega = \frac{1}{\mathscr{V}_\omega} \int_{\mathscr{V}_\omega} \mathbf{v}_\omega dV = \frac{1}{\mathscr{V}_\omega} \int_{A_{p\eta}} \ell_\omega \mathbf{v}_p dA \quad \left(= \frac{1}{\mathscr{V}_\omega} \int_{A_{p\eta}} \ell_\omega \mathbf{v}_\eta dA \right) \tag{2.120}$$

The stress term can be expressed in terms of the boundary conditions

$$\begin{aligned}
&\int_{\mathscr{A}_{\omega\eta}+\mathscr{A}_{\omega p}} \mathbf{n}\cdot\varepsilon_\omega\left(-p_\omega\mathbf{I}+\mu_\gamma\nabla\mathbf{v}_\omega\right)\mathrm{d}A \\
&\quad=\int_{\mathscr{A}_{\omega\eta}} \mathbf{n}_{\omega\eta}\cdot\varepsilon_\omega\left(-p_\omega\mathbf{I}+\mu_\gamma\nabla\mathbf{v}_\omega\right)\mathrm{d}A+\int_{\mathscr{A}_{\omega p}} \mathbf{n}_{\omega p}\varepsilon_\omega\cdot\left(-p_\omega\mathbf{I}+\mu_\gamma\nabla\mathbf{v}_\omega\right)\mathrm{d}A \\
&\quad=\int_{\mathscr{A}_{\omega\eta}} \mathbf{n}_{\omega\eta}\cdot\left(-p_\eta\mathbf{I}+\mu_\gamma\nabla\mathbf{v}_\eta\right)\mathrm{d}A+\int_{\mathscr{A}_{\omega p}} \mathbf{n}_{\omega p}\cdot\varepsilon_p\left(-p_p\mathbf{I}+\mu_\gamma\nabla\mathbf{v}_p\right)\mathrm{d}A \\
&\quad=\int_{A_{p\eta}} \mathbf{n}_{p\eta}\cdot\left[\left(-p_\eta\mathbf{I}+\mu_\gamma\nabla\mathbf{v}_\eta\right)-\varepsilon_p\left(-p_p\mathbf{I}+\mu_\gamma\nabla\mathbf{v}_p\right)\right]dA
\end{aligned} \tag{2.121}$$

In this way, Eq. (2.119) takes the form

$$\int_{\mathscr{A}_{\eta p}}\left[\rho_\gamma\ell_\omega\frac{\partial\left(\varepsilon_p\mathbf{v}_p\right)}{\partial t}-\mathbf{n}_{p\eta}\cdot\left[\left(-p_\eta\mathbf{I}+\mu_\gamma\nabla\mathbf{v}_\eta\right)-\varepsilon_p\left(-p_p\mathbf{I}+\mu_\gamma\nabla\mathbf{v}_p\right)\right]+\mu_\gamma\mathbf{K}_\omega^{-1}\cdot\varepsilon_\omega\varepsilon_p\ell_\omega\mathbf{v}_p\right]\mathrm{d}A=0 \tag{2.122}$$

Notice that all the terms that are not related to the stress are multiplied by the width of the ω-region. Considering the minute thickness of this region (active layer), all these terms become negligible compared to the stress except for the last term in the right hand (permeability). It is worth to mention that when the permeability of the active layer increases, the jump condition may lead to the continuity of stress.
Now we can summarize the conditions of the dividing surface (replacing the active layer) associated with the momentum equaltion at the interface $\eta-p$.

$$at\ \ \mathscr{A}_{p\eta},\quad \mathbf{v}_\eta=\varepsilon_p\mathbf{v}_p \tag{2.123a}$$

$$at\ \ \mathscr{A}_{p\eta},\quad \rho_\gamma\delta\frac{\partial\left(\varepsilon_p\mathbf{v}_p\right)}{\partial t}=\mathbf{n}_{p\eta}\cdot\left[\left(-p_\eta\mathbf{I}+\mu_\gamma\nabla\mathbf{v}_\eta\right)-\varepsilon_p\left(-p_p\mathbf{I}+\mu_\gamma\nabla\mathbf{v}_p\right)\right]-\mu_\gamma\mathbf{K}_\omega^{-1}\varepsilon_\omega\ell_\omega\varepsilon_p\cdot\mathbf{v}_p \tag{2.123b}$$

9.3 INTRINSIC AVERAGED EQUATIONS OF TRANSPORT FOR CHEMICAL SPECIES IN EACH PHASE

For the transport of chemical species (species A), the corresponding upscaled intrinsic equations in each domain are listed with respect to the simple notations described in the previous section

In the fluid phase $-\eta$

$$\frac{\partial c_{A\eta}}{\partial t}+\nabla\cdot\left(\mathbf{v}_\eta c_{A\eta}\right)=\nabla\cdot\left(\mathscr{D}_\gamma\nabla c_{A\eta}\right) \tag{2.124}$$

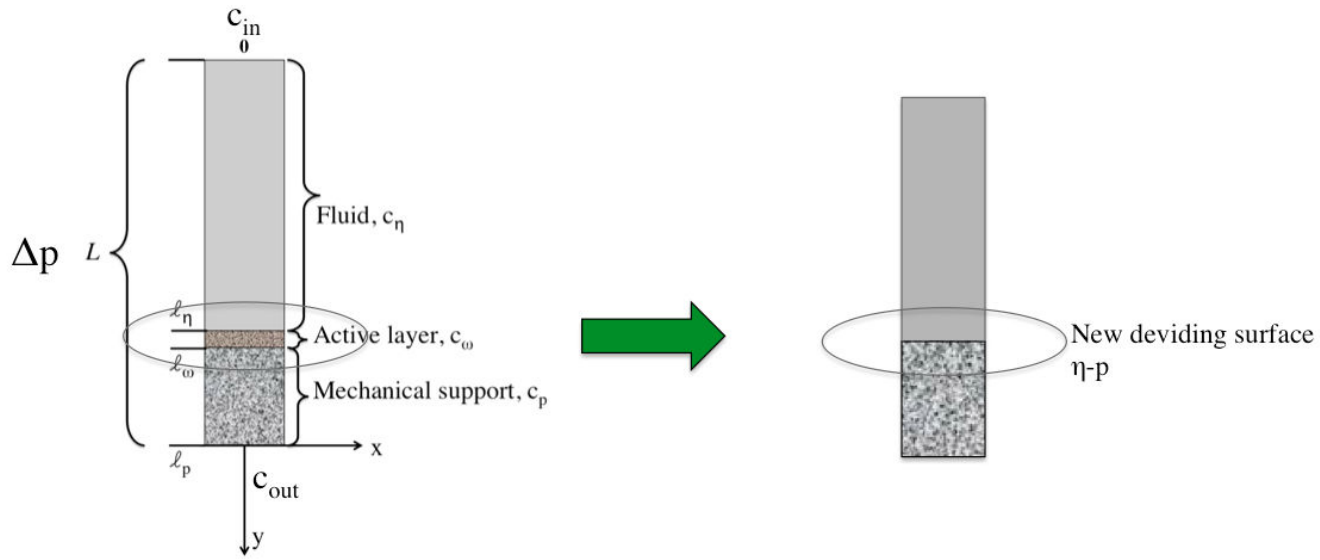

Figure 2.4: Demonstration of a 3 domain system (fluid-active layer-porous membrane) and a 2 domain system (fluid-porous membrane) with a new deciding surface replacing the membrane active layer

In the active layer $-\ \omega$

$$(1+\varepsilon_\omega^{-1}a_\omega f'_\omega(c_{A\omega}))\frac{\partial c_{A\omega}}{\partial t}+\varepsilon_\omega^{-1}f_\omega(c_{A\omega})\frac{\mathrm{d}a_\omega}{\mathrm{d}t}+\nabla\cdot(\mathbf{v}_\omega c_{A\omega})=\nabla\cdot(\mathbf{D}^*_\omega\cdot\nabla c_{A\omega}) \quad (2.125)$$

In the mechanical support $-\ p$

$$\frac{\partial c_{Ap}}{\partial t}+\nabla\cdot(\mathbf{v}_p c_{Ap})=\nabla\cdot\left(\mathbf{D}^*_p\cdot\nabla c_{Ap}\right) \quad (2.126)$$

It is worth to mention that the effective diffusivity (in the absence of dispersion) in the membrane active layer and mechanical support are calculated by the Maxwell equation in function of porosity.

$$\frac{\mathbf{D}^*_\alpha}{\mathscr{D}_\gamma}=\frac{2}{3-\varepsilon_\gamma} \quad (2.127)$$

We can also assume continuity at the boundary conditions as the first approach. Therefore

we have

$$at \ \mathscr{A}_{\omega\eta} \quad c_{A\omega} = c_{A\eta} \tag{2.128a}$$
$$at \ \mathscr{A}_{\omega\eta} \quad \mathbf{n}_{\omega\eta} \cdot \varepsilon_\omega \left(\mathbf{v}_\omega c_{A\omega} - \mathbf{D}^*_\omega \cdot \nabla c_{A\omega}\right) = \mathbf{n}_{\omega\eta} \cdot \left(\mathbf{v}_\eta c_{A\eta} - \mathscr{D}_\gamma \nabla c_{A\eta}\right) \tag{2.128b}$$
$$at \ \mathscr{A}_{\omega p} \quad c_{A\omega} = c_{Ap} \tag{2.128c}$$
$$at \ \mathscr{A}_{\omega p} \quad \mathbf{n}_{\omega p} \cdot \varepsilon_\omega \left(\mathbf{v}_\omega c_{A\omega} - \mathbf{D}^*_\omega \cdot \nabla c_{A\omega}\right) = \mathbf{n}_{\omega p} \cdot \varepsilon_p \left(\mathbf{v}_p c_{Ap} - \mathbf{D}^*_p \cdot \nabla c_{Ap}\right) \tag{2.128d}$$

Finally, let us apply the averaging operator to Eq. (2.125) (transport of chemical species in the active layer), the result is

$$\left(\varepsilon_\omega + a_\omega \overline{f'}_\omega\right) \frac{\mathrm{d}\overline{c}_{A\omega}}{\mathrm{d}t} + \overline{f}_\omega \frac{\mathrm{d}a_\omega}{\mathrm{d}t} + \frac{1}{\mathscr{V}_\omega} \int\limits_{\mathscr{A}_\omega} \mathbf{n}_\omega \cdot \varepsilon_\omega \left(\mathbf{v}_\omega c_{A\omega} - \mathbf{D}^*_\omega \cdot \nabla c_{A\omega}\right) dA = 0 \tag{2.129}$$

Where

$$\overline{f}_\omega = f_\omega(\overline{c}_{A\omega}), \quad \text{and} \overline{f'}_\omega = f'_\omega(\overline{c}_{A\omega}) \tag{2.130}$$

The overall flux in the ω region can be written as a sum at the $\omega - \eta$ and $\omega - p$ interfaces which gives rise to

$$\begin{aligned}
&\int\limits_{\mathscr{A}_{\omega\eta}+\mathscr{A}_{\omega p}} \mathbf{n}_\omega \cdot \varepsilon_\omega \left(\mathbf{v}_\omega c_{A\omega} - \mathbf{D}^*_\omega \cdot \nabla c_{A\omega}\right) dA \\
&= \int\limits_{\mathscr{A}_{\omega\eta}} \mathbf{n}_{\omega\eta} \cdot \varepsilon_\omega \left(\mathbf{v}_\omega c_{A\omega} - \mathbf{D}^*_\omega \cdot \nabla c_{A\omega}\right) dA + \int\limits_{\mathscr{A}_{\omega p}} \mathbf{n}_{\omega p} \cdot \varepsilon_\omega \left(\mathbf{v}_\omega c_{A\omega} - \mathbf{D}^*_\omega \cdot \nabla c_{A\omega}\right) dA \\
&= \int\limits_{\mathscr{A}_{\omega\eta}} \mathbf{n}_{\omega\eta} \cdot \left(\mathbf{v}_\eta c_{A\eta} - \mathscr{D}_\gamma \nabla c_{A\eta}\right) dA + \int\limits_{\mathscr{A}_{\omega p}} \mathbf{n}_{\omega p} \cdot \varepsilon_p \left(\mathbf{v}_p c_{Ap} - \mathbf{D}^*_p \cdot \nabla c_{Ap}\right) dA \\
&\equiv \int\limits_{\mathscr{A}_{p\eta}} \mathbf{n}_{p\eta} \cdot \left[\mathbf{v}_\eta c_{A\eta} - \mathscr{D}_\gamma \nabla c_{A\eta} - \varepsilon_p \left(\mathbf{v}_p c_{Ap} - \mathbf{D}^*_p \cdot \nabla c_{Ap}\right)\right] dA
\end{aligned} \tag{2.131}$$

Furthermore, we now propose the following identity

$$\int\limits_{\mathscr{V}_\omega} c_{A\omega} dV \equiv \int\limits_{\mathscr{A}_{p\eta}} \ell_\omega \; c_{A\omega}|_{p\eta} \, dA \tag{2.132}$$

which seems reasonable based on the separation of characteristic lengths of the system $\delta \ll L_\eta, L_p$; with L_α ($\alpha = \eta, p$) being the characteristic length associated to the α-region. At this state it should be pointed out that with this assumption the ω inter region does not exist anymore and as a result all the information of the velocity and concentration profiles in this region are eliminated. Furthermore, on the basis of the continuity of the concentration fields we have $c_{A\omega}|_{p\eta} = c_{Ap} = c_{A\eta}$. If one accepts the above identities, one

may rewrite Eq. (2.129) as

$$\int_{\mathscr{A}_{p\eta}} \varepsilon_p \left[1+\varepsilon_\omega^{-1} a_\omega \overline{f'}_\omega\right] \ell_\omega \frac{\partial \overline{c}_{Ap}}{\partial t} + \ell_\omega \overline{f}_\omega \frac{\mathrm{d}a_\omega}{\mathrm{d}t} + \mathbf{n}_{p\eta} \cdot \left[\mathbf{v}_\eta c_{A\eta} - \mathscr{D}_\gamma \nabla c_{A\eta} - \varepsilon_p \left(\mathbf{v}_p c_{Ap} - \mathbf{D}_p^* \cdot \nabla c_{Ap}\right)\right] dA = 0 \quad (2.133)$$

From which, we can extract the following boundary condition

$$\begin{aligned} at \;\; \mathscr{A}_{p\eta} \quad & \varepsilon_p \left[1+\varepsilon_\omega^{-1} a_\omega \overline{f'}_\omega\right] \ell_\omega \frac{\partial c_p}{\partial t} + \ell_\omega \overline{f}_\omega \frac{\mathrm{d}a_\omega}{\mathrm{d}t} \\ & = -\mathbf{n}_{p\eta} \cdot \left[\left(\mathbf{v}_\eta c_{A\eta} - \mathscr{D}_\gamma \nabla c_{A\eta}\right) - \varepsilon_p \left(\mathbf{v}_p c_{Ap} - \mathbf{D}_p^* \cdot \nabla c_{Ap}\right)\right] \end{aligned} \quad (2.134)$$

As the first approach, we can also impose the continuity of the intrinsic concentration fields at the interface. Likewise the jump condition for the stress tensor at the interface, all terms for the flux jump condition are multiplied by the thickness of the active layer. This way we may suppose for the moderate rates of the adsorption phenomenan, we will have the continuity of total flux at the dividing $\eta - p$ surface.

$$at \;\; \mathscr{A}_{p\eta} \quad c_{Ap} = c_{A\eta} \quad (2.135)$$

With the aim of providing a qualitative insight of the macroscopic transport, we solved the model consisting of eqs. (2.105) and (2.106); which are coupled by eqs. (2.134), (2.135). As a first approach we solved this model in a thin 2D portion of the system while the filtration flow is only on the y direction. The dimensions of this simplified system are the following: width = 50μm, height = 700 μm, of which the porous medium has a height of 200 μm. The physical properties of the L-Glutathione (diffusivity, density) are used in the first calculations and the corresponding linear adsorption coefficient for this species were used from experimental characterization. A very thin active layer (1μ m) is taken in the Eq. (2.133). The fluid is fed from the top of the system and it leaves it at the bottom. The objective of these simulations is to show how the use of jump conditions allow us to observe the drastic changes in the concentration and velocity fields due to the active layer.

Assuming that this portion of the system is taken in a position that is not influenced by the inlets and exits phenomena, one can assume fully developed transport conditions. This allows us to impose periodic boundary conditions at the horizontal inlets and outlets (see blue lines in Fig. 2.5).

Furthermore, at the top of the system (say at $y = H$) we imposed the following boundary conditions:

$$at \;\; y = H, \quad c_{A\eta} = c_{in}; p_\eta = p_{in} \quad (2.136)$$

where c_{in} and p_{in} are known constants. As a matter of convenience, let us define a di-

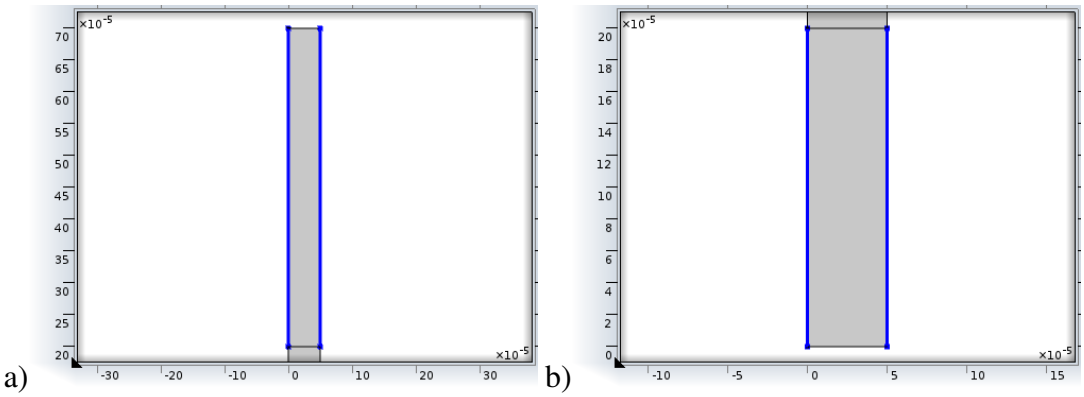

Figure 2.5: Horizontal inlets and outlets of the system in a) the fluid region and b) in porous medium region.

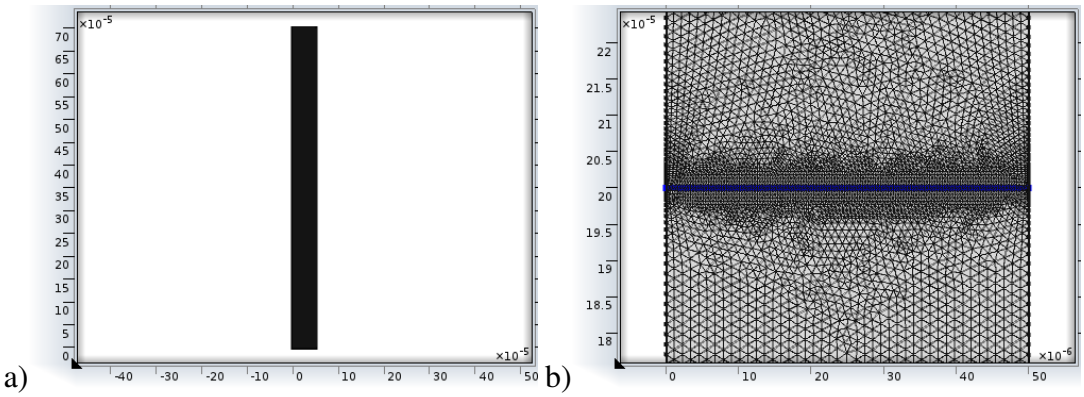

Figure 2.6: a) Example of the system concentration field in the y direction and b) zoom at the fluid-porous medium boundary.

mensionless concentration as

$$C_\alpha = \frac{c_{A\alpha}}{c_{in}}, \quad \alpha = \eta, p \tag{2.137}$$

in addition, we took $p_{in} = 2$ bar in our simulations. Finally, at the vertical outlet (say $y = 0$) we impose the following boundary conditions

$$at \;\; y = 0, \quad \mathbf{D}_p^* \mathbf{n} \cdot \nabla c_p = k(c_p - c_\infty); p = p_{out} \tag{2.138}$$

with $p_{out} = 1$ bar. In this way, flow is vertically enforced in the system because of a pressure difference of 1 bar. Here k is the mass transfer coefficient which is null if we assume the fully developed transport conditions.

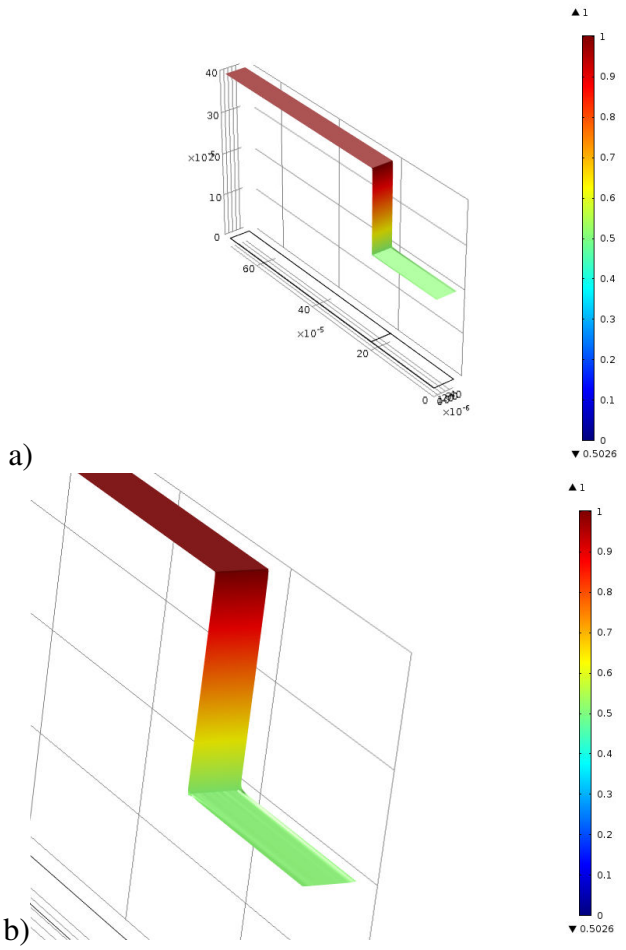

Figure 2.7: a) Example of the system fields and b) zoom at the fluid-porous medium boundary.

9.4 NUMERICAL RESULTS AND DISCUSSION

The simulations are run in Comsol 4.3.b using the coupled creeping flow and transport for diluted species modules. We chose an extremely fine mesh with a special refinement at the fluid-porous medium boundary (see Fig. 2.6).Complete mesh consists of 52378 domain elements and 1288 boundary elements. The approximate calculation time is about 10 minutes. With these results we obtained velocity and concentration profiles in the system. We verified that the volumetric flow rate is the same in the fluid and the porous medium by noting that the superficial average velocity value was the same in both sides. In Fig. 2.7 we show an example of the profile of the macroscopic concentration. It should be pointed out that the concentration decreases quite drastically near the fluid-porous medium boundary, thus illustrating the importance of the transport phenomena at the dividing surface.

The macroscopic concentration field has been evaluated for different values of the fil-

tration velocity and the results are shown in fig.**??**. The filtration velocity affects significantly the concentration jump at the fluid-porous interface. For low values of the filtration velocity (Pe$\ll$ 100) , the characteristic times of diffusion and convection phenomena are close enough and therefore particles can diffuse both in the fluid phase and the porous membrane; Thus the concentration differences between fluid and porous medium are quite moderate whereas for high values of the velocity (Pe$\gg$100), the convective velocity of particles becomes the more important and therefore more drastic changes in the concentration fields is observed.

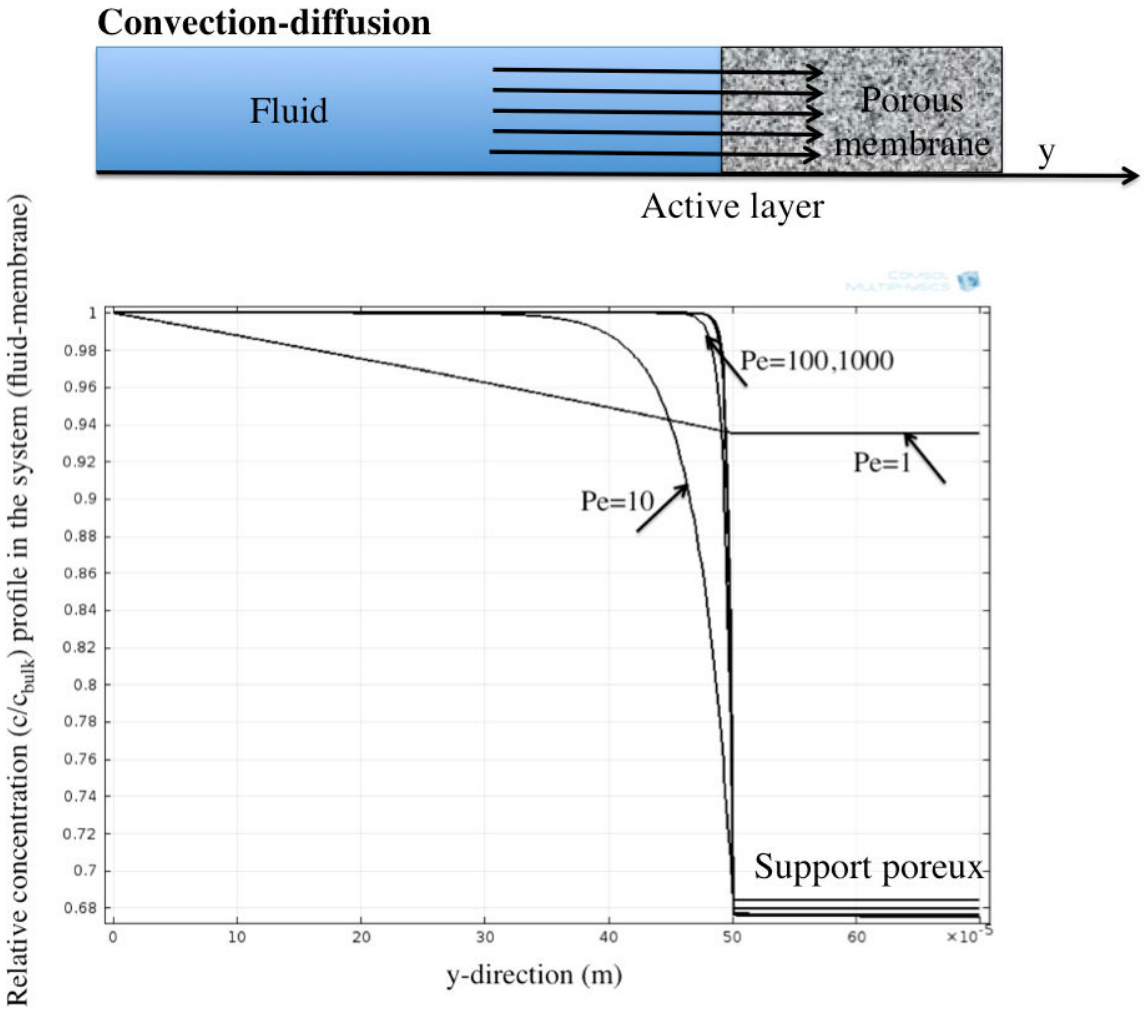

Figure 2.8: Parametric study of the concentration field in the fluid and through the membrane corresponding to different values of the filtration velocity

9.5 NEW CONCENTRATION JUMP CONDITION IN A STATIONARY STATE SYSTEM

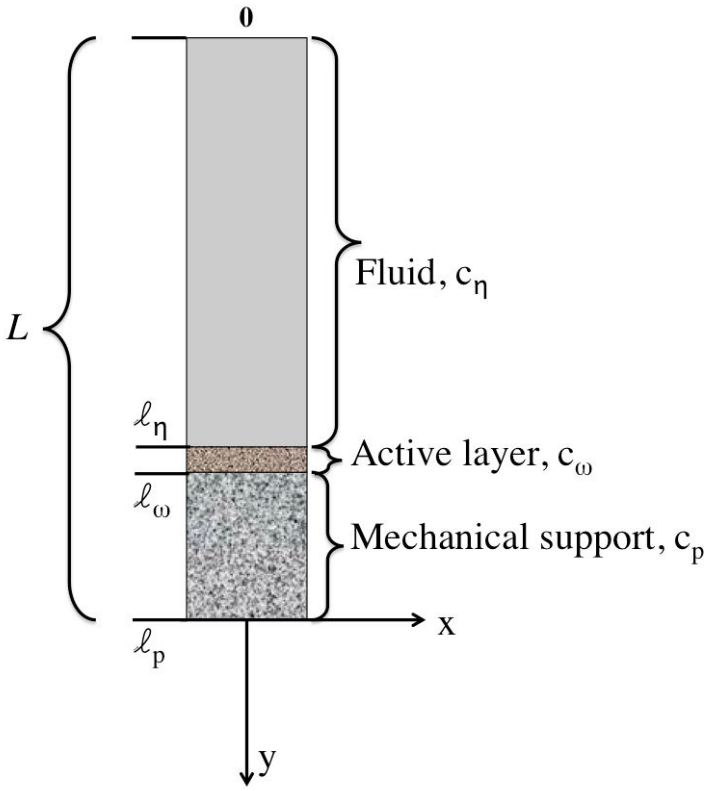

Figure 2.9: Representative three domains including fluid phase membrane active layer and mechanical support. The flow is in the y-direction and the velocity profile is uniform in this direction

The objective of this section is to determine the jump condition for the concentration field at the stationary state conditions for active layer. This way the transport equation of the species A in this layer can be written as the sum of convection and diffusion. This can be interesting since the concentration difference between the fluid phase and the membrane porous medium due to adsorption at the membrane active layer can be calculated, thus we are not obliged to assume the continuity of concentration fields at the interfaces. First let us calculate the experimental characteristic time for each phenomenon in each layer.The mass transport governing equations in each domain are given.
Here we recall that the superficial velocity field $\mathbf{V} = \mathbf{v}_\eta = \varepsilon_\omega \mathbf{v}_\omega = \varepsilon_p \mathbf{v}_p$, is conserved in the global system.
In the fluid phase

With $\mathscr{D}_\gamma \approx 10^{-11} - 10^{-10}$ m^2/s

$$\tau_{\text{diff}} = \frac{\ell_\eta^2}{\mathscr{D}_\gamma} \approx 500 - 5000\text{s} \tag{2.139a}$$

$$\tau_{\text{conv}} = \frac{\ell_\eta}{\mathbf{v}_\eta} \approx 0.07\text{s} \tag{2.139b}$$

$$\text{Pe}_\eta = \frac{\ell_\eta \mathbf{v}_\eta}{\mathscr{D}_\gamma} = \frac{\tau_{\text{diff}}}{\tau_{\text{conv}}} = 7 \times 10^3 \tag{2.139c}$$

In the membrane active layer

$$\tau_{\text{diff}} = \frac{\ell_\omega^2}{\varepsilon_\omega \mathbf{D}_\omega^*} \approx 0.03\text{s} \tag{2.140a}$$

$$\tau_{\text{conv}} = \frac{\ell_\omega}{\mathbf{v}_\omega} \approx 0.001\text{s} \tag{2.140b}$$

$$\text{Pe}_\omega = \frac{\ell_\omega \mathbf{v}_\omega}{\mathbf{D}_\omega^*} = \frac{\tau_{\text{diff}}}{\tau_{\text{conv}}} = 30 \tag{2.140c}$$

In the mechanical support

$$\tau_{\text{diff}} = \frac{\ell_p^2}{\varepsilon_p \mathbf{D}_\mathbf{p}^*} \approx 150\text{s} \tag{2.141a}$$

$$\tau_{\text{conv}} = \frac{\ell_\omega}{\mathbf{v}_p} \approx 0.03\text{s} \tag{2.141b}$$

$$\text{Pe}_p = \frac{\ell_p \mathbf{v}_p}{\mathbf{D}_p^*} = \frac{\tau_{\text{diff}}}{\tau_{\text{conv}}} = 5000 \tag{2.141c}$$

Comparing the order of magnitudes of the Peclet numbers in all three regions, one can conclude that the transport phenomena in the active layer ω would be quickly attain the stationary state compared to the other regions. With this assumption the equations for mass transport in the membrane active layer can be expressed as

$$\nabla \cdot (\mathbf{v}_\omega c_{A\omega}) = \nabla \cdot \mathbf{D}_\omega^* \cdot \nabla c_{A\omega} \tag{2.142}$$

Moreover if we assume that the transport phenomena is in only one direction (y), then one can write

$$\mathbf{v}_\omega(y) X = \mathbf{D}_\omega^* \frac{\text{d}X}{\text{dy}} \quad \text{with} \quad X = \frac{\text{d}c_\omega}{\text{dy}} \quad \text{and} \quad \mathbf{v}_\omega(y) = -v_0 = cst \tag{2.143}$$

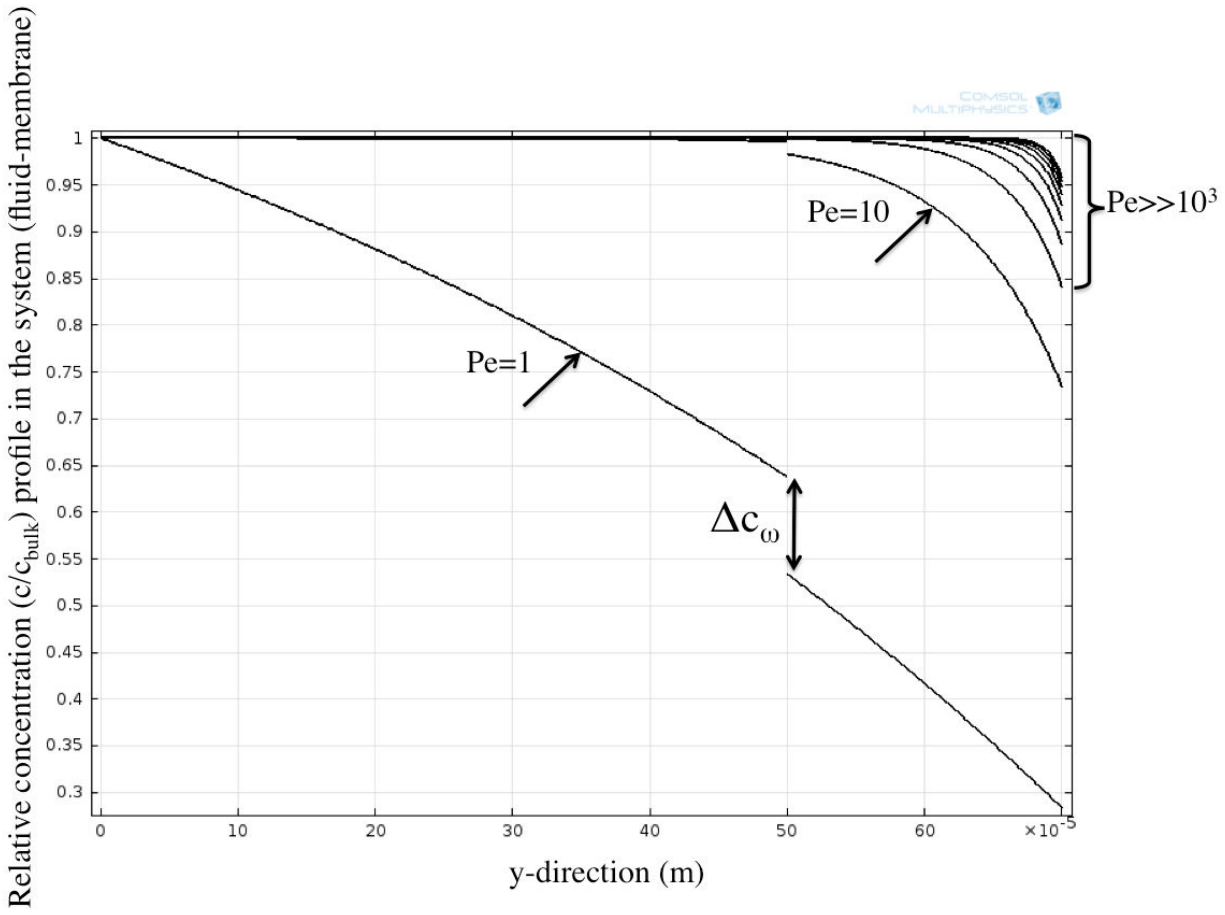

Figure 2.10: Concentration difference in the fluid and porous medium region for different values of Pe numbers.

Eq. (2.143) can be analytically solved

$$X_\omega(\mathrm{y}) = X_\omega(0)\exp\left(\frac{-v_0}{\mathbf{D}^*_\omega}\mathrm{y}\right) \tag{2.144}$$

$$c_\omega(\mathrm{y}) = c_\omega(0) - X_\omega(0)\frac{\mathbf{D}^*_\omega}{v_0}\left[\exp\left(\frac{-v_0}{\mathbf{D}^*_\omega}\mathrm{y}\right) - 1\right] \tag{2.145}$$

and then

$$\frac{c_\omega(\mathrm{y}) - c_\omega(0)}{c_\omega(\ell_\omega) - c_\omega(0)} = \frac{\exp\left(-\frac{v_0\mathrm{y}}{\mathbf{D}^*_\omega}\right) - 1}{\exp\left(-\frac{v_0\ell_\omega}{\mathbf{D}^*_\omega}\right) - 1} = \frac{1 - \exp\left(\text{-Pe}_\omega\frac{\mathrm{y}}{\ell_\omega}\right)}{1 - \exp\left(\text{-Pe}_\omega\right)} \tag{2.146}$$

Assuming the stationary state in the ω region, the flux passing through any cross section of the ω-region in the increasing $\mathbf{y}$ direction will be conserved which gives rise to

$$\phi_\omega = \mathbf{y}\cdot\varepsilon_\omega\left(\mathbf{D}^*_\omega\nabla c_\omega + \mathbf{v}_y c_\omega\right)(0) = \mathbf{y}\cdot\varepsilon_\omega\left(-\mathbf{D}^*_\omega\nabla c_\omega + \mathbf{v}_y c_\omega\right)(\ell_\omega) \tag{2.147}$$

ϕ_ω is given by

$$\begin{aligned}\phi_\omega &= -\varepsilon_\omega\left(\mathbf{D}^*_\omega\frac{\mathrm{d}c_\omega}{\mathrm{dy}}(0) + \mathbf{v}_y c_\omega(0)\right)\\ &= -\varepsilon_\omega\left(\mathbf{D}^*_\omega X_\omega(0) - v_0 c_\omega(0)\right)\\ &= \frac{\left[c_\omega(0) - c_\omega(\ell_\omega)\right]v_0}{1-\exp\left(-\mathrm{Pe}_\omega\right)} - v_0 c_\omega(0)\end{aligned} \tag{2.148}$$

To summarize at the new dividing surface $\eta - p$, we will have the continuity of the total flux and a jump condition for the concentration field.

$$\begin{aligned}&-\mathbf{n}\cdot\left(-\mathscr{D}_\gamma\nabla c_\eta + v_0 c_\eta\right) = -\varepsilon_p\mathbf{n}\cdot\left(-\mathbf{D}^*_p\nabla c_p + v_0 c_p\right)\\ &c_p - c_\eta = \left[\frac{\ell_\omega}{\mathbf{D}^*_\omega}\phi + \mathrm{Pe}_\omega c_p\right]\left[\frac{1-\exp\left(-\mathrm{Pe}_\omega\right)}{\left(\mathrm{Pe}_\omega\right)}\right] = \frac{\ell_\omega}{\mathbf{D}^*_\omega}\left[\frac{1-\exp\left(-\mathrm{Pe}_\omega\right)}{\left(\mathrm{Pe}_\omega\right)}\right]\end{aligned} \tag{2.149}$$

And ϕ is the convective-diffusive flux passing through the $\eta - p$ interface in the $p - \eta$ direction

$$\phi = -\varepsilon_p\mathbf{n}_{p\eta}\cdot\left(\mathbf{D}^*_p\nabla c_p + \mathbf{v}_p c_p\right) = \mathbf{n}_{p\eta}\cdot\left(-\mathscr{D}_\gamma\nabla c_\eta + \mathbf{v}_\eta c_\eta\right) \tag{2.150}$$

This new jump condition imposes the continuity of the fluxes and jump in the concentration fields at the new $\eta - p$ dividing surface which can only be assumed in a stationary state situation in the membrane active layer whilst the governing equations in the fluid phase and membrane porous support may remain time dependent. The main advantage of this new jump condition is that the concentration difference between fluid and support porous medium is directly related to the mass transfer phenomena in the active layer. The jump in the concentration is due to mass transfer in the membrane active layer. The results of this new jump condition are presented in Fig. 2.10. The analytical expression of the concentration difference in the fluid phase and porous medium is given in Eq. (2.149). The results proved that for low Peclet numbers, the concentration jump is only due to the diffusion in the active layer ($\frac{\ell_\omega}{\mathbf{D}^*_\omega}$). However for considerable values of Peclet number ($\gg 10^3$), the right hand term in equation (2.149) becomes null and thus the concentration filed remains continuous.

10 CONCLUSIONS AND DISCUSSION

During the filtration process of protein solutions through the membranes, adsorption to the membrane interface is one of the fouling mechanisms leading to membrane pore

size reduction and consequent permeate flux decline. Different studies have shown that the protein adsorption to the membrane inner pores affects the membrane performance irreversibly[7],[132], [149],[162],[207].

The objective of this chapter was to develop an upscaled model for description of protein adsorption during a filtration process. Experiments confirmed that membrane is composed of three layers. It should be pointed out that in reality, proteins may transport and adsorb in all membrane layers, However, we have assumed that the variations of permeabilities in membrane layers due to protein adsorption are negligible except for the membrane active layer.Thus, in the first study, we only developed a model of protein adsorption in a very thin active layer of the membrane. An original averaged description of the membrane structure was described. Instead of determination the additional resistances in terms of observed mechanisms, we derived the evolution of the membrane structure with time. Convection and diffusion were taken into account as local transport phenomena. Adsorption is the result of mass transport between membrane and the fluid phase and it represented the interfacial phenomenon. The volume averaging method is used for deriving the upscaled equations from their local counterparts.The simplifications of different terms (with contribution on pore-scale and membrane-scale transport mechanisms) were based on estimation of order of magnitudes or length-scale constraints (e.g. interfacial velocity due to adsorption was neglected compared to average velocity field [29]). A classical closure problem for the momentum transport has been identified whereas the closure problem for the mass conservation equation included two source terms (due to diffusion and adsorption).The upscaled closed set of equations in the fluid phase consist of the averaged continuity equation, non-stationary Stokes equation for momentum transport, the direct expression of its porosity in function of adsorption rate and averaged mass conservation equation for proteins. The accumulation term in the upscaled mass conservation equation is modified and includes the adsorption phenomenon at the interface. Compared to the classical models [255], the upscaled equations of mass and momentum transport both represented explicit expressions of porous structural evolution with time.

Experiments are directly coupled with the model development at two levels: the pore scale experiments are done to characterize the membrane structure and proteins adsorption isotherms. The local diffusivity of the proteins is also needed as initial data and is taken from literature. The microfiltration experiments confirmed that protein adsorption is a complicated phenomenon in which different parameters (solution chemistry, membrane properties, operational conditions) play important roles. The effect of these parameters are not involved in the proposed model and can be subject of future study. It is with to mention that the electrostatic interactions between particles and the membrane surface could be taken into account by adding some source terms in the local equations of the mass transport. In the work of [258] the Smoluchowski has been used to understand the effect of these interactions on the mass transport phenomena. However the experimental characterization of these interactions remains challenging both at local and macroscopic scales.

Since the closure problems for both mass and momentum transport equations were classical, we have used the expression of the effective diffusivity (Maxwell) and permeability (Kozeny-carman) to determine these effective properties in the membrane active layer and support porous structure.
Consequently the macroscopic numerical simulations were run to validate the system performance qualitatively. The membrane active layer was replaced with a (virtual) dividing surface between bulk fluid and the support porous medium. Here we recall that the jump conditions were assumed only to overcome the numerical difficulties related to the small characteristic length of the membrane active layer. Two cases have been studied: In the first study, a jump condition for the mass flux was imposed which was due to the adsorption in the active layer of the membrane, however the continuity of the intrinsic concentrations in the bulk fluid and the membrane porous medium was assumed. In the second study, a jump condition for the concentration fields and a condition of the continuity of the mass flux was supposed. This second condition could be applied only if the transport phenomenon in the active layer would attain the stationary state. Another study which contains a jump condition both for the concentration fields and mass flux would be subject of the future study.

UPSCALED MODELING OF MASS AND MOMENTUM TRANSPORT IN BIOFILMS

List of symbols

$-_\beta$	Related to the fluid phase
$-_\omega$	Related to the EPS region
$-_\sigma$	Related to the cell region
$-_\eta$	Related to the water channel region
$A_{\eta\omega}$	interfacial area contained within the biofilm between $\eta-\omega$ regions, m^2
$A_{\omega\sigma}$	interfacial area contained within the biofilm between $\omega-\sigma$ regions, m^2
$\mathbf{b}_\alpha^{\eta\omega}$	second-order tensor used to represent $\tilde{\mathbf{T}}_\alpha$ at $\eta-\omega$ interface
$\mathbf{B}_\alpha^{\eta\omega}$	second-order tensor used to represent $\tilde{\mathbf{v}}_\alpha$ at $\eta-\omega$ interface
$c_{i\eta}$	concentration of species i is the η region, $molm^{-3}$
$c_{i\omega}$	concentration of species i is the ω region, $molm^{-3}$
$c_{i\sigma}$	concentration of species i is the σ region, $molm^{-3}$
$\langle c_{i\eta}\rangle$	superficial average concentration of species i in the η region, $molm^{-3}$
$\langle c_{i\eta}\rangle^\eta$	intrinsic average concentration of species i in the η region, $molm^{-3}$
$\langle c_{i\omega}\rangle$	superficial average concentration of species i in the ω region, $molm^{-3}$
$\langle c_{i\omega}\rangle^\omega$	intrinsic average concentration of species i in the ω region, $molm^{-3}$
$\langle c_{i\sigma}\rangle$	superficial average concentration of species i in the σ region, $molm^{-3}$
$\langle c_{i\sigma}\rangle^\sigma$	intrinsic average concentration of species i in the σ region, $molm^{-3}$
$\{c_i\}$	equilibrium weighed average concentration for species i, $molm^{-3}$
$\hat{c}_{i\eta}$	biofilm-scale spatial deviation for species i in the η-region
$\hat{c}_{i\omega}$	biofilm-scale spatial deviation for species i in the ω-region
$\hat{c}_{i\sigma}$	biofilm-scale spatial deviation for species i in the σ-region
$\tilde{c}_{i\eta}$	spatial deviation concentration for species i in the η region,$molm^{-3}$
$\tilde{c}_{i\omega}$	spatial deviation concentration for species i in the ω region,$molm^{-3}$
$\tilde{c}_{i\sigma}$	spatial deviation concentration for species i in the σ region,$molm^{-3}$
$\mathbf{c}_\omega^{\eta\omega}$	vector used to represent $\tilde{p}_\eta$ at the $\eta\omega$ interface, m^{-1}
$\mathbf{c}_\omega^{\omega\sigma}$	vector used to represent $\tilde{p}_\eta$ at the $\sigma\omega$ interface, m^{-1}
$\mathbf{d}_{i\eta}$	vector field used to represent $\tilde{c}_{i\eta}$
$\mathbf{d}_{i\omega}$	vector field used to represent $\tilde{c}_{i\omega}$
$\mathbf{d}_{i\sigma}$	vector field used to represent $\tilde{c}_{i\sigma}$
$D_{i\eta}$	mixture diffusivity for species i in η region, m^2s^{-1}
$D_{i\omega}$	mixture diffusivity for species i in ω region, m^2s^{-1}
$D_{i\sigma}$	mixture diffusivity for species i in σ region, m^2s^{-1}

$\mathbf{D}_{i,\text{eff}}$	effective diffusivity for species i in the biofilm, m^2s^{-1}
$\mathbf{D}_{i,\text{dis}}$	effective dispersion for species i in the biofilm, m^2s^{-1}
E_0	surface concentration of transporter proteins for cell productions, molm^{-2}
K_A	half saturation constant for Monod kinetic form, molm^{-3}
$k_i^{\omega\sigma}$	cell membrane permeability for species i (at $\omega-\sigma$ interface)
$k_i^{\omega\eta}$	mass transfer coefficient for species i (at $\omega-\sigma$ interface)
$K_{\text{eq},B}$	phase equilibrium coefficient for species B
$K_{\text{eq},C}$	phase equilibrium coefficient for species C
$K_{\text{eq},D}$	phase equilibrium coefficient for species D
$\mathbf{K}_\omega$	permeability tensor of ω-region (EPS fibers) (m^2)
$\mathbf{K}_{\omega\sigma}$	permeability tensor of $\omega-\sigma$-region (biofilm matrix) (m^2)
$\mathbf{K}$	permeability tensor of the biofilm
$\ell_{\eta\omega}$	local-scale characteristic length associated with $\eta-\omega$ region, m
$\ell_{\omega\sigma}$	local-scale characteristic length associated with $\omega-\sigma$ region, m
ℓ_η	Characteristic length for the η-region, m
ℓ_ω	Characteristic length for the η-region, m
ℓ_σ	Characteristic length for the σ-region, m
ℓ_{bf}	Characteristic length for the biofilm, m
L	Characteristic length for the averaged volume, m
$\mathbf{M}_i$	molar weight of species i, kgmol^{-1}
$\mathbf{n}_{\eta\omega}$	-$\mathbf{n}_{\omega\eta}$, unit normal vector directed from the η-region to ω-region
$\mathbf{n}_{\omega\sigma}$	-$\mathbf{n}_{\sigma\omega}$, unit normal vector directed from the ω-region to σ-region
$\mathbf{n}_{\omega\eta}\cdot\mathbf{w}_{\omega\eta}$	displacement velocity at $\omega-\eta$ interface
$\mathbf{n}_{\omega\sigma}\cdot\mathbf{w}_{\omega\sigma}$	displacement velocity at $\omega-\sigma$ interface
p_β	local pressure of β phase (fluid), Pa
p_η	local pressure of η region, Pa
p_ω	local pressure of ω region, Pa
$\langle p_\eta\rangle^\eta$	intrinsic average pressure in the η region, Pa
$\langle p_\omega\rangle^\omega$	intrinsic average pressure in the ω region, Pa
$\{p\}$	equilibrium pressure in the biofilm, Pa
$\tilde{p}_\eta$	spatial deviation of pressure in the η region, Pa
$\tilde{p}_\omega$	spatial deviation of pressure in the ω region, Pa
r_0	radius of the averaging volume, m
R_i	rate of production of species i in the σ-region, $\text{molm}^{-2}\text{s}^{-1}$
$\mathbf{T}_\beta$	viscous stress tensor of β phase (fluid), Pa

$\mathbf{T}_\eta$	viscous stress tensor of η region, Pa
$\mathbf{T}_\omega$	viscous stress tensor of ω region, Pa
$\mathbf{T}_\sigma$	viscous stress tensor of η region, Pa
$\langle \mathbf{T}_\eta \rangle^\eta$	intrinsic average viscous tensor of η region, Pa
$\langle \mathbf{T}_\omega \rangle^\omega$	intrinsic average viscous tensor of ω region (fluid), Pa
$\tilde{\mathbf{T}}_\eta$	intrinsic average viscous tensor of η region, Pa
$\tilde{\mathbf{T}}_\omega$	intrinsic average viscous tensor of ω region, Pa
$\mathbf{v}_{i\eta}$	velocity of species i in the η-region, ms^{-1}
$\mathbf{v}_{i\omega}$	velocity of species i in the ω-region, ms^{-1}
$\mathbf{v}_{i\sigma}$	velocity of species i in the σ-region, ms^{-1}
$\mathbf{v}_\eta$	velocity of the η-region, ms^{-1}
$\mathbf{v}_\omega$	velocity of the ω-region, ms^{-1}
$\mathbf{v}_\sigma$	velocity of the σ-region, ms^{-1}
$\langle \mathbf{v}_\eta \rangle$	superficial average velocity of η region, ms^{-1}
$\langle \mathbf{v}_\eta \rangle^\eta$	intrinsic average velocity of η region, ms^{-1}
$\langle \mathbf{v}_\omega \rangle$	superficial average velocity of ω region, ms^{-1}
$\langle \mathbf{v}_\omega \rangle^\omega$	intrinsic average velocity of ω region, ms^{-1}
$\{\mathbf{v}\}$	equilibrium velocity in the biofilm,ms^{-1}
$\tilde{\mathbf{v}}_\eta$	spatial deviation of the velocity in the η region, ms^{-1}
$\tilde{\mathbf{v}}_\omega$	spatial deviation of the velocity in the ω region, ms^{-1}
V	averaging volume m^{-3}
V_η	volume of the η-region in the averaged volume m^{-3}
V_ω	volume of the ω-region in the averaged volume m^{-3}
V_σ	volume of the σ-region in the averaged volume m^{-3}

Greek letters

α_1	equilibrium coefficient defined in reaction equation
α_2	reaction rate parameter in cells, mol s m^{-3}
α_3	reaction rate parameter in cells, s
α_4	reaction rate parameter in cells, s
α_5	reaction rate parameter in cells, m^3s mol^{-1}
ε_η	volume fraction of the η-region
ε_ω	volume fraction of the ω-region
ε_σ	volume fraction of the σ-region
μ_A	maximum specific substrate utilization parameter, $molm^3s^{-1}$
μ_β	Dynamic viscosity of the fluid phase, Pa.s
$\rho_{i\eta}$	mass density of species i in the η-region, kg m^{-3}
$\rho_{i\omega}$	mass density of species i in the ω-region, kg m^{-3}
$\rho_{i\sigma}$	mass density of species i in the σ-region, kg m^{-3}
ρ_η	total mass density in the η-region, kg m^{-3}
ρ_ω	total mass density in the ω-region, kg m^{-3}
ρ_σ	total mass density in the σ-region, kg m^{-3}
$\langle\rho_\eta\rangle^\eta$	intrinsic average mass density in the η-region, kg m^{-3}
$\langle\rho_\omega\rangle^\omega$	intrinsic average mass density in the ω-region, kg m^{-3}
$\langle\rho_\sigma\rangle^\sigma$	intrinsic average mass density in the σ-region, kg m^{-3}
$\{\rho\}$	equilibrium mass density in the biofilm, kg m^{-3}
$\tilde{\rho}_\eta$	spatial deviation mass density in the η-region
$\tilde{\rho}_\omega$	spatial deviation mass density in the ω-region
$\tilde{\rho}_\sigma$	spatial deviation mass density in the σ-region

A biofilm is an assemblage of surface-associated microbial cells embedded in a slimy matrix of extracellular polymeric compounds. Biofilms are ubiquitous in natural and industrial systems. Among the problems associated with biofilms, energy losses, equipment damage, product contamination and medical infections are reported. In the particular case of membrane filtration systems, biofilm development induces a decline of process performance. Consequently cleaning procedures and replacement of the membranes are required. Biofilm development is a very complicated process governed by several coupled physical, chemical and biological phenomena. Mathematical modeling of biofilms is then crucial to get a better understanding of involved phenomena. It is an essential tool to make predictions that might help enhancing or reducing biofilm formation.
Several modeling approaches describing biofilm development have been proposed since the early 1980s. The description of the highly heterogeneity of biofilms in space and time is challenging. Recently, models and techniques developed for porous media have been used to study biofilms. In these models, mechanisms at microscopic scale are first identified and described. Afterwards, by using an upscaling method, the description of macroscopic phenomena is obtained.
The goal of this study is to propose an upscaled biofilm model that takes into account transport (diffusion and convection) and reaction mechanisms at biofilm scale. At microscopic scale, the biofilm is represented by a set of three regions (cells, exopolysaccharides gel and water channels). The gelatinous EPS region is composed itself by two phases, a fluid and a solid (EPS fibers). First, conservation equations for mass and momentum transport are derived for each region, in unsteady state. Thereafter, a first upscaling with the volume averaging method is applied to reach a scale (intermediate scale) where the EPS matrix can be described as a continuum. Another upscaling is then performed to reach biofilm scale (macroscopic scale). Local mass and momentum equilibrium cases are presented in this work. Although, non-equilibrium conditions are more realistic, they are rarely assumed in models described in the literature. Our model is able to predict the evolution with time of the biofilm structural properties (porosity, diffusivity, permeability) and the profiles of species concentration and velocities. Numerical simulations are performed to determine the total permeability tensor of the biofilm which includes both permeabilities of the EPS fibers and biofilm matrix.

1 INTRODUCTION

A biofilm is an assemblage of surface-associated microbial cells that are enclosed in a matrix of hydrated Extracellular Polymeric Substances (EPS) mainly composed of exopolysacharides, proteins and nucleic acids [38]. Non cellular materials such as mineral crystals, corrosion particles, clay or blood components depending on the environment in which the biofilm was developed, may also be found in biofilm matrix.

Biofilms may form on a wide variety of surfaces including living tissues, medical or dental devices, industrial or potable water system piping, in dairy industry and in natural aquatic systems. Biofilm formation (biofouling) causes technical and economic losses in many industries and in medical environments. Corrosion [145], energy losses and blockages in condenser tubes, membrane systems, water [146] and wastewater circuits, heating systems [128], heat exchangers, and even on ship hulls have been associated with biofilms. General processes leading to biofilm formation are the following: (1) preconditioning of the material surface by macromolecules from the aqueous medium, (2) Transport of cells in suspension (planktonic cells) from the bulk liquid to the surface, followed by reversible (3) and irreversible (4) adsorption of cells, (5) biofilm growth and polymers excretion on the surface, (6) biofilm detachment, erosion and sloughing [227].

The attachment of microorganisms to surfaces and subsequent biofilm development are very complex processes, strongly affected by several variables associated to cell properties, the substratum and the surrounding environmental conditions of the bulk liquid [70],[71].

Biofilm architecture is heterogeneous, both in space and time, constantly changing due to internal and external processes. It contains microcolonies encased in the EPS matrix separated from other micro-colonies by interstitial voids (water channels). Liquid flow occurs in these water channels allowing diffusion of nutrients, metabolites and even antimicrobial agents [70], [50],[23]. Biofilm structure is largely influenced by environmental conditions including the nutrient diffusion, convection and bulk shear stress. Additionally, sessile microorganisms (biofilm associated organisms) differ largely from their planktonic counterparts (freely suspended) concerning genes transcription.

The understanding and modeling of mass transport and reaction in biofilms has developed substantially in the past decades. Nowadays, mathematical modeling is an essential tool to understand the phenomena (physical, chemical and biological) involved in biofilm development and activity. It also helps providing clues to struggle against biofouling in engineering systems and to predict process performances in different industrial applications.

One critical point that should be taken into account when developing a biofilm model is its heterogeneity 1) Structural: biofilm thickness, roughness, porosity and relative permeability; 2) Chemical: gradient of chemical species, pH variations which induce and create a high diversity of reactions (aerobic and anaerobic); 3) Biological: diversity of microbial species and physiological states (growing and dead cells, at different growth rates)and 4)

Physical: biofilm density and viscosity, EPS properties, species diffusivity in the matrix [60].

Moreover, very different length scales are found in a biofilm. They vary from a few nanometers (size of extracellular polymeric fibers), to several micrometers or centimeters (biofilm thickness), with the size of bacterial cells ($1 - 2$ μm) as an intermediate length scale.

The first attempts of biofilm modeling consisted in the development of continuum models primarily in one space dimension [106]. Here, biofilms are described as homogenous and continuous structures. In these models, the evolution of biofilm thickness and the spatial distribution of microbial species and nutrients in the biofilm are predicted with time. Additionally, diffusion is usually the only transport phenomenon taken into account. Due to their simplicity, one-dimensional biofilm models have difficulties characterizing the multidimensional biofilm structure [245].

The Cellular Automaton (CA) model has been widely applied to model biofilm heterogeneous structures. When CA model is used, the physical space is divided in an array of small compartments, which are allowed to fill up with biomass to a predetermined maximum. Once a compartment is full or overflowing, a simple rule-based system is employed in order to locate the compartment in which the extra biomass will be placed. For example, the generation of a new cell in one compartment requires that the CA algorithm decides where to locate the new cell, based on the occupancy of neighboring compartments. The decisions are made based on a set of rules that act locally, but apply globally [54]. Although the main principles are the same, the rules governing the biomass spreading differ from a model to another. The randomness in the step of biomass distribution is pointed out as a drawback of this approach. Literature contains CA models that incorporate the following biological mechanisms: cell division, cell movement, cell to cell communication and diffusion of nutrients[196], [199], [245]. However the influence of surrounding fluid is not included in CA modeling approach. However, it was also found that the hydrodynamics of the bulk fluid plays an important role in shaping the structure of biofilms [71] through both the nutrients convection and the detachment of biomass by shear stress. Therefore, more recently, several biofilm models coupling biofilm development to bulk fluid were developed [199],[200],[202].

More recently, an increasing interest of the research community in considering the multiscale characteristics of a biofilm (from the nanometer (EPS, protein in the matrix) to the millimeter/centimeter (biofilm thickness)) in model development is reported. The idea that biofilm models should be upscaled directly from microscopic scale has been first proposed by Wanner and Gujer [248],[251]. The main advantages of the upscaled techniques, in general, and the volume averaging, in particular, are the following: 1) the resulting model relates the microscopic parameters to the observable macroscopic ones. For instance, the effective diffusivity at macroscopic scale takes into account local diffusivities, the microstructure and dispersion caused by the local velocity field; 2) indicates under what conditions the conservation equations (mass, momentum) are valid.

These works include upscaling reactive solute transport within the matrix, cellular growth

and diffusion of nutrients. In addition, the effective properties provide some additional information from both local (cell) scale and biofilm structure (porosity...) [260], [262], [263].
In general, most of the work with the volume averaging method focused on local mass equilibrium conditions in a representative elementary volume and on the continuity or not (jump conditions) of quantities at the interface between phases in a porous region or between porous regions. Under these circumstances, all intrinsic concentrations can be assumed to be equal in a representative elementary volume and one mass balance equation is sufficient to describe mass transport. However, it should be noted that non-equilibrium conditions with moving interfaces are closer to reality.

2 PRESENTATION OF THE MODEL

During filtration of water containing bacteria through a porous membrane, the microorganisms that are present can attach to the membrane surface and form a biofilm that will progressively decrease the performance of the process by increasing the resistance to the flow (or decreasing global permeability). This phenomenon causes a fouling of the membrane in surface. Furthermore, the biofilm produces chemical species that can enter the membrane and eventually lead to its fouling in volume.
A model for membrane fouling in volume caused by adsorption has already been developed in another article and the objective of this work is to model the influence of the biofilm on fouling. It aims at predicting first the evolution with time of the species concentration profiles and particularly at the biofilm-membrane interface, in order to give input data for the adsorption model, and secondly the evolution with time of the biofilm structural parameters (porosities, dimensions), in order to quantify its impact on the global permeability.
The smallest scale considered in this study is the continuum mechanics one. At this scale, the resolution of transport phenomena equations inside the biofilm would be very complex and very demanding numerically. Therefore, the model developed here provides convection-diffusion-reaction balance equations at biofilm scale by upscaling with the volume averaging method, starting from equations at continuum mechanics scale. When a description at large scale is needed, this method has the advantage to provide a link with phenomena at small scale, which avoids using empirical laws.
As the objective of this first model is to obtain qualitative results, many simplifying hypotheses are made. Neither the initial attachment of the cells to the membrane surface or the biofilm detachment due to shear stress will be taken into account (see [199],[201],[213] for additional information). The model only deals with an already existing layer of biofilm contaning bacteria in the same biological state. Here, the biofilm is described geometrically by a parallelepiped completely covering the top rectangular surface of the membrane and only its thickness can evolve with time. No spatial distribution of the structural biofilm parameters is considered in this first version

of the model. In future work, the model will be able to treat a biofilm made of several layers and biofilm heterogeneity with space and time will then be taken into account. The presence of the supporting membrane will only be accounted for through boundary conditions at biofilm scale.
From a structural point of view, the biofilm is represented as a set of three regions: a cellular region (σ), a gelatinous region (ω) and a fluid region (η). The σ-region, composed of all the microorganisms in the system, is modeled as a fluid. The cell wall, and in particular its barrier effect for species, is taken into account in the boundary conditions at the $\omega - \sigma$ interface, using a simple carrier model [137], [138]. For their growth, and following [260, 261], bacteria use a substrate (species A) and an electron acceptor (species B) to form EPS (species C), terminal products (species D) and intercellular products (species E) which increase the cell mass. While species E always remains in the cell, the other species can enter or leave bacteria. Species D is assumed to be water only. The reaction model is represented in Fig.3.1.

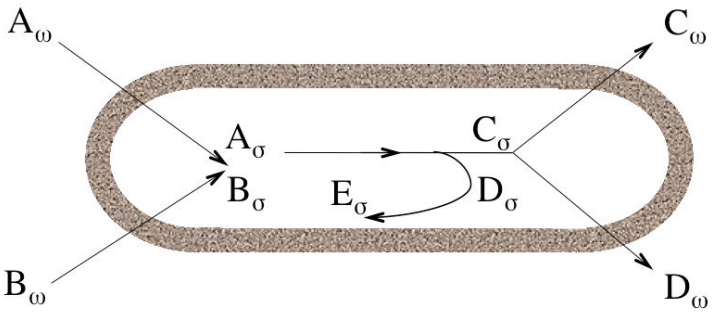

Figure 3.1: Reactants and products in a bacterial cell

The ω-region is a two-phase porous medium containing a solid phase made of EPS fibers and a fluid phase made of a mixture of species A, B, C diluted in water (D). The η-region represents biofilm water channels and contains the same kind of mixture. Because the biofilm is already formed, it is plausible to assume that the cell region σ is completely surrounded by the EPS region ω and that there is no contact between σ and η-regions. All the regions with their characteristic length scales are presented in Fig. 3.2.
First, balance equations will be written at the smallest scale considered here, e.g. the continuum mechanics scale (microscopic scale) in unsteady state, in order to obtain at the end time evolution of macroscopic quantities. Using the Representative Elementary Volume (REV) described in Fig. 3.3, the volume averaging method will then be used in the three regions to reach a scale where the ω-region can be described as a one-phase continuum (intermediate scale). Another upscaling will then be applied to get to the biofilm scale (macroscopic scale), in the cases of local mass/momentum equilibrium and non-equilibrium. Many existing models make the assumption of local equilibrium, but

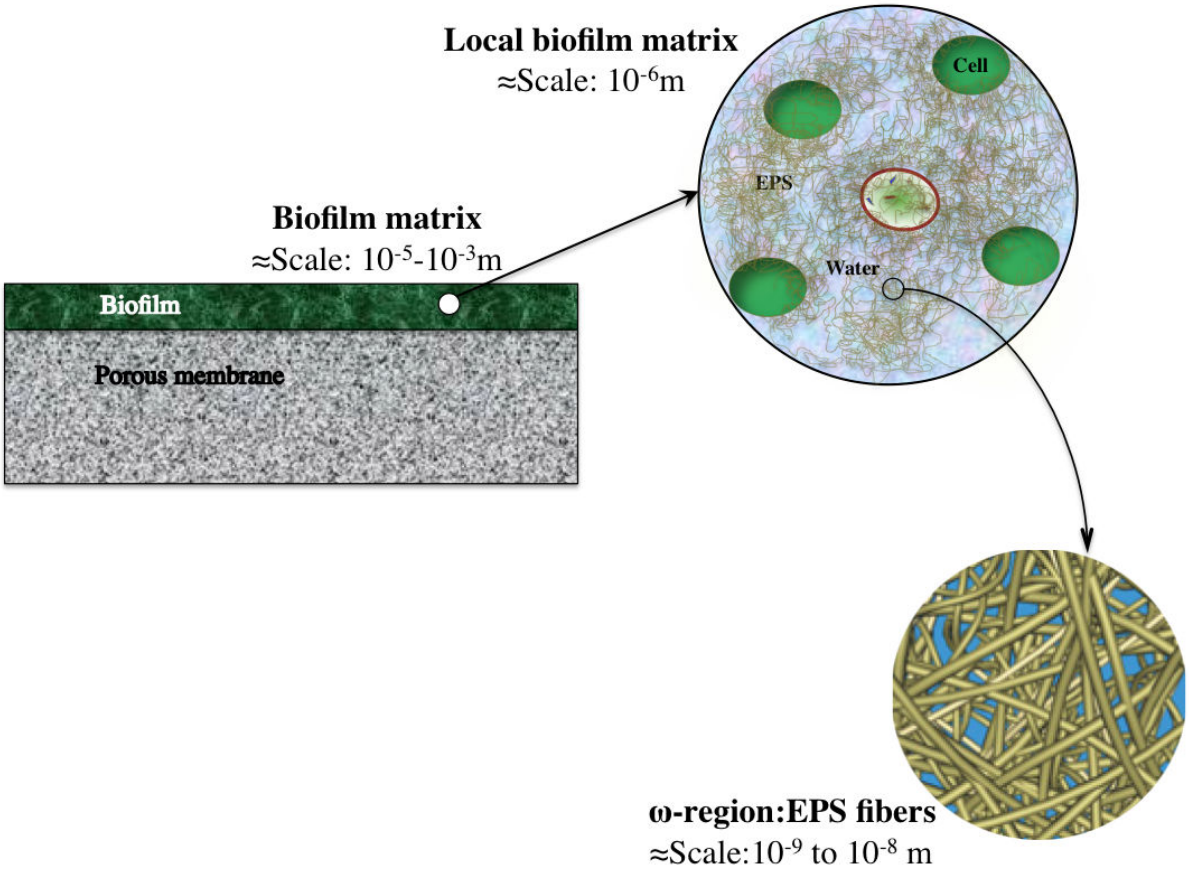

Figure 3.2: Hiearchical biofilm structure with constituting regions of interest

in fact, it relies on precise time and length scale constraints that are not always verified. Transport properties at macroscopic scale, such as permeability and effective diffusivity, will be determined by solving associate problems, called closure problems, in domains at small scale that are representative of the biofilm structure. These properties are functions of small scale parameters such as structure and biophysical properties. The evolution with time of macroscopic quantities (concentration fields, velocity fields, porosities) will finally be determined.

In future work, a link between the evolution with time of the biofilm thickness and these macroscopic quantities will be determined, modeling the biofilm growth. Experimental data will also be performed to characterize properties at microscopic scale (diffusivities, equilibrium constants...) and at macroscopic scale (initial porosities) and to validate the numerical results of the macroscopic model.

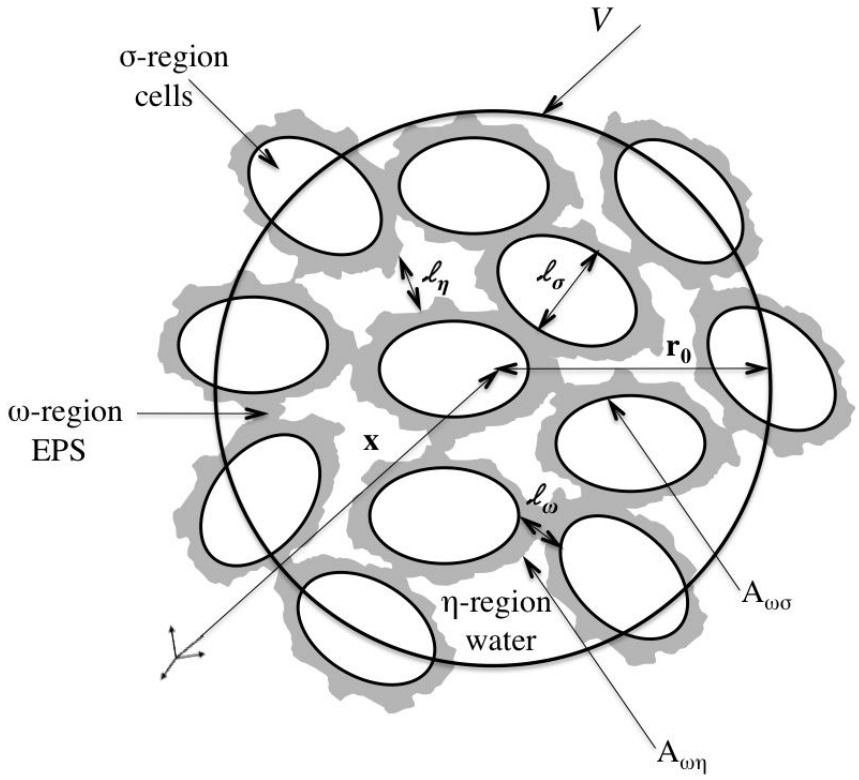

Figure 3.3: Representative Elementary Volume of the biofilm matrix with characteristic length scale of each region

3 MODEL AT MICROSCOPIC SCALE

3.1 ω-REGION (EPS GEL)

As seen in Fig. 3.2, the ω-region is composed of two phases, namely a fluid phase β and a solid phase κ (EPS fibers). It is assumed that the microstructure of this region does not evolve anymore. Microscopic conservation equations in the ω-region are

$$\frac{\partial \rho_\beta}{\partial t} + \nabla \cdot (\rho_\beta \mathbf{v}_\beta) = 0 \quad \text{in the } \beta\text{-phase} \tag{3.1a}$$

$$\frac{\partial (\rho_\beta \mathbf{v}_\beta)}{\partial t} = \rho_\beta \mathbf{g} + \nabla \cdot \mathbf{T}_\beta \quad \text{in the } \beta\text{-phase} \tag{3.1b}$$

$$\frac{\partial c_{i\beta}}{\partial t} + \nabla \cdot (c_{i\beta} \mathbf{v}_{i\beta}) = 0 \quad i = A \rightarrow C \quad \text{in the } \beta\text{-phase} \tag{3.1c}$$

$$c_{E\beta} = 0 \quad \text{in the } \beta\text{-phase} \tag{3.1d}$$

For momentum equation, inertial transport has been neglected in front of viscous stress (low Reynolds number). Note that because there are five species (A, B, C, D, E), five conservation equations are needed: continuity equation and conservation equations for species A, B, C, E were chosen here. Conservation equation for solvent D (water) can be deduced from these equations by linear combination.

Stress tensor is defined by

$$\mathbf{T}_\beta = -p_\beta \mathbf{I} + \mu_\beta \left[\nabla \mathbf{v}_\beta + (\nabla \mathbf{v}_\beta)^T\right] + \left(k_\beta - \frac{2}{3}\mu_\beta\right)(\nabla \cdot \mathbf{v}_\beta) \quad \text{in the } \beta\text{-phase} \tag{3.2}$$

where k_β is the volume viscosity. Since density relative variations are small (because species A, B and C are diluted in water D), it can be shown that

$$\mathbf{T}_\beta \approx -p_\beta \mathbf{I} + \mu_\beta \left[\nabla \mathbf{v}_\beta + (\nabla \mathbf{v}_\beta)^T\right] \quad \text{in the } \beta\text{-phase} \tag{3.3}$$

under some constaints on time/length scales.

Since species A, B, C, E are diluted in solvent D and because the effect of specific body forces (and in particular gravity) is neglected [27, 134], diffusion of species follows Fick's law

$$c_{i\beta}\mathbf{v}_{i\beta} = c_{i\beta}\mathbf{v}_\beta - D_{i\beta}\nabla c_{i\beta} \quad i = A, B, C, E \quad \text{in the } \beta\text{-phase} \tag{3.4}$$

where $D_{i\beta}$ is the diffusivity of species i in the β-phase with respect to solvent D, assumed constant in the following.

For boundary conditions at the fluid-solid interface, it is assumed that the fibers structure does not evolve anymore (null fluid-solid interface velocity) and that no species can enter these fibers (null concentration of species inside the solid). Then

$$\mathbf{v}_{i\beta} = \mathbf{0} \quad i = A \to E \quad \text{at the } \beta - \kappa \text{ interface} \tag{3.5}$$

$$\mathbf{v}_\beta = \mathbf{0} \quad \text{at the } \beta - \kappa \text{ interface} \tag{3.6}$$

3.2 η-REGION (WATER CHANNELS)

In this region, there is only a fluid phase β. As for phase β of ω-region, the microscopic conservation equations in this phase are

$$\frac{\partial \rho_\beta}{\partial t} + \nabla \cdot (\rho_\beta \mathbf{v}_\beta) = 0 \quad \text{in the } \beta\text{-phase} \tag{3.7a}$$

$$\frac{\partial (\rho_\beta \mathbf{v}_\beta)}{\partial t} = \rho_\beta \mathbf{g} + \nabla \cdot \mathbf{T}_\beta \quad \text{in the } \beta\text{-phase} \tag{3.7b}$$

$$\frac{\partial c_{i\beta}}{\partial t} + \nabla \cdot (c_{i\beta}\mathbf{v}_{i\beta}) = 0 \quad i = A, B, C \quad \text{in the } \beta\text{-phase} \tag{3.7c}$$

$$c_{E\beta} = 0 \quad \text{in the } \beta\text{-phase} \tag{3.7d}$$

with

$$\mathbf{T}_\beta \approx -p_\beta \mathbf{I} + \mu_\beta \left[\nabla \mathbf{v}_\beta + (\nabla \mathbf{v}_\beta)^T\right] \quad \text{in the } \beta\text{-phase} \tag{3.8}$$

and

$$c_{i\beta}\mathbf{v}_{i\beta} = c_{i\beta}\mathbf{v}_\beta - D_{i\beta}\nabla c_{i\beta} \quad i = A, B, C, E \quad \text{in the } \beta\text{-phase} \tag{3.9}$$

3.3 σ-REGION (CELLS)

In this region, there is only a fluid phase γ. A biochemical process occurs there, represented by the reaction

$$A + \eta_1 B \rightarrow \eta_2 C + \eta_3 D + \eta_4 E \tag{3.10}$$

The molar reaction rate for species i, R_i, is assumed to have a Michaelis-Menten form [261], with a limiting substrate (A) and an electron acceptor (B) in excess. The microscopic conservation equations in this phase are then

$$\frac{\partial \rho_\gamma}{\partial t} + \nabla \cdot (\rho_\gamma \mathbf{v}_\gamma) = 0 \quad \text{in the } \gamma\text{-phase} \tag{3.11a}$$

$$\frac{\partial (\rho_\gamma \mathbf{v}_\gamma)}{\partial t} = \rho_\gamma \mathbf{g} + \nabla \cdot \mathbf{T}_\gamma \quad \text{in the } \gamma\text{-phase} \tag{3.11b}$$

$$\frac{\partial c_{i\gamma}}{\partial t} + \nabla \cdot (c_{i\gamma}\mathbf{v}_{i\gamma}) = R_i(c_{A\gamma}) \quad i = A, B, C, E \quad \text{in the } \gamma\text{-phase} \tag{3.11c}$$

with

$$\mathbf{T}_\gamma \approx -p_\gamma \mathbf{I} + \mu_\gamma \left[\nabla \mathbf{v}_\gamma + (\nabla \mathbf{v}_\gamma)^T\right] \quad \text{in the } \gamma\text{-phase} \tag{3.12}$$

$$c_{i\gamma}\mathbf{v}_{i\gamma} = c_{i\gamma}\mathbf{v}_\gamma - D_{i\gamma}\nabla c_{i\gamma} \quad i = A, B, C, E \quad \text{in the } \gamma\text{-phase} \tag{3.13}$$

and molar reaction rates depending only on $c_{A\gamma}$

$$R_A(c_{A\gamma}) = -\mu_A \frac{c_{A\gamma}}{K_A + c_{A\gamma}} \quad \text{in the } \gamma\text{-phase} \quad \text{(substrate)} \tag{3.14a}$$

$$R_B(c_{A\gamma}) = -\eta_1 \mu_A \frac{c_{A\gamma}}{K_A + c_{A\gamma}} \quad \text{in the } \gamma\text{-phase} \quad \text{(electron acceptor)} \tag{3.14b}$$

$$R_C(c_{A\gamma}) = +\eta_2 \mu_A \frac{c_{A\gamma}}{K_A + c_{A\gamma}} \quad \text{in the } \gamma\text{-phase} \quad \text{(EPS)} \tag{3.14c}$$

$$R_D(c_{A\gamma}) = +\eta_3 \mu_A \frac{c_{A\gamma}}{K_A + c_{A\gamma}} \quad \text{in the } \gamma\text{-phase} \quad \text{(water)} \tag{3.14d}$$

$$R_E(c_{A\gamma}) = +\eta_4 \mu_A \frac{c_{A\gamma}}{K_A + c_{A\gamma}} \quad \text{in the } \gamma\text{-phase} \quad \text{(intercellular products)} \tag{3.14e}$$

The equality $M_A + \eta_1 M_B = \eta_2 M_C + \eta_3 M_D + \eta_4 M_E$, which leads to $\sum_{i=A\rightarrow E} M_i R_i(c_{A\gamma}) = 0$, was also used to obtain (3.11a).

4 UPSCALED MODEL AT INTERMEDIATE SCALE

In the next equations, according to [255], the definition of superficial average of any function associated with an α-phase or α-region ($\alpha = \beta, \gamma, \omega, \eta, \sigma$) is used

$$\langle \psi_\alpha \rangle = \frac{1}{V} \int_{V_{\alpha(t)}} \psi_\alpha \mathrm{d}V \tag{3.15a}$$

as well as the definition of the intrinsic average

$$\langle \psi_\alpha \rangle^\alpha = \frac{1}{V_\alpha(t)} \int_{V_{\alpha(t)}} \psi_\alpha \mathrm{d}V \tag{3.15b}$$

The region where the average is taken is designated with an index: for example $\langle \psi_\beta \rangle_\omega$ is the superficial average of ψ_β (defined in the β-phase) in the ω-region.

4.1 ω-REGION (EPS GEL)

The volume-averaged form of the conservation equations can be written as

$$\frac{\partial \langle \rho_\beta \rangle_\omega^\beta}{\partial t} + \nabla \cdot \left(\langle \rho_\beta \rangle_\omega^\beta \langle \mathbf{v}_\beta \rangle_\omega^\beta \right) = 0 \quad \text{in the } \omega\text{-region} \tag{3.16a}$$

$$\frac{\partial \left(\langle \rho_\beta \rangle_\omega^\beta \langle \mathbf{v}_\beta \rangle_\omega^\beta \right)}{\partial t} = \langle \rho_\beta \rangle_\omega^\beta \mathbf{g} + \nabla \cdot \langle \mathbf{T}_\beta \rangle_\omega^\beta - \mu_\beta \mathbf{K}^{-1} \cdot \varepsilon_{\beta,\omega} \langle \mathbf{v}_\beta \rangle_\omega^\beta \quad \text{in the } \omega\text{-region} \tag{3.16b}$$

$$\frac{\partial \langle c_{i\beta} \rangle_\omega^\beta}{\partial t} + \nabla \cdot \left(\langle c_{i\beta} \rangle_\omega^\beta \langle \mathbf{v}_\beta \rangle_\omega^\beta \right) = D_{i\beta} \nabla^2 \langle c_{i\beta} \rangle_\omega^\beta \quad i = A \to C \quad \text{in the } \omega\text{-region} \tag{3.16c}$$

$$\langle c_{E\beta} \rangle_\omega^\beta = 0 \quad \text{in the } \omega\text{-region} \tag{3.16d}$$

with

$$\langle \mathbf{T}_\beta \rangle_\omega^\beta = -\langle p_\beta \rangle_\omega^\beta \mathbf{I} + \mu_\beta \left[\nabla \langle \mathbf{v}_\beta \rangle_\omega^\beta + \left(\nabla \langle \mathbf{v}_\beta \rangle_\omega^\beta \right)^T \right] \quad \text{in the } \omega\text{-region} \tag{3.17}$$

and $\mathbf{K}$ denotes the permeability tensor, which is uniform and constant with time because the fibrous structure does not evolve. In deriving the above expressions, the dispersive transport was assumed negligible compared to the convective one and the fact that the porosity $\varepsilon_{\beta,\omega}$ is uniform and constant with time was used.

To simplify notations, the following changes are made

$$\begin{aligned}
\langle \rho_\beta \rangle_\omega^\beta &\rightarrow \rho_\omega && \text{(3.18a)}\\
\langle \mathbf{v}_\beta \rangle_\omega^\beta &\rightarrow \mathbf{v}_\omega && \text{(3.18b)}\\
\langle p_\beta \rangle_\omega^\beta &\rightarrow p_\omega && \text{(3.18c)}\\
\mathbf{K}^{-1}\varepsilon_{\beta,\omega} &\rightarrow \mathbf{K}_\omega^{-1} && \text{(3.18d)}\\
\langle c_{i\beta} \rangle_\omega^\beta &\rightarrow c_{i\omega} && \text{(3.18e)}\\
\langle \mathbf{v}_{i\beta} \rangle_\omega^\beta &\rightarrow \mathbf{v}_{i\omega} && \text{(3.18f)}
\end{aligned}$$

so that Eqs. (3.16) take the form

$$\frac{\partial \rho_\omega}{\partial t} + \nabla \cdot (\rho_\omega \mathbf{v}_\omega) = 0 \quad \text{in the } \omega\text{-region} \tag{3.19a}$$

$$\frac{\partial (\rho_\omega \mathbf{v}_\omega)}{\partial t} = \rho_\omega \mathbf{g} + \nabla \cdot \mathbf{T}_\omega - \mu_\beta \mathbf{K}_\omega^{-1} \cdot \mathbf{v}_\omega \quad \text{in the } \omega\text{-region} \tag{3.19b}$$

$$\frac{\partial c_{i\omega}}{\partial t} + \nabla \cdot (c_{i\omega} \mathbf{v}_\omega) = D_{i\beta} \nabla^2 c_{i\omega} \quad i = A \rightarrow C \quad \text{in the } \omega\text{-region} \tag{3.19c}$$

$$c_{E\omega} = 0 \quad \text{in the } \omega\text{-region} \tag{3.19d}$$

with

$$\mathbf{T}_\omega = -p_\omega \mathbf{I} + \mu_\beta \left[\nabla \mathbf{v}_\omega + (\nabla \mathbf{v}_\omega)^T \right] \quad \text{in the } \omega\text{-region} \tag{3.20}$$

4.2 η-REGION (WATER CHANNELS)

Applying an averaging operator of the same size as the one used for the ω-region and because there is no fluid-solid interface, and with the same kind of assumptions as for the ω-region

$$\frac{\partial \langle \rho_\beta \rangle_\eta^\beta}{\partial t} + \nabla \cdot (\langle \rho_\beta \rangle_\eta^\beta \langle \mathbf{v}_\beta \rangle_\eta^\beta) = 0 \quad \text{in the } \eta\text{-region} \tag{3.21a}$$

$$\frac{\partial \left(\langle \rho_\beta \rangle_\eta^\beta \langle \mathbf{v}_\beta \rangle_\eta^\beta \right)}{\partial t} = \langle \rho_\beta \rangle_\eta^\beta \mathbf{g} + \nabla \cdot \langle \mathbf{T}_\beta \rangle_\eta^\beta \quad \text{in the } \eta\text{-region} \tag{3.21b}$$

$$\frac{\partial \langle c_{i\beta} \rangle_\eta^\beta}{\partial t} + \nabla \cdot (\langle c_{i\beta} \rangle_\eta^\beta \langle \mathbf{v}_\beta \rangle_\eta^\beta) = D_{i\beta} \nabla^2 \langle c_{i\beta} \rangle_\eta^\beta \quad i = A \rightarrow C \quad \text{in the } \eta\text{-region} \tag{3.21c}$$

$$\langle c_{E\beta} \rangle_\eta^\beta = 0 \quad \text{in the } \eta\text{-region} \tag{3.21d}$$

with

$$\langle \mathbf{T}_\beta \rangle_\eta^\beta = -\langle p_\beta \rangle_\eta^\beta \mathbf{I} + \mu_\beta \left[\nabla \langle \mathbf{v}_\beta \rangle_\eta^\beta + \left(\nabla \langle \mathbf{v}_\beta \rangle_\eta^\beta \right)^T \right] \quad \text{in the } \eta\text{-region} \tag{3.22}$$

To simplify notations, the following changes are made

$$\langle \rho_\beta \rangle_\eta^\beta \rightarrow \rho_\eta \tag{3.23a}$$
$$\langle \mathbf{v}_\beta \rangle_\eta^\beta \rightarrow \mathbf{v}_\eta \tag{3.23b}$$
$$\langle p_\beta \rangle_\eta^\beta \rightarrow p_\eta \tag{3.23c}$$
$$\langle c_{i\beta} \rangle_\eta^\beta \rightarrow c_{i\eta} \tag{3.23d}$$
$$\langle \mathbf{v}_{i\beta} \rangle_\eta^\beta \rightarrow \mathbf{v}_{i\eta} \tag{3.23e}$$

so that conservation equations for this region can be written as

$$\frac{\partial \rho_\eta}{\partial t} + \nabla \cdot (\rho_\eta \mathbf{v}_\eta) = 0 \quad \text{in the } \eta\text{-region} \tag{3.24a}$$
$$\frac{\partial (\rho_\eta \mathbf{v}_\eta)}{\partial t} = \rho_\eta \mathbf{g} + \nabla \cdot \mathbf{T}_\eta \quad \text{in the } \eta\text{-region} \tag{3.24b}$$
$$\frac{\partial c_{i\eta}}{\partial t} + \nabla \cdot (c_{i\eta} \mathbf{v}_\eta) = D_{i\beta} \nabla^2 c_{i\eta} \quad i = A \rightarrow C \quad \text{in the } \eta\text{-region} \tag{3.24c}$$
$$c_{E\eta} = 0 \quad \text{in the } \eta\text{-region} \tag{3.24d}$$

with

$$\mathbf{T}_\eta = -p_\eta \mathbf{I} + \mu_\beta \left[\nabla \mathbf{v}_\eta + (\nabla \mathbf{v}_\eta)^T \right] \quad \text{in the } \eta\text{-region} \tag{3.25}$$

4.3 σ-REGION (CELLS)

Following the same method as for η-region, conservation equations at this scale are

$$\frac{\partial \langle \rho_\gamma \rangle_\sigma^\gamma}{\partial t} + \nabla \cdot (\langle \rho_\gamma \rangle_\sigma^\gamma \langle \mathbf{v}_\gamma \rangle_\sigma^\gamma) = 0 \quad \text{in the } \sigma\text{-region} \tag{3.26a}$$
$$\frac{\partial (\langle \rho_\gamma \rangle_\sigma^\gamma \langle \mathbf{v}_\gamma \rangle_\sigma^\gamma)}{\partial t} = \langle \rho_\gamma \rangle_\sigma^\gamma \mathbf{g} + \nabla \cdot \langle \mathbf{T}_\gamma \rangle_\sigma^\gamma \quad \text{in the } \sigma\text{-region} \tag{3.26b}$$
$$\frac{\partial \langle c_{i\gamma} \rangle_\sigma^\gamma}{\partial t} + \nabla \cdot (\langle c_{i\gamma} \rangle_\sigma^\gamma \langle \mathbf{v}_\gamma \rangle_\sigma^\gamma) = D_{i\gamma} \nabla^2 \langle c_{i\gamma} \rangle_\sigma^\gamma + R_i(\langle c_{A\gamma} \rangle_\sigma^\gamma) \quad i = A, B, C, E \quad \text{in the } \sigma\text{-region} \tag{3.26c}$$

with

$$\langle \mathbf{T}_\gamma \rangle_\sigma^\gamma = -\langle p_\gamma \rangle_\sigma^\gamma \mathbf{I} + \mu_\gamma \left[\nabla \langle \mathbf{v}_\gamma \rangle_\sigma^\gamma + (\nabla \langle \mathbf{v}_\gamma \rangle_\sigma^\gamma)^T \right] \quad \text{in the } \sigma\text{-region} \tag{3.27}$$

To obtain the expression of the upscaled reaction rate, the length scale constraints $\ell_\omega, \ell_\sigma \ll r_0$ and ${r_0}^2 \ll {\ell_{bf}}^2$, where ℓ_{bf} is the macroscopic biofilm thickness, were used (see [261]).

To simplify notations, the following changes are made

$$\langle \rho_\gamma \rangle_\sigma^\gamma \rightarrow \rho_\sigma \tag{3.28a}$$
$$\langle \mathbf{v}_\gamma \rangle_\sigma^\gamma \rightarrow \mathbf{v}_\sigma \tag{3.28b}$$
$$\langle c_{i\gamma} \rangle_\sigma^\gamma \rightarrow c_{i\sigma} \tag{3.28c}$$
$$\langle \mathbf{v}_{i\gamma} \rangle_\sigma^\gamma \rightarrow \mathbf{v}_{i\sigma} \tag{3.28d}$$

in order to write the corresponding conservation equations for this region as

$$\frac{\partial \rho_\sigma}{\partial t} + \nabla \cdot (\rho_\sigma \mathbf{v}_\sigma) = 0 \quad \text{in the } \sigma\text{-region} \tag{3.29a}$$
$$\frac{\partial (\rho_\sigma \mathbf{v}_\sigma)}{\partial t} = \rho_\sigma \mathbf{g} + \nabla \cdot \mathbf{T}_\sigma \quad \text{in the } \sigma\text{-region} \tag{3.29b}$$
$$\frac{\partial c_{i\sigma}}{\partial t} + \nabla \cdot (c_{i\sigma} \mathbf{v}_\sigma) = D_{i\gamma} \nabla^2 c_{i\sigma} + R_i(c_{A\sigma}) \quad i = A, B, C, E \quad \text{in the } \sigma\text{-region} \tag{3.29c}$$

with

$$\mathbf{T}_\sigma = -p_\sigma \mathbf{I} + \mu_\gamma \left[\nabla \mathbf{v}_\sigma + (\nabla \mathbf{v}_\sigma)^T \right] \quad \text{in the } \sigma\text{-region} \tag{3.30}$$

and

$$R_A(c_{A\sigma}) = -\mu_A \frac{c_{A\sigma}}{K_A + c_{A\sigma}} \quad \text{in the } \sigma\text{-region} \quad \text{(substrate)} \tag{3.31a}$$
$$R_B(c_{A\sigma}) = -\eta_1 \mu_A \frac{c_{A\sigma}}{K_A + c_{A\sigma}} \quad \text{in the } \sigma\text{-region} \quad \text{(electron acceptor)} \tag{3.31b}$$
$$R_C(c_{A\sigma}) = +\eta_2 \mu_A \frac{c_{A\sigma}}{K_A + c_{A\sigma}} \quad \text{in the } \sigma\text{-region} \quad \text{(EPS)} \tag{3.31c}$$
$$R_D(c_{A\sigma}) = +\eta_3 \mu_A \frac{c_{A\sigma}}{K_A + c_{A\sigma}} \quad \text{in the } \sigma\text{-region} \quad \text{(water)} \tag{3.31d}$$
$$R_E(c_{A\sigma}) = +\eta_4 \mu_A \frac{c_{A\sigma}}{K_A + c_{A\sigma}} \quad \text{in the } \sigma\text{-region} \quad \text{(intercellular products)} \tag{3.31e}$$

4.4 JUMP CONDITIONS

4.4.1 $\eta - \omega$ INTERFACE (CHANNELS - EPS GEL)

Species mass fluxes

Following [240], the jump condition for the molar flux of each species at the interface between homogeneous η and ω regions is

$$\mathbf{n}_{\eta\omega} \cdot c_{i\eta}(\mathbf{v}_{i\eta} - \mathbf{w}_{\eta\omega}) = \mathbf{n}_{\eta\omega} \cdot c_{i\omega}(\mathbf{v}_{i\omega} - \mathbf{w}_{\eta\omega}) \quad i = A \rightarrow E \quad \text{at } A_{\eta\omega} \tag{3.32}$$

The following constitutive equation are also used

$$\mathbf{n}_{\eta\omega} \cdot c_{i\eta}(\mathbf{v}_{i\eta} - \mathbf{w}_{\eta\omega}) = k_i^{\eta\omega}(c_{i\eta} - c_{i\omega}) \quad i = A \to E \quad \text{at } A_{\eta\omega} \tag{3.33}$$

where $k_i^{\eta\omega}$ is the transfer coefficient for species i at the $\eta - \omega$ interface.

Total mass flux

Summing Eq. (3.32) over i after multiplying by respective molar mass leads to the balance of total mass flux

$$\mathbf{n}_{\eta\omega} \cdot \rho_\eta(\mathbf{v}_\eta - \mathbf{w}_{\eta\omega}) = \mathbf{n}_{\eta\omega} \cdot \rho_\omega(\mathbf{v}_\omega - \mathbf{w}_{\eta\omega}) \quad \text{at } A_{\eta\omega} \tag{3.34}$$

Furthermore, the result of summing Eqs. (3.33) over i after multiplying by respective molar mass is

$$\mathbf{n}_{\eta\omega} \cdot \rho_\eta(\mathbf{v}_\eta - \mathbf{w}_{\eta\omega}) = \sum_{i=A\to E} M_i k_i^{\eta\omega} \left(c_{i\eta} - c_{i\omega}\right) \quad \text{at } A_{\eta\omega} \tag{3.35}$$

Integrated species mass fluxes

Integrating Eq. (3.33) gives

$$\frac{1}{V}\int_{A_{\eta\omega}} \mathbf{n}_{\eta\omega} \cdot c_{i\eta}\left(\mathbf{v}_{i\eta} - \mathbf{w}_{\eta\omega}\right) \mathrm{d}A = a_{\eta\omega} k_i^{\eta\omega}\left(\langle c_{i\eta}\rangle^\eta - \langle c_{i\omega}\rangle^\omega\right) \quad i = A \to E \quad \text{at } A_{\eta\omega} \tag{3.36}$$

where area averaged concentrations and volume averaged concentrations were equalized (under some length scales constraints). $a_{\eta\omega}$ is the specific area of the $\eta - \omega$ interface, which is assumed to be a function of time but not of space (spatial variations neglected).

Integrated total mass flux

Therefore, the total mass flux through the channels-EPS interface in a REV, per unit volume of REV, is obtained by summing Eq. (3.36) over i after multiplying by respective molar mass

$$\begin{aligned}\frac{1}{V}\int_{A_{\eta\omega}} \mathbf{n}_{\eta\omega} \cdot \rho_\eta\left(\mathbf{v}_\eta - \mathbf{w}_{\eta\omega}\right) \mathrm{d}A &= a_{\eta\omega} \sum_{i=A\to E} M_i k_i^{\eta\omega}\left(\langle c_{i\eta}\rangle^\eta - \langle c_{i\omega}\rangle^\omega\right) \\ &= \frac{\varepsilon_{\beta,\omega}}{V}\int_{A_{\eta\omega}} \mathbf{n}_{\eta\omega} \cdot \rho_\omega\left(\mathbf{v}_\omega - \mathbf{w}_{\eta\omega}\right) \mathrm{d}A\end{aligned} \tag{3.37}$$

Stress tensor

A jump condition on stress tensor is needed to have a well-posed problem, since ω and η regions behave like fluids. The general form of the momentum transport jump

condition [229] gives

$$(\mathbf{T}_\eta - \varepsilon_{\beta,\omega}\mathbf{T}_\omega)\cdot\mathbf{n}_{\eta\omega} = 0 \quad \text{at } A_{\eta\omega} \tag{3.38}$$

where it was assumed that the inter-regional volumetric and superficial stress is negligible compared to the normal momentum transport taking place across the inter-region, that transport at the inter-region takes place under quasi-steady conditions and that momentum transport due to the deformation of the interface is negligible with respect to the normal momentum transport and that inertial contributions are negligible.

4.4.2 $\omega - \sigma$ INTERFACE (EPS GEL - CELLS)

Species mass fluxes

Using [240], the jump condition for the molar flux of each species at the interface between homogeneous ω and σ regions is

$$\mathbf{n}_{\omega\sigma}\cdot c_{i\omega}(\mathbf{v}_{i\omega} - \mathbf{w}_{\omega\sigma}) = \mathbf{n}_{\omega\sigma}\cdot c_{i\sigma}(\mathbf{v}_{i\sigma} - \mathbf{w}_{\omega\sigma}) \quad i = A \to E \quad \text{at } A_{\omega\sigma} \tag{3.39}$$

where $\varepsilon_{\beta,\omega}$ is a constant.

Following the work of Wood and Whitaker [261], the species that can enter or leave the cell are the substrate (species A), the electron acceptor (species B), exopolymers (species C) and water (species D). Intercellular products (species E) cannot cross the cell wall and then stay in the cell. The following consitutive equations are then used, taking into account the presence of the cell wall

$$\mathbf{n}_{\omega\sigma}\cdot c_{A\omega}(\mathbf{v}_{A\omega} - \mathbf{w}_{\omega\sigma}) = \frac{E_0(c_{A\omega} - \alpha_1 c_{A\sigma})}{\alpha_2 + \alpha_3 c_{A\omega} + \alpha_4 c_{A\sigma} + \alpha_5 c_{A\omega}c_{A\sigma}} \quad \text{at } A_{\omega\sigma} \tag{3.40a}$$

$$\mathbf{n}_{\omega\sigma}\cdot c_{B\omega}(\mathbf{v}_{B\omega} - \mathbf{w}_{\omega\sigma}) = k_B^{\omega\sigma}(c_{B\omega} - K_{eq,B}^{r\omega\sigma}c_{B\sigma}) \quad \text{at } A_{\omega\sigma} \tag{3.40b}$$

$$\mathbf{n}_{\omega\sigma}\cdot c_{C\omega}(\mathbf{v}_{C\omega} - \mathbf{w}_{\omega\sigma}) = k_C^{\omega\sigma}(c_{C\omega} - K_{eq,C}^{r\omega\sigma}c_{C\sigma}) \quad \text{at } A_{\omega\sigma} \tag{3.40c}$$

$$\mathbf{n}_{\omega\sigma}\cdot c_{D\omega}(\mathbf{v}_{D\omega} - \mathbf{w}_{\omega\sigma}) = k_D^{\omega\sigma}(c_{D\omega} - K_{eq,D}^{r\omega\sigma}c_{D\sigma}) \quad \text{at } A_{\omega\sigma} \tag{3.40d}$$

$$\mathbf{n}_{\omega\sigma}\cdot c_{E\omega}(\mathbf{v}_{E\omega} - \mathbf{w}_{\omega\sigma}) = 0 \quad \text{at } A_{\omega\sigma} \tag{3.40e}$$

The constitutive equation given by Eq. (3.40a) is based on the simple carrier model, in which E_0 is the surface concentration of transporter proteins, α_1 is an equilibrium coefficient, $\alpha_3, \alpha_4, \alpha_5$ are the reaction rate parameters detailed in [260]. Moreover, $k_i^{\omega\sigma}$ is the transfert coefficient for species i through the $\omega - \sigma$ interface (taking into account the cell membrane permeability) and $K_{eq,i}^{r\omega\sigma}$ is the equilibrium coefficient of species i between ω and σ regions.

Total mass flux

Summing Eq. (3.39) over i after multiplying by molar mass leads to the balance of total mass flux

$$\mathbf{n}_{\omega\sigma}\cdot\rho_\omega(\mathbf{v}_\omega - \mathbf{w}_{\omega\sigma}) = \mathbf{n}_{\omega\sigma}\cdot\rho_\sigma(\mathbf{v}_\sigma - \mathbf{w}_{\omega\sigma}) \quad \text{at } A_{\omega\sigma} \tag{3.41}$$

Furthermore, the result of summing Eqs. (3.41) after multiplying by respective molar mass is

$$\mathbf{n}_{\omega\sigma}\cdot\rho_{\omega}(\mathbf{v}_{\omega}-\mathbf{w}_{\omega\sigma})=\frac{M_A E_0(c_{A\omega}-\alpha_1 c_{A\sigma})}{\alpha_2+\alpha_3 c_{A\omega}+\alpha_4 c_{A\sigma}+\alpha_5 c_{A\omega}c_{A\sigma}}$$
$$+\sum_{i=B\to D} M_i k_i^{\omega\sigma}(c_{i\omega}-K_{eq,i}^{\omega\sigma}c_{i\sigma}) \quad \text{at } A_{\omega\sigma} \tag{3.42}$$

Integrated species mass fluxes

From Eqs. (3.40), one obtains, under some length scales constraints,

$$\frac{1}{V}\int_{A_{\omega\sigma}}\mathbf{n}_{\omega\sigma}\cdot c_{A\omega}\left(\mathbf{v}_{A\omega}-\mathbf{w}_{\omega\sigma}\right)\mathrm{d}A=\frac{a_{\omega\sigma}E_0(\langle c_{A\omega}\rangle^{\omega}-\alpha_1\langle c_{A\sigma}\rangle^{\sigma})}{\alpha_2+\alpha_3\langle c_{A\omega}\rangle^{\omega}+\alpha_4\langle c_{A\sigma}\rangle^{\sigma}+\alpha_5\langle c_{A\omega}\rangle^{\omega}\langle c_{A\sigma}\rangle^{\sigma}} \tag{3.43a}$$

$$\frac{1}{V}\int_{A_{\omega\sigma}}\mathbf{n}_{\omega\sigma}\cdot c_{i\omega}\left(\mathbf{v}_{i\omega}-\mathbf{w}_{\omega\sigma}\right)\mathrm{d}A=a_{\omega\sigma}k_i^{\omega\sigma}\left(\langle c_{i\omega}\rangle^{\omega}-K_{eq,i}^{\omega\sigma}\langle c_{i\sigma}\rangle^{\sigma}\right)\quad i=B\to D$$

$$\frac{1}{V}\int_{A_{\omega\sigma}}\mathbf{n}_{\omega\sigma}\cdot c_{E\omega}\left(\mathbf{v}_{E\omega}-\mathbf{w}_{\omega\sigma}\right)\mathrm{d}A=0 \tag{3.43b}$$

where area averaged concentrations and volume averaged concentrations were equalized.

Integrated total mass flux

Therefore, the total mass flux through the cells-EPS interface in a REV, per unit volume of REV, is obtained by summing Eqs. (3.43) after multiplying by respective molar mass

$$\begin{aligned}&\frac{1}{V}\int_{A_{\omega\sigma}}\mathbf{n}_{\omega\sigma}\cdot\rho_{\omega}\left(\mathbf{v}_{\omega}-\mathbf{w}_{\omega\sigma}\right)\mathrm{d}A\\ =&a_{\omega\sigma}\frac{M_A E_0(\langle c_{A\omega}\rangle^{\omega}-\alpha_1\langle c_{A\sigma}\rangle^{\sigma})}{\alpha_2+\alpha_3\langle c_{A\omega}\rangle^{\omega}+\alpha_4\langle c_{A\sigma}\rangle^{\sigma}+\alpha_5\langle c_{A\omega}\rangle^{\omega}\langle c_{A\sigma}\rangle^{\sigma}}+a_{\omega\sigma}\sum_{i=B\to D}M_i k_i^{\omega\sigma}\left(\langle c_{i\omega}\rangle^{\omega}-K_{eq,i}^{\omega\sigma}\langle c_{i\sigma}\rangle^{\sigma}\right)\\ =&\frac{1}{V}\int_{A_{\omega\sigma}}\mathbf{n}_{\omega\sigma}\cdot\rho_{\sigma}\left(\mathbf{v}_{\sigma}-\mathbf{w}_{\omega\sigma}\right)\mathrm{d}A\end{aligned} \tag{3.44}$$

Stress tensor

The general form of the momentum transport boundary condition [229] gives

$$(\mathbf{T}_{\omega}-\mathbf{T}_{\sigma})\cdot\mathbf{n}_{\omega\sigma}=0 \tag{3.45}$$

with the same assumptions as for the jump condition (3.38).

4.5 SYSTEM OF EQUATIONS

Finally, the conservation equations of mass (total and for each species) and momentum for the three regions can be expressed by

ω-region

$$\frac{\partial \rho_\omega}{\partial t} + \nabla \cdot (\rho_\omega \mathbf{v}_\omega) = 0 \quad \text{in the } \omega\text{-region} \tag{3.46a}$$

$$\frac{\partial (\rho_\omega \mathbf{v}_\omega)}{\partial t} = \rho_\omega \mathbf{g} + \nabla \cdot \mathbf{T}_\omega - \mu_\beta \mathbf{K}_\omega^{-1} \cdot \mathbf{v}_\omega, \quad \text{in the } \omega\text{-region} \tag{3.46b}$$

$$\text{with} \quad \mathbf{T}_\omega = -p_\omega \mathbf{I} + \mu_\beta \left[\nabla \mathbf{v}_\omega + (\nabla \mathbf{v}_\omega)^T\right] \tag{3.46c}$$

$$\frac{\partial c_{i\omega}}{\partial t} + \nabla \cdot (c_{i\omega} \mathbf{v}_\omega) = D_{i\beta} \nabla^2 c_{i\omega} \quad i = A, B, C \quad \text{in the } \omega\text{-region} \tag{3.46d}$$

$$c_{E\omega} = 0 \quad \text{in the } \omega\text{-region} \tag{3.46e}$$

η-region

$$\frac{\partial \rho_\eta}{\partial t} + \nabla \cdot (\rho_\eta \mathbf{v}_\eta) = 0 \quad \text{in the } \eta\text{-region} \tag{3.47a}$$

$$\frac{\partial (\rho_\eta \mathbf{v}_\eta)}{\partial t} = \rho_\eta \mathbf{g} + \nabla \cdot \mathbf{T}_\eta, \quad \text{in the } \eta\text{-region} \tag{3.47b}$$

$$\text{with} \quad \mathbf{T}_\eta = -p_\eta \mathbf{I} + \mu_\beta \left[\nabla \mathbf{v}_\eta + (\nabla \mathbf{v}_\eta)^T\right] \tag{3.47c}$$

$$\frac{\partial c_{i\eta}}{\partial t} + \nabla \cdot (c_{i\eta} \mathbf{v}_\eta) = D_{i\beta} \nabla^2 c_{i\eta} \quad i = A, B, C \quad \text{in the } \eta\text{-region} \tag{3.47d}$$

$$c_{E\eta} = 0 \quad \text{in the } \eta\text{-region} \tag{3.47e}$$

σ-region

$$\frac{\partial \rho_\sigma}{\partial t} + \nabla \cdot (\rho_\sigma \mathbf{v}_\sigma) = 0 \quad \text{in the } \sigma\text{-region} \tag{3.48a}$$

$$\frac{\partial (\rho_\sigma \mathbf{v}_\sigma)}{\partial t} = \rho_\sigma \mathbf{g} + \nabla \cdot \mathbf{T}_\sigma \quad \text{in the } \sigma\text{-region} \tag{3.48b}$$

$$\text{with} \quad \mathbf{T}_\sigma = -p_\sigma \mathbf{I} + \mu_\gamma \left[\nabla \mathbf{v}_\sigma + (\nabla \mathbf{v}_\sigma)^T\right] \tag{3.48c}$$

$$\frac{\partial c_{i\sigma}}{\partial t} + \nabla \cdot (c_{i\sigma} \mathbf{v}_\sigma) = D_{i\gamma} \nabla^2 c_{i\sigma} + R_i(c_{A\sigma}) \quad i = A, B, C, E \quad \text{in the } \sigma\text{-region} \tag{3.48d}$$

along with boundary/jump conditions

$\eta - \omega$ **inter-region**

$$\mathbf{n}_{\eta\omega} \cdot c_{i\eta}(\mathbf{v}_{i\eta} - \mathbf{w}_{\eta\omega}) = \varepsilon_{\beta,\omega}\mathbf{n}_{\eta\omega} \cdot c_{i\omega}(\mathbf{v}_{i\omega} - \mathbf{w}_{\eta\omega}) = k_i^{\eta\omega}(c_{i\eta} - c_{i\omega}) \quad i = A, B, C, E \quad \text{at } A_{\eta\omega} \tag{3.49a}$$

$$\mathbf{n}_{\eta\omega} \cdot \rho_{\eta}(\mathbf{v}_{\eta} - \mathbf{w}_{\eta\omega}) = \varepsilon_{\beta,\omega}\mathbf{n}_{\eta\omega} \cdot \rho_{\omega}(\mathbf{v}_{\omega} - \mathbf{w}_{\eta\omega}) = \sum_{i=A\to E} M_i k_i^{\eta\omega}\,(c_{i\eta} - c_{i\omega}) \quad \text{at } A_{\eta\omega} \tag{3.49b}$$

$$(\mathbf{T}_{\eta} - \mathbf{T}_{\omega}) \cdot \mathbf{n}_{\eta\omega} = 0 \quad \text{at } A_{\eta\omega} \tag{3.49c}$$

$\omega - \sigma$ **inter-region**

$$\begin{aligned} &\mathbf{n}_{\omega\sigma} \cdot c_{A\omega}(\mathbf{v}_{A\omega} - \mathbf{w}_{\omega\sigma}) \\ &= \mathbf{n}_{\omega\sigma} \cdot c_{A\sigma}(\mathbf{v}_{A\sigma} - \mathbf{w}_{\omega\sigma}) = \frac{E_0(c_{A\omega} - \alpha_1 c_{A\sigma})}{\alpha_2 + \alpha_3 c_{A\omega} + \alpha_4 c_{A\sigma} + \alpha_5 c_{A\omega}c_{A\sigma}} \quad \text{at } A_{\omega\sigma} \end{aligned} \tag{3.50a}$$

$$\begin{aligned} &\mathbf{n}_{\omega\sigma} \cdot c_{i\omega}(\mathbf{v}_{i\omega} - \mathbf{w}_{\omega\sigma}) = \mathbf{n}_{\omega\sigma} \cdot c_{i\sigma}(\mathbf{v}_{i\sigma} - \mathbf{w}_{\omega\sigma}) \\ &= k_i^{\omega\sigma}(c_{i\omega} - K_{eq,i}^{\omega\sigma} c_{i\sigma}) \quad i = B, C \quad \text{at } A_{\omega\sigma} \end{aligned} \tag{3.50b}$$

$$\mathbf{n}_{\omega\sigma} \cdot c_{E\omega}(\mathbf{v}_{E\omega} - \mathbf{w}_{\omega\sigma}) = \mathbf{n}_{\omega\sigma} \cdot c_{E\sigma}(\mathbf{v}_{E\sigma} - \mathbf{w}_{\omega\sigma}) = 0 \quad \text{at } A_{\omega\sigma} \tag{3.50c}$$

$$\begin{aligned} &\mathbf{n}_{\omega\sigma} \cdot \rho_{\omega}(\mathbf{v}_{\omega} - \mathbf{w}_{\omega\sigma}) = \mathbf{n}_{\omega\sigma} \cdot \rho_{\sigma}(\mathbf{v}_{\sigma} - \mathbf{w}_{\omega\sigma}) \\ &= \frac{M_A E_0(c_{A\omega} - \alpha_1 c_{A\sigma})}{\alpha_2 + \alpha_3 c_{A\omega} + \alpha_4 c_{A\sigma} + \alpha_5 c_{A\omega}c_{A\sigma}} + \sum_{i=B,C,D} M_i k_i^{\omega\sigma}(c_{i\omega} - K_{eq,i}^{\omega\sigma} c_{i\sigma}) \quad \text{at } A_{\omega\sigma} \end{aligned} \tag{3.50d}$$

$$(\mathbf{T}_{\omega} - \mathbf{T}_{\sigma}) \cdot \mathbf{n}_{\omega\sigma} = 0 \quad \text{at } A_{\omega\sigma} \tag{3.50e}$$

This problem is well-posed: the number of equations and the number of boundary conditions are correct. Adding transport equations and boundary conditions for species D (solvent, water) would be redundant.

5 UPSCALED MODEL AT MACROSCOPIC SCALE

The development of the macroscopic model is first based on the intuitive idea that the intrisic velocity in the σ-region should not play a significant influence on the whole system hydrodynamics and on species transport. For hydrodynamics, the conditions under which the convective effects involving this velocity are negligible will be assumed to be verified. For species transport, diffusion in the σ-region will be supposed to be much more efficient than convection. Therefore, solving for the continuity-momentum equations in the σ-region will not be necessary anymore.

Even with these assumptions, the general system is in non local equilibrium: it is very difficult (if not impossible) to solve closure problems and to obtain a set of closed macroscopic equations. Furthermore, the objective of this work is to predict biofilm growth and a precise knowledge of the different velocity and concentration fields should not be necessary. In the following, local mechanical and mass equilibrium are assumed between ω-region and η-region. Indeed, if the porosity of the fibers in the ω-region is moderate, the flows in the η and ω regions are very similar. Therefore, the assumption of local mechanical equilibrium makes sense. That way, the mechanical problem reduces to the determination of one (equilibrium) velocity. For the same reasons, local mass equilibrium between these two regions will be assumed.

5.1 MASS BALANCE EQUATIONS

5.1.1 GENERAL EXPRESSIONS

Applying the averaging theorems to Eqs. (3.46a), (3.47a) and (3.48a) gives rise to

$$\frac{\partial \langle \rho_\omega \rangle_\omega}{\partial t} + \frac{1}{V} \int_{A_{\omega\sigma}} \mathbf{n}_{\omega\sigma} \cdot \rho_\omega \left(\mathbf{v}_\omega - \mathbf{w}_{\omega\sigma} \right) \mathrm{d}A + \frac{1}{V} \int_{A_{\eta\omega}} \mathbf{n}_{\omega\eta} \cdot \rho_\omega \left(\mathbf{v}_\omega - \mathbf{w}_{\eta\omega} \right) \mathrm{d}A + \nabla \cdot \langle \rho_\omega \mathbf{v}_\omega \rangle_\omega = 0 \tag{3.51a}$$

$$\frac{\partial \langle \rho_\eta \rangle_\eta}{\partial t} + \frac{1}{V} \int_{A_{\eta\omega}} \mathbf{n}_{\eta\omega} \cdot \rho_\eta \left(\mathbf{v}_\eta - \mathbf{w}_{\eta\omega} \right) \mathrm{d}A + \nabla \cdot \langle \rho_\eta \mathbf{v}_\eta \rangle_\eta = 0 \tag{3.51b}$$

$$\frac{\partial \langle \rho_\sigma \rangle_\sigma}{\partial t} + \frac{1}{V} \int_{A_{\omega\sigma}} \mathbf{n}_{\sigma\omega} \cdot \rho_\sigma \left(\mathbf{v}_\sigma - \mathbf{w}_{\omega\sigma} \right) \mathrm{d}A + \nabla \cdot \langle \rho_\sigma \mathbf{v}_\sigma \rangle_\sigma = 0 \tag{3.51c}$$

The density and velocity fields in the convective terms are now decomposed according to [91]

$$\rho_\alpha = \langle \rho_\alpha \rangle^\alpha + \tilde{\rho}_\alpha, \quad \alpha = \omega, \eta, \sigma \tag{3.52a}$$

$$\mathbf{v}_\alpha = \langle \mathbf{v}_\alpha \rangle^\alpha + \tilde{\mathbf{v}}_\alpha, \quad \alpha = \omega, \eta, \sigma \tag{3.52b}$$

Using

$$\langle \rho_\alpha \mathbf{v}_\alpha \rangle_\alpha = \langle \rho_\alpha \rangle^\alpha \langle \mathbf{v}_\alpha \rangle_\alpha + \langle \tilde{\rho}_\alpha \tilde{\mathbf{v}}_\alpha \rangle_\alpha \tag{3.53}$$

$$\nabla \cdot \langle \tilde{\rho}_\alpha \tilde{\mathbf{v}}_\alpha \rangle_\alpha \ll \nabla \cdot \left(\langle \rho_\alpha \rangle^\alpha \langle \mathbf{v}_\alpha \rangle_\alpha \right) \tag{3.54}$$

leads to

$$\langle\rho_\omega\rangle^\omega\frac{\partial\varepsilon_\omega}{\partial t}+\varepsilon_\omega\langle\rho_\omega\rangle^\omega\nabla\cdot\langle\mathbf{v}_\omega\rangle^\omega$$
$$=-\frac{1}{V}\int\limits_{A_{\omega\sigma}}\mathbf{n}_{\omega\sigma}\cdot\rho_\omega\left(\mathbf{v}_\omega-\mathbf{w}_{\omega\sigma}\right)\mathrm{d}A-\frac{1}{V}\int\limits_{A_{\eta\omega}}\mathbf{n}_{\omega\eta}\cdot\rho_\omega\left(\mathbf{v}_\omega-\mathbf{w}_{\eta\omega}\right)\mathrm{d}A \tag{3.55a}$$

$$\langle\rho_\eta\rangle^\eta\frac{\partial\varepsilon_\eta}{\partial t}+\varepsilon_\eta\langle\rho_\eta\rangle^\eta\nabla\cdot\langle\mathbf{v}_\eta\rangle^\eta=\frac{1}{V}\int\limits_{A_{\eta\omega}}\mathbf{n}_{\omega\eta}\cdot\rho_\eta\left(\mathbf{v}_\eta-\mathbf{w}_{\eta\omega}\right)\mathrm{d}A \tag{3.55b}$$

$$\langle\rho_\sigma\rangle^\sigma\frac{\partial\varepsilon_\sigma}{\partial t}+\varepsilon_\sigma\langle\rho_\sigma\rangle^\sigma\nabla\cdot\langle\mathbf{v}_\sigma\rangle^\sigma=\frac{1}{V}\int\limits_{A_{\omega\sigma}}\mathbf{n}_{\omega\sigma}\cdot\rho_\sigma\left(\mathbf{v}_\sigma-\mathbf{w}_{\omega\sigma}\right)\mathrm{d}A \tag{3.55c}$$

where $\langle.\rangle_\alpha=\varepsilon_\alpha\langle.\rangle^\alpha$ $(\alpha=\omega,\eta,\sigma)$ was used and intrinsic densities $\langle\rho_\alpha\rangle^\alpha$ were assumed to be almost constant in space and time, which is a reasonable hypothesis.

5.1.2 σ-REGION

For the σ-region, Eq. (3.55c) can be simplified again because the convective effects are assumed to be neglegible. It gives

$$\frac{\partial\varepsilon_\sigma}{\partial t}=\frac{1}{\langle\rho_\sigma\rangle^\sigma}\frac{1}{V}\int\limits_{A_{\omega\sigma}}\mathbf{n}_{\omega\sigma}\cdot\rho_\sigma\left(\mathbf{v}_\sigma-\mathbf{w}_{\omega\sigma}\right)\mathrm{d}A \tag{3.56}$$

The length scale associated with this approximation is detailed in Appendix B.

The integration of Eq. (3.44) into Eq. (3.56) finally gives

$$\frac{\partial\varepsilon_\sigma}{\partial t}=\frac{a_{\omega\sigma}}{\langle\rho_\sigma\rangle^\sigma}\frac{M_AE_0(\langle c_{A\omega}\rangle^\omega-\alpha_1\langle c_{A\sigma}\rangle^\sigma)}{\alpha_2+\alpha_3\langle c_{A\omega}\rangle^\omega+\alpha_4\langle c_{A\sigma}\rangle^\sigma+\alpha_5\langle c_{A\omega}\rangle^\omega\langle c_{A\sigma}\rangle^\sigma}$$
$$+\frac{a_{\omega\sigma}}{\langle\rho_\sigma\rangle^\sigma}\sum_{i=B\to D}M_ik_i^{\omega\sigma}\left(\langle c_{i\omega}\rangle^\omega-K_{eq,i}^{\omega\sigma}\langle c_{i\sigma}\rangle^\sigma\right) \tag{3.57}$$

The macroscopic mass balance equation in the σ-region, which is useless because the velocity field $\mathbf{v}_\sigma$ will not be needed anywhere, has turned into a useful closed macroscopic equation for the evolution with time of ε_σ.

5.1.3 $\eta - \omega$-REGION

In the same manner as for the σ-region, the expressions

$$\frac{\partial \varepsilon_\omega}{\partial t} = -\frac{1}{V}\int_{A_{\eta\omega}} \mathbf{n}_{\eta\omega}\cdot\mathbf{w}_{\eta\omega}\mathrm{d}A + \frac{1}{V}\int_{A_{\omega\sigma}} \mathbf{n}_{\omega\sigma}\cdot\mathbf{w}_{\omega\sigma}\mathrm{d}A \tag{3.58a}$$

$$\frac{\partial \varepsilon_\eta}{\partial t} = \frac{1}{V}\int_{A_{\eta\omega}} \mathbf{n}_{\eta\omega}\cdot\mathbf{w}_{\eta\omega}\mathrm{d}A \tag{3.58b}$$

can not be used under this form. But because there is local $\omega - \eta$ equilibrium, the time evolution of the global $\eta\omega$-region porosity, $\varepsilon_{\omega\eta} = \varepsilon_\omega + \varepsilon_\eta$, can be obtained by

$$\frac{\partial \varepsilon_{\omega\eta}}{\partial t} = -\frac{\partial \varepsilon_\sigma}{\partial t} \tag{3.59}$$

and Eq. (3.57).

In order to get the equilibrium version for the mass balance equation, the porosity-weighted density, velocity and pressure for the $\eta\omega$-region are defined as

$$(\varepsilon_\omega + \varepsilon_\eta)\{\rho\} = \varepsilon_\omega\langle\rho_\omega\rangle^\omega + \varepsilon_\eta\langle\rho_\eta\rangle^\eta \tag{3.60}$$

$$(\varepsilon_\omega + \varepsilon_\eta)\{\mathbf{v}\} = \varepsilon_\omega\langle\mathbf{v}_\omega\rangle^\omega + \varepsilon_\eta\langle\mathbf{v}_\eta\rangle^\eta \tag{3.61}$$

$$(\varepsilon_\omega + \varepsilon_\eta)\{p\} = \varepsilon_\omega\langle p_\omega\rangle^\omega + \varepsilon_\eta\langle p_\eta\rangle^\eta \tag{3.62}$$

Local mass equilibrium ($\langle\rho_\omega\rangle^\omega \approx \langle\rho_\eta\rangle^\eta \approx \{\rho\}$) and local mechanical equilibrium ($\langle\mathbf{v}_\omega\rangle^\omega \approx \langle\mathbf{v}_\eta\rangle^\eta \approx \{\mathbf{v}\}$, $\langle p_\omega\rangle^\omega \approx \langle p_\eta\rangle^\eta \approx \{p\}$) are assumed to be valid. The conditions of validity of equilibrium are not detailed here.

Summing Eq. (3.55a) multiplied by $\varepsilon_{\beta,\omega}$ and Eq. (3.55b) leads to

$$\frac{1}{\varepsilon_\omega + \varepsilon_\eta}\frac{\partial\left(\varepsilon_\omega + \varepsilon_\eta\right)\{\rho\}}{\partial t} + \{\rho\}\nabla\cdot\{\mathbf{v}\} = -\frac{1}{\varepsilon_\omega + \varepsilon_\eta}\frac{1}{V}\int\limits_{A_{\omega\sigma}} \mathbf{n}_{\omega\sigma}\cdot\rho_\omega\left(\mathbf{v}_\omega - \mathbf{w}_{\omega\sigma}\right)\mathrm{d}A \tag{3.63a}$$

With Eq. (3.44), it finally gives

$$\begin{aligned}&\frac{1}{\varepsilon_\omega + \varepsilon_\eta}\frac{\partial\left(\varepsilon_\omega + \varepsilon_\eta\right)\{\rho\}}{\partial t} + \{\rho\}\nabla\cdot\{\mathbf{v}\}\\ &= -\frac{a_{\omega\sigma}}{\varepsilon_\omega + \varepsilon_\eta}\frac{M_A E_0(\langle c_{A\omega}\rangle^\omega - \alpha_1\langle c_{A\sigma}\rangle^\sigma)}{\alpha_2 + \alpha_3\langle c_{A\omega}\rangle^\omega + \alpha_4\langle c_{A\sigma}\rangle^\sigma + \alpha_5\langle c_{A\omega}\rangle^\omega\langle c_{A\sigma}\rangle^\sigma} - a_{\omega\sigma}\sum_{i=B\to D} M_i k_i^{\omega\sigma}\left(\langle c_{i\omega}\rangle^\omega - K_{eq,i}^{\omega\sigma}\langle c_{i\sigma}\rangle^\sigma\right)\end{aligned} \tag{3.64a}$$

which is the equilibrium version of the mass balance equation.

5.1.4 SPECIFIC AREA EVOLUTION

The specific surface area is defined by

$$a_{\omega\sigma} = \frac{A_{\omega\sigma}}{V} = \varepsilon_\sigma \frac{A_{\omega\sigma}}{V_\sigma} \tag{3.65}$$

With the approximations

$$\frac{A_{\omega\sigma}}{V_\sigma} \sim \frac{\varepsilon_\sigma}{l_\sigma} \sim \varepsilon_\sigma \left(V_\sigma\right)^{-1/3} \tag{3.66}$$

the following equation is proposed for the expression of specific surface area

$$\frac{a_{\omega\sigma}}{{a_{\omega\sigma}}^0} = \left(\frac{\varepsilon_\sigma}{{\varepsilon_\sigma}^0}\right)^{2/3} \tag{3.67}$$

reminding that $\varepsilon_\sigma = V_\sigma/V$. Once porositiy ε_σ is known at time t, specific area $a_{\omega\sigma}$ at time t can be calculated from Eq. (3.67), provided the initial values $a^0_{\omega\sigma}$ and ${\varepsilon_\sigma}^0$ are known.

5.2 MOMENTUM BALANCE EQUATIONS

The following results, obtained by applying the spatial averaging theorems to the constant quantity 1 in the three regions, are reminded

$$\nabla\varepsilon_\omega = \frac{1}{V}\int_{A_{\eta\omega}} \mathbf{n}_{\eta\omega}\mathrm{d}A + \frac{1}{V}\int_{A_{\omega\sigma}} \mathbf{n}_{\omega\sigma}\mathrm{d}A \tag{3.68a}$$

$$\nabla\varepsilon_\eta = -\frac{1}{V}\int_{A_{\eta\omega}} \mathbf{n}_{\eta\omega}\mathrm{d}A \tag{3.68b}$$

$$\nabla\varepsilon_\sigma = -\frac{1}{V}\int_{A_{\omega\sigma}} \mathbf{n}_{\sigma\omega}\mathrm{d}A \tag{3.68c}$$

Since spatial homogeneity is assumed in the three regions, these three quantities are almost zero.

5.2.1 GENERAL EXPRESSIONS

Applying the superficial averaging theorem to Eq. (3.46b) in the ω-region leads to

$$\left\langle \frac{\partial(\rho_\omega \mathbf{v}_\omega)}{\partial t} \right\rangle_\omega = \langle\rho_\omega\rangle_\omega \mathbf{g} + \langle\nabla\cdot\mathbf{T}_\omega\rangle_\omega - \mu_\beta \mathbf{K}_\omega^{-1}\cdot\langle\mathbf{v}_\omega\rangle_\omega \tag{3.69}$$

because the permeability $\mathbf{K}_\omega$ is a constant. The stress tensor is given by Eq. (3.46c)

$$\mathbf{T}_\omega = -p_\omega\mathbf{I} + \mu_\beta\left[\nabla\mathbf{v}_\omega + (\nabla\mathbf{v}_\omega)^T\right] \tag{3.70}$$

Each term in Eq. (3.69) will now be treated separately, using the general transport theorem [229] and the spatial averaging theorem [105].

Accumulation term

The accumulation term can be written

$$\left\langle \frac{\partial(\rho_\omega \mathbf{v}_\omega)}{\partial t} \right\rangle_\omega = \frac{\partial \langle \rho_\omega \mathbf{v}_\omega \rangle_\omega}{\partial t} - \frac{1}{V} \int\limits_{A_{\eta\omega}} (\mathbf{n}_{\omega\eta} \cdot \mathbf{w}_{\eta\omega}) \, \rho_\omega \mathbf{v}_\omega \mathrm{d}A - \frac{1}{V} \int\limits_{A_{\omega\sigma}} (\mathbf{n}_{\omega\sigma} \cdot \mathbf{w}_{\omega\sigma}) \, \rho_\omega \mathbf{v}_\omega \mathrm{d}A \tag{3.71}$$

Following [261], $\langle \rho_\omega \mathbf{v}_\omega \rangle_\omega \approx \langle \rho_\omega \rangle^\omega \langle \mathbf{v}_\omega \rangle_\omega$ (with a length scale constraint). $\langle \rho_\omega \rangle^\omega$ being a constant, Eq. (3.71) becomes

$$\left\langle \frac{\partial(\rho_\omega \mathbf{v}_\omega)}{\partial t} \right\rangle_\omega = \langle \rho_\omega \rangle^\omega \frac{\partial \langle \mathbf{v}_\omega \rangle_\omega}{\partial t} - \frac{1}{V} \int\limits_{A_{\eta\omega}} \mathbf{n}_{\omega\eta} \cdot (\rho_\omega \mathbf{w}_{\eta\omega} \mathbf{v}_\omega) \, \mathrm{d}A - \frac{1}{V} \int\limits_{A_{\omega\sigma}} \mathbf{n}_{\omega\sigma} \cdot (\rho_\omega \mathbf{w}_{\omega\sigma} \mathbf{v}_\omega) \, \mathrm{d}A \tag{3.72}$$

Stress term

The stress term can be expressed as

$$\langle \nabla \cdot \mathbf{T}_\omega \rangle_\omega = \nabla \cdot \langle \mathbf{T}_\omega \rangle_\omega + \frac{1}{V} \int\limits_{A_{\eta\omega}} \mathbf{n}_{\omega\eta} \cdot \mathbf{T}_\omega \mathrm{d}A + \frac{1}{V} \int\limits_{A_{\omega\sigma}} \mathbf{n}_{\omega\sigma} \cdot \mathbf{T}_\omega \mathrm{d}A \tag{3.73}$$

On the basis of the spatial averaging theorem [105]

$$\begin{aligned} \nabla \cdot \langle \mathbf{T}_\omega \rangle_\omega = & - \nabla \langle p_\omega \rangle_\omega + \mu_\beta \nabla^2 \langle \mathbf{v}_\omega \rangle_\omega \\ & + \mu_\beta \nabla \cdot \left(\frac{1}{V} \int\limits_{A_{\eta\omega}} \left[\mathbf{n}_{\omega\eta} \mathbf{v}_\omega + (\mathbf{n}_{\omega\eta} \mathbf{v}_\omega)^T \right] \mathrm{d}A + \frac{1}{V} \int\limits_{A_{\omega\sigma}} \left[\mathbf{n}_{\omega\sigma} \mathbf{v}_\omega + (\mathbf{n}_{\omega\sigma} \mathbf{v}_\omega)^T \right] \mathrm{d}A \right) \end{aligned} \tag{3.74}$$

where the term in $\nabla (\nabla \cdot \langle \mathbf{v}_\omega \rangle_\omega)$ was neglected. This assumption is valid under some constaints on time/length scales but it is reasonable since $\langle \rho_\omega \rangle^\omega$ was taken as a constant

In addition, using the relation between superficial and intrinsic averages into Eq. (3.74) yields, after neglecting the spatial variations of ε_ω,

$$\begin{aligned} \nabla \cdot \langle \mathbf{T}_\omega \rangle_\omega = & - \varepsilon_\omega \nabla \langle p_\omega \rangle^\omega + \varepsilon_\omega \mu_\beta \nabla^2 \langle \mathbf{v}_\omega \rangle^\omega \\ & + \mu_\beta \nabla \cdot \left(\frac{1}{V} \int\limits_{A_{\eta\omega}} \left[\mathbf{n}_{\omega\eta} \mathbf{v}_\omega + (\mathbf{n}_{\omega\eta} \mathbf{v}_\omega)^T \right] \mathrm{d}A + \frac{1}{V} \int\limits_{A_{\omega\sigma}} \left[\mathbf{n}_{\omega\sigma} \mathbf{v}_\omega + (\mathbf{n}_{\omega\sigma} \mathbf{v}_\omega)^T \right] \mathrm{d}A \right) \end{aligned} \tag{3.75}$$

In this way, Eq. (3.73) takes the form

$$\langle \nabla \cdot \mathbf{T}_\omega \rangle_\omega = -\varepsilon_\omega \nabla \langle p_\omega \rangle^\omega + \varepsilon_\omega \mu_\beta \nabla^2 \langle \mathbf{v}_\omega \rangle^\omega + \frac{1}{V} \int\limits_{A_{\eta\omega}} \mathbf{n}_{\omega\eta} \cdot \mathbf{T}_\omega \mathrm{d}A + \frac{1}{V} \int\limits_{A_{\omega\sigma}} \mathbf{n}_{\omega\sigma} \cdot \mathbf{T}_\omega \mathrm{d}A$$
$$+ \mu_\beta \nabla \cdot \left(\frac{1}{V} \int\limits_{A_{\eta\omega}} \left[\mathbf{n}_{\omega\eta} \mathbf{v}_\omega + (\mathbf{n}_{\omega\eta} \mathbf{v}_\omega)^T \right] \mathrm{d}A + \frac{1}{V} \int\limits_{A_{\omega\sigma}} \left[\mathbf{n}_{\omega\sigma} \mathbf{v}_\omega + (\mathbf{n}_{\omega\sigma} \mathbf{v}_\omega)^T \right] \mathrm{d}A \right) \tag{3.76}$$

Momentum balance equation

Substitution of Eqs. (3.72) and (3.76) into Eq. (3.69) yields

$$\langle \rho_\omega \rangle^\omega \frac{\partial \langle \mathbf{v}_\omega \rangle_\omega}{\partial t} = \varepsilon_\omega \langle \rho_\omega \rangle^\omega \mathbf{g} - \varepsilon_\omega \nabla \langle p_\omega \rangle^\omega + \varepsilon_\omega \mu_\beta \nabla^2 \langle \mathbf{v}_\omega \rangle^\omega - \varepsilon_\omega \mu_\beta \mathbf{K}_\omega^{-1} \cdot \langle \mathbf{v}_\omega \rangle^\omega$$
$$+ \frac{1}{V} \int\limits_{A_{\eta\omega}} \mathbf{n}_{\omega\eta} \cdot (\mathbf{T}_\omega + \rho_\omega \mathbf{v}_\omega \mathbf{w}_{\eta\omega}) \, \mathrm{d}A + \frac{1}{V} \int\limits_{A_{\omega\sigma}} \mathbf{n}_{\omega\sigma} \cdot (\mathbf{T}_\omega + \rho_\omega \mathbf{v}_\omega \mathbf{w}_{\omega\sigma}) \, \mathrm{d}A$$
$$+ \mu_\beta \nabla \cdot \left(\frac{1}{V} \int\limits_{A_{\eta\omega}} \left[\mathbf{n}_{\omega\eta} \mathbf{v}_\omega + (\mathbf{n}_{\omega\eta} \mathbf{v}_\omega)^T \right] \mathrm{d}A + \frac{1}{V} \int\limits_{A_{\omega\sigma}} \left[\mathbf{n}_{\omega\sigma} \mathbf{v}_\omega + (\mathbf{n}_{\omega\sigma} \mathbf{v}_\omega)^T \right] \mathrm{d}A \right) \tag{3.77}$$

With the estimates

$$\mu_\beta \nabla \cdot \left(\frac{1}{V} \int\limits_{A_{\eta\omega}} \left[\mathbf{n}_{\omega\eta} \mathbf{v}_\omega + (\mathbf{n}_{\omega\eta} \mathbf{v}_\omega)^T \right] \mathrm{d}A \right) = \mathbf{O}\left(\frac{\mu_\beta v_\omega}{L \ell_{\omega\eta}} \right) \tag{3.78a}$$

$$\mu_\beta \nabla \cdot \left(\frac{1}{V} \int\limits_{A_{\omega\sigma}} \left[\mathbf{n}_{\omega\sigma} \mathbf{v}_\omega + (\mathbf{n}_{\omega\sigma} \mathbf{v}_\omega)^T \right] \mathrm{d}A \right) = \mathbf{O}\left(\frac{\mu_\beta v_\omega}{L \ell_{\omega\sigma}} \right) \tag{3.78b}$$

$$\frac{1}{V} \int\limits_{A_{\eta\omega}} \mathbf{n}_{\omega\eta} \cdot (\rho_\omega \mathbf{w}_{\eta\omega} \mathbf{v}_\omega) \, \mathrm{d}A = \mathbf{O}\left(\frac{\rho_\omega w_{\omega\eta} v_\omega}{\ell_{\omega\eta}} \right) \quad ; \quad \frac{1}{V} \int\limits_{A_{\omega\sigma}} \mathbf{n}_{\omega\sigma} \cdot (\rho_\omega \mathbf{w}_{\omega\sigma} \mathbf{v}_\omega) \, \mathrm{d}A = \mathbf{O}\left(\frac{\rho_\omega w_{\omega\sigma} v_\omega}{\ell_{\omega\sigma}} \right) \tag{3.78c}$$

$$\frac{1}{V} \int\limits_{A_{\eta\omega}} \mathbf{n}_{\omega\eta} \cdot \mathbf{T}_\omega \mathrm{d}A = \mathbf{O}\left(\frac{\mu_\beta v_\omega}{\ell_{\omega\eta} \ell_\omega} \right) \quad ; \quad \frac{1}{V} \int\limits_{A_{\omega\sigma}} \mathbf{n}_{\omega\sigma} \cdot \mathbf{T}_\omega \mathrm{d}A = \mathbf{O}\left(\frac{\mu_\beta v_\omega}{\ell_{\omega\sigma} \ell_\omega} \right) \tag{3.78d}$$

and the constraints

$$\frac{\rho_\omega w_{\omega\sigma}\ell_\omega}{\mu_\beta} \ll 1 \quad ; \quad \frac{\rho_\omega w_{\omega\eta}\ell_\omega}{\mu_\beta} \ll 1 \quad ; \quad \ell_\omega \ll L \tag{3.79}$$

the first ones being justified if the interfaces $\omega - \sigma$ and $\omega - \eta$ move slowly, Eq. (3.77) can be reduced to

$$\begin{aligned}\langle\rho_\omega\rangle^\omega \frac{\partial\langle\mathbf{v}_\omega\rangle_\omega}{\partial t} =& \varepsilon_\omega \langle\rho_\omega\rangle^\omega \mathbf{g} - \varepsilon_\omega\nabla\langle p_\omega\rangle^\omega + \varepsilon_\omega\mu_\beta\nabla^2\langle\mathbf{v}_\omega\rangle^\omega - \varepsilon_\omega\mu_\beta\mathbf{K}_\omega^{-1}\cdot\langle\mathbf{v}_\omega\rangle^\omega \\ &+ \frac{1}{V}\int\limits_{A_{\eta\omega}} \mathbf{n}_{\omega\eta}\cdot\mathbf{T}_\omega \mathrm{d}A + \frac{1}{V}\int\limits_{A_{\omega\sigma}} \mathbf{n}_{\omega\sigma}\cdot\mathbf{T}_\omega \mathrm{d}A\end{aligned} \tag{3.80}$$

Finally, taking into account the assumption of spatial homogeneity, this equation becomes

$$\begin{aligned}\langle\rho_\omega\rangle^\omega \frac{\partial\left(\varepsilon_\omega\langle\mathbf{v}_\omega\rangle^\omega\right)}{\partial t} =& \varepsilon_\omega \langle\rho_\omega\rangle^\omega \mathbf{g} - \varepsilon_\omega\nabla\langle p_\omega\rangle^\omega + \varepsilon_\omega\mu_\beta\nabla^2\langle\mathbf{v}_\omega\rangle^\omega - \varepsilon_\omega\mu_\beta\mathbf{K}_\omega^{-1}\cdot\langle\mathbf{v}_\omega\rangle^\omega \\ &+ \frac{1}{V}\int\limits_{A_{\eta\omega}} \mathbf{n}_{\omega\eta}\cdot\tilde{\mathbf{T}}_\omega \mathrm{d}A + \frac{1}{V}\int\limits_{A_{\omega\sigma}} \mathbf{n}_{\omega\sigma}\cdot\tilde{\mathbf{T}}_\omega \mathrm{d}A\end{aligned} \tag{3.81}$$

The corresponding expression for the η-region is

$$\langle\rho_\eta\rangle^\eta \frac{\partial\left(\varepsilon_\eta\langle\mathbf{v}_\eta\rangle^\eta\right)}{\partial t} = \varepsilon_\eta \langle\rho_\eta\rangle^\eta \mathbf{g} - \varepsilon_\eta\nabla\langle p_\eta\rangle^\eta + \varepsilon_\eta\mu_\beta\nabla^2\langle\mathbf{v}_\eta\rangle^\eta + \frac{1}{V}\int\limits_{A_{\eta\omega}} \mathbf{n}_{\eta\omega}\cdot\mathbf{T}_\eta \mathrm{d}A \tag{3.82}$$

From boundary condition (3.38), the following relation can be deduced

$$\mathbf{n}_{\eta\omega}\cdot\mathbf{T}_\eta = -\mathbf{n}_{\omega\eta}\cdot\mathbf{T}_\omega \quad \text{at } A_{\eta\omega} \tag{3.83}$$

because $\mathbf{T}_\eta$ and $\mathbf{T}_\omega$ are symmetrical, and then Eq. (3.82) becomes

$$\langle\rho_\eta\rangle^\eta \frac{\partial(\varepsilon_\eta\langle\mathbf{v}_\eta\rangle^\eta)}{\partial t} = \varepsilon_\eta \langle\rho_\eta\rangle^\eta \mathbf{g} - \varepsilon_\eta\nabla\langle p_\eta\rangle^\eta + \varepsilon_\eta\mu_\beta\nabla^2\langle\mathbf{v}_\eta\rangle^\eta - \frac{1}{V}\int\limits_{A_{\eta\omega}} \mathbf{n}_{\omega\eta}\cdot\tilde{\mathbf{T}}_\omega \mathrm{d}A \tag{3.84}$$

where the assumption of spatial homogeneity of the η-region was used.

In the same manner, the averaged momentum balance equation in the σ-region is

$$\langle\rho_\sigma\rangle^\sigma \frac{\partial(\varepsilon_\sigma\langle\mathbf{v}_\sigma\rangle^\sigma)}{\partial t} = \varepsilon_\sigma \langle\rho_\sigma\rangle^\sigma \mathbf{g} - \varepsilon_\sigma\nabla\langle p_\sigma\rangle^\sigma + \varepsilon_\sigma\mu_\gamma\nabla^2\langle\mathbf{v}_\sigma\rangle^\sigma - \frac{1}{V}\int\limits_{A_{\omega\sigma}} \mathbf{n}_{\omega\sigma}\cdot\tilde{\mathbf{T}}_\omega \mathrm{d}A \tag{3.85}$$

where boundary condition (3.45) and spatial homogeneity of the σ-region were used.

5.2.2 σ-REGION

In the model developed here, Eq. (3.85) is not useful anymore because all the convective contributions of the σ-region are neglected.

5.2.3 $\eta\omega$-REGION

The local mechanical equilibrium model results from adding Eqs. (3.81) multiplied by $\varepsilon_{\beta,\omega}$ and (3.84)

$$\frac{1}{\varepsilon_\omega+\varepsilon_\eta}\frac{\partial\left(\left(\varepsilon_\omega+\varepsilon_\eta\right)\{\rho\}\{\mathbf{v}\}\right)}{\partial t}=\{\rho\}\mathbf{g}-\nabla\{p\}+\mu_\beta\nabla^2\{\mathbf{v}\}-\mu_\beta\mathbf{K}^{-1}\cdot\frac{\varepsilon_\omega}{\varepsilon_\omega\varepsilon_{\beta,\omega}+\varepsilon_\eta}\{\mathbf{v}\} \tag{3.86}$$

where

$$\mathbf{K}^{-1}=\mathbf{K}_\omega^{-1}+\varepsilon_\omega\mathbf{K}_{\omega\sigma}^{-1} \tag{3.87a}$$

$$\frac{1}{V_\omega}\int\limits_{A_{\omega\sigma}(t)}\mathbf{n}_{\omega\sigma}\cdot\tilde{\mathbf{T}}_\omega dA=-\mu_\beta\varepsilon_\omega\mathbf{K}_{\omega\sigma}^{-1}\cdot\{\mathbf{v}\} \tag{3.87b}$$

5.3 MASS OF SPECIES BALANCE EQUATIONS

The developments are given for the upscaled form of conservation equation for species A, but they are very similar for the other species.

5.3.1 GENERAL EXPRESSION

Taking the superficial average of Eq. (3.46d) leads to the non-closed macroscopic balance for species A in the ω-region

$$\begin{aligned}&\underbrace{\frac{\partial}{\partial t}\left(\varepsilon_\omega\langle c_{A\omega}\rangle^\omega\right)}_{\text{Accumulation}}+\underbrace{\varepsilon_\omega\langle\mathbf{v}_\omega\rangle^\omega\nabla\cdot\langle c_{A\omega}\rangle^\omega}_{\text{Convection}}+\underbrace{\nabla\cdot\langle\tilde{\mathbf{v}}_\omega\tilde{c}_{A\omega}\rangle}_{\text{Dispersion}}\\&=\underbrace{\nabla\cdot\left[\varepsilon_\omega D_{A\beta}\left(\nabla\langle c_{A\omega}\rangle^\omega+\frac{1}{V_\omega}\int_{A_{\eta\omega}}\mathbf{n}_{\omega\eta}\tilde{c}_{A\omega}\mathrm{d}A+\frac{1}{V_\omega}\int_{A_{\omega\sigma}}\mathbf{n}_{\omega\sigma}\tilde{c}_{A\omega}\mathrm{d}A\right)\right]}_{\text{Diffusion}}\\&+\underbrace{\frac{1}{V}\int_{A_{\eta\omega}}\mathbf{n}_{\eta\omega}\cdot c_{A\omega}(\mathbf{v}_{A\omega}-\mathbf{w}_{\eta\omega})\mathrm{d}A-\frac{1}{V}\int_{A_{\omega\sigma}}\mathbf{n}_{\omega\sigma}\cdot c_{A\omega}(\mathbf{v}_{A\omega}-\mathbf{w}_{\omega\sigma})\mathrm{d}A}_{\text{Interfacial flux}}\end{aligned} \tag{3.88}$$

The same procedure is applied for developing the non-closed macroscopic balance for species A in the η-region from Eq. (3.47d)

$$\underbrace{\frac{\partial}{\partial t}\left(\varepsilon_\eta \langle c_{A\eta}\rangle^\eta\right)}_{\text{Accumulation}} + \underbrace{\varepsilon_\eta \langle \mathbf{v}_\eta\rangle^\eta \nabla\cdot\langle c_{A\eta}\rangle^\eta}_{\text{Convection}} + \underbrace{\nabla\cdot\langle\tilde{\mathbf{v}}_\eta \tilde{c}_{A\eta}\rangle}_{\text{Dispersion}}$$
$$= \underbrace{\nabla\cdot\left[\varepsilon_\eta D_{A\beta}\left(\nabla\langle c_{A\eta}\rangle^\eta + \frac{1}{V_\eta}\int_{A_{\eta\omega}} \mathbf{n}_{\eta\omega}\tilde{c}_{A\eta}\mathrm{d}A\right)\right]}_{\text{Diffusion}} - \underbrace{\frac{1}{V}\int_{A_{\eta\omega}} \mathbf{n}_{\eta\omega}\cdot c_{A\eta}(\mathbf{v}_{A\eta}-\mathbf{w}_{\eta\omega})\mathrm{d}A}_{\text{Interfacial flux}} \tag{3.89}$$

In the same manner, the non-closed macroscopic balance equation for species A in the σ-region is obtained from Eq. (3.48d)

$$\underbrace{\frac{\partial}{\partial t}\left(\varepsilon_\sigma \langle c_{A\sigma}\rangle^\sigma\right)}_{\text{Accumulation}} + \underbrace{\varepsilon_\sigma \langle \mathbf{v}_\sigma\rangle^\sigma \nabla\cdot\langle c_{A\sigma}\rangle^\sigma}_{\text{Convection}} + \underbrace{\nabla\cdot\langle\tilde{\mathbf{v}}_\sigma \tilde{c}_{A\sigma}\rangle}_{\text{Dispersion}}$$
$$= \underbrace{\nabla\cdot\left[\varepsilon_\sigma D_{A\gamma}\left(\nabla\langle c_{A\sigma}\rangle^\sigma + \frac{1}{V_\sigma}\int_{A_{\omega\sigma}} \mathbf{n}_{\sigma\omega}\tilde{c}_{A\sigma}\mathrm{d}A\right)\right]}_{\text{Diffusion}} + \underbrace{\frac{1}{V}\int_{A_{\omega\sigma}} \mathbf{n}_{\omega\sigma}\cdot c_{A\sigma}(\mathbf{v}_{A\sigma}-\mathbf{w}_{\omega\sigma})\mathrm{d}A}_{\text{Interfacial flux}}$$
$$- \underbrace{\mu_A \varepsilon_\sigma \frac{\langle c_{A\sigma}\rangle^\sigma}{K_A + \langle c_{A\sigma}\rangle^\sigma}}_{\text{Reaction}} \tag{3.90}$$

where the average reaction rate was obtained assuming that the variation of coefficients μ_A and K_A are negligible within the average volume and that $\tilde{c}_{A\sigma} \ll \langle c_{A\sigma}\rangle^\sigma$. The conditions of validity of these assumptions can be found in [260].

Chapter 4

6 CLOSURE PROBLEM

In the previous section, the balance equations for mass, momentum and species concentration have been given for each region. However, they contain several non-closed terms. In the following section, the closed form of the macroscopic model and closure problems are determined. The effective properties of each region can then be obtained by solving closure problems, and reflect both microscopic biophysical properties and structure. In the following section, the derivations for the ω-region is presented and the analysis is then extended to the other regions.

6.1 MASS BALANCE EQUATION

Starting from Eq. (3.46a)

$$\frac{\partial \rho_\omega}{\partial t} + \nabla \cdot (\rho_\omega \mathbf{v}_\omega) = 0 \tag{3.91}$$

and using Gray's decomposition leads to

$$\frac{\partial \tilde{\rho}_\omega}{\partial t} + \langle \rho_\omega \rangle^\omega \nabla \cdot \langle \mathbf{v}_\omega \rangle^\omega + \tilde{\rho}_\omega \nabla \cdot \langle \mathbf{v}_\omega \rangle^\omega + \langle \mathbf{v}_\omega \rangle^\omega \cdot \nabla \tilde{\rho}_\omega + \langle \rho_\omega \rangle^\omega \nabla \cdot \tilde{\mathbf{v}}_\omega + \nabla \cdot (\tilde{\rho}_\omega \tilde{\mathbf{v}}_\omega) = 0 \tag{3.92}$$

because $\langle \rho_\omega \rangle^\omega$ has been assumed to be a constant in space and time. With the assumption that the order of magnitude of the deviations of the velocity can, at most, be on the same order as the intrinsic averaged velocity, the following orders of magnitude can be obtained

$$\langle \rho_\omega \rangle^\omega \nabla \cdot \langle \mathbf{v}_\omega \rangle^\omega = \mathbf{O}\left(\frac{\langle \rho_\omega \rangle^\omega \langle v_\omega \rangle^\omega}{L} \right) \tag{3.93a}$$

$$\tilde{\rho}_\omega \nabla \cdot \langle \mathbf{v}_\omega \rangle^\omega = \mathbf{O}\left(\frac{\tilde{\rho}_\omega \langle v_\omega \rangle^\omega}{L} \right) \tag{3.93b}$$

$$\langle \mathbf{v}_\omega \rangle^\omega \cdot \nabla \tilde{\rho}_\omega = \mathbf{O}\left(\frac{\tilde{\rho}_\omega \langle v_\omega \rangle^\omega}{\ell_\omega} \right) \tag{3.93c}$$

$$\langle \rho_\omega \rangle^\omega \nabla \cdot \tilde{\mathbf{v}}_\omega = \mathbf{O}\left(\frac{\langle \rho_\omega \rangle^\omega \langle v_\omega \rangle^\omega}{\ell_\omega} \right) \tag{3.93d}$$

$$\nabla \cdot (\tilde{\rho}_\omega \tilde{\mathbf{v}}_\omega) = \mathbf{O}\left(\frac{\tilde{\rho}_\omega \langle v_\omega \rangle^\omega}{\ell_\omega} \right) \tag{3.93e}$$

Consequently, on the basis of the assumption $\tilde{\rho}_\omega \ll \langle \rho_\omega \rangle^\omega$ and the length-scale constraint $\ell_\omega \ll L$, it gives

$$\frac{\partial \tilde{\rho}_\omega}{\partial t} + \langle \rho_\omega \rangle^\omega \nabla \cdot \tilde{\mathbf{v}}_\omega = 0 \tag{3.94}$$

As a final simplification, quasi-steady state is assumed for the closure problem. To derive the constraint behind this assumption, the order of magnitude of the first term in this equation

$$\frac{\partial \tilde{\rho}_\omega}{\partial t} = \mathbf{O}\left(\frac{\tilde{\rho}_\omega}{t^*_{\tilde{\rho}_\omega}} \right) \tag{3.95}$$

is compared to the estimate given above. It leads us to conclude that whenever the following estimation is valid

$$t^*_{\tilde{\rho}_\omega} \gg \frac{\tilde{\rho}_\omega \ell_\omega}{\langle \rho_\omega \rangle^\omega \langle v_\omega \rangle^\omega} \tag{3.96}$$

Eq. (3.94) may be written as follows

$$\nabla \cdot \tilde{\mathbf{v}}_\omega = 0 \tag{3.97}$$

Extending the analysis to the η-region, it can immediately be deduced that

$$\nabla \cdot \tilde{\mathbf{v}}_\eta = 0 \tag{3.98}$$

6.2 MOMENTUM TRANSPORT EQUATION

In order to derive the local momentum closure equation, the averaged momentum equation of the ω-region, Eq. (3.81), divided by ε_ω

$$\begin{aligned}&\langle\rho_\omega\rangle^\omega \frac{\partial\langle\mathbf{v}_\omega\rangle^\omega}{\partial t} + \langle\rho_\omega\rangle^\omega\langle\mathbf{v}_\omega\rangle^\omega \frac{\partial \ln\varepsilon_\omega}{\partial t}\\ =&\rho_\omega\mathbf{g} - \nabla\langle p_\omega\rangle^\omega + \mu_\beta\nabla^2\langle\mathbf{v}_\omega\rangle^\omega - \mu_\beta\mathbf{K}_\omega^{-1}\cdot\langle\mathbf{v}_\omega\rangle^\omega + \frac{1}{V_\omega}\int\limits_{A_{\eta\omega}}\mathbf{n}_{\omega\eta}\cdot\tilde{\mathbf{T}}_\omega \mathrm{d}A + \frac{1}{V_\omega}\int\limits_{A_{\omega\sigma}}\mathbf{n}_{\omega\sigma}\cdot\tilde{\mathbf{T}}_\omega \mathrm{d}A\end{aligned} \tag{3.99}$$

is substracted from the microscopic one, Eq. (3.19b)

$$\frac{\partial(\rho_\omega\mathbf{v}_\omega)}{\partial t} = \rho_\omega\mathbf{g} - \nabla p_\omega + \mu_\beta\nabla^2\mathbf{v}_\omega - \mu_\beta\mathbf{K}_\omega^{-1}\cdot\mathbf{v}_\omega \quad \text{in the } \omega\text{-region} \tag{3.100}$$

where the term in $\nabla(\nabla\cdot\mathbf{v}_\omega)$ was neglected, with the same proof as before. Assuming that $\tilde{\rho}_\omega \ll \langle\rho_\omega\rangle^\omega$, it leads to

$$\begin{aligned}&\langle\rho_\omega\rangle^\omega \frac{\partial\tilde{\mathbf{v}}_\omega}{\partial t} - \langle\rho_\omega\rangle^\omega\langle\mathbf{v}_\omega\rangle^\omega \frac{\partial \ln\varepsilon_\omega}{\partial t}\\ =&-\nabla\tilde{p}_\omega + \mu_\beta\nabla^2\tilde{\mathbf{v}}_\omega - \mu_\beta\mathbf{K}_\omega^{-1}\cdot\tilde{\mathbf{v}}_\omega - \frac{1}{V_\omega}\int\limits_{A_{\eta\omega}}\mathbf{n}_{\omega\eta}\cdot\tilde{\mathbf{T}}_\omega \mathrm{d}A - \frac{1}{V_\omega}\int\limits_{A_{\omega\sigma}}\mathbf{n}_{\omega\sigma}\cdot\tilde{\mathbf{T}}_\omega \mathrm{d}A\end{aligned} \tag{3.101}$$

In order to derive the time-scale constraint that supports the quasi-steady assumption, the order of magnitude of the first term on the left handside of the above equation

$$\langle\rho_\omega\rangle^\omega \frac{\partial\tilde{\mathbf{v}}_\omega}{\partial t} = \mathbf{O}\left(\frac{\langle\rho_\omega\rangle^\omega\tilde{v}_\omega}{t^*_{\tilde{v}_\omega}}\right) \tag{3.102}$$

can be compared to

$$\mu_\beta\nabla^2\tilde{\mathbf{v}}_\omega = \mathbf{O}\left(\frac{\mu_\beta\langle v_\omega\rangle^\omega}{\ell_\omega^2}\right) \tag{3.103}$$

where the velocity deviations were considered to be, at most, of the same order of magnitude as the intrinsic average velocity. It leads to the following constraint

$$t^*_{\tilde{v}_\omega} \gg \frac{\ell^2_\omega}{\left(\dfrac{\mu_\beta}{\langle\rho_\omega\rangle^\omega}\right)} \tag{3.104}$$

To further simplify this expression, the term

$$\langle\rho_\omega\rangle^\omega\langle\mathbf{v}_\omega\rangle^\omega\frac{\partial \ln\varepsilon_\omega}{\partial t} = \mathbf{O}\left(\langle\rho_\omega\rangle^\omega\langle v_\omega\rangle^\omega\frac{\langle v_\omega\rangle^\omega}{L}\right) \tag{3.105}$$

which order of magnitude has been deduced from Eq. (3.55a), is negligible compared to

$$\mu_\beta\nabla^2\tilde{\mathbf{v}}_\omega = \mathbf{O}\left(\frac{\mu_\beta\langle v_\omega\rangle^\omega}{\ell^2_\omega}\right) \tag{3.106}$$

if the following constraint is met

$$\frac{\langle\rho_\omega\rangle^\omega\langle v_\omega\rangle^\omega L}{\mu_\beta}\left(\frac{\ell_\omega}{L}\right)^2 \ll 1 \tag{3.107}$$

Consequently, and assuming the two previous constraints, Eq. (3.101) reduces to

$$0 = -\nabla\tilde{p}_\omega + \mu_\beta\nabla^2\tilde{\mathbf{v}}_\omega - \mu_\beta\mathbf{K}^{-1}_\omega\cdot\tilde{\mathbf{v}}_\omega - \frac{1}{V_\omega}\int\limits_{A_{\eta\omega}}\mathbf{n}_{\omega\eta}\cdot\tilde{\mathbf{T}}_\omega\mathrm{d}A - \frac{1}{V_\omega}\int\limits_{A_{\omega\sigma}}\mathbf{n}_{\omega\sigma}\cdot\tilde{\mathbf{T}}_\omega\mathrm{d}A \tag{3.108a}$$

Extending the derivations to the η-region leads to

$$0 = -\nabla\tilde{p}_\eta + \mu_\beta\nabla^2\tilde{\mathbf{v}}_\eta + \frac{1}{V_\eta}\int\limits_{A_{\eta\omega}}\mathbf{n}_{\omega\eta}\cdot\tilde{\mathbf{T}}_\omega\mathrm{d}A \tag{3.108b}$$

6.3 MASS CONSERVATION FOR SPECIES i

In order to continue the analysis of deriving one equation of mass conservation for species A, we need to develop the closure problem for spatial deviations of concentration $\tilde{c}_{A\omega}, \tilde{c}_{A\eta}$ and $\tilde{c}_{A\sigma}$. The complete procedure for determination the sources and definition of the closure variables is detailed in [260]. It has been shown that the deviation concentration

can be expressed as

$$\tilde{c}_{A\omega} = \mathbf{d}_{A\omega} \cdot \nabla\{c_A\} \tag{3.109a}$$

$$\tilde{c}_{A\eta} = \mathbf{d}_{A\eta} \cdot \nabla\{c_A\} \tag{3.109b}$$

$$\tilde{c}_{A\sigma} = \alpha_1^{-1}\mathbf{d}_{A\sigma} \cdot \nabla\{c_A\} \tag{3.109c}$$

Where $\mathbf{d}_{A\omega}, \mathbf{d}_{A\eta}$ and $\mathbf{d}_{A\sigma}$ are the closure variables which represent the effects of microstructure of the biofilm to its effective dispersion tensor.

7 CLOSED MODELS

7.1 EQUILIBRIUM MODEL FOR MOMENTUM TRANSPORT

If **local mass equilibrium conditions** are applicable, we have the following models for mass transport in biofilms:

$$\langle\rho_\sigma\rangle^\sigma \frac{\partial\varepsilon_\sigma}{\partial t} - \langle\rho_\sigma\rangle^\sigma \varepsilon_\sigma \overline{\mu M}\left(\frac{\langle c_{A\sigma}\rangle^\sigma}{\langle c_{A\sigma}\rangle^\sigma + K_A}\right) = 0 \tag{3.110a}$$

$$\frac{\partial\{\rho\}}{\partial t} + \langle\rho_\sigma\rangle^\sigma \varepsilon_\sigma \overline{\mu M}\left(\frac{\langle c_{A\sigma}\rangle^\sigma}{\langle c_{A\sigma}\rangle^\sigma + K_A}\right) + \{\rho\}\nabla\cdot\{\mathbf{v}\} = 0 \tag{3.110b}$$

Likewise, **the equilibrium model for the momentum transport** results from adding Eqs. (3.81) and (3.82)

$$\{\rho\}\frac{\partial\{\mathbf{v}\}}{\partial t} = -\nabla\{p\} + \{\rho\}\mathbf{g} + \mu_\beta\nabla^2\{\mathbf{v}\} + \mu_\beta\nabla\left(\nabla\cdot\{\mathbf{v}\}\right) - \mu_\beta\mathbf{K}^{-1}\cdot\varepsilon_\omega\{\mathbf{v}\} \tag{3.111}$$

where

$$\{\mathbf{v}\} = \varepsilon_\eta\langle\mathbf{v}_\eta\rangle^\eta + \varepsilon_\omega\langle\mathbf{v}_\omega\rangle^\omega \tag{3.112a}$$

$$\{\rho\} = \langle\rho_\eta\rangle^\eta = \langle\rho_\omega\rangle^\omega \tag{3.112b}$$

$$\{p\} = \varepsilon_\eta\langle p_\eta\rangle^\eta + \varepsilon_\omega\langle p_\omega\rangle^\omega \tag{3.112c}$$

$$\mathbf{K}^{-1} = \mathbf{K}_\omega^{-1} + \varepsilon_\omega\mathbf{K}_{\omega\sigma}^{-1} \tag{3.112d}$$

$$\frac{1}{V_\omega}\int_{A_{\omega\sigma}} \mathbf{n}_{\omega\sigma}\cdot\tilde{\mathbf{T}}_\omega \mathrm{d}A = -\mu_\beta\varepsilon_\omega\mathbf{K}_{\omega\sigma}^{-1}\cdot\{\mathbf{v}_\omega\} \tag{3.112e}$$

If there is equilibrium between only the η- and ω-regions, we have that the following assumptions are acceptable

$$\langle p_\eta \rangle^\eta = \langle p_\omega \rangle^\omega = \{p\} \tag{3.113a}$$

$$\nabla \langle \mathbf{v}_\eta \rangle^\eta = \nabla \langle \mathbf{v}_\omega \rangle^\omega = \nabla \{\mathbf{v}\} \tag{3.113b}$$

7.2 BOUNDARY CONDITIONS OF THE EQUILIBRIUM MODEL

If one assume that the fluid viscosity is the same in the η-and ω-regions, we have

$\omega - \eta$ inter-region

$$\mathbf{n}_{\eta\omega} \cdot (\tilde{\mathbf{T}}_\eta - \tilde{\mathbf{T}}_\omega) = 0 \tag{3.114}$$

These are the flux boundary conditions for the **η-ω-Equilibrium model**. In the last expression we used

$$\{\mathbf{T}\} = -\{p\}\mathbf{I} + \mu_\beta \left(\nabla \{\mathbf{v}\}\right) \tag{3.115}$$

The velocity boundary conditions for **η-ω-Equilibrium model** are:

$\omega - \eta$ inter-region

$$\mathbf{n}_{\omega\eta} \cdot (\tilde{\mathbf{v}}_\omega - \tilde{\mathbf{v}}_\eta) = 0 \tag{3.116a}$$

$\omega - \sigma$ dividing surface

$$\tilde{\mathbf{v}}_\omega = -\underbrace{\{\mathbf{v}\}}_{\text{source}} \tag{3.116b}$$

And the periodic conditions for the equilibrium model are the same as the non-equilibrium model. The proposition of the closure problem in this case is as following:

$$\tilde{\mathbf{v}}_\alpha = \mathbf{B}_\alpha \cdot \{\mathbf{v}\} \tag{3.117a}$$

$$\frac{\tilde{p}_\alpha}{\mu_\alpha} = \mathbf{c}_\alpha \cdot \{\mathbf{v}\} \tag{3.117b}$$

Finally the **equilibrium model** for momentum transport in biofilm would be expressed.

$$\{\rho\}\frac{\partial \{\mathbf{v}\}}{\partial t} = -\nabla\{p\} + \{\rho\}\mathbf{g} + \mu_\beta \nabla^2 \{\mathbf{v}\} - \mu_\beta \mathbf{K}^{-1} \cdot \varepsilon_\omega \{\mathbf{v}\} \tag{3.118}$$

where

$$\varepsilon_\omega \mathbf{K}_{\omega\sigma}^{-1} = -\frac{1}{V_\omega}\int_{A_{\omega\sigma}} \mathbf{n}_{\omega\sigma} \cdot \tilde{\mathbf{T}}_\omega \mathrm{d}A = c - \frac{1}{V_\omega}\int_{A_{\omega\sigma}} \mathbf{n}_{\omega\sigma} \cdot (-\mathbf{c}_\omega + \nabla \mathbf{B}_\omega)\mathrm{d}A \tag{3.119}$$

7.3 EQUILIBRIUM MODEL FOR MASS CONSERVATION OF SPECIES i

If we use the definition of deviation concentrations (3.109) in function of closure variables and averaged concentration, the closed form of Eq. (3.135) will be derived.

$$\frac{\partial}{\partial t}\left[\left(\varepsilon_\omega+\varepsilon_\eta+\alpha_1^{-1}\varepsilon_\sigma\right)\{c_A\}\right]+\varepsilon_\omega\langle\mathbf{v}_\omega\rangle^\omega\nabla\cdot\{c_A\}+\varepsilon_\eta\langle\mathbf{v}_\eta\rangle^\eta\nabla\cdot\{c_A\}$$
$$=\nabla\cdot(\mathbf{D}_A^*\cdot\nabla\{c_A\})-\mu_A\varepsilon_\sigma\frac{\{c_A\}}{\alpha_1K_A+\{c_A\}} \tag{3.120}$$

Where $\mathbf{D}_A^*$ (total dispersion tensor) is the sum of effective diffusivity and dispersion effects due to convection. The effective diffusivity tensor is defined by

$$\mathbf{D}_{\text{A,eff}}=\left(\varepsilon_\omega D_{A\beta}+\varepsilon_\eta D_{A\beta}+\alpha_1^{-1}\varepsilon_\sigma D_{A\gamma}\right)\mathbf{I}+\frac{D_{A\beta}}{V}\int_{A_{\eta\omega}}\mathbf{n}_{\omega\eta}\mathbf{d}_{A\omega}\mathrm{d}A$$
$$+\frac{D_{A\beta}}{V}\int_{A_{\omega\sigma}}\mathbf{n}_{\omega\sigma}\mathbf{d}_{A\omega}\mathrm{d}A+\frac{D_{A\beta}}{V}\int_{A_{\eta\omega}}\mathbf{n}_{\eta\omega}\mathbf{d}_{A\eta}\mathrm{d}A+\frac{\alpha_1^{-1}D_{A\gamma}}{V}\int_{A\sigma\omega}\mathbf{n}_{\sigma\omega}\mathbf{d}_{A\sigma}\mathrm{d}A \tag{3.121}$$

And the dispersion tensor due to hydrodynamics can also be defined as

$$\mathbf{D}_{\text{A,dis}}=-\langle\tilde{\mathbf{v}}_\omega\tilde{\mathbf{d}}_{A\omega}\rangle-\langle\tilde{\mathbf{v}}_\eta\tilde{\mathbf{d}}_{A\eta}\rangle \tag{3.122}$$

$$\mathbf{D}_A^*=\mathbf{D}_{\text{A,eff}}+\mathbf{D}_{\text{A,dis}} \tag{3.123}$$

Moreover if the conditions of mechanical equilibrium are also satisfied, one can express Eq. (3.120) as

$$\frac{\partial}{\partial t}\left[\left(\varepsilon_\omega+\varepsilon_\eta+\alpha_1^{-1}\varepsilon_\sigma\right)\{c_A\}\right]+\{\mathbf{v}\}\nabla\cdot\{c_A\}=\nabla\cdot(\mathbf{D}_A^*\cdot\nabla\{c_A\})$$
$$-\mu_A\varepsilon_\sigma\frac{\{c_A\}}{\alpha_1K_A+\{c_A\}} \tag{3.124}$$

Where $\{\mathbf{v}\}$ is the averaged equilibrium convection velocity between ω andη regions. (See Appendix B).

$$\{\mathbf{v}\}=\varepsilon_\omega\langle\mathbf{v}_\omega\rangle^\omega+\varepsilon_\eta\langle\mathbf{v}_\eta\rangle^\eta \tag{3.125}$$

Likewise, the same weight average concentration can be defined

$$\{c_B\} = \varepsilon_\eta \langle c_{B\eta}\rangle^\eta + \varepsilon_\omega \langle c_{B\omega}\rangle^\omega + K_{eq,B}\varepsilon_\sigma \langle c_{B\sigma}\rangle^\sigma \tag{3.126a}$$

$$\{c_C\} = \varepsilon_\eta \langle c_{C\eta}\rangle^\eta + \varepsilon_\omega \langle c_{C\omega}\rangle^\omega + K_{eq,C}\varepsilon_\sigma \langle c_{C\sigma}\rangle^\sigma \tag{3.126b}$$

$$\{c_D\} = \varepsilon_\eta \langle c_{D\eta}\rangle^\eta + \varepsilon_\omega \langle c_{D\omega}\rangle^\omega + K_{eq,D}\varepsilon_\sigma \langle c_{D\sigma}\rangle^\sigma \tag{3.126c}$$

$$\{c_E\} = \varepsilon_\sigma \langle c_{E\sigma}\rangle^\sigma \tag{3.126d}$$

The same steps of analysis can be done to derive the one equation averaged weight concentration for other species.

$$\frac{\partial}{\partial t}\left[\left(\varepsilon_\omega + \varepsilon_\eta + K_{eq,B}^{-1}\varepsilon_\sigma\right)\{c_B\}\right] + \varepsilon_\omega \langle \mathbf{v}_\omega\rangle^\omega \nabla\cdot\{c_B\} + \varepsilon_\eta \langle \mathbf{v}_\eta\rangle^\eta \nabla\cdot\{c_B\}$$
$$= \nabla\cdot(\mathbf{D}_B^*\cdot\nabla\{c_B\}) - \eta_1\mu_A\varepsilon_\sigma\frac{\{c_A\}}{\alpha_1 K_A + \{c_A\}} \tag{3.127a}$$

$$\frac{\partial}{\partial t}\left[\left(\varepsilon_\omega + \varepsilon_\eta + K_{eq,C}^{-1}\varepsilon_\sigma\right)\{c_C\}\right] + \varepsilon_\omega \langle \mathbf{v}_\omega\rangle^\omega \nabla\cdot\{c_C\} + \varepsilon_\eta \langle \mathbf{v}_\eta\rangle^\eta \nabla\cdot\{c_C\}$$
$$= \nabla\cdot(\mathbf{D}_C^*\cdot\nabla\{c_C\}) + \eta_2\mu_A\varepsilon_\sigma\frac{\{c_A\}}{\alpha_1 K_A + \{c_A\}} \tag{3.127b}$$

$$\frac{\partial}{\partial t}\left[\left(\varepsilon_\omega + \varepsilon_\eta + K_{eq,D}^{-1}\varepsilon_\sigma\right)\{c_D\}\right] + \varepsilon_\omega \langle \mathbf{v}_\omega\rangle^\omega \nabla\cdot\{c_D\} + \varepsilon_\eta \langle \mathbf{v}_\eta\rangle^\eta \nabla\cdot\{c_D\}$$
$$= \nabla\cdot(\mathbf{D}_D^*\cdot\nabla\{c_D\}) + \eta_3\mu_A\varepsilon_\sigma\frac{\{c_A\}}{\alpha_1 K_A + \{c_A\}} \tag{3.127c}$$

$$\frac{\partial\{c_E\}}{\partial t} = \nabla\cdot(\mathbf{D}_E^*\cdot\nabla\{c_E\}) + \eta_4\mu_A\varepsilon_\sigma\frac{\{c_A\}}{\alpha_1 K_A + \{c_A\}} \tag{3.127d}$$

7.4 LOCAL MASS EQUILIBRIUM

In order to obtain the closed form of conservation equations for species A in the three regions, (3.88), (3.89) and (3.90), the interfacial fluxes could be developed by using boundary conditions (3.49a) and (3.50a). It would lead to a set of three coupled equations for averaged concentrations and then to coupled closure problems, which are very difficult to solve. That is why, in the scope of this work, an equilibrium one-equation model is developed.

The idea of a one-equation model is to define a concentration in the REV that would be representative of what is happening in the three regions and then to determine its conservation equation. It should be equal, in the case of (approximate) local mass equilibrium, i.e.

$$\langle c_{A\eta}\rangle^\eta \approx \langle c_{A\omega}\rangle^\omega \approx \alpha_1 \langle c_{A\sigma}\rangle^\sigma \tag{3.128}$$

to this same value. The *equilibrium weighted average concentration*, mentioned by [260], is then defined as

$$\{c_A\} = \varepsilon_\eta \langle c_{A\eta}\rangle^\eta + \varepsilon_\omega \langle c_{A\omega}\rangle^\omega + \alpha_1 \varepsilon_\sigma \langle c_{A\sigma}\rangle^\sigma \tag{3.129}$$

It is worth noticing that $\{c_A\}$ is different from $\varepsilon_\eta \langle c_{A\eta}\rangle^\eta + \varepsilon_\omega \langle c_{A\omega}\rangle^\omega + \varepsilon_\sigma \langle c_{A\sigma}\rangle^\sigma$, which is the spatial average concentration of species A in the whole volume of the REV, $\frac{1}{V}\int_V c_A \mathrm{d}A$. To find the conservation equation for $\{c_A\}$, the sum of Eqs. (3.88), (3.89) and (3.90) can be made to discard the interfacial fluxes terms

$$\begin{aligned}
&\frac{\partial}{\partial t}\left[\varepsilon_\omega \langle c_{A\omega}\rangle^\omega + \varepsilon_\eta \langle c_{A\eta}\rangle^\eta + \varepsilon_\sigma \langle c_{A\sigma}\rangle^\sigma\right] + \varepsilon_\omega \langle \mathbf{v}_\omega\rangle^\omega \nabla \cdot \langle c_{A\omega}\rangle^\omega + \varepsilon_\eta \langle \mathbf{v}_\eta\rangle^\eta \nabla \cdot \langle c_{A\eta}\rangle^\eta \\
&= \nabla \cdot \left[\varepsilon_\omega D_{A\beta} \nabla \langle c_{A\omega}\rangle^\omega + \varepsilon_\eta D_{A\beta} \nabla \langle c_{A\eta}\rangle^\eta + \varepsilon_\sigma D_{A\gamma} \nabla \langle c_{A\sigma}\rangle^\sigma\right] \\
&+ \nabla \cdot \Big[\frac{D_{A\beta}}{V}\int_{A_{\eta\omega}} \mathbf{n}_{\omega\eta} \tilde{c}_{A\omega} \mathrm{d}A + \frac{D_{A\beta}}{V}\int_{A_{\omega\sigma}} \mathbf{n}_{\omega\sigma} \tilde{c}_{A\omega} \mathrm{d}A + \frac{D_{A\beta}}{V}\int_{A_{\eta\omega}} \mathbf{n}_{\eta\omega} \tilde{c}_{A\eta} \mathrm{d}A \\
&+ \frac{D_{A\gamma}}{V}\int_{A_{\omega\sigma}} \mathbf{n}_{\sigma\omega} \tilde{c}_{A\sigma} \mathrm{d}A\Big] - \nabla \cdot \langle \tilde{\mathbf{v}}_\omega \tilde{c}_{A\omega}\rangle - \nabla \cdot \langle \tilde{\mathbf{v}}_\eta \tilde{c}_{A\eta}\rangle - \mu_A \varepsilon_\sigma \frac{\langle c_{A\sigma}\rangle^\sigma}{K_A + \langle c_{A\sigma}\rangle^\sigma}
\end{aligned} \tag{3.130}$$

The average concentration of each region can be decomposed as the sum of the equilibrium weighted average concentration and a deviation

$$\langle c_{A\omega}\rangle^\omega = \{c_A\} + \hat{c}_{A\omega} \tag{3.131a}$$
$$\langle c_{A\eta}\rangle^\eta = \{c_A\} + \hat{c}_{A\eta} \tag{3.131b}$$
$$\alpha_1 \langle c_{A\sigma}\rangle^\sigma = \{c_A\} + \hat{c}_{A\sigma} \tag{3.131c}$$

Substituting Eq. (3.131) in Eq. (3.130) leads to

$$\begin{aligned}
&\frac{\partial}{\partial t}\left[\left(\varepsilon_\omega + \varepsilon_\eta + \alpha_1^{-1}\varepsilon_\sigma\right)\{c_A\}\right] + \varepsilon_\omega \langle \mathbf{v}_\omega\rangle^\omega \nabla \cdot \{c_A\} + \varepsilon_\eta \langle \mathbf{v}_\eta\rangle^\eta \nabla \cdot \{c_A\} \\
&= \nabla \cdot \left[\left(\varepsilon_\omega D_{A\beta} + \varepsilon_\eta D_{A\beta} + \alpha_1^{-1}\varepsilon_\sigma D_{A\gamma}\right)\nabla\{c_A\}\right] + \nabla \cdot \Big[\frac{D_{A\beta}}{V}\int_{A_{\eta\omega}} \mathbf{n}_{\omega\eta} \tilde{c}_{A\omega} \mathrm{d}A \\
&+ \frac{D_{A\beta}}{V}\int_{A_{\omega\sigma}} \mathbf{n}_{\omega\sigma} \tilde{c}_{A\omega} \mathrm{d}A + \frac{D_{A\beta}}{V}\int_{A_{\eta\omega}} \mathbf{n}_{\eta\omega} \tilde{c}_{A\eta} \mathrm{d}A + \frac{D_{A\gamma}}{V}\int_{A_{\omega\sigma}} \mathbf{n}_{\sigma\omega} \tilde{c}_{A\sigma} \mathrm{d}A\Big] \\
&- \nabla \cdot \langle \tilde{\mathbf{v}}_\omega \tilde{c}_{A\omega}\rangle - \nabla \cdot \langle \tilde{\mathbf{v}}_\eta \tilde{c}_{A\eta}\rangle - \mu_A \varepsilon_\sigma \frac{\{c_A\}}{\alpha_1 K_A + \{c_A\}} \\
&- \frac{\partial}{\partial t}\left(\varepsilon_\omega \hat{c}_{A\omega} + \varepsilon_\eta \hat{c}_{A\eta} + \alpha_1^{-1}\varepsilon_\sigma \hat{c}_{A\sigma}\right) + \nabla \cdot \left[\varepsilon_\omega D_{A\beta} \nabla \hat{c}_{A\omega} + \varepsilon_\eta D_{A\beta} \nabla \hat{c}_{A\eta} + \alpha_1^{-1}\varepsilon_\sigma D_{A\gamma} \nabla \hat{c}_{A\sigma}\right] \\
&- \varepsilon_\omega \langle \mathbf{v}_\omega\rangle^\omega \nabla \cdot \hat{c}_{A\omega} - \varepsilon_\eta \langle \mathbf{v}_\eta\rangle^\eta \nabla \cdot \hat{c}_{A\eta} - \mu_A \varepsilon_\sigma \frac{\hat{c}_{A\sigma}}{\{c_A\} + \alpha_1 K_A + \hat{c}_{A\sigma}}\left(\frac{\alpha_1 K_A}{\{c_A\} + \alpha_1 K_A}\right)
\end{aligned} \tag{3.132}$$

Using Eq. (3.129), spatial deviations are worth

$$\hat{c}_{A\omega} = \varepsilon_\sigma(\langle c_{A\omega}\rangle^\omega - \alpha_1\langle c_{A\sigma}\rangle^\sigma) + \varepsilon_\eta(\langle c_{A\omega}\rangle^\omega - \langle c_{A\eta}\rangle^\eta) \tag{3.133a}$$

$$\hat{c}_{A\eta} = \varepsilon_\sigma(\langle c_{A\eta}\rangle^\eta - \alpha_1\langle c_{A\sigma}\rangle^\sigma) + \varepsilon_\omega(\langle c_{A\eta}\rangle^\eta - \langle c_{A\omega}\rangle^\omega) \tag{3.133b}$$

$$\hat{c}_{A\sigma} = \varepsilon_\omega(\alpha_1\langle c_{A\sigma}\rangle^\sigma - \langle c_{A\omega}\rangle^\omega) + \varepsilon_\eta(\alpha_1\langle c_{A\sigma}\rangle^\sigma - \langle c_{A\eta}\rangle^\eta) \tag{3.133c}$$

Inserting these expressions in Eq. (3.132) gives

$$\begin{aligned}
&\frac{\partial}{\partial t}\left[\left(\varepsilon_\omega + \varepsilon_\eta + \alpha_1^{-1}\varepsilon_\sigma\right)\{c_A\}\right] + \varepsilon_\omega\langle\mathbf{v}_\omega\rangle^\omega\nabla\cdot\{c_A\} + \varepsilon_\eta\langle\mathbf{v}_\eta\rangle^\eta\nabla\cdot\{c_A\} \\
&= \nabla\cdot\left[\left(\varepsilon_\omega D_{A\beta} + \varepsilon_\eta D_{A\beta} + \alpha_1^{-1}\varepsilon_\sigma D_{A\gamma}\right)\nabla\{c_A\}\right] + \nabla\cdot\Big[\frac{D_{A\beta}}{V}\int_{A_{\eta\omega}}\mathbf{n}_{\omega\eta}\tilde{c}_{A\omega}\mathrm{d}A \\
&+ \frac{D_{A\beta}}{V}\int_{A_{\omega\sigma}}\mathbf{n}_{\omega\sigma}\tilde{c}_{A\omega}\mathrm{d}A + \frac{D_{A\beta}}{V}\int_{A_{\eta\omega}}\mathbf{n}_{\eta\omega}\tilde{c}_{A\eta}\mathrm{d}A + \frac{D_{A\gamma}}{V}\int_{A_{\omega\sigma}}\mathbf{n}_{\sigma\omega}\tilde{c}_{A\sigma}\mathrm{d}A\Big] \\
&- \nabla\cdot\langle\tilde{\mathbf{v}}_\omega\tilde{c}_{A\omega}\rangle - \nabla\cdot\langle\tilde{\mathbf{v}}_\eta\tilde{c}_{A\eta}\rangle - \mu_A\varepsilon_\sigma\frac{\{c_A\}}{\alpha_1 K_A + \{c_A\}} \\
&\underbrace{- \varepsilon_\omega\varepsilon_\sigma(1-\alpha_1^{-1})\frac{\partial}{\partial t}(\langle c_{A\omega}\rangle^\omega - \alpha_1\langle c_{A\sigma}\rangle^\sigma) - \varepsilon_\eta\varepsilon_\sigma(1-\alpha_1^{-1})\frac{\partial}{\partial t}(\langle c_{A\eta}\rangle^\eta - \alpha_1\langle c_{A\sigma}\rangle^\sigma)}_{\text{Nonequilibrium accumulation}} \\
&\underbrace{+ \nabla\cdot\left[\varepsilon_\omega\varepsilon_\sigma(D_{A\beta} - \alpha_1^{-1}D_{A\gamma})\nabla(\langle c_{A\omega}\rangle^\omega - \alpha_1\langle c_{A\sigma}\rangle^\sigma)\right]}_{\text{Nonequilibrium diffusion}} \\
&\underbrace{+ \nabla\cdot\left[\varepsilon_\eta\varepsilon_\sigma(D_{A\beta} - \alpha_1^{-1}D_{A\gamma})\nabla(\langle c_{A\eta}\rangle^\eta - \alpha_1\langle c_{A\sigma}\rangle^\sigma)\right]}_{\text{Nonequilibrium diffusion}} \\
&\underbrace{- \mu_A\varepsilon_\sigma\frac{\varepsilon_\omega(\alpha_1\langle c_{A\sigma}\rangle^\sigma - \langle c_{A\omega}\rangle^\omega) + \varepsilon_\eta(\alpha_1\langle c_{A\sigma}\rangle^\sigma - \langle c_{A\eta}\rangle^\eta)}{\{c_A\} + \alpha_1 K_A + \varepsilon_\omega(\alpha_1\langle c_{A\sigma}\rangle^\sigma - \langle c_{A\omega}\rangle^\omega) + \varepsilon_\eta(\alpha_1\langle c_{A\sigma}\rangle^\sigma - \langle c_{A\eta}\rangle^\eta)}}_{\text{Nonequilibrium reaction}} \\
&\underbrace{- \varepsilon_\omega\langle\mathbf{v}_\omega\rangle^\omega\nabla\cdot[\varepsilon_\sigma(\langle c_{A\omega}\rangle^\omega - \alpha_1\langle c_{A\sigma}\rangle^\sigma) + \varepsilon_\eta(\langle c_{A\omega}\rangle^\omega - \langle c_{A\eta}\rangle^\eta)]}_{\text{Nonequilibrium convection}} \\
&\underbrace{- \varepsilon_\omega\langle\mathbf{v}_\omega\rangle^\omega\nabla\cdot[\varepsilon_\sigma(\langle c_{A\eta}\rangle^\eta - \alpha_1\langle c_{A\sigma}\rangle^\sigma) + \varepsilon_\omega(\langle c_{A\eta}\rangle^\eta - \langle c_{A\omega}\rangle^\omega)]}_{\text{Nonequilibrium convection}}
\end{aligned} \tag{3.134}$$

In order to get a one-equation model for $\{c_A\}$, the terms involving $\langle c_{A\omega}\rangle^\omega - \alpha_1\langle c_{A\sigma}\rangle^\sigma$ and $\langle c_{A\eta}\rangle^\eta - \alpha_1\langle c_{A\sigma}\rangle^\sigma$, $\langle c_{A\eta}\rangle^\eta - \langle c_{A\omega}\rangle^\omega$ should be negligible, and the deviations should be expressed in terms of $\{c_A\}$ (which will be the case through the closure problems). Assuming it is true (with length/time scale constraints), Eq. (3.134) can be simplified

into

$$\begin{aligned}
& \frac{\partial}{\partial t}\left[\left(\varepsilon_\omega+\varepsilon_\eta+\alpha_1^{-1}\varepsilon_\sigma\right)\{c_A\}\right]+\varepsilon_\omega\langle\mathbf{v}_\omega\rangle^\omega\nabla\cdot\{c_A\}+\varepsilon_\eta\langle\mathbf{v}_\eta\rangle^\eta\nabla\cdot\{c_A\} \\
= \quad & \nabla\cdot\left[\left(\varepsilon_\omega D_{A\beta}+\varepsilon_\eta D_{A\beta}+\alpha_1^{-1}\varepsilon_\sigma D_{A\gamma}\right)\nabla\{c_A\}\right] \\
& +\nabla\cdot\left[\frac{D_{A\beta}}{V}\int_{A_{\eta\omega}}\mathbf{n}_{\omega\eta}\tilde{c}_{A\omega}\mathrm{d}A+\frac{D_{A\beta}}{V}\int_{A_{\omega\sigma}}\mathbf{n}_{\omega\sigma}\tilde{c}_{A\omega}\mathrm{d}A\right. \\
& \left.+\frac{D_{A\beta}}{V}\int_{A_{\eta\omega}}\mathbf{n}_{\eta\omega}\tilde{c}_{A\eta}\mathrm{d}A+\frac{D_{A\gamma}}{V}\int_{A_{\omega\sigma}}\mathbf{n}_{\sigma\omega}\tilde{c}_{A\sigma}\mathrm{d}A\right] \\
& -\nabla\cdot\langle\tilde{\mathbf{v}}_\omega\tilde{c}_{A\omega}\rangle-\nabla\cdot\langle\tilde{\mathbf{v}}_\eta\tilde{c}_{A\eta}\rangle-\mu_A\varepsilon_\sigma\frac{\{c_A\}}{\alpha_1 K_A+\{c_A\}}
\end{aligned} \tag{3.135}$$

One should keep in mind that in general, the non-equilibrium terms are not negligible and the conditions under which the assumption of equilibrium conditions are valid should always be verified [260].

8 CALCULATIONS OF THE HYDRAULIC PERMEABILITY TENSOR

8.1 STRUCTURAL INFORMATION: PERIODIC UNIT CELLS

The local closure problems are solved in periodic representative cellular region fig.3.4. A bacillus shape is chosen to model the bacterial structure which is in good agreement with the real structure of many bacterial cells. The relation between the large and small axis in a bacillus is given by

$$R=1+\frac{b_\sigma}{r_\sigma} \tag{3.136}$$

The EPS is composed of a hydrogel matrix around each cell with the thickness of δ_ω and the dimensions of the rectangular unit cells are

$$L_{\mathrm{x}}=2(\ell_x+b_\sigma+r_\sigma+\delta_\omega) \tag{3.137a}$$
$$L_{\mathrm{y}}=2(\ell_y+r_\sigma+\delta_\omega) \tag{3.137b}$$

ℓ_{x} and ℓ_{y} are the length of the spacing between two adjacent bacillus and is occupied by water channels in the biofilm representative unit cell. The ratio of interstitial spacing is defined by

$$R'=\frac{\text{head-to-head distance}}{\text{body-to-body-distance}}=\frac{\ell_{\mathrm{y}}}{\ell_{\mathrm{x}}} \tag{3.138}$$

In the first set of numerical simulations we study the effect of the EPS layer thickness on biofilm permeability. For this purpose ℓ_y andℓ_x are considered as constant values. Here

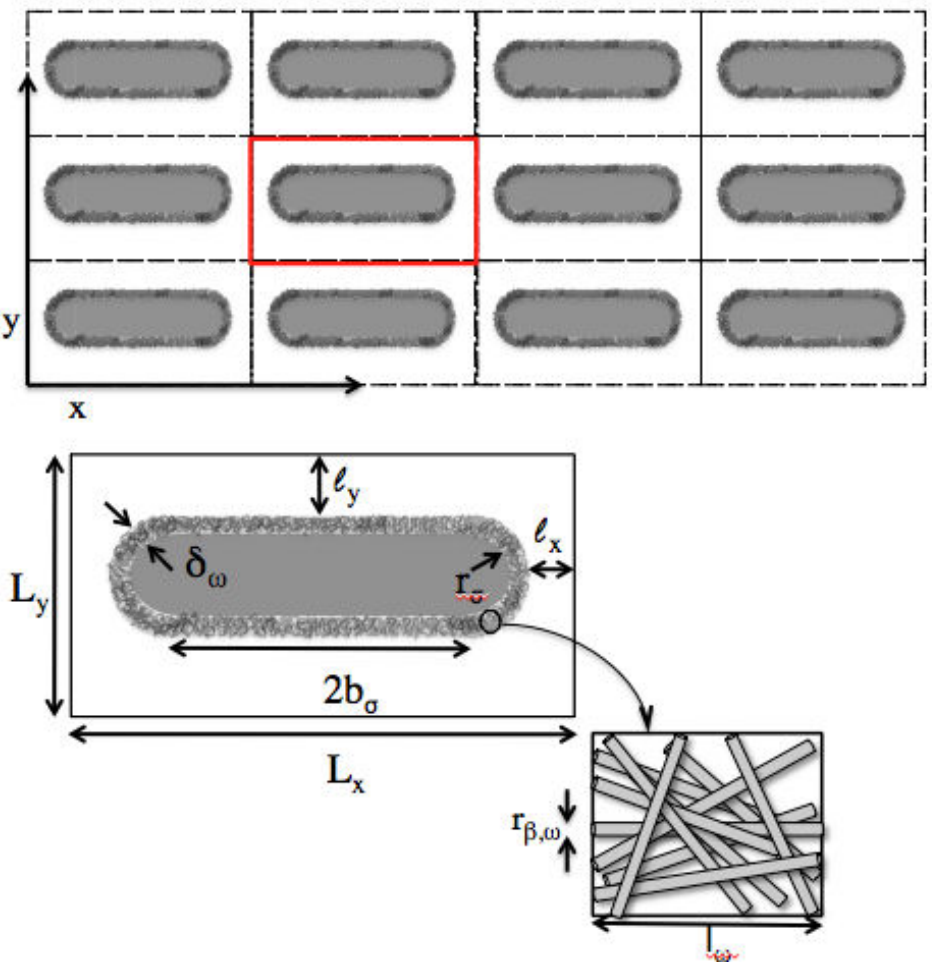

Figure 3.4: biofilm representative cellulare regions with subscale EPS fibers

we present the porosity of each region according to the geometry definitions given in Fig. 3.4.

$$\varepsilon_\sigma = \frac{\pi r_\sigma^2}{L_x L_y}(1 + 4\frac{b_\sigma}{r_\sigma}) \tag{3.139a}$$

$$\varepsilon_\omega = \frac{r_\sigma^2}{L_x L_y}(1 + \frac{\delta_\omega}{r_\sigma})\left[\pi\left(1 + \frac{\delta_\omega}{r_\sigma}\right) + \frac{4b_\sigma}{r_\sigma}\right] - \varepsilon_\sigma \tag{3.139b}$$

$$\varepsilon_\eta = 1 - \varepsilon_\sigma - \varepsilon_\omega \tag{3.139c}$$

For each given geometry, two components of the permeability (perpendicular and parallel) to the fluid flow through the bacterial cells are calculated and presented.

8.2 NUMERICAL SOLUTION OF THE CLOSURE PROBLEM

We recall briefly the local closure problem in each region with the corresponding boundary conditions as

$$\nabla \cdot \tilde{\mathbf{v}}_\alpha = 0, \quad \alpha = \eta, \omega. \tag{3.140a}$$

$$0 = -\nabla \tilde{p}_\eta + \mu_\beta \nabla^2 \tilde{\mathbf{v}}_\eta + \frac{1}{V_\eta} \left(\int_{A_{\eta\omega}} \mathbf{n}_{\omega\eta} \cdot (-\mathbf{I}\tilde{p}_\omega + \mu_\beta \nabla \tilde{\mathbf{v}}_\omega) \, \mathrm{d}A \right) \tag{3.140b}$$

$$0 = -\nabla \tilde{p}_\omega + \mu_\beta \nabla^2 \tilde{\mathbf{v}}_\omega - \mu_\beta \mathbf{K}_\omega^{-1} \cdot \tilde{\mathbf{v}}_\omega - \frac{1}{V_\omega} \left(\int_{A_{\eta\omega}} \mathbf{n}_{\omega\eta} \cdot (-\mathbf{I}\tilde{p}_\omega + \mu_\beta \nabla \tilde{\mathbf{v}}_\omega) \, \mathrm{d}A \right) \tag{3.140c}$$

$$- \frac{1}{V_\omega} \left(\int_{A_{\omega\sigma}} \mathbf{n}_{\omega\sigma} \cdot (-\mathbf{I}\tilde{p}_\omega + \mu_\beta \nabla \tilde{\mathbf{v}}_\omega) \, \mathrm{d}A \right)$$

$\omega - \eta$ dividing surface

$$\mathbf{n}_{\eta\omega} \cdot (\tilde{\mathbf{T}}_\eta - \tilde{\mathbf{T}}_\omega) = 0 \tag{3.141a}$$

$$\mathbf{n}_{\omega\eta} \cdot (\tilde{\mathbf{v}}_\omega - \tilde{\mathbf{v}}_\eta) = 0 \tag{3.141b}$$

$\omega - \sigma$ dividing surface

$$\tilde{\mathbf{v}}_\omega = -\langle \mathbf{v}_\omega \rangle^\omega \quad \text{No-slip condition} \tag{3.142}$$

defining the closure variables as

$$\tilde{\mathbf{v}}_\alpha = \mathbf{B}_\alpha \cdot \langle \mathbf{v}_\alpha \rangle^\alpha \tag{3.143a}$$

$$\tilde{p}_\alpha = \mu_\alpha \mathbf{c}_\alpha \cdot \langle \mathbf{v}_\alpha \rangle^\alpha \tag{3.143b}$$

If one uses the closure variables in the closure problems, it gives rise to

$$\nabla \cdot \mathbf{B}_\alpha = 0, \quad \alpha = \eta, \omega. \tag{3.144a}$$

$$0 = -\nabla \mathbf{c}_\eta + \nabla^2 \mathbf{B}_\eta + \frac{1}{V_\eta} \left(\int_{A_{\eta\omega}} \mathbf{n}_{\omega\eta} \cdot (-\mathbf{I}\mathbf{c}_\omega + \nabla \mathbf{B}_\omega) \, \mathrm{d}A \right) \tag{3.144b}$$

$$0 = -\nabla \mathbf{c}_\omega + \nabla^2 \mathbf{B}_\omega - \mathbf{K}_\omega^{-1} \cdot \mathbf{B}_\omega - \frac{1}{V_\omega} \left(\int_{A_{\eta\omega}} \mathbf{n}_{\omega\eta} \cdot (-\mathbf{I}\mathbf{c}_\omega + \nabla \mathbf{B}_\omega) \, \mathrm{d}A \right) \tag{3.144c}$$

$$- \frac{1}{V_\omega} \left(\int_{A_{\omega\sigma}} \mathbf{n}_{\omega\sigma} \cdot (-\mathbf{I}\mathbf{c}_\omega + \nabla \mathbf{B}_\omega) \, \mathrm{d}A \right)$$

$\omega - \eta$ dividing surface

$$\mathbf{n}_{\eta\omega} \cdot (-\mathbf{I}\mathbf{c}_\eta + \nabla \mathbf{B}_\eta) = \mathbf{n}_{\omega\eta} \cdot (-\mathbf{I}\mathbf{c}_\omega + \nabla \mathbf{B}_\omega) \tag{3.145a}$$

$$\mathbf{n}_{\omega\eta} \cdot \mathbf{B}_\omega = \mathbf{n}_{\eta\omega} \cdot \mathbf{B}_\eta \tag{3.145b}$$

$\omega - \sigma$ dividing surface

$$\mathbf{B}_\omega = -\mathbf{I} \tag{3.146}$$

As presented in eqs. (3.144), it should be pointed out that one may simultaneously solve two integral differential equations for the determination of the permeability tensor of the biofilm matrix (EPS-cells-water channels). However, we recall that the complete expression of the total permeability tensor includes also the permeability of the EPS fibers.

$$\mathbf{K}^{-1} = \mathbf{K}_\omega^{-1} + \varepsilon_\omega \mathbf{K}_{\omega\sigma}^{-1} \tag{3.147}$$

Eq. (3.147) includes the permeability of two porous media at 2 scales (biofilm and EPS). If one wants to express this equation as a non-dimensional equation this would take the following form

$$\left(L_{\mathrm{x}}^2 \mathbf{K}\right)^{-1} = \left(\ell_\omega^2 \mathbf{K}_\omega\right)^{-1} + \varepsilon_\omega \left(L_{\mathrm{x}}^2 \mathbf{K}_{\omega\sigma}\right)^{-1} \tag{3.148}$$

$$\mathbf{K}^{-1} = \left(\frac{L_{\mathrm{x}}}{\ell_\omega}\right)^2 \mathbf{K}_\omega^{-1} + \varepsilon_\omega \mathbf{K}_{\omega\sigma}^{-1} \tag{3.149}$$

The first right term in Eq. (3.147), is the permeability due to the fibers in the EPS region

which can be calculated independently in function of porosity and equivalent fiber size.

$$\mathbf{K}_\omega = f_1\left(\ell_\omega, \varepsilon_{\beta,\omega}\right) \tag{3.150}$$

This can be calculated from the solution of the closure problem expressed in [**?**]. The numerical simulations of the closure problems in periodic unit cells of non-touching cylinders in cubes have been done [11]. The following expression has been derived by fitting the numerical results for calculating the effective permeability in the porous medium in 3D unit cells.

$$K_{\beta,\omega}/\ell^2_{\text{cell}} = 1.606 \times 10^{-4} + 2.047 \times 10^{-5}\exp(8.397\varepsilon_{\beta,\omega}) \tag{3.151}$$

This is the dimensionless form of the permeability which can be used to determine the permeability of the fibers in the EPS sub scale. It is evident that the porosity and permeability of the fibers affect significantly the biofilm total permeability tensor, however for a fixed value of the fiber porosity, the permeability remains constant. In this study, the range of the porosity for the EPS was set from 0.2 to 0.8 which includes both dense/packed and loose arrangements of the biofilm.

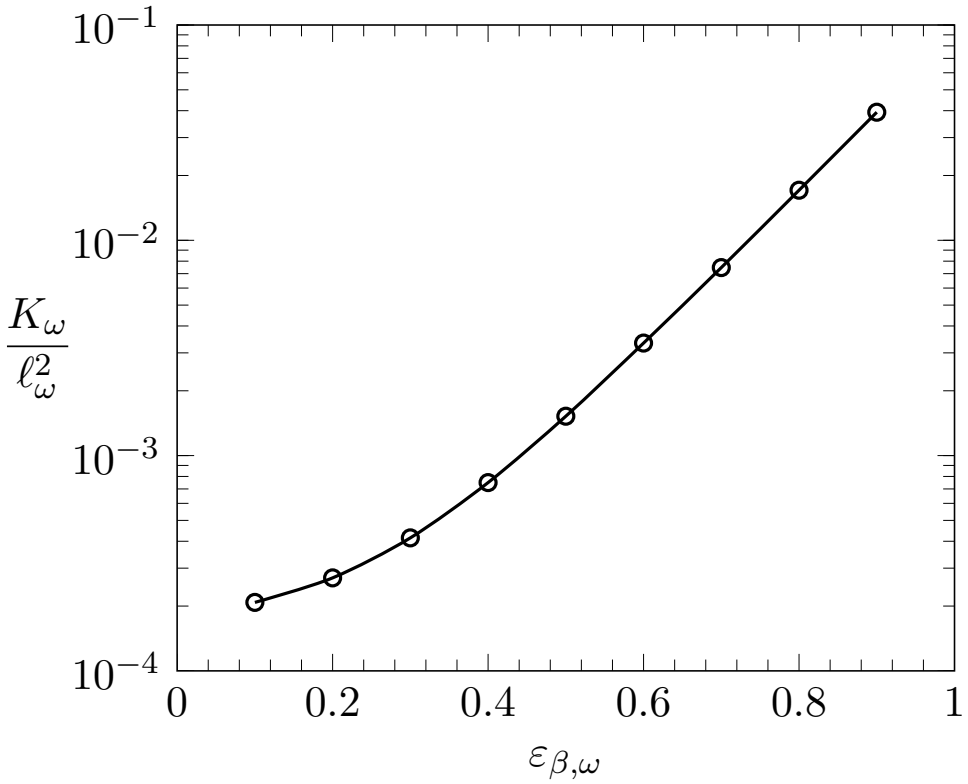

Figure 3.5: Solution of the closure problem: permeability in function of porosity [11]

Now we focus more precisely on the second right term in the Eq. (3.147) which itself depends on the porosity of the bacterial cells, EPS and water channels. Geometrically, the biofilm permeability depends on

$$\mathbf{K}_{\omega\sigma} = f_2\left(L_\mathrm{x}, L_\mathrm{y}, b_\sigma, r_\sigma, \delta_\omega, \mathbf{K}_\omega, \ell_\omega\right) \tag{3.152}$$

It is clear that for each numerical simulation we can not modify all the parameters otherwise the results can not then be interpreted properly. For this reason, on one hand we study the effect of the EPS thickness and subsequents of its porosity on the total permeability tensor and on the other hand the relative diastance between two unit cells with a fixed thickness for the EPS region (space occupied by the water channels). Other affecting parameters including the size of the bacterial cells (small and large axis) remain constant in all the numerical simulations. This way the number of parameters influencing the permeability reduces and Eq. (3.152) will depend on two parameters at the biofilm scale plus permeability of the EPS fibers. It should also be pointed out that in general, all components of the total permeability tensor must be calculated numerically, however in this work, we only investigate on determining the xx and yy components of this tensor assuming that the permeability tensor is symmetric based on the work of [122].

$$\frac{\mathbf{K}_{\omega\sigma}}{L_\mathrm{x}^2} = f_3\left(\frac{L_\mathrm{y}}{L_\mathrm{x}}, \frac{\delta_\omega}{L_\mathrm{x}}, \frac{\mathbf{K}_\omega}{\ell_\omega^2}, \frac{L_\mathrm{x}}{\ell_\mathrm{x}}\right) \tag{3.153}$$

It is worth to mention that the ratio $\dfrac{L_\mathrm{x}}{\ell_\mathrm{x}}$ depends on the size of the representative cellular regions at the biofilm scale and EPS sub scale. In this work this ratio is fixed to 100. The characteristic length scale of the bacterial cells is in order of μm (corresponding to the real geometry of numerous bacterial cells) while the characteristic fiber size in the EPS is in order of some nanometers ($\sim$ 10 nm). One should also keep in mind that the characteristic length of the fibers in the EPS region depends highly on the conditions under which the biofilm are developed.

Assuming the fixed ratio of $\dfrac{L_\mathrm{x}}{\ell_\mathrm{x}}$ Eq. (3.153) can be expressed as

$$\frac{\mathbf{K}_{\omega\sigma}}{L_\mathrm{x}^2} = f_3'\left(\frac{L_\mathrm{y}}{L_\mathrm{x}}, \frac{\delta_\omega}{L_\mathrm{x}}, \varepsilon_{\beta\omega}\right) \tag{3.154}$$

The boundary value problems defined by Eqs. (3.144) have been solved for calculation of the $\mathbf{K}_{\omega\sigma}$ using the Comsol 4.3.b version. An extremely mesh with fine a special refinement at the fluid-EPS-cell medium boundary (see Fig.3.6

9 RESULTS AND DISCUSSION

In the first set of results, the xx and yy components of the total permeability tensor of the biofilm matrix are presented in function of the EPS porosity (δ_ω) (Fig. 3.7 and 3.8).

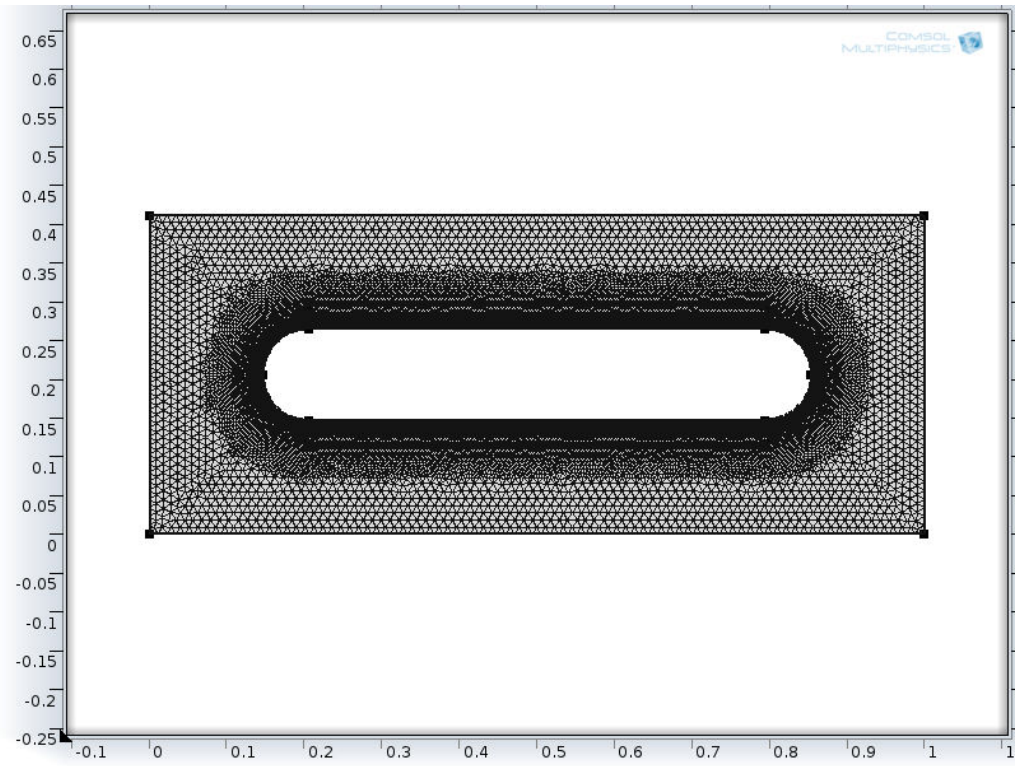

Figure 3.6: Example of the periodic cell mesh with special refinement at the fluid-porous medium boundaries

In each plot the parallel and perpendicular components of the permeability tensor are demonstrated in function of the fiber's porosity in the EPS (from 0.2 to 0.8). The ratio of $\frac{\ell_y}{\ell_x}$ is fixed to 2 and ℓ_x was set 1 μm. when the porosity values of the fibers inside the EPS is small (dense EPS matrix), the total permeability tensor is less affected by the cell-EPS permeability. In this case the EPS matrix acts like a quasi impermeable solid and as a result there is no significant fluid flow inside the EPS. However at higher values of $\varepsilon_{\beta,\omega}$ ($>$0.6) the effects of the EPS-cell porous medium becomes more important and it affects the total permeability tensor. The xx component of the total permeability tensor $\mathbf{K}_{xx(\mathrm{tot})}$ increases slightly with different values of ε_ω. However the perpendicular component of the total permeability tensor $\mathbf{K}_{yy(\mathrm{tot})}$ increases more significantly in function of ε_ω. When ε_ω (related to δ_ω) increases, the volume of the bacterial cells decreases compared to the total volume of the representative cellular region. In other words, the relative friction between the passing fluid channels and the bacterial cells decreases.

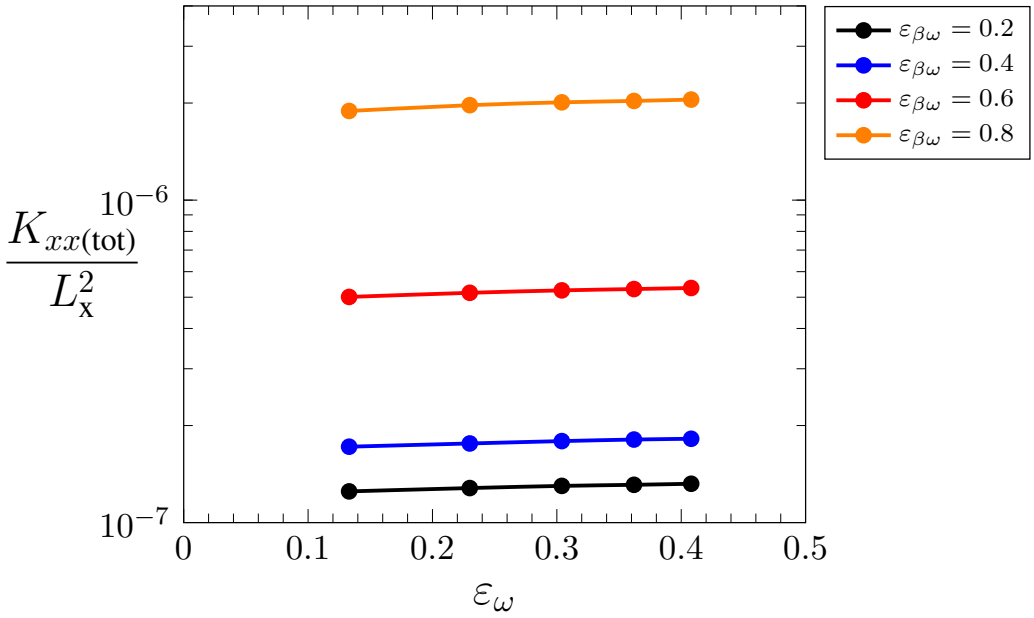

Figure 3.7: xx-component values of the total permeability tensor in function of EPS porosity, R'=2

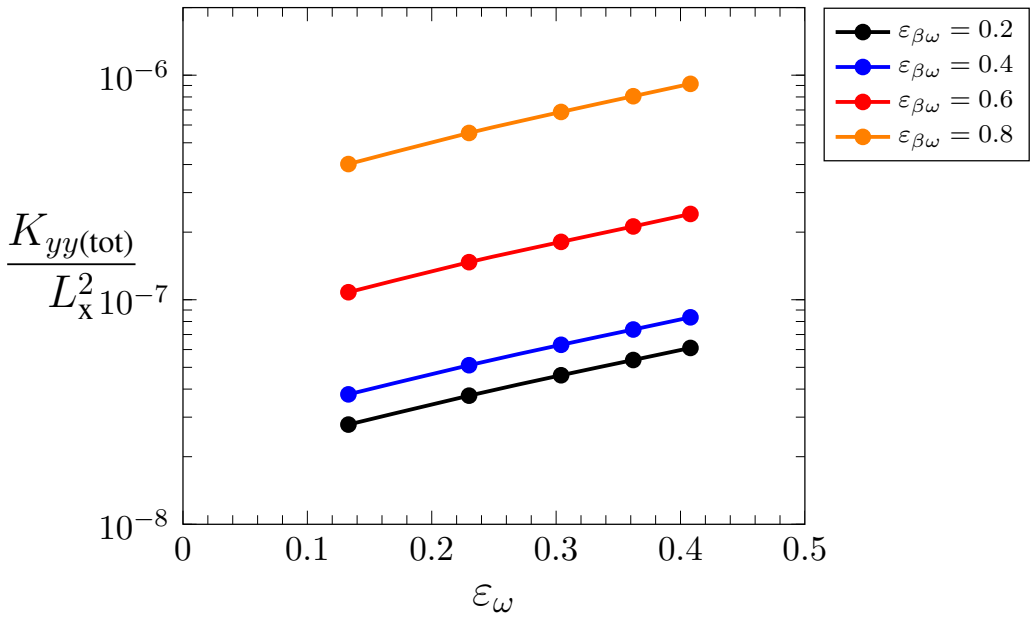

Figure 3.8: yy-component values of the total permeability tensor in function of EPS porosity,$R' = 2$

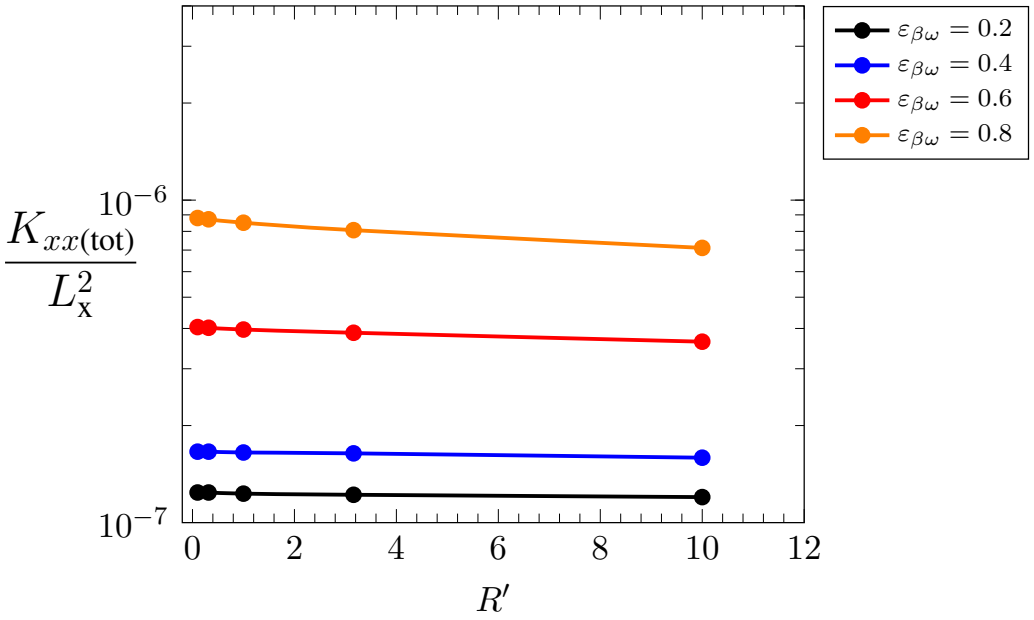

Figure 3.9: xx-component values of the total permeability tensor in function of R', $\delta_\omega = 5 \times 10^{-7} \mu$m

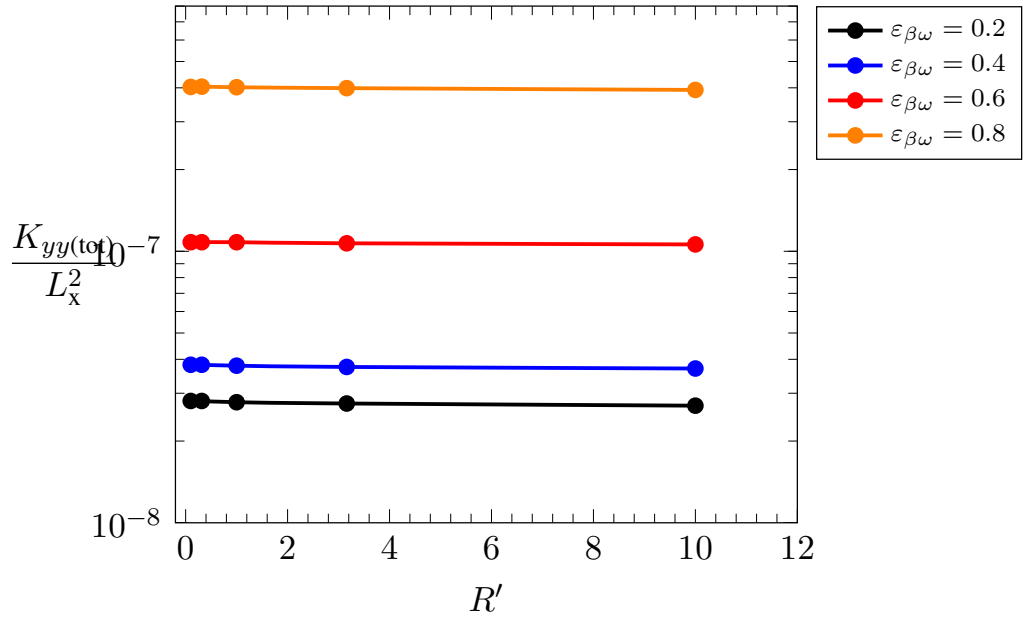

Figure 3.10: yy-component values of the total permeability tensor in function of R' (ℓ_x/ℓ_y), $\delta_\omega = 5 \times 10^{-7} \mu$m

In Fig.3.9 and 3.10, the parallel and perpendicular omponents (xx and yy) of the total permeability tensor are presented in function of the relative distance between head-to-

head and body-to-body of bacterial arrays. Likewise the first set of results, the significant effects of the cell-EPS porous interface on the total permeability tensor are more important at the higher values of the fibers porosity.

The relative permeability ($\frac{\mathbf{K}_{xx}}{\mathbf{K}_{yy}}$) of both total permeability ($\mathbf{K}$) and the biofilm matrix ($\mathbf{K}_{\omega\sigma}$) are presented in Fig. 3.11-3.14. When porosity of the EPS region (ε_ω) increases, the relative permeability slightly decreases. This can be reasonable since the resistance to the flow will reduce in both directions. For variable values of the distance between two unit cells (R'), when the porosity of fibers is larger than 0.6 (highly hydrated EPS) the parallel and perpendicular components of the permeability tensor are more close; however for more dense structures ($\varepsilon_{\beta,\omega} \ll 0.4$) evident differences are observed.

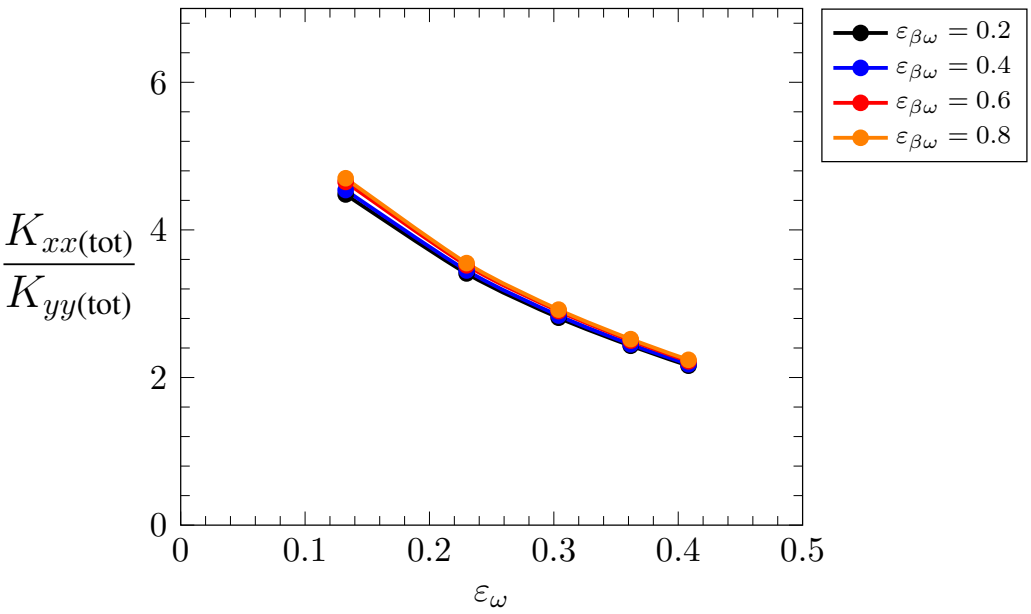

Figure 3.11: Ratio of $\frac{K_{xx(\text{tot})}}{K_{yy(\text{tot})}}$ (total permeability tensor) for different values of EPS porosity

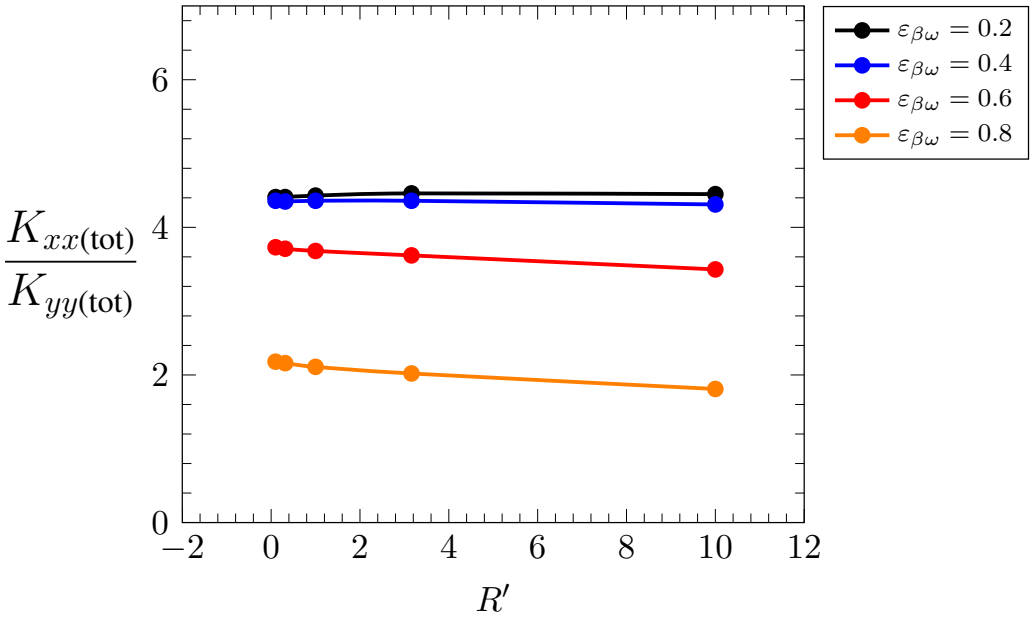

Figure 3.12: Ratio of $\frac{K_{xx}}{K_{yy}}$ (total permeability tensor) for different values of R', $\delta_\omega = 5 \times 10^{-7} \mu$m

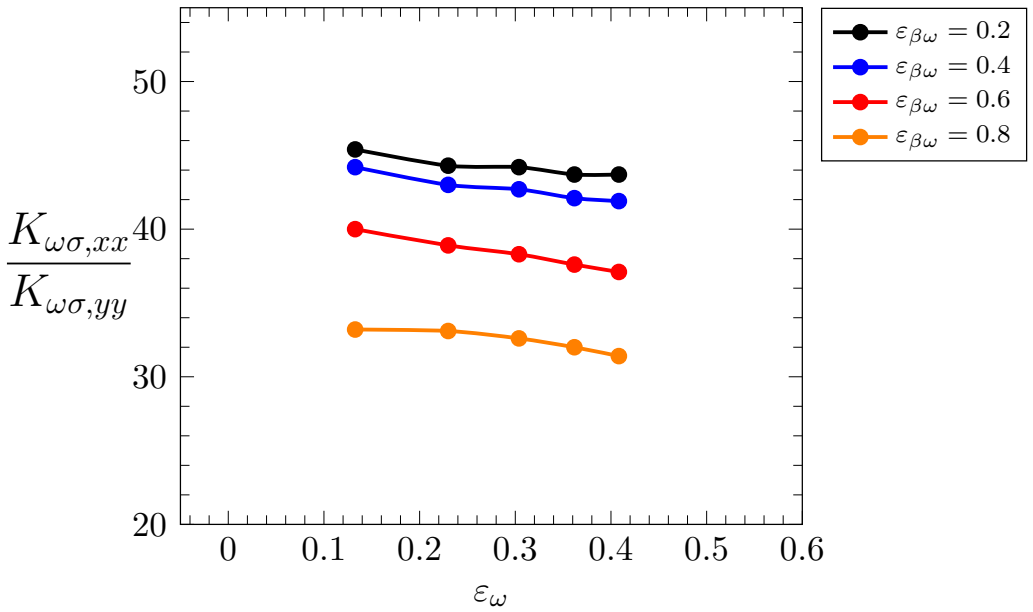

Figure 3.13: Ratio of $\frac{K_{\omega\sigma,xx}}{K_{\omega\sigma,yy}}$ (permeability due to EPS-cell porous structure) for different values of biofilm porosity, $R' = 2$

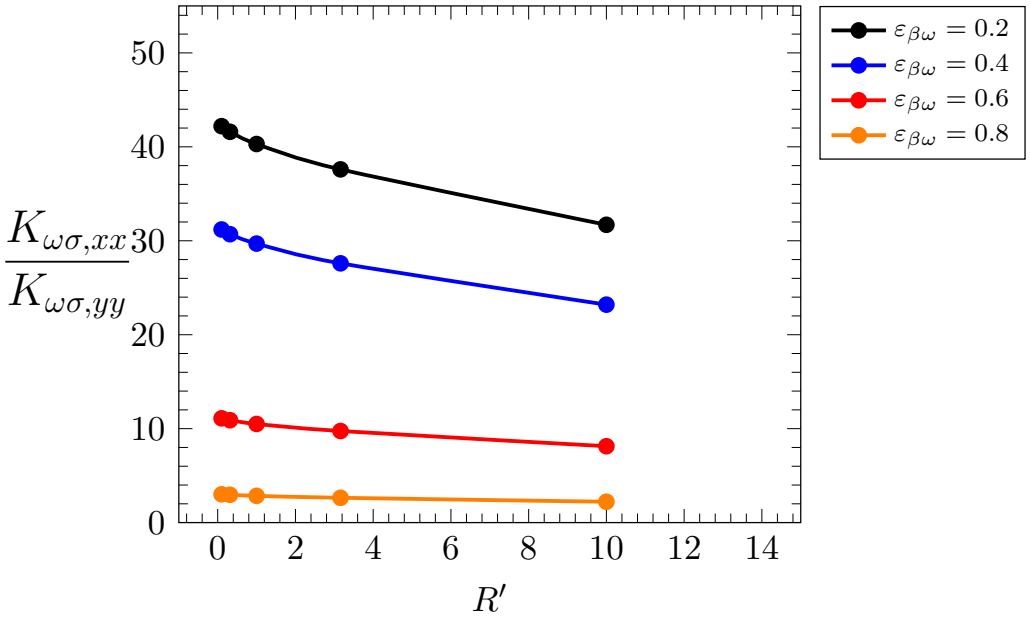

Figure 3.14: Ratio of $\frac{K_{\omega\sigma,xx}}{K_{\omega\sigma,yy}}$ (permeability due to EPS-cell porous structure) for different values of biofilm porosity, $\delta_\omega = 5 \times 10^{-7} \mu$m

10 CONCLUSIONS

Modeling of the porous media involving with biological activity is a challenging task since it must deal with cellular activity, interfacial mass transport and consequent biomass production. Moreover, the surrounding environmental conditions (e.g. velocity, solution chemistry) can highly affect the transport phenomena in the porous media.
In this work, a preliminary biofilm model able to predict the evolution of its structural properties (porosity, diffusivity) and profiles of velocity and species concentration with time has been presented. At any point in the biofilm, the structural evolution is due to transport of chemical species and cellular reaction inside the cells. Three different regions (cells, EPS, water channels) have been identified within the biofilm volume, and EPS matrix was assumed to be in contact with other regions (no direct contact between water channels and cells). The model was based on local transport mechanisms involved with each region, convection and diffusion in ω (EPS) and η (water channels), whereas only diffusion was taken into account in σ (cells) region. Cellular reaction occurred at cell-EPS interface and is modeled as function of singles species (glucose) by Michaelis-Menton kinetics. No reaction took place in EPS and water channels. The mass and momentum equations, with mass conservation equations for each species at local scale were given. The upscaled equations have been derived with use of volume averaging method and associated theorems. The convective averaged velocity fields in η and ω regions can be determined by the averaged non-stationary stokes equations. In the momentum transport problem, an equilibrium model and the associated closure problems have been proposed. the conditions for validation of the equilibrium conditions were presented in Appendix.B. The upscaled mass conservation equations has been also presented under the equilibrium conditions. This latter would be required for the numerical simulations of the macroscopic model (equilibrium concentration field for each species).The porosity evolution of each region was expressed in function of averaged quantities (concentration, mass density, velocity). Numerical simulations were run to determine the total permeability tensor which depends both on the permeability of the fibers in the EPS (sub scale) and the permeability due to the biofilm matrix. The results confirmed that in the case of dense fibers the total permeability tensor is limited by the fibers permeability $\mathbf{K}_{\omega}$, however for loose fibers the permeability of the biofilm matrix $\mathbf{K}_{\omega\sigma}$ can play more important role.
This model will be further developed. So far, the biofilm-scale evolution of each region does not provide data of the overall biomass growth. The final goal is to predict biofilm structural evolution and heterogeneity by establishing a relation giving the rate of change of the biofilm thickness as a function of the macroscopic parameters.

General Conclusions and Perspectives

For the past decades, a great interest in using pressure-driven membrane technologies, as separation techniques, for the design of industrial installations has been rised. They are used for the purification and separation of different solutions in several industrial fields (e.g. waste water treatment, food and pharmacy). Compactness and high efficiency of membrane filtration systems are reported as the main advantages of this technology.

During filtration, solutes and suspended particles with different natures (microorganisms, natural organic matter, inorganic suspended solids, salts, etc.) accumulate incessantly on the membrane surface. This results in a(n) (1) flow flux decline, (2) modification of the membrane properties (selectivity and lifetime) and (3) increase of operational costs. This phenomenon is called fouling and up to now, represents the main disadvantage of using membrane technologies. For this reason, different fouling mechanisms (cake formation, pore constriction, pore blockage) have been studied and models describing each fouling mechanism have been proposed to get a better understanding of the membrane systems and to reduce fouling impact.

The objective of this study was to develop a mechanistic understanding of the membrane fouling developed in the presence of solutions containing bacteria and to propose an upscaled model for membrane fouling.

The literature review revealed that during the filtration of liquid media containing microbial cells, the membrane performance is affected by two major factors (1) the irreversible attachment of the cells to the membrane surface leading to biofilm formation (2) the penetration and blockage of the membrane internal pores by extra cellular products (issued from the biofilm). Briefly, the biofilm develops an additional dynamic resistance to the flow at the top of the membrane surface whereas the membrane structure itself, evolves due to the deposition/adsorption of extracellular polymers produced by the biofilm.

Both porous media (membrane and biofilm) are highly complex and difficult to characterize. Moreover, the mechanisms involved in the structural evolution of each porous media are quite different. The cellular reaction is mainly responsible for biomass production and subsequent biofilm structural modifications, whereas protein adsorption to the inner pores affects majorly the membrane structure. All these complexities leaded us to study biofilm and membrane porous structures separately in order to provide a precise description of the involving mechanisms on each of them.

Experiments were performed to (1) evaluate the effects of protein adsorption on the membrane system's performance, (2) characterize the local protein adsorption phenomenon (2) and (3) determine the structural properties of the original (non-used) membrane (porosity, pore size distribution, permeability, etc.). Experiments provided essential data to the local model development and will be further used to validate it. The membrane-scale and biofilm-scale models were both based on the description of the local phenomena at discontinuous pore scale. The local equations of mass and momentum transport with appropriate boundary conditions (adsorption in the membrane and cellular reaction in the biofilm) were set. Consequently, the upscaled models were both derived by application of the volume averaging method and its associated theorems. The upscaled models predicted in particular the macroscopic evolution of the porous structures (membrane and biofilm)

with time. The effective properties associated with each porous structure (diffusivity and permeability) were also determined.

It is worth to mention that in both models several simplifications have been made to derive the closed form of the upscaled equations. These simplifications were mainly based on the comparison of the order of magnitude of each term or associated length scales. However, one should keep in mind that numerical calculations of the effective properties and subsequent comparison of the numerical results with data from experiments are essential to validate the conditions under which the simplifications are valid.

In the adsorption model, macroscopic numerical simulations were run to validate the model qualitatively. Due to the tiny size of the membrane active layer, we proposed to replace this layer with a virtual dividing surface between the fluid phase and porous medium in which the information about the membrane active layer will be found in the boundary conditions. It is worth to mention that this kind of jump conditions can be interesting in other studies as well in order to overcome the pure numerical difficulties.

In the biofilm model, the the local closure problems have been solved numerically in order to determine the total permeability tensor of the biofilm. The results showed that the permeability of the fibers inside the EPS matrice has a significant influence on the permeability tensor. Two different geometries of the representative cellular regions have been chosen in order to determine their influence on the permeability tensor. When the thickness of the EPS matrice increases, the fluid has less difficulty to pass though the bacterial cells in both xx and yy directions and thus the representative region becomes more permeable.

Some highlights of the models and performed/ongoing experiments will be pointed out below:

The first model (protein adsorption model) was based on the assumption that when proteins reach the membrane surface they either adsorb to the interface or pass through it. However experiments confirmed that this hypothesis was only valid for small proteins where the steric exclusion was negligible. The experiments with BSA solutions clearly confirmed that the steric hindrance of the large molecules on the membrane surface contributed to the membrane fouling along with adsorption. Consequently in future work, it would be desirable to develop a coupled model taking into account effects of electrostatic interaction and particle size on the fouling mechanisms. However the validation of such models require running direct numerical simulation (DNS) in which particles are determined to either pass through the membrane or adsorb/block on its surface. This modeling approach can be subject of future studies in this domain.

Experiments were only carried out with solutions of a single protein in water at pH $\sim$ 7. However, it has been remarked by several studies that the solution chemistry (pH and ionic strength) [75], [116], [167], protein's mixture (single or binary) [75], [81],[109], [132], membrane-protein electrostatic/hydrophobic interactions [5], [43], [62], and operational conditions [111], significantly affect protein adsorption both quantitatively and qualitatively. Therefore experimental sensitivity tests can be performed to (1) determine

the most important parameters affecting membrane fouling by proteins (2) identify the underlying mechanisms and (3) further improve the modeling approach.

Recently, confocal scanning laser microscopy (CSLM) has been directly used to observe the microfiltration membrane performance and to reconstruct the membrane structure with deposited proteins on it [46],[47], [81], [268]. This approach can be applied to qualitatively infer the protein deposition/adsorption to the membrane. The amount of accumulated protein on the membrane surface can be also quantified by FTIR-ATR in parallel. In future, one can use a combination of these techniques in order to get a more clear observation of the fouling phenomenon.

The second model (biofilm model) provided the averaged mass and momentum transport equations in each identified region (Cells, EPS and water channels), with the specific evolution of their porosity with time. We remind that the porosity evolution was due to the interfacial mass flux of species and cellular reaction. In future work, a direct connection between the porosity evolution and the biomass growth at the biofilm scale will be constructed. The numerical results can be then compared to experimental data. The upscaled equations for mass conservation of species under the equilibrium conditions have also been derived. If the local mass equilibrium conditions are valid, one can use one mass concentration equation for each species in the biofilm volume.

In the biofilm model, information of the biofilm's structure is absolutely needed to determine the model parameters (structure, kinetics, transport). For this purpose, experiments of biofilm formation and development will be carried out with a model bacterium in a microfiltration membrane system.

Structural parameters of the biofilm can be obtained directly from Confocal Laser Scanning Microscopy (CLSM) image stacks. In fact, CLSM allows non-destructive examination of biofilms and can be used for their visualization and quantification when combined with the application of specific staining. In our work, bacteria in the biofilm can be stained with a specific nucleic acid, and fluorescent labeled lectins, which are specific to polysaccharides, can be also used. Quantitative parameters describing the physical structure of biofilms (bio-volumes, porosity, thickness, substratum coverage etc.) can then be extracted from three-dimensional CLSM images by using appropriate image analysis software ([38], [100], [267]). Additionally, biofilm permeability can also be measured as described by [73].

In order to determine the spatial distribution of the different species in the biofilm, micro-sensors can be used. It has been shown that micro-sensors are useful tools to study biofilms. They are needle-shaped devices and can quantify the concentration of specific compounds. Due to their small sensing tip, highly localized measurements are possible [23].

The first experimental essays will provide parameters to establish the initial conditions of our model. Thereafter, a sensitivity analysis could be performed in order to determine the influence of the parameters on the numerical results. One may expect to identify the parameters that affect biofilm structure significantly and which should be then experimentally measured. Biofilm characterization under different conditions (hydrodynamic,

substrate concentrations...) will also be performed experimentally. Data from these assays will then be compared to numerical results for model validation.
The final objective consists of developing a coupled model describing the fouling in the membrane volume (caused by protein adsorption), and on its surface (biofilm formation) to predict the overall membrane fouling and its effects on membrane system's performance.

APPENDIX A

Here we recall the non-closed form of deviation equation of the mass conservation equation of proteins.

$$\begin{aligned} &\underbrace{\frac{\partial \tilde{c}_{A\gamma}}{\partial t}}_{\text{Accumulation}} \underbrace{-\varepsilon_\gamma^{-1} a_{\gamma\kappa} \frac{\partial}{\partial t}\left[f(\langle c_{A\gamma}\rangle^\gamma)\right]}_{\text{Adsorptive source}} + \underbrace{\mathbf{v}_\gamma \cdot \nabla \tilde{c}_{A\gamma}}_{\text{Convection}} + \underbrace{\tilde{\mathbf{v}}_\gamma \cdot \nabla \langle c_{A\gamma}\rangle^\gamma}_{\text{Convective source}} \\ = \; &\underbrace{\nabla \cdot (\mathscr{D}_\gamma \nabla \tilde{c}_{A\gamma})}_{\text{Diffusion}} \underbrace{-\varepsilon_\gamma^{-1} \nabla \cdot \left(\frac{\mathscr{D}_\gamma}{V} \int_{A_{\gamma\kappa}} \mathbf{n}_{\gamma\kappa} \tilde{c}_{A\gamma} \mathrm{d}A \right)}_{\text{Non-local diffusion}} + \underbrace{\varepsilon_\gamma^{-1} \nabla \cdot \langle \tilde{\mathbf{v}}_\gamma \tilde{c}_{A\gamma} \rangle}_{\text{Non-local convection}} \end{aligned} \tag{A.1}$$

The objective of this part is to make an estimation each term in order to determine the sources and consequently to propose a closure problem. We begin the process of simplifying Eq. (A.1) by examining the non-local diffusion term

$$\frac{1}{V} \int_{A_{\gamma\kappa}(t)} \tilde{c}_{A\gamma} \mathbf{n}_{\gamma\kappa} \mathrm{d}A \;=\; \mathbf{O}\left(a_v \tilde{c}_{A\gamma}\right) \tag{A.2}$$

Since we are dealing with an average quantity, we can estimate if the divergence as

$$\nabla \cdot \left\{ \frac{1}{V} \int_{A_{\gamma\kappa}(t)} \tilde{c}_{A\gamma} \mathbf{n}_{\gamma\kappa} \mathrm{d}A \right\} \;=\; \mathbf{O}\left(\frac{a_v \tilde{c}_{A\gamma}}{L} \right) \tag{A.3}$$

On the basis of Eq. A.3 we estimate the non-local diffusion term in Eq. (A.1) as

$$\varepsilon_\gamma^{-1} \mathscr{D}_\gamma \nabla \cdot \left[\frac{1}{V} \int_{A_{\gamma\kappa}(t)} \tilde{c}_{A\gamma} \mathbf{n}_{\gamma\kappa} \mathrm{d}A \right] \;=\; \mathbf{O}\left(\frac{\varepsilon_\gamma^{-1} a_v \mathscr{D}_\gamma \tilde{c}_{A\gamma}}{L} \right) \tag{A.4}$$

For most porous media, a reasonable representation of the interfacial area per unit volume is given by

$$a_v \approx \ell_\gamma^{-1} \tag{A.5}$$

this leads to the following form of our estimate for the non-local term

$$\varepsilon_\gamma^{-1}\mathscr{D}_\gamma\nabla\cdot\left[\frac{1}{V}\int_{A_{\gamma\kappa}(t)}\tilde{c}_{A\gamma}\mathbf{n}_{\gamma\kappa}\mathrm{d}A\right] \;=\; \mathbf{O}\left(\frac{\varepsilon_\gamma^{-1}a_v\mathscr{D}_\gamma\tilde{c}_{A\gamma}}{\ell_\gamma L}\right) \tag{A.6}$$

while our estimation of the diffusion term in Eq. (A.1) is given by

$$\mathscr{D}_\gamma\nabla\cdot(\nabla\tilde{c}_{A\gamma}) \;=\; \mathbf{O}\left(\frac{\mathscr{D}_\gamma\tilde{c}_{A\gamma}}{\ell_\gamma^2}\right) \tag{A.7}$$

At this point by use of the length scale constraint $\ell_\gamma << L$ we can discard the diffusive source likewise.

$$\varepsilon_\gamma^{-1}\mathscr{D}_\gamma\nabla\cdot\left[\frac{1}{V}\int_{A_{\gamma\kappa}(t)}\tilde{c}_{A\gamma}\mathbf{n}_{\gamma\kappa}\mathrm{d}A\right] << \mathscr{D}_\gamma\nabla\cdot(\nabla\tilde{c}_{A\gamma}) \tag{A.8}$$

The order of magnitude of the non-local convective transport term can be expressed as

$$\varepsilon_\gamma^{-1}\nabla\cdot\langle\tilde{\mathbf{v}}_\gamma\tilde{c}_{A\gamma}\rangle \;=\; \mathbf{O}\left(\frac{\langle\mathbf{v}_\gamma\rangle^\gamma\,\tilde{c}_{A\gamma}}{L}\right) \tag{A.9}$$

here we supposed that $\tilde{\mathbf{v}}_\gamma$ has the same order of magnitude as $\langle\mathbf{v}_\gamma\rangle^\gamma$, and we have used L as the characteristic length associated with$t$ $\langle\tilde{\mathbf{v}}_\gamma\tilde{c}_{A\gamma}\rangle$. The order of magnitude of the $local$ convective transport is given by

$$\mathbf{v}_\gamma\cdot\nabla\tilde{c}_{A\gamma} \;=\; \mathbf{O}\left(\frac{\langle\mathbf{v}_\gamma\rangle^\gamma\,\tilde{c}_{A\gamma}}{\ell_\gamma}\right) \tag{A.10}$$

and this indicates that the non-local convective transport can be neglected when ever $\ell_\gamma << L$.

Under these circumstances our transport equation for the spatial deviation concentration takes the form

$$\begin{aligned}&\frac{\partial\tilde{c}_{A\gamma}}{\partial t}-\varepsilon_\gamma^{-1}a_{\gamma\kappa}\frac{\partial}{\partial t}\left[f(\langle c_{A\gamma}\rangle^\gamma)\right]+\mathbf{v}_\gamma\cdot\nabla\tilde{c}_{A\gamma}+\tilde{\mathbf{v}}_\gamma\cdot\nabla\langle c_{A\gamma}\rangle^\gamma \qquad (A.11)\\ =\;&\mathscr{D}_\gamma\nabla\cdot(\nabla\tilde{c}_{A\gamma})\end{aligned}$$

we can complete the closure problem for $\tilde{c}_{A\gamma}$ by writing the initial and boundary conditions if we use the spatial deviation decomposition on the interfacial boundary condition

for $\tilde{c}_{A\gamma}$ to express

$$-\mathscr{D}_\gamma \nabla \langle c_{A\gamma}\rangle^\gamma \cdot \mathbf{n}_{\gamma\kappa} - \mathscr{D}_\gamma \nabla \tilde{c}_{A\gamma} \cdot \mathbf{n}_{\gamma\kappa} = \frac{\partial}{\partial t}\left[f(\langle c_{A\gamma}\rangle^\gamma) + f(\tilde{c}_{A\gamma})\right] \tag{A.12}$$

Now we assume that on the basis of $\tilde{c}_{A\gamma} \ll \langle c_{A\gamma}\rangle^\gamma$ the variations of $f(\tilde{c}_{A\gamma})$ are negligible compared to $f(\langle c_{A\gamma}\rangle^\gamma)$

$$\text{B.C.1} \quad -\mathscr{D}_\gamma \nabla \langle c_{A\gamma}\rangle^\gamma \cdot \mathbf{n}_{\gamma\kappa} - \frac{\partial}{\partial t} f \langle c_{A\gamma}\rangle^\gamma = \mathscr{D}_\gamma \nabla \tilde{c}_{A\gamma} \cdot \mathbf{n}_{\gamma\kappa} \tag{A.13a}$$

It should be noted that the spatial deviation concentration will not, in general, be known at the entrances and exits of macroscopic system.

$$\text{B.C.2} \quad \tilde{c}_{A\gamma} = \mathcal{F}(\mathbf{r}, t) \quad \text{on } A_{\gamma e} \tag{A.13b}$$

$$\text{I.C} \quad \tilde{c}_{A\gamma} = \mathcal{G}(\mathbf{r}) \quad \text{at } t = 0 \tag{A.13c}$$

While many dispersion processes will be inherently unsteady, the closure problem for $\tilde{c}_{A\gamma}$ will be quasi-steady whenever the following constraint is satisfied

$$\frac{\mathscr{D}_\gamma t^*}{\delta_\gamma^2} >> 1 \tag{A.14}$$

This constraint is based on the estimation of the diffusive transport term given by

$$\nabla \cdot (\mathscr{D}_\gamma \nabla \tilde{c}_{A\gamma}) = \mathbf{O}\left(\frac{\mathscr{D}_\gamma \tilde{c}_{A\gamma}}{\delta_\gamma^2}\right) \tag{A.15}$$

Where δ_γ is the characteristic length of the diffusion process along with the inequality

$$\frac{\partial \tilde{c}_{A\gamma}}{\partial t} << \nabla \cdot (\mathscr{D}_\gamma \nabla \tilde{c}_{A\gamma}) \tag{A.16}$$

when the transport process is purely diffusive, we can conclude that

$$\delta_\gamma \approx \ell_\gamma \quad \text{diffusive process} \tag{A.17}$$

On the other hand when convective transport is important, the situation is more complex. The qausi-steady closure problem takes the form

$$\mathbf{v}_\gamma \cdot \nabla \tilde{c}_{A\gamma} + \tilde{\mathbf{v}}_\gamma \cdot \nabla \langle c_{A\gamma}\rangle^\gamma = \mathscr{D}_\gamma \nabla \cdot (\nabla \tilde{c}_{A\gamma}) \tag{A.18}$$

with boundary conditions

$$\text{B.C.1} \quad -\mathscr{D}_\gamma \nabla \langle c_{A\gamma} \rangle^\gamma \cdot \mathbf{n}_{\gamma\kappa} - \frac{\partial}{\partial t}(f \langle c_{A\gamma} \rangle^\gamma) = \mathscr{D}_\gamma \nabla \tilde{c}_{A\gamma} \cdot \mathbf{n}_{\gamma\kappa} \quad \text{on } A_{\gamma\kappa} \tag{A.19a}$$

$$\text{B.C.2} \quad \tilde{c}_{A\gamma} = \mathcal{F}(\mathbf{r}, t) \quad \text{on } A_{\gamma e} \tag{A.19b}$$

it is clear that $\tilde{c}_{A\gamma}$ will depend on $\mathbf{r}, t$, and $\nabla \cdot \langle c_{A\gamma} \rangle^\gamma$.

We are now in a position to estimate the magnitude of $\tilde{c}_{A\gamma}$ on the basis of volume and surface sources. The derivatives of the average concentration are estimated according to

$$\nabla \langle c_{A\gamma} \rangle^\gamma = \mathbf{O}\left(\frac{\Delta \langle c_{A\gamma} \rangle^\gamma}{L}\right) \tag{A.20}$$

$$\frac{\partial}{\partial t} f \langle c_{A\gamma} \rangle^\gamma \approx \frac{\partial \langle c_{A\gamma} \rangle^\gamma}{\partial t} f' \langle c_{A\gamma} \rangle^\gamma = \mathbf{O}\left[\frac{\Delta \langle c_{A\gamma} \rangle^\gamma}{t^*} f' \langle c_{A\gamma} \rangle^\gamma\right] \tag{A.21}$$

Where t^* is the characteristic time scale of the adsorption at the membrane scale.

$$\underbrace{-\varepsilon_\gamma^{-1} a_{\gamma\kappa} \frac{\partial}{\partial t}\left[f(\langle c_{A\gamma} \rangle^\gamma)\right]}_{\text{Adsorptive source}} + \underbrace{\mathbf{v}_\gamma \cdot \nabla \tilde{c}_{A\gamma}}_{\text{Covection}} + \underbrace{\tilde{\mathbf{v}}_\gamma \cdot \nabla \langle c_{A\gamma} \rangle^\gamma}_{\text{Convective source}} = \underbrace{\mathscr{D}_\gamma \nabla \cdot (\nabla \tilde{c}_{A\gamma})}_{\text{diffusion}} \tag{A.22}$$

$$\underbrace{-\mathscr{D}_\gamma \nabla \langle c_{A\gamma} \rangle^\gamma \cdot \mathbf{n}_{\gamma\kappa}}_{\text{Diffusive source}} \underbrace{- \frac{\partial}{\partial t} f(\langle c_{A\gamma} \rangle^\gamma)}_{\text{Adsorptive source}} = \mathscr{D}_\gamma \nabla \tilde{c}_{A\gamma} \cdot \mathbf{n}_{\gamma\kappa} \quad \text{on } A_{\gamma\kappa} \tag{A.23}$$

APPENDIX B

1 LOCAL MASS EQUILIBRIUM

To derive the length-scale constraints, it is convenient to write the closed non-equilibrium equations as follows

$$\frac{\langle\rho_\eta\rangle^\eta}{\varepsilon_\eta}\frac{\partial\varepsilon_\eta}{\partial t}+\frac{a_{\omega\eta}}{\varepsilon_\eta}\sum_{i=1}^{i=5}k_i^{\eta\omega}(\langle c_{i\eta}\rangle^\eta-K_{eq,i}^{\eta\omega}\langle c_{i\omega}\rangle^\omega)+\langle\rho_\eta\rangle^\eta\nabla\cdot\langle\mathbf{v}_\eta\rangle^\eta=0 \tag{B.1a}$$

$$\frac{\langle\rho_\omega\rangle^\omega}{\varepsilon_\omega}\frac{\partial\varepsilon_\omega}{\partial t}+\frac{\langle\rho_\sigma\rangle^\sigma\varepsilon_\sigma\overline{\mu M}}{\varepsilon_\omega}\left(\frac{\langle c_{A\sigma}\rangle^\sigma}{\langle c_{A\sigma}\rangle^\sigma+K_A}\right)-\frac{a_{\omega\eta}}{\varepsilon_\omega}\sum_{i=1}^{i=5}k_i^{\eta\omega}(\langle c_{i\eta}\rangle^\eta-K_{eq,i}^{\eta\omega}\langle c_{i\omega}\rangle^\omega)$$
$$+\langle\rho_\omega\rangle^\omega\nabla\cdot\langle\mathbf{v}_\omega\rangle^\omega=0 \tag{B.1b}$$

Each average density can be decomposed according to

$$\langle\rho_\eta\rangle^\eta=\{\rho\}+\varepsilon_\omega(\langle\rho_\eta\rangle^\eta-\langle\rho_\omega\rangle^\omega) \tag{B.2}$$

$$\langle\rho_\omega\rangle^\omega=\{\rho\}-\varepsilon_\eta(\langle\rho_\eta\rangle^\eta-\langle\rho_\omega\rangle^\omega) \tag{B.3}$$

Taking these decomposition into account, we have the following result from subtracting eqs. (B.1)

$$\{\rho\}\left(\frac{\partial \ln \varepsilon_\eta}{\partial t}-\frac{\partial \ln \varepsilon_\omega}{\partial t}+\nabla\cdot\left(\langle \mathbf{v}_\eta\rangle^\eta-\langle \mathbf{v}_\omega\rangle^\omega\right)\right)$$
$$+\left(\langle\rho_\eta\rangle^\eta-\langle\rho_\omega\rangle^\omega\right)\left(\varepsilon_\omega\frac{\partial \ln \varepsilon_\eta}{\partial t}+\varepsilon_\eta\frac{\partial \ln \varepsilon_\omega}{\partial t}+\nabla\cdot\left(\varepsilon_\omega\langle \mathbf{v}_\eta\rangle^\eta+\varepsilon_\eta\langle \mathbf{v}_\omega\rangle^\omega\right)\right)$$
$$+\frac{a_{\omega\eta}\varepsilon_{\omega\eta}}{\varepsilon_\eta\varepsilon_\omega}\sum_{i=1}^{i=5}k_i^{\eta\omega}(\langle c_{i\eta}\rangle^\eta-K_{eq,i}^{\eta\omega}\langle c_{i\omega}\rangle^\omega)-\frac{\langle\rho_\sigma\rangle^\sigma\varepsilon_\sigma\overline{\mu M}}{\varepsilon_\omega}\left(\frac{\langle c_{A\sigma}\rangle^\sigma}{\langle c_{A\sigma}\rangle^\sigma+K_A}\right)=0 \quad \text{(B.4)}$$

where, for simplicity we introduced

$$\varepsilon_{\omega\eta}=\varepsilon_\omega+\varepsilon_\eta \quad \text{(B.5)}$$

To make further progress we provide the following orders of magnitude estimates

$$\frac{a_{\omega\eta}\varepsilon_{\omega\eta}}{\varepsilon_\eta\varepsilon_\omega}\sum_{i=1}^{i=5}k_i^{\eta\omega}(\langle c_{i\eta}\rangle^\eta-K_{eq,i}^{\eta\omega}\langle c_{i\omega}\rangle^\omega)=\mathbf{O}\left(\frac{\varepsilon_{\omega\eta}}{\varepsilon_\eta\varepsilon_\omega\overline{M}}\,a_{\omega\eta}k^{\omega\eta}(\langle\rho_\eta\rangle^\eta-\langle\rho_\omega\rangle^\omega)\right) \quad \text{(B.6a)}$$

$$\frac{\langle\rho_\sigma\rangle^\sigma\varepsilon_\sigma\overline{\mu M}}{\varepsilon_\omega}\left(\frac{\langle c_{A\sigma}\rangle^\sigma}{\langle c_{A\sigma}\rangle^\sigma+K_A}\right)=\mathbf{O}\left(\phi^2\nabla\cdot\langle \mathbf{v}_\omega\rangle^\omega\right) \quad \text{(B.6b)}$$

with $k^{\omega\eta}$ being an interfacial mass transport coefficient that is on the same order of magnitude as $k_i^{\omega\eta}$ and ϕ is a Thiele modulus.

Under these circumstances we may write the following estimates

$$\{\rho\}\,\mathbf{O}\left(\frac{1}{t^*}+\frac{\langle v_\eta\rangle^\eta-\langle v_\omega\rangle^\omega}{L}+\frac{\phi^2\langle v_\omega\rangle^\omega}{L}\right)$$
$$+\left(\langle\rho_\eta\rangle^\eta-\langle\rho_\omega\rangle^\omega\right)\mathbf{O}\left(\frac{\varepsilon_\omega}{t^*}+\frac{\varepsilon_\eta}{t^*}+\frac{\varepsilon_\omega\langle v_\eta\rangle^\eta+\varepsilon_\eta\langle v_\omega\rangle^\omega}{L}+\frac{\phi^2\varepsilon_\eta\langle v_\omega\rangle^\omega}{L}+\frac{k^{\omega\eta}}{\ell_{\omega\eta}\overline{M}}\right)=0 \quad \text{(B.7)}$$

here we have assumed that $t_\eta^*=\mathbf{O}(t_\omega^*)=\mathbf{O}(t^*)$ and that $L_\eta=\mathbf{O}(L_\omega)=\mathbf{O}(L)$. In addition, we introduced

$$\ell_{\omega\eta}=\frac{\varepsilon_\omega\varepsilon_\eta}{\varepsilon_{\omega\eta}a_{\omega\eta}} \quad \text{(B.8)}$$

It follows thus,

$$\frac{\left(\langle\rho_\eta\rangle^\eta - \langle\rho_\omega\rangle^\omega\right)}{\{\rho\}} = \mathbf{O}\left\{\frac{\ell_{\omega\eta}}{L}\left[\frac{\frac{\overline{M}L}{t^* k^{\omega\eta}} + \frac{\overline{M}(\langle v_\eta\rangle^\eta - \langle v_\omega\rangle^\omega)}{k^{\omega\eta}} + \frac{\phi^2\overline{M}\langle v_\omega\rangle^\omega}{k^{\omega\eta}}}{\frac{\varepsilon_\omega\ell_{\omega\eta}\overline{M}}{k^{\omega\eta}t^*} + \frac{\varepsilon_\eta\ell_{\omega\eta}\overline{M}}{k^{\omega\eta}t^*} + \frac{\ell_{\omega\eta}}{L}\left(\frac{\varepsilon_\omega\langle v_\eta\rangle^\eta + \varepsilon_\eta\langle v_\omega\rangle^\omega}{k^{\omega\eta}/\overline{M}} + \frac{\phi^2\varepsilon_\eta\langle v_\omega\rangle^\omega\overline{M}}{k^{\omega\eta}}\right) + 1}\right]\right\} \tag{B.9}$$

Notice that the order of magnitude of the term between square braces in the above estimate is about the unity. This leads us to conclude that under the length-scale constraint

$$\frac{\ell_{\omega\eta}}{L} \ll 1 \tag{B.10}$$

it is reasonable to assume that

$$\left(\langle\rho_\eta\rangle^\eta - \langle\rho_\omega\rangle^\omega\right) \ll \{\rho\} \tag{B.11}$$

which is the justification for the local mass equilibrium assumption.

2 CONSTRAINTS FOR NEGLIGIBLE EFFECTS OF THE σ-REGION VELOCITY

2.1 MASS BALANCE EQUATION IN THE σ-REGION

The objective is to find under which condition the convective effects in Eq. (3.55c) can be neglected. To do so, the order of magnitude of the time evolution of ε_σ is needed. Applying the spatial averaging theorem to the constant quantity 1 in the σ-region leads to

$$\left\langle\frac{\partial 1}{\partial t}\right\rangle_\sigma = 0 = \frac{\partial\langle 1\rangle_\sigma}{\partial t} - \frac{1}{V}\int_{A_{\omega\sigma}} \mathbf{n}_{\sigma\omega}\cdot\mathbf{w}_{\omega\sigma}\mathrm{d}A \tag{B.12}$$

and then, with $\langle 1\rangle_\sigma = \varepsilon_\sigma$,

$$\frac{\partial\varepsilon_\sigma}{\partial t} = -\frac{1}{V}\int_{A_{\omega\sigma}} \mathbf{n}_{\omega\sigma}\cdot\mathbf{w}_{\omega\sigma}\mathrm{d}A \tag{B.13}$$

Remark: the system of equations at intermediate scale is well-posed. $\mathbf{n}_{\omega\sigma}\cdot\mathbf{w}_{\omega\sigma}$ could then be determined numerically, but not literally. Therefore, the surface integral in Eq. (B.13) cannot be expressed as a function of average quantities. Consequently, it cannot be used to obtain the time evolution of ε_σ, which is mandatory for predicting the biofilm growth.

The following order of magnitude can now be deduced

$$\langle \rho_\sigma \rangle^\sigma \frac{\partial \varepsilon_\sigma}{\partial t} = \mathbf{O}\left(\frac{\varepsilon_\sigma \langle \rho_\sigma \rangle^\sigma w_{\omega\sigma}}{l_\sigma} \right) \tag{B.14}$$

After a comparison with

$$\varepsilon_\sigma \langle \rho_\sigma \rangle^\sigma \nabla \cdot \langle \mathbf{v}_\sigma \rangle^\sigma = \mathbf{O}\left(\frac{\varepsilon_\sigma \langle \rho_\sigma \rangle^\sigma \langle v_\sigma \rangle^\sigma}{L_{v_\sigma}} \right) \tag{B.15}$$

Eq. (3.55c) can be simplified into

$$\frac{\partial \varepsilon_\sigma}{\partial t} = \frac{1}{\langle \rho_\sigma \rangle^\sigma} \frac{1}{V} \int_{A_{\omega\sigma}} \mathbf{n}_{\omega\sigma} \cdot \rho_\sigma \left(\mathbf{v}_\sigma - \mathbf{w}_{\omega\sigma} \right) \mathrm{d}A \tag{B.16}$$

when the following inequality holds

$$\frac{\langle v_\sigma \rangle^\sigma}{\mathbf{w}_{\omega\sigma}} \ll \frac{L_{v_\sigma}}{\ell_\sigma} \tag{B.17}$$

The velocity in the σ-region should then be at least an order of magnitude higher than the $\omega - \sigma$ interface velocity.

BIBLIOGRAPHY

[1] Total protein kit, micro lowry, peterson's modification.

[2] Sethuraman A, Han M, Kane RS, and Belfort G. 18 effect of surface wettability on the adhesion of proteins. *Langmuir*, 31(18):7779–7788, 2004.

[3] A.B. Abell, K.L. Willis, and D.A. Lange. Mercury intrusion porosimetry and image analysis of cement-based materials. *Journal of Colloid and Interface Science*, 211:39–44, 1999.

[4] P. Aimar and P. Bacchin. Slow colloidal aggregation and membrane fouling. *Journal of Membrane Science*, 360(1-2):70–76, Sep 2010.

[5] P. Aimar, S. Baklouti, and V. Sanchez. Membrane-solute interactions: Influence on pure solvent transfer during ultrafiltration. *Journal of membrane science*, 29:207–224, 1986.

[6] a.L. Ahmed, K.K. Lau, M.Z. Abu Bakar, and S.R. Abd. Shukor. Integrated cfd simulation of concentration polarization in narrow membrane channel. *Computers and Chemical Engineering*, 29:2087–2095, 2005.

[7] J.D. Andrade, V. Hlady, and A.P. Wei. Adsorption of complex proteins at interfaces. *Journal of Pure & Appl. Chem.*, 64(11):1777–1781, 1992.

[8] L. De Angelis and M. M. Fidalgo de Cortalezzi. Ceramic membrane filtration of organic compounds: Effect of concentration, ph, and mixtures interactions on fouling. *Separation and Purification Technology*, 118:762–775, 2013.

[9] B. A. ANNOUS, P. M. FRATAMICO, and J. L. SMITH. Quorum sensing in biofilms: Why bacteria behave the way they do. *Journal of Food Science*, 74(1):24–37, 2009.

[10] A. Al Ashhab, M. Herzberg, and O. Gillor. Biofouling of reverse-osmosis membranes during tertiary wastewater desalination: Microbial community composition. *Water Research*, 50:341–349, 2014.

[11] C.G. Auguilar-Madera, F.J Valdés-Parada, B. Goyeau, and J.A. Ochoa-Tapia. Convective heat transfer in a channel partially filled with a porous medium. *International Journal of Thermar Sciences*, 50:1355–1368, 2011.

[12] P. Bacchin, P. Aimar, and R. Field. Critical and sustainable fluxes: Theory, experiments and applications. *Journal of Membrane Science*, 281(1-2):42–69, 2008.

[13] P. Bacchin, B. Espinasse, Y. Bessiere, D. F. Fletcher, and P. Aimar. Numerical simulation of colloidal dispersion filtration: description of critical flux and comparison with experimental results. *Desalination*, 192:74–81, 2006.

[14] P Bacchin, D Si-Hassen, V Starov, M.J Clifton, and P Aimar. A unifying model for concentration polarization, gel-layer formation and particle deposition in cross-flow membrane filtration of colloidal suspensions. *Chemical Engineering Science*, 57(1):77 – 91, 2002.

[15] R. Baker. *Membrane Technology and Applications*. John wiley and sons, 2000.

[16] R. Bakke, M. G. Trulear, J.A. Robinson, and W.G. characklis. Activity of pseudomonas aroginosa in steady state biofilms. *Biotechnol. Bioeng.*, 26:1418–1424, 1984.

[17] T. Barbari. Basic principles of membrane technologies. *Journal of Membrane Science*, 72(3):211–312, Sep 1992.

[18] Y. Bashan and H. Levanony. Active attachment of azosporillumbrasilense cd to quartz sand and to a light-textured soil by protein bridging. *J. Gen. Microbial*, 134:2269–79, 1988.

[19] H.H. Beeftink and P. Staugard. Structure and dynamics of anaerobic bacterial aggregates in gas-lift reactor. *Appl. Environ. Microbiol.*, 52(5):1139–1146, 1986.

[20] D. Beer, V. O'Flaharty, J. Thaveesri, and P. Lens. Distribution of exttracellular polysaccharides and flotation of anaeerobic sludge. *Appl. Microbiol. Biotechnol.*, 46:197–201, 1996.

[21] D. Beer, P. Stoodly, and Z. Lewandowski. Effetc of biofilm structures on oxygen distribution and mass transfer. *Biotechnol. Bioeng*, 43:1131–1138, 1994.

[22] D. De Beer, P. Stoodly, and Z. Lewandowski. Liquid flow in heterogenous biofilms. *Biotechnol. Bioeng*, 44:636–641, 1994.

[23] Dirk Beer and Paul Stoodley. *Microbial Biofilms*. Springer New York, 2006.

[24] L. BÉGOIN. *Analyse de modules spirales industriels d'ultrafiltration de fluides laitiers. Physico-chimie du nettoyage de membranes en polyéthersulfone d'ultrafiltration de lait écrémé*. PhD thesis, Université de Rennes 1, Laboratoire Rennais de Chimie et Ingénierie des Procédés Université de Rennes 1, Jul 2004.

[25] B. Bendinger, H.H.M. Rijnaarts, K. Altendorf, and A.J.B. Zehnder. Physicochemical cell surface and adhesive properties of coryneform bacteria related to the presence and chain length of mycolic acids. *Appl. Environ. Microbiol*, 59:3973–77, 1993.

[26] M. Bénesse, L.L. Coq, and C. Solliec. Collection efficiency of a woven filter made of multifiber yarn: Experimental characterization during loading and clean filter modeling based on a two-tier single fiber approach. *ournal of Aerosol Science*, 37:974–989, 2006.

[27] R. B. Bird, W. E. Stewart, and E. N. Lightfoot. *Transport Phenomena*. Wiley, 2nd edition, 2006.

[28] S. Bottero, Tomas Storck, T. J. Heimovaara, M.C.M. van Loosdrecht, M.V. Enzienc, and C. Picioreanu. Biofilm development and the dynamics of preferential flow paths in porous media. *Biofouling*, 29(9):1069–1086.

[29] P. Bousquet-Melou, B. Goyeau, M. Quintard, F. Fichot, and D. Gobin. Average momentum equation for interdendritic flow in a solidifying columnar mushy zone. *International Journal of Heat and Mass Transfer*, 45(17):3651 – 3665, 2002.

[30] W. R. Bowen and T. A. Doneva. Atomic force microscopy studies of nanofiltration membranes: surface morphology, pore size distribution and adhesion. *Desalination*, 129:163–172, 2000.

[31] W. R. Bowen and Q. Gan. Properties of microfiltration membranes: Adsorption of bovine serum albumin at polyvinylidene fluoride membranes. *Journal of Colloid and Interface Science*, 144(1):254–262, jun 1991.

[32] W. R. Bowen, N. Hilal, R. W. Lovitt, and C. J. Wright. direct measurement of biological adhesion using an atomic force microscope. *Journal of Membrane Science*, 154:205–212, 1999.

[33] W.R. Bowen and A. Hermindez J.I. Calvo b. Steps of membrane blocking in flux decline during protein microfiltration. *Journal of Membrane Science*, 101:153–165, 1995.

[34] W.R. Bowen and P.M. Williams. Quantitative predictive modelling of ultrafiltration processes: colloidal science approaches. *Advances in Colloidal Interface*, 134/135:3–11, 2007.

[35] Maria G.E.G. Bremer, Jérôme Duval, Willem Norde, and Johannes Lyklema. Electrostatic interactions between immunoglobulin (igg) molecules and a charged sorbent. *Colloids and Surfaces A: Physicochemical and Engineering Aspects*, 205(1-3):29–42, 2004.

[36] P. J. Bremer, G.G. Geesey, and B. Drake. Atomic force microscopy examination of the topography of a hydrated bacterial biofilm on a copper surface. *Curr. Microbial*, 24:223–230, 1992.

[37] P.J. Bremer, G.G. Geesey, and B. Drake. Atomic force microscopy examination of the topography of a hydrated bacterial biofilm on a copper surface. *Curr. Microbial*, 24:223–230, 1992.

[38] A. Bridier, F. Dubois-Brissonnet, A. Bouberta, V. Thomas, and R. Briandet. The biofilm architecture of sixty opputunistic pathogens deciphered using a hith throughput clsm method. *Journal of Microbial Methods*, 82:64–70, 2010.

[39] J.P.F. De Bruijn, F.N. Salazar, and R. Bórquez. Membrane blocking in ultrafiltration: A new approach to fouling. *Food and Bioproducts Processing*, 83(3):211 – 219, 2005.

[40] J. Bruyers and F. Drummond. Local macromolecule diffusion coefficients in structurally non-uniform bacterial biofilms using fluorescence recovery after photobleaching (frap). *Biotechnology and Bioengineering*, 60(4):462–473, 1996.

[41] Sz.S. Bucs, A.I. Radu, V. Lavric, J.S. Vrouwenvelder, and C. Picioreanu. Effect of different commercial feed spacers on biofouling of reverse osmosismembrane systems: A numerical study. *Desalination*, 2013.

[42] Burns and Zydney. Effect of solution ph on protein transport through ultrafiltration membranes. *Biotechnol Bioeng*, 64(1):27–37, Jul 1999.

[43] A.L. Burns, D.B. Zydney. Contribution to electrostatic interactions on protein transport in membrane systems. *AIChE J.*, 47(1101), 2001.

[44] R. Chan and V. Chen. Characterization of protein fouling on membranes: opportunities and challenges. *Journal of Membrane Science*, 242(1-2):169–188, 2004.

[45] W.G. Characklis, G.A. McFeters, and K.C. Marshall. *Physiological ecology in biofilm systems*. John wiley and sons, 1990.

[46] C. Charcosset. Characterization of microporous membrane morphology using confocal scanning laser microscopy. *Chemical Engineering Science*, 55(22):5351–5358, 2000.

[47] C. Charcosset and J. Bernengo. Comparison of microporous membrane morphologies using confocal scanning laser microscopy. *Journal of Membrane Science*, 168(1-2):53–62, 2000.

[48] J. Chayen, L. Bitensky, and R. Butcher. *Practical histochemistry*. John wiley and sons, 1973.

[49] M. Cheryan. *Ultrafiltration and microfiltration handbook*. Technomic, Lancaster, USA, 1998.

[50] R.A.N. Chmielewski and J.F. Frank. Biofilm formation and control in food processing facilities. *Comprehensive Reviews in Food Science and Food Safety*, 2(1):22–32, 2003.

[51] S.W. Choi, J.Y. Yoon, S. Haam, J.K. Jung, J.H. kim, and W.S. Kim. Modeling of the permeate flux during microfiltration of bsa adsorbed microspheres in a stirred cell. *Journal of Colloid and Interface Science*, 228:270–278, 2000.

[52] B.E. Christensen and W.G. Characklis. *Physical and chemical properties of biofilms*. W.G. Characklis and K. C. Marshall, john wiley and sons, newyork edition, 1990.

[53] W. M. Clark, A. Bansal, M. Sontakke, and Y. H. Ma. Protein adsorption and fouling in ceramic ultrafiltration membranes. *Journal of Membrane Science*, 55:21–38, 1991.

[54] C.Laspidou, A. Kungolos P., and Samaras. Cellular-automata and individual-based approaches for the modeling of biofilmstructures: Pros and cons. *Desalination*, 250:390–394, 2010.

[55] M.M. Cowan, T.M. Waren, and M. Fletcher. Mixed species colonization of solid surfaces in labratory biofilms. *Biofouling*, 3:23–34, 1991.

[56] Z. Cui. Protein separation using ultrafiltration — an example of multi-scale complex systems. *China Particuology*, 3(6):343–348, 2005.

[57] Monroe D.) looking for chinks in the armor of bacterial biofilms. *PLoS. Biol*, 5(11), Monroe D.

[58] A. Danielsson, B. Norkrans, and A. Bjornsson. On bacterial adhesion-the effect of certain enzymes on adhered cells in a marine pseudomonasspecies. *Bot. Marina*, 20:7–13, 1977.

[59] D.G. Davies, M.R. Parsek, J.P. Pearson, B.H. Iglewski, J.W. Costerton, and E.P. Greenberg. The involvement of cell-to-cell signals in the development of a bacterial biofilm. *Science*, 289:295–298, 1998.

[60] Y. Davit. *Multiple-scale analysis of transport phenomena in porous media with biofilms*. PhD thesis, Université de Toulouse, 2010.

[61] C. D. de Gooijer, R. H. Wijffels, and J. Tramper. Growth and substrate consumption of nitrobacter agilis cells immobilized in carrageenan: Part 1. dynamic modeling. *Biotechnol. Bioeng.*, 38(224-231), 1991.

[62] Emilio J. de la Casa, Antonio Guadix, Rubén Ibáñez, Fernando Camacho, and Emilia M. Guadix. A combined fouling model to describe the influence of the electrostatic environment on the cross-flow microfiltration of {BSA}. *Journal of Membrane Science*, 318(1–2):247 – 254, 2008.

[63] C. de M. Coutinho, M. C. Chiu, R. C. Basso, A. P. B. Ribeiro, L. A. G. Gonçalves, and L. A. Viotto. State of art of the application of membrane technology to vegetable oils: A review. *Food Research International*, 42(5-6):536–550, 2009.

[64] A.L. Decho. Exopolymer microenvironments of microbial flora: multiple and interactive effects on trophic relationships. *Role of bacterial exopolymeric capsules in Limnol. Oceanogr.*, 38(8):1633–1645, 1993.

[65] D. Delaunay. *Nettoyage éco-efficace de membranes planes et spirales d'ultrafiltration de lait écrémé Approches physico-chimiques et hydrodynamiques concertées*. PhD thesis, L'UNIVERSITÉ DE RENNES 1, 2007.

[66] David Delaunay, Murielle Rabiller-Baudry, José M. Gozálvez-Zafrilla, Béatrice Balannec, Matthieu Frappart, and Lydie Paugam. Mapping of protein fouling by ftir-atr as experimental tool to study membrane fouling and fluid velocity profile in various geometries and validation by {CFD} simulation. *Chemical Engineering and Processing: Process Intensification*, 47(7):1106 – 1117, 2008. ¡ce:title¿Euromembrane 2006¡/ce:title¿.

[67] S. M. Ghasemi Demneh, B. Nasernejad, and H. Modarres. Modeling investigation of membrane biofouling phenomena by considering the adsorption of protein, polysaccharide and humic acid. *Colloids and Surfaces B: Biointerfaces*, 88:108–114, 2011.

[68] Q. Derekx, P. Bacchin, D. Veyret, K. Glucina, and P. Moulin. Simulation of particle capture in a microfiltration membrane. *Water Science Technology*, 64(6):1368–73, 2011.

[69] d.G. Green. Cellular automata models in biology. *Math. Comp. Mod*, 13:69–74, 1990.

[70] R. M. Donlan and J. W. Costerton. Biofilms: Survival mechanisms of clinically relevant microorganisms. *Clinical Microbiology Review*, 15(2):167–193, 2002.

[71] R.M. Donlan. Biofilms: Microbial life on surfaces. *Emerging Infectious Deseases*, 8(9):881–889, Sep 2004.

[72] R.M. Donlan, W.O. Pipes, and T.L. Yohe. Biofilm fomation on cast iron substrata in water distribution systems. *Water Res*, 28:1497–1503, 1994.

[73] C. Dreszer, H.C. Flemming, A. Zwijnenburg, J.C. Kruithof, and J.S.Vrouwenvelder. Impact of biofilm accumulation on transmembrane and feed channel pressure drop: effects of crossflow velocity, feed spacer and biodegradable nutrient. *Water Research*, 2013.

[74] Chase Duclos-Orsello, Weiyi Li, and Chia-Chi Ho. A three mechanism model to describe fouling of microfiltration membranes. *Journal of Membrane Science*, 280(1–2):856 – 866, 2006.

[75] Ulla M. Elofsson, Marie A. Paulsson, and Thomas Arnebrant. Adsorption of -lactoglobulin a and b: Effects of ionic strength and phosphate ions. *Colloids and Surfaces B: Biointerfaces*, 8(3):163 – 169, 1997.

[76] B. Espinasse, P. Bacchin, and P. Aimar. Filtration method characterizing the reversibility of colloidal fouling layers at a membrane surface. *Journal of colloid and interface science*, 320(2):483–490, 2008.

[77] Frank B. F. and Belfort G. Atomic force microscopy for low adhesion surfaces: Thermodynamic criteria, critical surface tension and intermolecular forces. *Langmuir*, 17(6):1905–1912, 2001.

[78] S. Fakhfakh, S. Baklouti, S. Baklouti, and J. Bouaziz. characterization and application in bsa solution of silica ceramic membranes. *Desalination*, 262:188–195, 2010.

[79] A.G. Fane, C.J.D. Fell, and A. Suki. The effect of ph and ionic environment on the ultrafiltration of protein solutions with retentive membranes. *Journal of Membrane Science*, 195-210, 1983.

[80] P. Fera, M.A. Siebel, W.G., and D. Prieur. Seasonal variations in bacterial colonization of stainless steel, aluminium, and polycarbonate surfaces is seawater flow system. *Biofouling*, 1:251–61, 1989.

[81] M. Ferrando, A. Rŏżek, M. Zator, F. López, and C. Güell. An approach to membrane fouling characterization by confocal scanning laser microscopy. *2005*, 250(1-2):283–293, Mar Journal of Membrane Science.

[82] M. Fletcher. *The application of interface reflection microscopy to the study of vacterial adhesion to solid surfaces*. Elsevier applied science, 1988.

[83] M. Fletcher. Attachment of pseudomonas fluorescens to glass and influence of electrolytes on bacterium-substratum separation distance. *J Bacteriol*, 170:2027–30, 1988.

[84] M. Fletcher and G.I. Leob. Influence of substratum characterization on the attachment of a marine pseudomonad to solid surfaces. *Appl. Environ. Microbiol*, 37:67–72, 1979.

[85] A. Fouladitajar, F. Zokaee Ashtiani, A. Okhovat, and B. Dabir. Membrane fouling in microfiltration of oil-in-water emulsions; a comparison between constant pressure blocking laws and genetic programming (gp) model. *Desalination*, 329:41–49, 2013.

[86] J.D. Fowler and C.R. Robertson. Hydraulic permeability of immobilized bacterial cell aggregates. *Appl. Environ. Microbiol*, 57(1):102–113, 1991.

[87] H. Fujikawa and M. Matsushita. Fractal growth of bacillus subtilis on agar plates. *J. Phys. Soc. Jpn.*, 58:3875–3878, 1989.

[88] Hiroshi Fujikawa. Diversity of the growth patterns of bacillus subtilis colonies on agar plates. {*FEMS*} *Microbiology Ecology*, 13(3):159 – 167, 1994.

[89] S. Fukuzaki, H. Urano, and K. Nagata. Adsorption of bovine serum albumin onto metal oxide surfaces. *Journal of Fermentation and Bioengineering*, 81:163–167, 1996.

[90] F. Golfier, B. D. Wood, L. Orgogozo, and M. Buès M. Quintard. Biofilms in porous media: development of macroscopic transport equations via volume averaging with closure for local mass equilibrium conditions. *Advances in water resources*, 32:463–485, 2009.

[91] W.G. Gray. A derivations of the equations for multiphase transport. *Chemical Engineering Sciences*, 30:229–233, 1975.

[92] T. Griebe and H. C. Flemming. Biocide-free antifouling strategy to protect ro membranes from biofouling. *Desalination*, 118:153–157, 1998.

[93] P.A. Gunning, A.B. Kirby, M.L. Parker, A.P. Gunning, and V.J. Morris. Comparative imaging of pseudomonas putida bacterial biofilms by scannig electrom microscopy and both dc contact and ac non-contact atomic force microscopy. *J. Appl. Bacteriol*, 81(3):276–282, 1996.

[94] M. Hasanizadeh and W.G. Gray. General conservation equations for multi-phase systems: 1. averaging procedure. *Advance in water resources*, 2:131–144, 1979.

[95] M. Hashinoa, K. Hiramia, T. Ishigamia, Y. Ohmukaia, T. Maruyamaa, N. Kubotab, and H. Matsuyamaa. Effect of kinds of membrane materials on membrane fouling with bsa. *Journal of Membrane Science*, 384:157–165, 2001.

[96] S. J. Haward, P. R. Shewry, M. J. Miles, and T. J. Mcmaster. Direct real-time imaging of protein adsorption onto hydrophilic and hydrophobic surfaces. *Biopolymers*, 93(1):74–84, 2010.

[97] Charles A. Haynes, Edward Sliwinsky, and Willem Norde. Structural and electrostatic properties of globular proteins at a polystyrene-water interface. *Journal of Colloid and Interface Science*, 164(2):394 – 409, 1994.

[98] J. Hermia. Constant pressure blocking filtration laws, application to power-law non-newtonian fluids. *Trans IChemE*, 60, 1982.

[99] C. HERRERO, P. Pradanos, J. I. Calvio, F. Tejerina, and A. Hernandez. Flux decline in protein microfiltration: Influence of operative parameters. *Journal of Colloid and Interface Science*, 187:344–355, May 1996.

[100] A. Heydorn, A. T. Nielsen, M. Hentzer, C. Sternberg, M. Givskov, B. K. Ersbøll, and S. Molin. Quantification of biofilm structures by the novel computer program comstat. *Microbiology (2000), 146,*, 146:2395–2407, 2000.

[101] N. Hilal, A. W. Mohammad, B. Atkin, and N. A. Darwish. Using atomic force microscopy towards improvement in nanofiltration membranes properties for desalination pre-treatment: a review. *Desalination*, 157:137–144, 2003.

[102] Chia-Chi Ho and A. L. Zydney. A combined pore blockage and cake filtration model for protein fouling during microfiltration. *Journal of Colloid and Interface Science*, 232(2):389–399, 2000.

[103] Chia-Chi Ho and Andrew L. Zydney. A combined pore blockage and cake filtration model for protein fouling during microfiltration. *Journal of Colloid and Interface Science*, 232(2):389 – 399, 2000.

[104] W. H. Howard and R. Lambert. Ultrafiltration in the ontario dairy industry. *Canadian Journal of Agricultural Economics*, 41(2):177–195, 1993.

[105] F.A. Howes and S. Whitaker. The spatial averaging theorem revisited. *Chemical Engineering Science*, 40:1387–1392, 1985.

[106] K M Hsieh, G A Murgel, L W Lion, and M L Shuler. Interactions of microbial biofilms with toxic trace metals: 2. prediction and verification of an integrated computer model of lead (ii) distribution in the presence of microbial activity. *Biotechnol Bioeng*, 44(2):232–9, Jun 1994.

[107] L. Huang and M.T. Morrissey. Finite elements analysis as a tool for cross flow membrane filter simulation. *Journal of Membrane Science*, 15(:19–30, 1999.

[108] I. H. Huisman and A. Hernàndez P. Pràdanos. The effect of protein-protein and protein-membrane interactions on membrane fouling in ultrafiltration. *Journal of Membrane Science*, 179(79), 2000.

[109] Kuo-Jen Hwang and Pan-Yu Sz. Filtration characteristics and membrane fouling in cross-flow microfiltration of bsa/dextran binary suspension. *Journal of Membrane Science*, 347:75–82, 2010.

[110] Kuo-Jen Hwang and Pan-Yu Sz. Effect of membrane pore size on the performance of cross-flow microfiltration of bsa/dextran mixtures. *Journal of Membrane Science*, 378:272–279, 2011.

[111] Kuo-Jen Hwang and Pan-Yu Sz. Membrane fouling mechanism and concentration effect in cross-flow microfiltration of bsa/dextran mixtures. *Chemical Engineering Journal*, 166:669–677, 2011.

[112] J. Jacob, P. Pradanos, J.I. Calvo, A. Hernandez, and G. Jonsson. Fouling kinetics and associated dynamics of structural modifications. *Colloids and Surfaces A: Physicochemical and Engineering Aspects*, 138:173–183, 1998.

[113] B. Jiaoa, A. Cassano, and E. Driolib. Recent advances on membrane processes for the concentration of fruit juices: a review. *Journal of Fod Engineering*, 63(3):303–324, 2004.

[114] R. Jiraratananon, D. Uttapap, and P. Samprranpibon. Cross-flow microfiltration of a colloidal suspension with the presence of macromolecules. *Journal of Membrane Science*, 140:57–66, 1998.

[115] K. L. Jones and C. R. O'Melia. Ultrafiltration of protein and humic substances: effect of solution chemistry on fouling and flux decline. *Journal of Membrane Science*, 193(2):163–173, 2001.

[116] Kimberly L. jones and charles R. O'melia. Protein and humic acid adsorption onti hydrophilic membrane surfaces: effects of ph anf ionic strength. *Journal of Membrane Science*, 165:31–46, 2000.

[117] B.B. Jørgensen. Diffusion processes and boundary layers in microbial mats. *Microbial Mats*, 35(243-253), 1994.

[118] B.B. Jørgensen and D;J. Des Marais. The diffusive boundary layer of sediments: oxygen microgradients over a microbial mat. *Limnol Oceanogr*, 35(6):1343–55, 1990.

[119] D. M. Kanani, X. Sun, , and R. Ghosh. Membrane fouling during microfiltration of protein solutions. *Journal of Membrane science*, 315(1-2):219, 2008.

[120] Seok-Tae Kang, E. M.V. Hoek Arun Subramani, M. A. Deshusses, and M. R. Matsumoto. Direct observation of biofouling in cross-flow microfiltration: mechanisms of deposition and release. *Journal of Membrane Science*, 244:151–165, 2004.

[121] G.E. Kapellos, T.S. Alexiou, and A.C. Payatakes. Hierarchical simulator of biofilm growth and dynamics in granular porous materials. *Advances in Watater resources*, 30:1648–1667, 2007.

[122] George E. Kapellos, Terpischori S. Alexiou, and Alkiviades C. Payatakes. a multiscale theoritical model for fluid flow in cellular biological media. *International journal of engineering science*, 51:241–271, 2012.

[123] M.C. Kaplan, A. Jegou, B. Chaufer, M. Rabiller-Baudry, and M.C. Michalsky. Adsorption of lysozyme on membrane material and cleaning with non ionic surfactant characterised through contact angle measurements. *Desalination*, 146:149–154, 2002.

[124] Martin Karlsson and Uno Carlsson. Protein adsorption orientation in the light of fluorescent probes: Mapping of the interaction between site-directly labeled human carbonic anhydrase {II} and silica nanoparticles. *Biophysical Journal*, 88(5):3536 – 3544, 2005.

[125] S.T. kelly, W.S. Opong, and A.L. Zydney. The influence of protein aggregation on the fouling of microfiltration membranes during stirred cell filtration. *Journal of Membrane Science*, 80(1-2):175–187, 1993.

[126] S.C. Kim, R. Sprung, Y. Chen, Y. Xu, H. Ball, J. Pei, T. Cheng, Y. Kho, H. Xiao, L. Xiao, N.V. Grishin, M. White, X. J.Yang, and Y. Zhao. Substrate and functional diversity of lysine acetylation revealed by a proteomics survey. *Molecular Cell*, 23(4):607–618, 2006.

[127] J.C. Kissel, P.L. Mccarty, and R.L. Street. Numerical-simulation of mixed-culture biofilm. *J. Environ. Eng*, 110:393–411, 1984.

[128] B. V. KJELLERUP, T. R. THOMSEN, J. L. NIELSEN, B. H. OLESEN, B. FRØLUND, and P. H. NIELSEN. Microbial diversity in biofilms from corroding heating systems. *Biofouling*, 21(1):19–29, 2005.

[129] M. K. Ko, K. D. Caleb, and J. Pellegrino. Determination of total protein adsorbed on solid (membrane) surface by a hydrolysis technique: single protein adsorption. *Journal of Membrane Science*, 93:21–30, 1994.

[130] J. A. Koehler, M. Ulbricht, and G. Belfort. Intermolecular forces between proteins and polymer films with relevance to filtration. *Langmuir*, 13(15):4162–4171, 1997.

[131] J. A. Koehler, M. Ulbricht, and G. Belfort. Intermolecular forces between a protein and a hydrophillic polysulfone film with relevance to filtration. *Langmuir*, 16:10419–10427, 2000.

[132] K. Konttufi and M. Vuofisto. Adsorption of globular proteins on polymeric microfiltrafion membranes. *Desalination*, 104:99–105, 1996.

[133] D.R. korber, J.R. Lawrence, B. Sutton, and D.E. Caldwell. Effect of laminar flow velocity on the kinetics of surface recolonization by mot^+ and mot^- $pseudomonas fluoroscens$. *Microb. Ecol*, 18:1–19, 1989.

[134] R. Krishna and J. A. Wesselingh. The maxwell-stefan approach to mass transfer. *Chemical Engineering Science*, 52(6):861–911, 1997.

[135] l. Zeman and A.L. Zydney. *Microfiltration and ultrafiltration: Principles and applications*. Marcel Dekker, Newyork, 1996.

[136] I. Langmuir. Vapor pressures, evaporation, condensation and adsorption. *J. Am. Chem. Soc*, 54(7):2798–2832, 1932.

[137] P. Lauger. Carrier-mediated ion transport. *Science*, 178:24–30, 1972.

[138] P. Lauger, R. Benz, G. Stark, E. Bamberg, P. C. Jordan, A. Fahr, and W. Brock. Relaxation studies of ion transport systems in lipid bilayer membranes. *Quarterly Reviews of Biophysics*, 14:513–598, 1981.

[139] J.R. Lawrence, D.R. Korber, B.D. Hoyle, J.W. Costerton, and D.E. Caldwell. Optical sectioning of microbial biofilms. *J. Bacteriol*, 173(20):6558–6567, 1991.

[140] J. Li, R.D. Sanderson, G.Y. Chai, and D.K. Hallbauer. Development of an ultrasonic technique for in situ investigating the properties of deposited protein during crossflow ultrafiltration. *Journal of Colloid and Interface Science*, 284:228–238, 2005.

[141] X. Li, Y. Zhang, and X. Fu. Adsorption of glutamicum onto polysulphone membrane. *Separation and Purification Technology*, 37:187–198, 2004.

[142] Xiufen Li, Yushan Zhang, and Xueqi Fuc. Adsorption of glutamicum onto polysulphone membrane. *Separation and Purification Technology*, 37:187–198, 2004.

[143] B. Little, P. Wagner, R.Ray, R. Pope, and R. Scheetz. Biofilms, an esem evaluation of artifacts introduced during preperation. *J. Ind. Microbiol.*, 8(4):213–222, 1991.

[144] G.I. Loeb and R.A. Neihof. Marine conditioning films. *Advances in chemistry*, 145:319–35, 1975.

[145] F.A. Lopes, P. Morin, R. Oliveira, and L. F. Melo. Interaction of desulfovibrio desulfuricans biofilms with stainless steel surface and its impact on bacterial metabolism. *Journal of Applied Microbiology*, 101:1087–1095, 2006.

[146] F.A. Lopes, P. Morin, R. Oliveira, and L.F. Melo. Impact of biofilms in simulated drinking water and urban heat supply systems. *International Journal of Envioronmental Engineering*, 1(3):276–294, 2009.

[147] D. López, H. Vlamakis, and R. Kolter. Biofilms. *Cold Spring Harbor Perspectives in Biology*, 2(7), 2010.

[148] Levia Lopez. *Ultrafiltration in rotary annular flow*. PhD thesis, Land university, Sweden, 1979.

[149] Livia Lopez and E Mathiasson. Solute adsorption as a source of fouling in ultrafiltration. *Land university press, Sweden*, pages 299–308, 1981.

[150] Rabe M, Verdes D, Rankl M, Artus GR, and Seeger S. A comprehensive study of concepts and phenomena of the nonspecific adsorption of β-lactoglobulin. *Chemphyschem*, 23(8):862–876, 2007.

[151] F. Macedonio, E. Drioli, A. A. Gusev, A. Bardow, R. Semiat, , and M. Kurihara. Efficient technologies for worldwide clean water supply. *hemical Engineering and Processing*, 51:2–17, Jan 2012.

[152] Z. Mai. *Membrane processes for water and wastewater treatment: study and modeling of interactions between membrane and organic matter*. PhD thesis, Ecole Centrale Paris, 2013.

[153] Martin Malmsten. Formation of adsorbed protein layers. *Journal of Colloid and Interface Science*, 207(2):186–199, 1998.

[154] S.S. Manickam, J. Gelb, and J.R. McCutcheon. Pore structure characterization of asymmetric membranes: Non-destructive characterization of porosity and tortuosity. *Journal of Membrane Science*, 2014.

[155] S.S. Manickam and J.R. McCutcheon. Characterization of polymeric nonwovens using porosimetry, porometry and x-ray computed tomography. *Journal of Membrane Science*, 407-408:108–115, 2012.

[156] Bernard Marcos, Christine Moresolib, Jana Skorepovab, and Brandi Vaughanb. Cfd modeling of a transient hollow fiber ultrafiltration system for protein concentration. *Journal of Membrane Science*, 337:136–144, 2009.

[157] A.D. Marshall, P.A. Munro, and G. Tragardh. The effect of protein fouling in microfiltration and ultrafiltration or permeate flux, protein retention and selectivity: a literature review. *Desalination*, 65(1):91, 1993.

[158] K.C. Marshall, R. Stout, and R. Mitchell. Mechanisms of the initial events in the sorption of marine bacteria to surfaces. *J. Gen. Microbial*, 68:337–48, 1971.

[159] F. Martinez, A. Martin, P. Pradanos, J.I. Calvo, L. Palacio, and A. Hernandez. Protein adsorption and deposition onto microfiltration membranes: The role of solute-solid interactions. *Journal of Colloid and Interface Science*, 221:254–261, 2000.

[160] E. Matiasson. The role of macromolecular adsorption in fouling of ultrafiltration membranes. *Journal of membrane science*, 16:23–36, 1983.

[161] M. Matsushita and H. Fujikawa. Diffusion-limited growth in bacterial colony formation. *Physica A*, 168:498–506, 1990.

[162] E. Matthiasson. The role of macromolecular adsorption in fouling of ultrafiltration membranes. *Journal of Membrane Science*, 16:23–36, 1983.

[163] R. Mcdonogh, G. Schaule, and H.C. Flemming. The permeability of biofouling layers on membranes. *Journal of Membrane Science*, 87:199–217, 1994.

[164] J. McGuire, V. Krisdhasima, Marie C. Wahlgren, and Thomas Arnebrant. *Comparative Adsorption Studies with Synthetic, Structural Stability and Charge Mutants of Bacteriophage T4 Lysozyme*. American Chemical Society, 1995.

[165] Joseph McGuire, Marie C. Wahlgren, and Thomas Arnebrant. Structural stability effects on the adsorption and dodecyltrimethylammonium bromide-mediated elutability of bacteriophage {T4} lysozyme at silica surfaces. *Journal of Colloid and Interface Science*, 170(1):182 – 192, 1995.

[166] M K Menon and A L Zydney. Effect of ion binding on protein transport through ultrafiltration membranes. *Biotechnol Bioeng*, 63(3):298–307, May 1999.

[167] H. Mo, K.G. Tay, and H.Y. Ng. Fouling of reverse osmosis membrane by protein (bsa): Effects of ph, calcium, magnesium, ionic strength and temperature. *Journal of Membrane Science*, 31:28–35, 2008.

[168] Huajuan Mo, Kwee Guan Tay, and How Yong Ng. Fouling of reverse osmosis membrane by protein (bsa): Effects of ph, calcium, magnesium, ionic strength and temperature. *Journal of Membrane Science*, 315:28–35, 2008.

[169] S. Mochizuki and A.L. Zydney. Sieving characteristics of albumin deposits formed during microfiltration. *Journal of Membrane Science*, 158(1):136–145, Jun 1993.

[170] K. Monkos. Viscosity of bovine serum albumin aqueous solutions as a function of temperature and concentration. *International Journal of Biological Macromolecules*, 18(1-2):61–68, 1996.

[171] E. Morin-Couallier, C. Fargues, R. Lewandowski, M. Decloux, and M.L. Lameloise. Reducing water consumption in beet distilleries by recycling the condensates to the fermentation phase. *Journal of Cleaner Production*, 16:655–663, 2008.

[172] S. Mortazavi. *Application of Membrane Separation Technology to Mitigation of Mine Effluent and Acidic Drainage*. Natural Resources Canada, 2008.

[173] M. J. Muñoz-Aguado, D. E. Wiley, and A. G. Fane. Enzymatic and detergent cleaning of a polysulfone ultrafiltration membrane fouled with bsa and whey. *Journal of Membrane Science*, 117:175–187, 1996.

[174] A. Nabe, E. Staude, and G. Belfort. Surface modification of polysulfone ultrafiltration membranes and fouling by bsa solutions. *Journal of Membrane Science*, 133:57–72, 1997.

[175] K. Nakamura and K. Matsumoto. Adsorption behavior of bsa in microfiltration with porous glass membrane. *Journal of Membrane Science*, 145:119–128, 1998.

[176] K. Nakamura and K. Matsumoto. Properties of protein adsorption onto pore surface during microfiltration: Effects of solution environment and membrane hydrophobicity. *Journal of Membrane Science*, 280:363–374, 2006.

[177] K. Nakamura and K. Matsumoto. rotein adsorption properties on a microfiltration membrane: A comparison between static and dynamic adsorption methods. *Journal of Membrane Science*, 285:126–136, 2006.

[178] K. Nakanishi, T. Sakiyama, and K. Imamura. On the adsorption of proteins on solid surfaces, a common but very complicated phenomenon. *Journal of Biosience and Bioengineering*, 91(3):233–244, 2001.

[179] T. Neu and J.R. Lawrence. Development and structure of microbial biofilms in river water studied by confocal laser scanning microscopy. *FEMS Microbial. Ecol*, 24:11–25, 1997.

[180] J.L. Nilsson. Fouling of an ultrafiltration membrane by a dissolved whey protein concentrate and some whey proteins. *Journal of Membrane Science*, 36:147–160, 1988.

[181] Willem Norde. Driving forces for protein adsorption at solid surfaces. *Macromolecular Symposia*, 103(1):5–18, 1996.

[182] Willem Norde. My voyage of discovery to proteins in flatland and beyond. *Colloids and Surfaces B: Biointerfaces*, 61(1):1 – 9, 2008.

[183] Willem Norde and Carla E Giacomelli. Bsa structural changes during homomolecular exchange between the adsorbed and the dissolved states. *Journal of Biotechnology*, 79(3):259 – 268, 2000.

[184] M. Nyström. Fouling of unmodified and modified polysulfone ultrafiltration membranes by ovalbumin. *Journal of Membrane Science*, 44:183–196, 1989.

[185] J.A. Ochoa-Tapia, J.A. del Río, and S. Whitaker. Bulk and surface diffusion in porous media, an application of the surface-averaging theorem. *Chemical Engineering Science*, 48(11):2061–2082, 1993.

[186] W.S. Opong and A.L. Zydney. Hydraulic permeability of protein layers deposited during ultrafiltration. *Journal of Colloid and Interface Science*, 142:41, 1991.

[187] S.F. Oppenheim, C.B. Phillips, and V.G.J. Rodgers. Analysis of initial protein surface coverage on fouled ultrafiltration membranes. *Journal of Colloid and Interface Science*, 184:639–651, 1996.

[188] L. Orgozozo, F. Golfier, M. Buès, and M. Quintard. Upscaling of transport process in porous media with biofilms in non-equilibrim conditions. *Advance in water resources*, 33:585–600, 2010.

[189] L. Palacio, C.-C. Hob, P. Prádanos, A. Hernández, and A.L. Zydney. Fouling with protein mixtures in microfiltration: Bsa–lysozyme and bsa–pepsin. *Journal of Membrane Science*, 222:41–51, 2003.

[190] L. Palacio, C.-C. Hob, P. Prádanos, A. Hernández, and A.L. Zydney. Fouling with protein mixtures in microfiltration: Bsa–lysozyme and bsa–pepsin. *Journal of Membrane Science*, 222:41–51, 2003.

[191] Sean P. Palecek and Andrew L. Zydney. Hydraulic permeability of protein deposits formed during microfiltration: effect of solution ph and ionic strength. *Journal of Membrane Science*, 95(1):71 – 81, 1994.

[192] D.M. Paterson. Biogenic structure of early sedimetn fabric visualized by low-temperature scanning electron microscopy. *J. Geol. Soc.*, 152:131–140, 1995.

[193] A. Persson, A.S. Jönsson, and G.Zacchi. Transmission of bsa during cross-flow microfiltration: influence of ph and salt concentration. *Journal of Membrane Science*, 223:11–21, 2003.

[194] R.J. Petersen. Review - composite reverse osmosis and nanofiltration membranes. *Journal of Membrane Science*, 83:81–150, 1993.

[195] C. Picioreanu, M.C.M. Loodrecht, and J.J. Heijnen. A new combined differential-discret cellular automaton approach for biofilm modeling: application for growth in gek beads. *Biotechnol. Bioeng.*, 57:718–731, 1998.

[196] C. Picioreanu, M.C.M. Loodrecht, and J.J. Heijnen. Discrete-differential modeling of biofilm structure. *Wat. Sci. Tech*, 58:101–116, 1999.

[197] C. Picioreanu, M.C.M. Loodrecht, and J.J. Heijnen. A theoritical study on the effect of surface roughness on mass transport and transformation in biofilms. *Biotechnol. Bioeng.*, 68:355–369, 2000.

[198] C. Picioreanu, M.C.M. Loodrecht, and J.J. Heijnen. Two-dimensional model of biofilm detachment caused by internal stress from liquid flow. *Biotechnol. Bioeng.*, 72:205–218, 2001.

[199] C Picioreanu, M C van Loosdrecht, and J J Heijnen. Mathematical modeling of biofilm structure with a hybrid differential-discrete cellular automaton approach. *Biotechnol Bioeng*, 58(1):101–16, Apr 1998.

[200] C Picioreanu, M C van Loosdrecht, and J J Heijnen. A theoretical study on the effect of surface roughness on mass transport and transformation in biofilms. *Biotechnol Bioeng*, 68(4):355–69, May 2000.

[201] C Picioreanu, M C van Loosdrecht, and J J Heijnen. Two-dimensional model of biofilm detachment caused by internal stress from liquid flow. *Biotechnol Bioeng*, 72(2):205–18, Jan 2001.

[202] Cristian Picioreanu, Jan-Ulrich Kreft, and Mark C M Van Loosdrecht. Particle-based multidimensional multispecies biofilm model. *Appl Environ Microbiol*, 70(5):3024–40, May 2004.

[203] H. Ploug and B.B. Jørgensen. A net-jet flow system for mass transfer and microsensor studies of sinking aggregates. *Marine Ecology*, 176:279–290, 1998.

[204] J.H. Pringle and M. Fletcher. Influence of substratum wettability on attachment of freshwater bacteria to solid surfaces. *Appl Environ Microbiol*, 45:811–17, 1983.

[205] P.S.Stewart, R.Murga, R.Srinivasan, and D. de beer. Biofilm structural heterogeneity visualized by three microscopic methods. *Wat. Res.*, 29(8):2006–2009, 1995.

[206] D. B. Hosaka R. L. Merson, G. Paredes. Concentrating fruit juices by reverse osmosis. *Ultrafiltration Membranes and Applications Polymer Science and Technology*, 13:405–413, 1980.

[207] Michael Rabe, Dorinel Verdes, and Stefan Seeger. Understanding of protein adsorption phenomena at solid surfaces. *Advances in Colloid and Interface Science*, 162(1–2):87 – 106, 2011.

[208] M. Rabiller-Baudry. Fractionnement de protéines en milieu modèle: mécanismes impliqués en ultrafiltration. C.F.D. Membranes (Ed.) Séminaire Fractionnement en milieu aqueux, 2013.

[209] M. Rabiller-Baudry, D. Delaunay L. Bégoin, L. Paugam, and B. Chaufer. A dual approach of membrane cleaning based on physico-chemistry and hydrodynamics: Application to pes membrane of dairy industry. *Chemical Engineering and Processing*, 47(3):267–275, 2008.

[210] A.I. radu, L. Bergwerff, M.C.M. Loodrecht, and C. Picioreanu. A two-dimensional mechanistic model for scaling in spiral wound membrane systems. *Chemical Engineering Journal*, 241:77–91, 2014.

[211] A.I. radu, J.S. Vrouwenvelder, M.C.M. Loodrecht, and C. Picioreanu. Effect of flow velocity, substrate concentration and hydraulic cleaning on biofouling of reverse osmosis feed channels. *Chemical Engineering Journal*, 188:30–39, 2014.

[212] A.I. Radu, J.S. Vrouwenvelder, M.C.M. Loodrecht, and C. Picioreanua. Modeling the effect of biofilm formation on reverse osmosis performance: flux, feed channel pressure drop and solute passage. *Journal of Membrane Science*, 365(1-2):1–15, 2010.

[213] A.I. Radu, J.S. Vrouwenvelder, M.C.M. van Loosdrecht, and C. Picioreanu. Modeling the effect of biofilm formation on reverse osmosis performance: Flux, feed channel pressure drop and solute passage. *Journal of Membrane science*, 365:1–15, 2010.

[214] M. Rahimi, S.S. Madaeni, and K. Abbasi. Cfd modeling of permeate flux in cross-flow microfiltration membrane. *Journal of Membrane Science*, 255:23–31, 2005.

[215] A. Rahimipour and S.S. Madaeni. Polyethersulfone (pes)/cellolose acetate phthalate (cap) blend ultrafiltration membranes: Preperation, morphology, performace and antifouling properties. *Journal of membrane science*, 305:299–312, 2007.

[216] B. E. Rittmann. Comparative performance of biofilm reactor types. *Biotechnol. Bioeng.*, 24:501–506, 1982.

[217] B.E. Rittmann and P.L. Mccarty. Model of steady-state-biofilm kinetics. *Biotechnol. Bioeng.*, 22(2359-2273), 1980.

[218] H.D.W. Roesink, M.A.M. Beerlage, W. Potman, Th. van den Boomgaard, M.H.V. Mulder, and C.A. Smolders. Characterization of new membrane materials by means of fouling experiments adsorption of bsa on polyetherimide-polyvinylpyrrolidone membranes. *Colloids and Surfaces*, 55:231–243, 1991.

[219] M. M. Rohani and A. L. Zydney. Effect of surface charge distribution on protein transport through semipermeable ultrafiltration membranes. *Journal of Membrane Science*, 337:324–331, 2009.

[220] M. Rosenberg and S. Kjelleberg. Hydrophobic interactions in bacterial adhesion. *Advances in Microbial ecology*, 9:353–93, 1986.

[221] S. Salgin, S. Takaç, and T.H. Özdamar. A parametric study on protein-membrane-ionic environment interactions for membrane fouling. *Separation Science Technology*, 40:1191–1212, 2005.

[222] Sema Salgın, Serpil Takaç, and Tunçer H. Özdamar. A parametric study on protein-membrane-ionic environment interaction for membrane fouling. *Separation Science Technology*, 40(1191), 2005.

[223] Sema Salgın, Serpil Takaç, and Tunçer H. Özdamar. Adsorption of bovine serum albumin on polyether sulfone ultrafiltration membranes: Determination of interfacial interaction energy and effective diffusion coefficient. *Journal of Membrane Science*, 278(1-2):251 – 260, 2006.

[224] J. E. E. Schmidt and B. K. Ahring. Extracellular polymers in granular sludge from different upflow anaerobic sludge blanket (uasb) reactors. *Applied Microbiology and Biotechnology*, 42:457–462, 1994.

[225] J. Schwinge, D.E. Wiley, and A.G. Fane. Novel spacer design improves observed flux. *Journal of Membrane Science*, 229(1-2):53–61, Feb 2004.

[226] D.A. shaw and T.J. Hanratty. Turbulent mass transfer to a wall for large schmidt numbers. *A.I.Ch.E.J*, 23:28–37, 1977.

[227] M. Simoes and M. J. Vieira L. C. Simoes b. A review of current and emergent biofilm control strategies. *LWT - Food Science and Technology*, 43:573–583, 2010.

[228] J. C. Slattery. *Advanced Transport Phenomena*. Cambridge University Press, 1999.

[229] J.C. Slattery. *Advanced Transport Phenomena*. Cambridge, 1999.

[230] P. S. Stewart, W. J. Drury, and R. Murga. Quantitative observations of heterogeneities in pseudomonas aeruginosa biofilms. *Appl. Environ. Microbiol*, 59(1):327–329, 1993.

[231] P. Stoodley, F. Jorgensen, P. Williams, and H.M. Lappin-Scott. *The role of hydrodynamics and ahl signaling molecules as determinants of structure of pseudomonas aeruginosa biofilms*. Bioline press, Cardiff, United Kingdom, 1999.

[232] P. Stoodley, Z. Lewandowski, J.D. Boyle, and H.M. Lappin-Scott. Structural deformation of bacterial biofilms by short-term fluctuations in fluid shear and in situ investigation of biofilm rheology. *Biotechnol. Bioeng.*, 65:83–92, 1999.

[233] A. Suki, A.G. Fane, and C.J.D. Fell. Flux decline in protein ultrafiltration. *Journal of Membrane Science*, 21(3):269–283, 1984.

[234] I. Sutherland. The biofilm matrix - an immobilized but dynamic microbial environment. *Trends in Microbiology*, 9:222–227, 2001.

[235] C. Y. Tang, T. H. Chong, and A. G. Fane. Colloidal interactions and fouling of nf and ro membranes: a review. *Advances in Colloid and Interface Science*, 164(1-2):126–143, 2011.

[236] K.M. Thormann, R.M. Saville, S. Shukla, D. A. Pelletier, and A.M. Spormann. Initial phases of biofilm formation in shewanella oneidensis mr-1. *Journal of bacteriology*, 186(23):8096–8104, 2004.

[237] S. Tolman, P. Meakin, and M. Matsushita. Cluster-size distribution in the incremental growth of dla clusters. *J. Phys. Soc. Jpn.*, 58:2721–2726, 1989.

[238] E. M. Tracey and R. H. Davis. Protein fouling of track-etched polycarbonate microfiltration membranes. *Journal of Colloid and Interface Science*, 167(1):104–116, Oct 1994.

[239] Shih-Chieh Tu, Varadarajan Ravindran, and Massoud Pirbazari. A pore diffusion transport model for forecasting the performance of membrane processes. *Journal of Membrane Science*, 265(1–2):29 – 50, 2005.

[240] F. J. Valdes-Parada, B. Goyeau, and J. A. Ochoa-Tapia. Diffusive mass transfer between a microporous medium and an homogeneous fluid: Jump boundary conditions. *Chemical Engineering Science*, 61(5):1692 – 1704, 2006.

[241] M. Vendruscolo and C. M. Dobson. More charges against aggregation. *Nature*, 555, 2007.

[242] J. Vicente, Y. Wyart, and P. Moulin. From 2d to 3d characterization of ceramic membranes. *Procedia Engineering*, 44:517–520, 2012.

[243] E. M. Vrijenhoek, S. Hong, and M. Elimelech. Influence of membrane surface properties on initial rate of colloidal fouling of reverse osmosis and nanofiltration membranes. *Journal of membrane science*, 188(1):115–128, 2001.

[244] J.S. Vrouwenvelder, C. Picioreanu, J.C. Kruithof, and M.C.M. Loodrecht. Biofouling in spiral wound membrane systems: Three-dimensional cfd model based evaluation of experimental data. *Journal of Membrane Science*, 346:71–85, 2010.

[245] Q. Wanga and T. Zhang. Review of mathematical models for biofilms. *Solid State Communications*, 150(21-22):1009–1022, 2010.

[246] O. Wanner. *Modeling population dynamics*. Wiley, 1989.

[247] O Wanner, A B Cunningham, and R Lundman. Modeling biofilm accumulation and mass transport in a porous medium under high substrate loading. *Biotechnol. Bioeng.*, 47(6):703–12, 1995.

[248] O Wanner, A B Cunningham, and R Lundman. Modeling biofilm accumulation and mass transport in a porous medium under high substrate loading. *Biotechnol Bioeng*, 47(6):703–12, Sep 1995.

[249] O. Wanner and W. Gujer. Competition in biofilms. *Wat. Sci. Tech*, 17:27–44, 1984.

[250] O. Wanner and W. Gujer. A multispecies biofilm model. *Wat. Sci. Tech*, 28:314–328, 1986.

[251] O. Wanner, W. Gujer. A multispecies biofilm model. *Biotechnology and Bioengineering*, 28:314–328, 1986.

[252] Christian F. Wertz and Maria M. Santore. Effect of surface hydrophobicity on adsorption and relaxation kinetics of albumin and fibrinogen: single-species and competitive behavior. *Langmuir*, 17(10):3006–3016, 2001.

[253] M. Wessling. Two-dimensional stochastic modeling of membrane fouling. *Separation and Purification Technology*, 24:375–387, 2001.

[254] S. Whitaker. The species mass jump condition at a singular surface. *Chemical Engineering Science*, 47(7):1677–1685, 1992.

[255] S. Whitaker. *The Method of Volume Averaging*. Kluwer Academic Publishers, 1999.

[256] R.H. Wijffels, C.D. de Gooijer, S. Kortekaas, and J. Tramper. Growth and substrate consumtion of nitrobacter agilis cells immobilized in carrageenan. part 2: Model evaluation. *Biotechnol. Bioeng.*, 38(232-240), 1991.

[257] S. Wolfram. Cellular automata as models for complexity. *Nature*, 311(419-424), 1984.

[258] B. D. Wood, M. Quintard, and S. Whitakerc. Estimation of adsorption rate coe!cients based on the smoluchowski equation. *Chemical Engineering Science*, 59:1905–1921, 2004.

[259] B.D. Wood, M. Quintard, and S. Whitaker. Calculation of effective diffusivities for biofilms and tissues. *Biotechnology and Bioengineering*, 77(5):495–516, 2001.

[260] B.D. Wood and S. Whitaker. Diffusion and reaction in biofilms. *Chemical Engineering Science*, 53(3):397–425, 1998.

[261] B.D. Wood and S. Whitaker. Cellular growth in biofilms. *Biotechnology and Bioengineering*, 64(6):657–670, 1999.

[262] B.D. Wood and S. Whitaker. Multi-species diffusion and reaction in biofilms and cellular media. *Chemical Engineering Science*, 55:3397–3418, 2000.

[263] Brian D Wood, Michel Quintard, and Stephen Whitaker. Calculation of effective diffusivities for biofilms and tissues. *Biotechnol Bioeng*, 77(5):495–516, Mar 2002.

[264] H. Xie, G.S. Cook, J.W. Costerton, G. Bruce, T.M. Rose, and R.J. Lamont. Intergenetic communication on dental plaque biofilms. *Journal of Bacteriology*, 182:7067–7069, 2000.

[265] P. Xu, J. E. Drewes, T.-U. Kim, C. Bellona, and G. Amy. Effect of membrane fouling on transport of organic contaminants in nf/ro membrane applications. *Journal of Membrane Science*, 279(1-2):165–175, 2006.

[266] Q. Yang, Y. Liu, and Y. Li. Control of protein (bsa) fouling in ro system by antiscalants. *Journal of Membrane Science*, 364:372–379, 2010.

[267] M. A. Yun, K. M. Yeona, J. S. Parka, Ch.H.Lee, and D. J. Lim. Characterization of biofilm structure and its effect on membrane permeability in mbr for dye wastewater treatment. *Water Research*, 40:45–52, 2006.

[268] M. Zator, M. Ferrando, F. Lopez, , and C. Guell. Membrane fouling characterization by confocal microscopy during filtration of bsa/dextran mixtures. *Journal of Membrane Science*, 301(1-2):57–66, 2011.

[269] T.C. Zhang and P.L. Bishop. Density,porosity and pore structure of biofilms. *Wat. Res.*, 28(11):2267–2277, 1994.

[270] B. Zhu, D. A. Clifford, and S. Chellam. Comparison of electrocoagulation and chemical coagulation pretreatment for enhanced virus removal using microfiltration membranes. *Water Research*, 39(13):3098–3108, 2005.

[271] Andrew L. Zydney. Stagnant film model for concentration polarization in membrane systems. *Journal of Membrane Science*, 130(1–2):275 – 281, 1997.

[272] Andrew L. Zydney. Protein separations using membrane filtration: New opportunities for whey fractionation. *International Dairy Journal*, 8(3):243 – 250, 1998.

List of Figures